Acta Pharmacologica Sinica (2011) 32: 1191–1192

www.nature.com/aps

Research Highlight

# Polymorphisms in miRNA binding site: new insight into small cell lung cancer susceptibility

Hong-yu LIU, Jun CHEN*

*Acta Pharmacologica Sinica* (2011) 32: 1191–1192; doi: 10.1038/aps.2011.124; published online 29 Aug 2011

Lung cancer is a leading cause in cancer-related deaths with less than 15% five-year survival worldwide. Small cell lung cancer (SCLC), which accounts for about 15%–18% of lung cancer, carries the worst prognosis within the lung cancer patients. SCLC differs from other lung cancers, so called non–small cell lung cancers (NSCLCs), in the specifically clinical and biologic characteristics. It exhibits aggressive behavior, with rapid growth, early spread to distant sites. Although exquisite sensitive to chemotherapy and radiation, SCLC recurs rapidly with only 5% of patients surviving five years and frequent association with distinct paraneoplastic syndromes[1].

The predominant cause of SCLC is tobacco smoking, and there is increasing information concerning molecular abnormalities involved in the pathogenesis of SCLC. Although it was proved that dominant oncogenes of the Myc family are frequently overexpressed in SCLC[2, 3], and the tumor suppressor genes (TSGs) p53 and retinoblastoma TSG are mutated and inactivated in more than 90% of SCLC[4–6], little is known about the genetic factors associated with the development of SCLC.

*Tianjin Key Laboratory of Lung Cancer Metastasis and Tumor Microenvironment; Tianjin Lung Cancer Institute; Tianjin Medical University General Hospital; Tianjin 300052, China*
* Correspondence: Jun CHEN (huntercj2004@yahoo.com)

CYP1A1 gene polymorphisms were reported to increase lung cancer risk in a high incidence region of Spain and the Thr461Asn polymorphism was associated with SCLC[7]. NQO1 protein may be involved in detoxification of free quinone which is associated with the development of SCLC. It was found in a UK population that individuals with reduced activity of the enzyme, due to a polymorphism of this gene, may increase the risk in developing the disease[8]. However, the genetic factors regulated by microRNAs (miRNAs) in development of SCLC are unclear.

miRNAs are a class of small non-coding RNA molecules that regulate gene expression through binding the 3′untranslated region (3′UTR) of mRNAs of target genes, resulting in mRNA cleavage or translation repression. It is estimated that about 30% of human genes are regulated by miRNAs[9]. As a result, miRNAs may regulate the expressions of proto-oncogenes or tumor suppressor genes, thus play important roles in tumorigenesis. Increasing evidence demonstrates that polymorphisms (SNPs) in the 3′UTR of genes targeted by miRNAs can disturb or obstruct miRNAs binding and consequentially influence regulation of the target genes, which might be associated with susceptibility to certain diseases including cancer. Xiong *et al*[10] recently identified SNPs within the 3′ UTR of miRNA genes deregulated in human SCLC, and investigated their associations with SCLC susceptibility in 666 patients with SCLC and 758 controls in a Chinese population[10]. They found that the SNP rs3134615 located in the 3′UTR of the L-MYC gene MYCL1 and the rs3134615T allele were associated with the significantly increased risk of SCLC, with the OR for carrying the GT or TT genotype being 2.08 (95% CI, 1.39–3.21; $P$=0.0004), as compared to the GG genotype. Reporter gene assays showed that MYCL1 was the target of hsa-miR-1827, which negatively regulates MYCL1 expression. The rs3134615 G to T change may inhibit the interaction of hsa-miR-1827 with MYCL1 3′UTR, resulting in higher constitutive expression of MYCL1. Because MYCL1 is a member of MYC oncogene family that play a critical role in carcinogenesis, individuals carrying the rs3134615 T allele would be expected to have elevated risk for the development of SCLC.

The results of Xiong *et al* provide a new insight into SCLC tumorigenesis and have potential implication in early detection and target treatment of SCLC.

1 van Meerbeeck JP, Fennell DA, De Ruysscher DK. Small-cell lung cancer. Lancet 2011 doi:10.1016/S0140-6736(11)60165–7.
2 Johnson BE, Russell E, Simmons AM, Phelps R, Steinberg SM, Ihde DC, *et al*. MYC family DNA amplification in 126 tumor cell lines from patients with small cell lung cancer. J Cell Biochem Suppl 1996; 24: 210–7.
3 Rygaard K, Vindeløv LL, Spang-Thomsen M.

Expression of myc family oncoproteins in small-cell lung-cancer cell lines and xenografts. Int J Cancer 1993; 54: 144–52.
4 Lohmann D, Pütz B, Reich U, Böhm J, Präuer H, Höfler H. Mutational spectrum of the p53 gene in human small-cell lung cancer and relationship to clinicopathological data. Am J Pathol 1993; 142: 907–15.
5 Jacobson DR, Fishman CL, Mills NE. Molecular genetic tumor markers in the early diagnosis and screening of non-small-cell lung cancer. Ann Oncol 1995; 6: S3–8..
6 Wistuba II, Gazdar AF, Minna JD.Molecular genetics of small cell lung carcinoma. Semin Oncol 2001; 28: 3–13.
7 San Jose C, Cabanillas A, Benitez J, Carrillo JA, Jimenez M, Gervasini G. CYP1A1 gene polymorhisms increase lung cancer risk in a high-incidence region of Spain: a case control study. BMC Cancer 2010; 10: 463.
8 Lewis SJ, Cherry NM, Niven RM, Barber PV, Povey AC. Polymorphisms in the NAD(P)H: quinone oxidoreductase gene and small cell lung cancer risk in a UK population. Lung Cancer 2001; 34: 177–83.
9 Winter J, Diederichs S. MicroRNA biogenesis and cancer. Methods Mol Biol 2011; 676: 3–22.
10 Xiong F, Wu C, Chang J, Yu D, Xu B, Yuan P, *et al*. Genetic variation in an miRNA-1827 binding site in MYCL1 alters susceptibility to small cell lung cancer. Cancer Res 2011; 71: 5175–81.

Acta Pharmacologica Sinica (2011) 32: 1193–1198
 1671-4083/11 $32.00
www.nature.com/aps

Review

# Genetic polymorphisms in Kawasaki disease

Ho-chang KUO[1, 2], Wei-chiao CHANG[3, 4, *]

[1]*Division of Allergy, Immunology and Rheumatology, Department of Pediatrics, Kaohsiung Chang Gung Memorial Hospital and* [2]*College of Medicine, Chang Gung University, Kaohsiung, Taiwan, China;* [3]*Department of Medical Genetics, Kaohsiung Medical University, Taiwan, China;* [4]*Cancer Center, Kaohsiung Medical University Hospital, Kaohsiung, Taiwan, China*

Kawasaki disease (KD) is an acute febrile systemic vasculitis, and the cause of KD is not well understood. It is likely due to multiple interactions between genes and environmental factors. The development of genetic association and genome-wide association studies (GWAS) has opened an avenue to better understanding the molecular mechanisms underlying KD. A novel ITPKC signaling pathway was recently found to be responsible for the susceptibility to KD. Furthermore, the GWAS demonstrated the functionally related susceptibility loci for KD in the Caucasian population. In the last decade, the identification of several genomic regions linked to the pathogenesis of KD has made a major breakthrough in understanding the genetics of KD. This review will focus on genetic polymorphisms associated with KD and describe some of the possible clinical implications and molecular mechanisms that can be used to explain how genetic variants regulate the pathogenesis in KD.

**Keywords:** Kawasaki disease; coronary artery lesions; intravenous immunoglobulin; genetics; SNP

*Acta Pharmacologica Sinica* (2011) 32: 1193–1198; doi: 10.1038/aps.2011.93; published online 5 Sep 2011

## Introduction

Kawasaki disease (KD)[1] is an acute, febrile systemic vasculitis that was first described by Kawasaki *et al*[2]. In developed countries, it is the leading cause of acquired heart diseases in children, though its etiology remains unknown[3–5]. KD occurs worldwide, most commonly in Asian countries, and mainly affects children less than 5 years of age. Japan, Korea, and Taiwan region have the highest incidence of KD ranging from 69 to 213 cases per 100 000 children under 5 years of age[6–8]. The incidence of KD has been increasing globally in recent years. The most serious complications of KD are coronary artery lesions (CAL), including myocardial infarction, coronary artery fistula formation[9], coronary artery dilatation/ectasia and coronary artery aneurysm[10].

The clinical characteristics of KD patients include prolonged fever longer than five days, diffuse mucosal inflammation, bilateral non-purulent conjunctivitis, dysmorphous skin rashes, indurative angioedema over the hands and feet, and cervical lymphadenopathy. In addition to the diagnostic criteria, there is a broad range of non-specific clinical features, including irritability, uveitis, aseptic meningitis, cough, vomiting, diarrhea, abdominal pain, gallbladder hydrops, urethritis, arthralgia, arthritis, hypoalbuminemia[5], liver function impairment and heart failure[4, 11].

Although the clinical features of KD are recognizable, the immuno-pathogenetic mechanism of this disease is still unclear, particularly the causative agent for CAL formation. Transforming growth factor-beta (TGF-β) is a candidate gene for KD pathogenesis because TGF-β-mediated T-cell activation and cardiovascular remodeling are regarded as important features of KD. Indeed, genetic polymorphisms of the TGF-β pathway, including *TGFB2*, *TGFBR2*, and *SMAD3*, are associated with susceptibility to KD and development of CAL in the European and US populations[12]. In the Asian population, we reported that monocytosis, eosinophilia, and eosinophil-related Th2 immune response (especially, plasma level of IL-5) are associated with CAL formation and/or initial intravenous immunoglobulin (IVIG) treatment response[13–16]. Immune-related genes, such as *CTLA-4*, *CASP3* and *ITPKC*, have also been suggested to influence the susceptibility to and the clinical status of KD[14, 15, 17–21].

The efficacy of IVIG administered during the acute phase of KD to reduce the prevalence of coronary artery abnormalities has been well established[22]. However, the mechanism of action of IVIG is still elusive. IVIG appears to have a generalized anti-inflammatory effect. Possible mechanisms of IVIG include the modulation of cytokine production, neutralization of bacterial super-antigens, suppression of antibody synthesis and inflammatory markers (CD40L, nitric oxide and iNOS expression)[23, 24], and provision of anti-idiotypic

* To whom correspondence should be addressed.
E-mail wcc@kmu.edu.tw
Received 2011-04-18 Accepted 2011-06-08

antibodies[9, 13, 16].

## The role of genetic polymorphisms in immune-related genes in the susceptibility to Kawasaki disease

The higher incidence of KD in Asia, in conjunction with a higher incidence of the disease in Asian descendants compared with other ethnic populations in the United States and Europe, suggests that a genetic predisposition might play an important role in the susceptibility to this disease[3, 4, 7, 10, 25–27]. There is also evidence that the incidence of KD is higher among siblings than in the general population[28]. Additionally, KD has a higher incidence rate among males than in females[5, 19]. Further evidence supports the hypothesis that genetic factors contribute to the susceptibility to KD[17]. For example, a number of genes have been reported to have significant associations with the susceptibility to KD in different populations. For instance, single nucleotide polymorphisms (SNPs) in the monocyte chemoattractant protein 1 (*MCP-1*)[29], *IL-10*[30–32], *CD40L*[33], *IL-4*[26], *CASP3*[20, 34], *IL-18*[35], *IL-1B*[36], *HLA-E*[37], C-C chemokine receptor 5 (*CCR5*)[38], and inositol 1, 4, 5-trisphosphate 3-kinase C (*ITPKC*)[21, 39] have been reported to be associated with the development of KD. In early 2011, Shimizu *et al*[12] first reported that genetic polymorphisms of TGFB2, TGFBR2, and SMAD3 are associated with susceptibility to Kawasaki disease and the development of coronary artery lesions. Taken together, these findings suggest that multiple polymorphic alleles influence KD susceptibility and that different ethnic populations, which have distinct allelic expression patterns, and different sexes may have different susceptibilities to KD[3]. Interestingly, there are some genes associated with susceptibility to KD, but not CAL formation. We hypothesize that the genes responsible for susceptibility and CAL formation may be distinct[20, 39, 40].

## Association between the genetic polymorphisms and CAL formation in KD

All KD patients were treated with IVIG, 2 g/kg in a single infusion for 12 h, together with aspirin[22]. This therapy was within 10 d of illness and, if possible, within 7 d of illness. From a serial analysis of coronary artery lesions ($n$=341) in Chang Gung Memorial Hospital-Kaohsiung[20], 35% of KD patients had dilatation during the acute phase, 17.2% had dilatation one month after disease onset, 10.2% still had dilatation at two months of follow-up, and 4% had persistent CAL for more than one year[39].

The most commonly used definition of CAL (also known as coronary artery abnormality, CAA or CALs) is based on the Japanese Ministry of Health criteria: maximum absolute internal diameter >3 mm in children younger than 5 years of age or >4 mm in children 5 years and older, or a segment 1.5 times larger than an adjacent segment, or the presence of luminal irregularity[41–43]. If the body surface area is known, then coronary arteries are normalized to this surface area and expressed as standard deviation units from the mean (Z scores)[44]. Several studies have analyzed CAL using other methods, including the aorta route dimension[12] and transient CAL (although the definition of "transient" varies among studies, from 30 d to 6–8 weeks after disease). Interestingly, some results have indicated that the genetic association was observed only with susceptibility, not with CAL formation. However, other studies have revealed inconsistent results (Table 1)[45–57]. These results indicate that the genes responsible for susceptibility and CAL formation may be different between populations[7, 32, 37, 38, 58–60]. Recently, several candidate genes have been proposed for

**Table 1.** Genes associated with susceptibility or coronary artery lesion (CAL) formation in KD.

| Gene | Abbreviation | Locus | Phenotypes | Reference |
|---|---|---|---|---|
| C-reactive protein | CRP | 1q21-q23 | Susceptibility | Cheung[59] |
| Tissue inhibitor of metalloproteinase 4 | TIMP4 | 3p25 | CAL | Ban[60] |
| C-C chemokine receptor 5 | CCR5 | 3p21 | Susceptibility | Jhang[38] |
| Angiotensin-II type-1 receptor | AGTR1 | 3q21-q25 | CAL | Fukazawa[45] |
| Vascular endothelial growth factor receptor 2 | VEGFR2 | 4q12 | CAL | Kariyazono[46] |
| Interleukin-4 | IL-4 | 5q31.1 | Susceptibility | Burns[26] |
| CD14 antigen | CD14 | 5q31.1 | CAL | Nishimura[47] |
| Vascular endothelial growth factor A | VEGFA | 6p12 | Susceptibility | Hsueh[48] |
| | | | CAL | Kariyazono[46] |
| Lymphotoxin-alpha | LTA | 6p21.3 | Susceptibility | Quasney[49] |
| Tumor necrosis factor-alpha | TNF-α | 6p21.3 | CAL | Quasney[49] |
| Interleukin-18 | IL-18 | 11q22.3-q22.3 | Susceptibility | Hsueh[51] |
| Matrix metalloproteinase-3 | MMP3 | 11q22.3 | CAL | Park[52] |
| Matrix metalloproteinase-13 | MMP13 | 11q22.3 | CAL | Ikeda[53] |
| Angiotensin-1 converting enzyme | ACE | 17q23 | Susceptibility | Wu[54] |
| | | | | Shim[55] |
| | | | CAL | Fukazawa[45] |
| Tissue inhibitor of metalloproteinase 2 | TIMP2 | 17q25 | CAL | Furuno[56] |
| Macrophage migration inhibitory factor | MIF | 22q11.2 | CAL | Simonini[57] |
| CD40 ligand | CD40L | Xq26 | CAL | Onouchi[33] |

the susceptibility to KD or the formation of CAL in different populations. Although there is evidence to support a role for each candidate gene in the susceptibility to KD and/or development of CAL, there is also evidence that cannot be easily fitted into any (Table 2). Most studies addressing this question are plagued with inconsistencies. First, the sample size varies dramatically across studies. Hence, a small sample size may not have sufficient power to detect minor genetic effects. Second, it is becoming clear that there are different genetic backgrounds within populations that due to variations in allele frequencies or heterogeneity of the phenotype, may also influence the results. Third, the incidence of KD in Asia is much higher than in other places. Thus, the role of environmental factors or infectious agents in the development of KD should also be considered.

## Genetic polymorphisms of the ITPKC signaling pathway in patients with Kawasaki disease

A major advancement in the genetic study of KD was provided by the discovery of *ITPKC*. ITPKC is an important molecule in the regulation of T cell activation, and it may function as a calcium channel modulator[21]. In 2008, Onouchi and colleagues first identified the functional polymorphism of *ITPKC* (rs28493229) that is significantly associated with the susceptibility to KD and coronary artery lesions in both Japanese and US children[21, 61]. Using cell-based functional studies, Onouchi *et al* further indicated that the risk allele (C allele) of ITPKC reduces the splicing efficiency of the *ITPKC* mRNA that, in turn, may contribute to the hyperactivation of $Ca^{2+}$-dependent NFAT pathways in T cells[21]. The identification of *ITPKC* has had an enormous effect on the field of genetic association studies of KD. These novel insights into genetic mechanism clearly provide a new understanding of the pathogenesis of KD. In contrast, the results obtained from the replication studies in the Taiwanese populations are strikingly controversial[62, 63]. A similar approach was taken by Chi *et al*[62]. These authors genotyped 385 KD patients and 1158 normal subjects. However, there were no significant differences in the genotype of rs28493229 between the controls and children with KD. The results from a study by Lin *et al*[63] in another independent medical center in Taipei indicated that the C allele of rs28493229 is associated with KD susceptibility. Recently, new results using meta-analysis showed that the rs28493229 SNP of *ITPKC* is associated with the susceptibility to KD in the Taiwanese population[39]. Regarding to the controversial results obtained for *ITPKC* genetic association studies in the Taiwanese population, we attribute them to population migration, due to the increase in genetic diversity between cities in the south or north of Taiwan[39].

*ITPKC* is involved in the $Ca^{2+}$-dependent NFAT signaling pathways in T cells[21]. In the non-excitable cells, such as T cells and mast cells, one of the main pathways to increase the intracellular $Ca^{2+}$ concentration is through store-operated calcium channels (SOC)[64]. The activation of store-operated calcium channels can be controlled by the expression level of $IP_3$. $IP_3$ binds to its receptor ($IP_3R$) on the endoplasmic reticulum (also called the calcium store) causing the release of calcium from stores[64]. An empty store results in the activation of both store-operated calcium channels and $Ca^{2+}$-dependent signaling pathways, including inflammatory reactions[65, 66] and apoptosis[64]. Onouchi *et al* reported that a G to A substitution in the 5′-untranslated region of *CASP3* (rs72689236) is associated with susceptibility to Kawasaki disease in Japanese and in Americans of European descent[34]. The *CASP3* (rs72689236) is replicated in the KD patients in the Taiwanese population. Kuo *et al* provided further evidence that the A allele of rs72689236 is very likely to be a risk allele in the development of aneurysms in patients with KD[20].

Another important molecule in the *ITPKC* signaling pathway is *ORAI1* (also known as *CRACM1*). *ORAI1* was identified by Feske *et al* in 2006[67]. Modified linkage analysis completed on data generated by single-nucleotide polymorphism arrays and an RNA interference screen led to an important finding. A single missense mutation in *ORAI1* was found in patients with severe combined immune deficiency (SCID) syndrome[67]. Furthermore, this mutation in *ORAI1* has been shown to cause dysfunctions in $Ca^{2+}$ release-activated $Ca^{2+}$ (CRAC) channels and impairs the immune system[67]. In 2011, a genetic polymorphism of *ORAI1* was reported to be associated with the risk and recurrence of calcium nephrolithiasis[68]. In the study of Kawasaki disease, no significant association between genotype and allele frequency of the five

**Table 2.** Controversial genetic effects on the susceptibility to KD or CAL formation between populations.

| Gene | Abbreviation | Locus | Phenotypes | Reference |
|---|---|---|---|---|
| Fc gamma receptor, low affinity IIIa receptor | FCGR3A | 1q23 | Susceptibility | Taniuchi[75]<br>Biezeveld[76] |
| Fc gamma receptor, low affinity IIa receptor | FCGR2A | 1q23 | CAL | Taniuchi[75]<br>Biezeveld[76] |
| Interleukin-10 | IL-10 | 1q31-q32 | Susceptibility<br>CAL | Hsueh[32]<br>Jin[58] |
| Tumor necrosis factor-alpha | TNF-alpha | 6p21.3 | CAL | Cheung[59]<br>Quasney[49] |
| CD40 ligand | CD40L | Xq26 | CAL | Onouchi[33]<br>Huang[77] |

*ORAI1* tSNPs was found. Additionally, there is no association between *ORAI1* polymorphisms and CAL formation or IVIG treatment responses[69]. However, this lack of association does not rule out the possibility that other genes in the ITPKC signaling pathways might contribute to the susceptibility or clinical status (CAL or IVIG treatment responses) of KD (Figure 1). For example, a mutation in *STIM1*, a key molecule in the regulation of SOC, has also been reported to be associated with an immunodeficiency syndrome[70]. Therefore, identification of genetic polymorphisms for *STIM1* and other genes related to the *ITPKC* pathway by direct DNA sequencing in a larger population may be helpful to better understand the pathogenesis of KD.

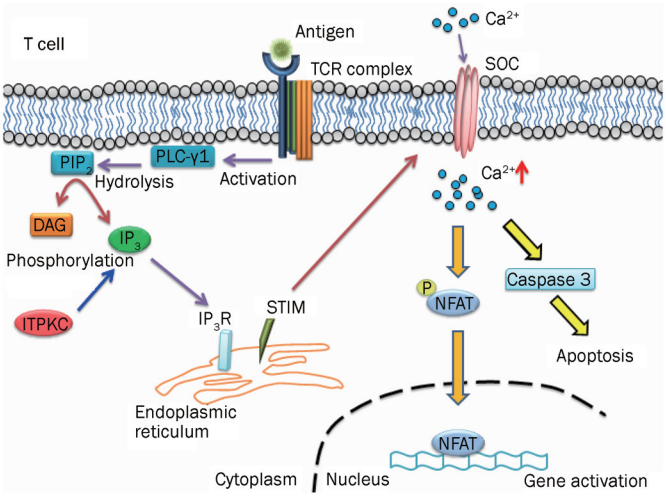


**Figure 1.** Model depicting the cellular pathways of ITPKC in T cells.

## Genome-wide association study (GWAS) in Kawasaki disease

In 2009, Burgner *et al* firstly performed a genome-wide association study (GWAS) on 119 Caucasian KD cases and 135 matched controls. Forty SNPs and six haplotypes were confirmed in an independent cohort of KD families[71]. This insightful work led to the identification of a SNP within the N-acetylated alpha-linked acidic dipeptidase-like 2 gene (*NAALADL2*; rs17531088), which was significantly associated with the susceptibility to KD. Although the function of *NAALADL2* remains unclear, mutations in the gene may be involved in the development of Cornelia de Lange syndrome[72]. In 2010, another GWAS was conducted by Kim *et al* in a Korean population. A total of 786 subjects (186 KD patients and 600 controls) were recruited. A locus in the 1p31 region was identified as a susceptibility locus for KD. Furthermore, the *PELI1* gene locus in the 2p13.3 region was confirmed to associate with the development of CAL in KD patients[73]. GWAS results from a Taiwanese population suggest another three novel susceptibility loci for KD[74]. However, the susceptibility loci reported by Kim *et al* in the Korean population cannot be replicated in a Taiwanese or Caucasian population. Hence, the results of the GWAS from independent groups support the hypothesis that susceptibility loci for KD and CAL formation can be distinct between different ethnic populations.

## Conclusion

Several major advances have been made in understanding the genetic effects of the susceptibility and clinical status of KD over the past decade. Very recently, genome-wide association has led two groups to identify novel susceptibility loci as being important for KD in the Asian population. Although the exact genes in the loci are still unclear at present, these loci could provide a new direction for future studies. Now that the sequencing of the human genome is complete and advanced genotyping tools are readily available to help identify candidate genes, we can expect to see more insightful researches begin to elucidate the genes responsible for KD susceptibility.

## Acknowledgements

This study was partly supported by funding from an Excellence for Cancer Research Center grant, Department of Health, Executive Yuan, Taiwan, China (No DOH100-TD-C-111-002), and a grant (NSC 100-2320-B-037-002) from the National Science Council, Taiwan, China, to Wei–chiao CHANG. A grant (NSC 98-2314-B-182A-004-MY3) from the National Science Council of Taiwan and a grant (NSC 100-2314-B-182A-048 -MY3) from Chang Gung Memorial Hospital, Taiwan, China (CMRPG891441 and CMRPG891241) also helped to support this study.

## References

1 Kawasaki T. Acute febrile mucocutaneous syndrome with lymphoid involvement with specific desquamation of the fingers and toes in children. Arerugi 1967; 16: 178–222.
2 Kawasaki T, Kosaki F, Okawa S, Shigematsu I, Yanagawa H. A new infantile acute febrile mucocutaneous lymph node syndrome (MLNS) prevailing in Japan. Pediatrics 1974; 54: 271–6.
3 Wang CL, Wu YT, Liu CA, Kuo HC, Yang KD. Kawasaki disease: infection, immunity and genetics. Pediatr Infect Dis J 2005; 24: 998–1004.
4 Burns JC, Glode MP. Kawasaki syndrome. Lancet 2004; 364: 533–44.
5 Kuo HC, Liang CD, Wang CL, Yu HR, Hwang KP, Yang KD. Serum albumin level predicts initial intravenous immunoglobulin treatment failure in Kawasaki disease. Acta Paediatr 2010; 99: 1578–83.
6 Park YW, Han JW, Park IS, Kim CH, Cha SH, Ma JS, *et al*. Kawasaki disease in Korea, 2003–2005. Pediatr Infect Dis J 2007; 26: 821–3.
7 Huang WC, Huang LM, Chang IS, Chang LY, Chiang BL, Chen PJ, *et al*. Epidemiologic features of Kawasaki disease in Taiwan, 2003–2006. Pediatrics 2009; 123: e401–5.
8 Nakamura Y, Yashiro M, Uehara R, Oki I, Kayaba K, Yanagawa H. Increasing incidence of Kawasaki disease in Japan: nationwide survey. Pediatr Int 2008; 50: 287–90.
9 Liang CD, Kuo HC, Yang KD, Wang CL, Ko SF. Coronary artery fistula associated with Kawasaki disease. Am Heart J 2009; 157: 584–8.
10 Newburger JW, Takahashi M, Gerber MA, Gewitz MH, Tani LY, Burns JC, *et al*. Diagnosis, treatment, and long-term management of Kawasaki disease: a statement for health professionals from the Committee on Rheumatic Fever, Endocarditis and Kawasaki Disease, Council on

Cardiovascular Disease in the Young, American Heart Association. Circulation 2004; 110: 2747–71.
11 Liu YC, Hou CP, Kuo CM, Liang CD, Kuo HC. Atypical kawasaki disease: literature review and clinical nursing. Hu Li Za Zhi 2010; 57: 104–10.
12 Shimizu C, Jain S, Davila S, Hibberd ML, Lin KO, Molkara D, *et al*. Transforming growth factor-beta signaling pathway in patients with Kawasaki disease. Circ Cardiovasc Genet 2011; 4: 16–25.
13 Kuo HC, Wang CL, Liang CD, Yu HR, Chen HH, Wang L, *et al*. Persistent monocytosis after intravenous immunoglobulin therapy correlated with the development of coronary artery lesions in patients with Kawasaki disease. J Microbiol Immunol Infect 2007; 40: 395–400.
14 Kuo HC, Wang CL, Liang CD, Yu HR, Huang CF, Wang L, *et al*. Association of lower eosinophil-related T helper 2 (Th2) cytokines with coronary artery lesions in Kawasaki disease. Pediatr Allergy Immunol 2009; 20: 266–72.
15 Kuo HC, Wang CL, Wang L, Yu HR, Yang KD. Patient characteristics and intravenous immunoglobulin product may affect eosinophils in Kawasaki disease. Pediatr Allergy Immunol 2008; 19: 184–5.
16 Kuo HC, Yang KD, Liang CD, Bong CN, Yu HR, Wang L, *et al*. The relationship of eosinophilia to intravenous immunoglobulin treatment failure in Kawasaki disease. Pediatr Allergy Immunol 2007; 18: 354–9.
17 Yu HR, Kuo HC, Sheen JM, Wang L, Lin IC, Wang CL, *et al*. A unique plasma proteomic profiling with imbalanced fibrinogen cascade in patients with Kawasaki disease. Pediatr Allergy Immunol 2009; 20: 699–707.
18 Kuo HC, Liang CD, Yu HR, Wang CL, Lin IC, Liu CA, *et al*. CTLA-4, position 49 A/G polymorphism associated with coronary artery lesions in Kawasaki disease. J Clin Immunol 2011; 31: 240–4.
19 Yu HR, Kuo HC, Huang EY, Liang CD, Hwang KP, Lin IC, *et al*. Plasma clusterin levels in predicting the occurrence of coronary artery lesions in patients with Kawasaki disease. Pediatr Cardiol 2010; 31: 1151–6.
20 Kuo HC, Yu HR, Juo SH, Yang KD, Wang YS, Liang CD, *et al*. CASP3 gene single-nucleotide polymorphism (rs72689236) and Kawasaki disease in Taiwanese children. J Hum Genet 2011; 56: 161–5.
21 Onouchi Y, Gunji T, Burns JC, Shimizu C, Newburger JW, Yashiro M, *et al*. ITPKC functional polymorphism associated with Kawasaki disease susceptibility and formation of coronary artery aneurysms. Nat Genet 2008; 40: 35–42.
22 Newburger JW, Takahashi M, Beiser AS, Burns JC, Bastian J, Chung KJ, *et al*. A single intravenous infusion of gamma globulin as compared with four infusions in the treatment of acute Kawasaki syndrome. N Engl J Med 1991; 324: 1633–9.
23 Wang CL, Wu YT, Liu CA, Lin MW, Lee CJ, Huang LT, *et al*. Expression of CD40 ligand on $CD4^+$ T-cells and platelets correlated to the coronary artery lesion and disease progress in Kawasaki disease. Pediatrics 2003; 111: E140–7.
24 Wang CL, Wu YT, Lee CJ, Liu HC, Huang LT, Yang KD. Decreased nitric oxide production after intravenous immunoglobulin treatment in patients with Kawasaki disease. J Pediatr 2002; 141: 560–5.
25 Nakamura Y, Yashiro M, Uehara R, Oki I, Watanabe M, Yanagawa H. Epidemiologic features of Kawasaki disease in Japan: results from the nationwide survey in 2005–2006. J Epidemiol 2008; 18: 167–72.
26 Burns JC, Shimizu C, Shike H, Newburger JW, Sundel RP, Baker AL, *et al*. Family-based association analysis implicates IL-4 in susceptibility to Kawasaki disease. Genes Immun 2005; 6: 438–44.
27 Yanagawa H, Nakamura Y, Yashiro M, Oki I, Hirata S, Zhang T, *et al*. Incidence survey of Kawasaki disease in 1997 and 1998 in Japan. Pediatrics 2001; 107: E33.
28 Dergun M, Kao A, Hauger SB, Newburger JW, Burns JC. Familial occurrence of Kawasaki syndrome in North America. Arch Pediatr Adolesc Med 2005; 159: 876–81.
29 Jibiki T, Terai M, Shima M, Ogawa A, Hamada H, Kanazawa M, *et al*. Monocyte chemoattractant protein 1 gene regulatory region polymorphism and serum levels of monocyte chemoattractant protein 1 in Japanese patients with Kawasaki disease. Arthritis Rheum 2001; 44: 2211–2.
30 Weng KP, Hsieh KS, Hwang YT, Huang SH, Lai TJ, Yuh YS, *et al*. IL-10 polymorphisms are associated with coronary artery lesions in acute stage of Kawasaki disease. Circ J 2010; 74: 983–9.
31 Hsieh KS, Lai TJ, Hwang YT, Lin MW, Weng KP, Chiu YT, *et al*. IL-10 promoter genetic polymorphisms and risk of Kawasaki disease in Taiwan. Dis Markers 2011; 30: 51–9.
32 Hsueh KC, Lin YJ, Chang JS, Wan L, Tsai YH, Tsai CH, *et al*. Association of interleukin-10 A-592C polymorphism in Taiwanese children with Kawasaki disease. J Korean Med Sci 2009; 24: 438–42.
33 Onouchi Y, Onoue S, Tamari M, Wakui K, Fukushima Y, Yashiro M, *et al*. CD40 ligand gene and Kawasaki disease. Eur J Hum Genet 2004; 12: 1062–8.
34 Onouchi Y, Ozaki K, Buns JC, Shimizu C, Hamada H, Honda T, *et al*. Common variants in CASP3 confer susceptibility to Kawasaki disease. Hum Mol Genet 2010; 19: 2898–906.
35 Chen SY, Wan L, Huang YC, Sheu JJ, Lan YC, Lai CH, *et al*. Interleukin-18 gene 105A/C genetic polymorphism is associated with the susceptibility of Kawasaki disease. J Clin Lab Anal 2009; 23: 71–6.
36 Weng KP, Hsieh KS, Ho TY, Huang SH, Lai CR, Chiu YT, *et al*. IL-1B polymorphism in association with initial intravenous immunoglobulin treatment failure in Taiwanese children with Kawasaki disease. Circ J 2010; 74: 544–51.
37 Lin YJ, Wan L, Wu JY, Sheu JJ, Lin CW, Lan YC, *et al*. HLA-E gene polymorphism associated with susceptibility to Kawasaki disease and formation of coronary artery aneurysms. Arthritis Rheum 2009; 60: 604–10.
38 Jhang WK, Kang MJ, Jin HS, Yu J, Kim BJ, Kim BS, *et al*. The CCR5 (-2135C/T) polymorphism may be associated with the development of Kawasaki disease in Korean children. J Clin Immunol 2009; 29: 22–8.
39 Kuo HC, Yang KD, Juo SH, Liang CD, Chen WC, Wang YS, *et al*. ITPKC single nucleotide polymorphism associated with the Kawasaki disease in a Taiwanese population. PLoS One 2011; 6: e17370.
40 Kuo HC, Wu CC, Yang TH, Yu HR, Liang CD, Chen YJ, *et al*. Non-Langerhans cell histiocytosis in a child with Kawasaki disease. BMJ Case Reports 2009; doi:10.1136/bcr.11.2008.1227.
41 Akagi T, Rose V, Benson LN, Newman A, Freedom RM. Outcome of coronary artery aneurysms after Kawasaki disease. J Pediatr 1992; 121: 689–94.
42 Shulman ST, De Inocencio J, Hirsch R. Kawasaki disease. Pediatr Clin North Am 1995; 42: 1205–22.
43 Wu MT, Hsieh KS, Lin CC, Yang CF, Pan HB. Images in cardiovascular medicine. Evaluation of coronary artery aneurysms in Kawasaki disease by multislice computed tomographic coronary angiography. Circulation 2004; 110: e339.
44 Newburger JW, Sleeper LA, McCrindle BW, Minich LL, Gersony W, Vetter VL, *et al*. Randomized trial of pulsed corticosteroid therapy for primary treatment of Kawasaki disease. N Engl J Med 2007; 356: 663–75.
45 Fukazawa R, Sonobe T, Hamamoto K, Hamaoka K, Sakata K, Asano T, *et al*. Possible synergic effect of angiotensin-I converting enzyme gene insertion/deletion polymorphism and angiotensin-II type-1 receptor 1166A/C gene polymorphism on ischemic heart disease in patients with Kawasaki disease. Pediatr Res 2004; 56: 597–601.

46 Kariyazono H, Ohno T, Khajoee V, Ihara K, Kusuhara K, Kinukawa N, *et al*. Association of vascular endothelial growth factor (VEGF) and VEGF receptor gene polymorphisms with coronary artery lesions of Kawasaki disease. Pediatr Res 2004; 56: 953–9.
47 Nishimura S, Zaitsu M, Hara M, Yokota G, Watanabe M, Ueda Y, *et al*. A polymorphism in the promoter of the CD14 gene (CD14/-159) is associated with the development of coronary artery lesions in patients with Kawasaki disease. J Pediatr 2003; 143: 357–62.
48 Hsueh KC, Lin YJ, Chang JS, Wan L, Tsai YH, Tsai CH, *et al*. Association of vascular endothelial growth factor C-634 G polymorphism in taiwanese children with Kawasaki disease. Pediatr Cardiol 2008; 29: 292–6.
49 Quasney MW, Bronstein DE, Cantor RM, Zhang Q, Stroupe C, Shike H, *et al*. Increased frequency of alleles associated with elevated tumor necrosis factor-alpha levels in children with Kawasaki disease. Pediatr Res 2001; 49: 686–90.
50 Cheung YF, Ho MH, Ip WK, Fok SF, Yung TC, Lau YL. Modulating effects of mannose binding lectin genotype on arterial stiffness in children after Kawasaki disease. Pediatr Res 2004; 56: 591–6.
51 Hsueh KC, Lin YJ, Chang JS, Wan L, Tsai YH, Tsai CH, *et al*. Influence of interleukin 18 promoter polymorphisms in susceptibility to Kawasaki disease in Taiwan. J Rheumatol 2008; 35: 1408–13.
52 Park JA, Shin KS, Kim YW. Polymorphism of matrix metalloproteinase-3 promoter gene as a risk factor for coronary artery lesions in Kawasaki disease. J Korean Med Sci 2005; 20: 607–11.
53 Ikeda K, Ihara K, Yamaguchi K, Muneuchi J, Ohno T, Mizuno Y, *et al*. Genetic analysis of MMP gene polymorphisms in patients with Kawasaki disease. Pediatr Res 2008; 63: 182–5.
54 Wu SF, Chang JS, Peng CT, Shi YR, Tsai FJ. Polymorphism of angiotensin-1 converting enzyme gene and Kawasaki disease. Pediatr Cardiol 2004; 25: 529–33.
55 Shim YH, Kim HS, Sohn S, Hong YM. Insertion/deletion polymorphism of angiotensin converting enzyme gene in Kawasaki disease. J Korean Med Sci 2006; 21: 208–11.
56 Furuno K, Takada H, Yamamoto K, Ikeda K, Ohno T, Khajoee V, *et al*. Tissue inhibitor of metalloproteinase 2 and coronary artery lesions in Kawasaki disease. J Pediatr 2007; 151: 155–60.
57 Simonini G, Corinaldesi E, Massai C, Falcini F, Fanti F, De Martino M, *et al*. Macrophage migration inhibitory factor -173 polymorphism and risk of coronary alterations in children with Kawasaki disease. Clin Exp Rheumatol 2009; 27: 1026–30.
58 Jin HS, Kim HB, Kim BS, Lee JK, Seo EJ, Yoo HW, *et al*. The IL-10 (-627 A/C) promoter polymorphism may be associated with coronary aneurysms and low serum albumin in Korean children with Kawasaki disease. Pediatr Res 2007; 61 : 584–7.
59 Cheung YF, Huang GY, Chen SB, Liu XQ, Xi L, Liang XC, *et al*. Inflammatory gene polymorphisms and susceptibility to Kawasaki disease and its arterial sequelae. Pediatrics 2008; 122: e608–14.
60 Ban JY, Yoon KL, Kim SK, Kang S, Chung JH. Promoter polymorphism (rs3755724, -55C/T) of tissue inhibitor of metalloproteinase 4 (TIMP4) as a risk factor for Kawasaki disease with coronary artery lesions in a Korean population. Pediatr Cardiol 2009; 30: 331–5.
61 Hata A, Onouchi Y. Susceptibility genes for Kawasaki disease: toward implementation of personalized medicine. J Hum Genet 2009; 54: 67–73.
62 Chi H, Huang FY, Chen MR, Chiu NC, Lee HC, Lin SP, *et al*. ITPKC gene SNP rs28493229 and Kawasaki disease in Taiwanese children. Hum Mol Genet 2010; 19: 1147–51.
63 Lin MT, Wang JK, Yeh JI, Sun LC, Chen PL, Wu JF, *et al*. Clinical implication of the C allele of the ITPKC gene SNP rs28493229 in Kawasaki disease: association with disease susceptibility and BCG scar reactivation. Pediatr Infect Dis J 2011; 30: 148–52.
64 Parekh AB, Putney JW Jr. Store-operated calcium channels. Physiol Rev 2005; 85: 757–810.
65 Chang WC, Nelson C, Parekh AB. $Ca^{2+}$ influx through CRAC channels activates cytosolic phospholipase A2, leukotriene C4 secretion, and expression of c-fos through ERK-dependent and -independent pathways in mast cells. FASEB J 2006; 20: 2381–3.
66 Chang WC, Parekh AB. Close functional coupling between $Ca^{2+}$ release-activated $Ca^{2+}$ channels, arachidonic acid release, and leukotriene C4 secretion. J Biol Chem 2004; 279: 29994–9.
67 Feske S, Gwack Y, Prakriya M, Srikanth S, Puppel SH, Tanasa B, *et al*. A mutation in Orai1 causes immune deficiency by abrogating CRAC channel function. Nature 2006; 441: 179–85.
68 Chou YH, Juo SH, Chiu YC, Liu ME, Chen WC, Chang CC, *et al*. A polymorphism of the ORAI1 gene is associated with the risk and recurrence of calcium nephrolithiasis. J Urol 2011; 185: 1742–6.
69 Kuo HC, Lin YJ, Juo SH, Hsu YW, Chen WC, Yang KD, *et al*. Lack of association between ORAI1/CRACM1 gene polymorphisms and Kawasaki disease in the Taiwanese children. J Clin Immunol 2011. 10.1007/s10875-011-9524-8.
70 Picard C, McCarl CA, Papolos A, Khalil S, Luthy K, Hivroz C, *et al*. STIM1 mutation associated with a syndrome of immunodeficiency and autoimmunity. N Engl J Med 2009; 360: 1971–80.
71 Burgner D, Davila S, Breunis WB, Ng SB, Li Y, Bonnard C, *et al*. A genome-wide association study identifies novel and functionally related susceptibility Loci for Kawasaki disease. PLoS Genet 2009; 5: e1000319.
72 Tonkin ET, Smith M, Eichhorn P, Jones S, Imamwerdi B, Lindsay S, *et al*. A giant novel gene undergoing extensive alternative splicing is severed by a Cornelia de Lange-associated translocation breakpoint at 3q26.3. Hum Genet 2004; 115: 139–48.
73 Kim JJ, Hong YM, Sohn S, Jang GY, Ha KS, Yun SW, *et al*. A genome-wide association analysis reveals 1p31 and 2p13.3 as susceptibility loci for Kawasaki disease. Hum Genet 2011; 129: 487–95.
74 Tsai FJ, Lee YC, Chang JS, Huang LM, Huang FY, Chiu NC, *et al*. Identification of novel susceptibility Loci for Kawasaki disease in a Han Chinese population by a genome-wide association study. PLoS One 2011; 6: e16853.
75 Taniuchi S, Masuda M, Teraguchi M, Ikemoto Y, Komiyama Y, Takahashi H, *et al*. Polymorphism of Fc gamma RIIa may affect the efficacy of gamma-globulin therapy in Kawasaki disease. J Clin Immunol 2005; 25: 309–13.
76 Biezeveld M, Geissler J, Merkus M, Kuipers IM, Ottenkamp J, Kuijpers T. The involvement of Fc gamma receptor gene polymorphisms in Kawasaki disease. Clin Exp Immunol 2007; 147: 106–11.
77 Huang FY, Chang TY, Chen MR, Chiu NC, Chi H, Lee HC, *et al*. Genetic polymorphisms in the CD40 ligand gene and Kawasaki disease. J Clin Immunol 2008; 28: 405–10.

Acta Pharmacologica Sinica (2011) 32: 1199–1207
 1671-4083/11 $32.00
www.nature.com/aps

Review

# The impact of cellular senescence in cancer therapy: is it true or not?

Yi ZHANG[1, *], Jin-ming YANG[2, *]

[1]*Department of Pharmacology, School of Pharmacy, Soochow University, Suzhou 215123, China;* [2]*Department of Pharmacology and Penn State Hershey Cancer Institute, the Pennsylvania State University College of Medicine, Hershey, PA 17033, USA*

Cellular senescence is defined as the physiological program of terminal growth arrest, which can be triggered by various endogenous or exogenous stress signals. Cellular senescence can be induced in response to oncogenic activation and acts as a barrier to tumorigenesis. Moreover, tumor cells can undergo senescence when exposed to chemotherapeutic agents. In addition to suppressing tumorigenesis, senescent cells remain metabolically active and may contribute to tumor formation and to therapy resistance. In the current review, we discuss the molecular regulation of cellular senescence, the potential implications of senescence in human cancers, and the possibility of exploiting cellular senescence for the treatment of cancers.

**Keywords:** senescence; oncogenesis; cancer therapy; cell survival; cell death

*Acta Pharmacologica Sinica* (2011) 32: 1199–1207; doi: 10.1038/aps.2011.108; published online 12 Sep 2011

## Introduction

Cellular senescence was originally defined as the proliferative arrest that occurs in normal cells after a number of cell divisions, even upon treatment with mitogens. This process of "replicative senescence" in normal cells results primarily from the shortening of, and other structural changes to, telomeres at the ends of chromosomes[1]. Cellular senescence was first described 50 years ago by Hayflick and Moorehead[2] and was called the "Hayflick limit". Senescent cells typically appear flattened and enlarged and show increased cytoplasmic granularity. In addition to the characteristic changes in morphology, senescent cells display several other differences from quiescent cells. These differences include senescence-associated β-galactosidase activity (SA-β-gal), senescence-associated heterochromatin foci (SAHF), and high expression levels of p16 and p21[3–5]. These senescence markers can be used to identify senescent cells both *in vitro* and *in vivo*. In addition to replicative senescence, cellular senescence can be induced by other types of stress, such as oncogene activation (Figure 1)[6]. The oncogenic protein Ras and its effectors, such as activated mutant RAF, MEK, and BRAF, have all been shown to cause senescence[7–9]. This form of cellular senescence is similar to the Hayflick limit; however, in contrast to Hayflick's observations, Ras-induced senescence is much more rapid and is independent of telomere shortening. Courtois-Cox and colleagues have referred to this form of cellular senescence as oncogene-induced senescence (OIS)[9]. Many laboratories have reported that OIS may act as a barrier to neoplastic transformation, and bypass of OIS is a prerequisite for tumorigenesis. Recent studies also suggest a link between OIS and induced-pluripotency in *in vitro* settings, supporting the idea that cellular senescence counteracts the induced-conversion of primary cells into pluripotent stem cells[10–12]. Thus, OIS may suppress

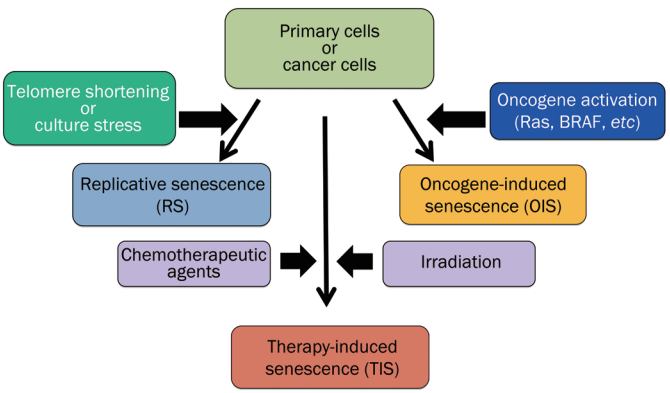


**Figure 1.** Induction of cellular senescence by various stimuli. Cells can activate intrinsic pathways to undergo replicative senescence (RS), oncogene-induced senescence (OIS) or therapy-induced senescence (TIS).

* To whom correspondence should be addressed.
E-mail juy16@psu.edu (Jin-ming YANG);
zhangyi@suda.edu.cn (Yi ZHANG)
Received 2011-05-23 Accepted 2011-06-30

tumor formation not only by inducing a persistent cell-cycle arrest, but also by limiting the generation of cancer stem cells. Therapy-induced senescence (TIS) is another form senescence that refers to the phenomenon of a subset of tumor cells being forced into a senescent state by therapeutic agents (Figure 1). The ability of therapeutic stimuli to induce tumor cell senescence has been noted for different treatments, including radiation and chemotherapeutic drugs (such as doxorubicin and cisplatin)[13, 14]. These observations indicate that cancer cells harbor signaling pathways/mechanisms that can be utilized to induce senescence. Recently, the ability of cancer cells to overcoming TIS has been proposed as one mechanism behind cancer recurrence and drug resistance. However, how TIS contributes to cancer recurrence and drug resistance remains an unanswered question[15, 16]. Although only certain therapeutics can induce senescence, and senescence does not occur in all the treated cells, TIS has clinical implications and significance in regard to the efficacy and effectiveness of treatment regimens. In the current review, we discuss the molecular regulation of the aforementioned forms of cellular senescence, the possible clinical implications of senescence in human cancer, and the potential for exploiting cellular senescence for the treatment of cancer.

## Replicative senescence and targeting of telomeres/telomerase in cancer

### Telomeres and replicative senescence

The phenomenon of replicative senescence (RS) was first observed in primary human cells that had a finite life span in cell culture. These primary human cells grew in culture but stopped dividing after a number of divisions[17]. RS mainly occurs in response to dysfunctional telomeres. Telomeres become slightly shorter after each cellular division and are eventually too short to allow the cell to divide, resulting in cellular senescence and apoptosis. Telomerase can prevent telomere erosion and the subsequent cellular senescence in highly proliferating cells. The dependence of replicative senescence on telomere shortening is evident, based on the fact that senescence can be bypassed by telomerase reverse transcriptase (hTERT), a catalytic subunit that elongates telomeres. In the presence of hTERT, RS is significantly reduced[18]. The majority of cancerous cells (>90%) express telomerase to maintain telomere length[19, 20]; however, cancer cells can also elongate their telomere through another mechanism termed alternative lengthening of telomeres (ALT)[20]. This alternative mechanism was discovered in some cancer cell lines in which telomere lengths were maintained in the absence of telomerase activity[16]. Thus, human cancer cells maintain their telomeres and consequently the ability to proliferate indefinitely making telomeres and telomerase ideal targets for therapeutic intervention in combating cancer.

### Telomerase, telomeres, and cancer therapy

Various therapeutic strategies targeting telomeres and telomerase have been developed, including gene therapy, immunotherapy, telomerase inhibitors and telomere-disrupting agents (Figure 2). Antisense gene therapies in which the hTERT mRNA or telomerase mRNA are targeted with RNAi or hammerhead ribozymes have been shown to selectively impact telomerase-positive cells. Such agents include antisense oligonucleotides, peptide nucleic acids (PNAs), and chemically modified PNAs such as GRN163L. GRN163L has been reported to inhibit telomerase activity in cancer cells, thereby promoting telomere shortening and subsequently cell cycle arrest and apoptosis[21]. To date, most studies have focused on searching for and testing natural agents or synthesizing chemical compounds that inhibit telomerase activity in cancer cells, resulting in loss of the telomere maintenance mechanism and induction of senescence and apoptosis. Several compounds, such as BIBR1532 {2-[(E)-3-naphtalen-2-yl-but-2-enoylamino]-benzoic acid}[22] and TNQX (2,3,7-trichloro-5-nitroquinoxaline)[23, 24], have been reported to possess these properties. Protein kinase C (PKC) and Akt have been shown to phosphorylate hTERT and to enhance telomerase activity[25]. Therefore, it is conceivable that inhibitors of these protein kinases could have inhibitory effects on telomerase activity. Recently, a different approach to targeting telomerase has been reported. Ugel and colleagues developed an adoptive cellular therapy by expanding high-avidity T cells reactive against telomerase epitopes. When these cells were injected back into transgenic mice, adenocarcinoma progression was hampered. A similar strategy was also effective against human cancer. In a mouse model, T cells reactive against human telomerase successfully abolished tumor growth of several types of human cancer cells[26]. Clinical trials are currently going on to evaluate these approaches, and it will be interesting to see whether or not

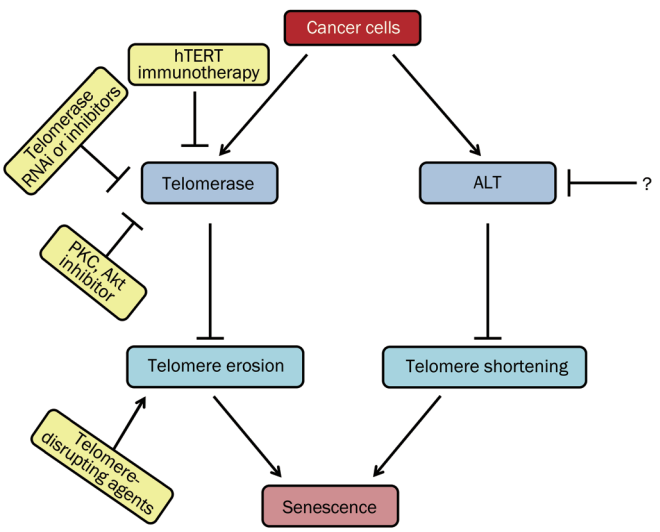


**Figure 2.** Pathways regulating RS and targeting RS for cancer therapy. RS mainly occurs in response to dysfunctional telomeres, which is the result of telomere erosion or telomere shortening. In cancer cells, telomerase or alternative lengthening of telomeres (ALT) can prevent telomere erosion or telomere shortening and subsequent cellular senescence. Various strategies to targeting telomeres and telomerase have been developed, including hTERT immunotherapy, telomerase inhibitors, telomere-disrupting agents and some protein kinase inhibitors.

these approaches will work in cancer patients. Currently, all of these approaches target telomerase and telomeres; no specific inhibitor has yet been designed to inhibit the ALT pathway. ALT-mediated telomere maintenance may underlie the observed resistance of some tumor cells to telomere-based therapies. This presents a fascinating area for future investigation, as combining ALT and telomere-based therapies may greatly improve outcomes for these therapies.

## Oncogene-induced senescence and its role in cancer treatment and development

Cellular senescence can also be induced by oncogenes, and this type of senescence is termed oncogene-induced senescence[9]. Unlike RS, the induction of OIS is much more rapid and cannot be bypassed by the expression of hTERT, indicating that OIS is independent of telomere attrition[27]. OIS is triggered by abnormal signaling within a cell, which is mediated by the protein products of oncogenes and is often accompanied by activation of tumor-suppressor networks. Critical signaling pathways shared by both RS and OIS are the p53 and p16/pRB (retinoblastoma tumor suppressor) pathways. Some oncogenes such as RAS, STAT5, and cyclin E not only induce senescence but also trigger a DNA-damage response, which is associated with DNA hyper-replication and appears to be involved in OIS[28]. It is now becoming increasingly clear that OIS is a crucial anticancer mechanism that prevents the growth of cells that are at risk for neoplastic transformation. Conversely, oncogenic stimuli that induce senescence also have the potential to initiate tumor promotion (Figure 3).

### Effector pathways and therapy

Signaling pathways known to regulate OIS include the p16/pRb and p19/p53/p21 pathways. Reduction of p53 function by dominant negative mutants, specific p53 antisense mRNA, oligonucleotides, or viral oncoproteins is sufficient to extend the lifespan of several cell-types in culture[29]. The protein MDM2 has p53 ubiquitin ligase activity and is part of the auto-regulatory feedback loop that regulates p53 activity. Overexpression of MDM2 targets p53 for degradation and results in loss of p53 function[30]. Furthermore, the human homologue of MDM2 is frequently overexpressed in melanoma[31], suggesting that alternative mechanisms for p53 inactivation occur in human cancers. Studies have demonstrated that restoring p53 activity by suppressing MDM2 overexpression (*eg*, by nutlin treatment) can achieve clinical benefits in patients with melanoma or other types of cancer. Activation of p53 induces the expression of p21, a cyclin-dependent kinase (CDK) inhibitor that has a direct inhibitory effect on cell cycle progression. In human cells, depletion of p21 is sufficient to bypass senescence[32]. However, in mouse embryonic fibroblasts, knockout of p21 does not overcome senescence[33, 34], suggesting that at least one additional downstream effector is needed for p53-induced senescence. Other proteins such as 14-3-3 and GADD45 are also believed to be involved in modulating cellular senescence[35, 36].

The retinoblastoma tumor suppressor, Rb, also plays a regulatory role in senescence. Overexpression of Rb or overexpression of various regulators of the pRb pathway such as CDK inhibitors leads to a senescent phenotype[37]. CDKs are

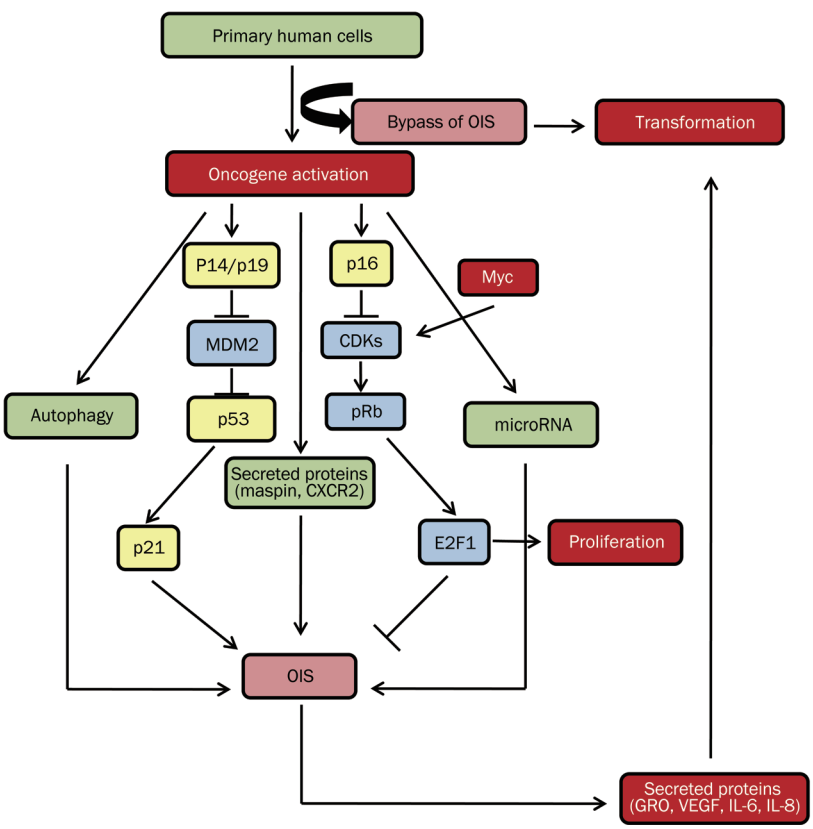


**Figure 3.** Pathways regulating OIS and neoplastic transformation. Primary human cells that acquire active oncogenes undergo OIS. When tumor suppressor genes are lost or oncogenes are over-expressed, cells bypass OIS and are eventually transformed. The most common pathways involved in OIS are the p53 and Rb pathways. OIS may also be induced by other mechanisms, such as secretion of senescence-inducing proteins, autophagy and miRNAs. Oncogenic stimuli that induce a senescence response may also have the potential to initiate tumor promotion.

enzymes that stimulate cell cycle progression by phosphorylating the Rb protein (pRb). One such CDK inhibitor is p16, which tightly binds to Rb to control its major effector, E2F, thereby preventing DNA replication and entry into the S phase of the cell cycle[38]. Cross-talk between effectors involved in OIS has also been revealed. For instance, myc, a gene that is involved in oncogenic signaling pathways, is able to induce cells to bypass senescence. Myc can bypass CDK4/6 inhibition by activating CDK-2-cyclin A/E and by up-regulating the CDK-activated phosphatase, cdc25A[39]. Therefore, inhibition of the CDKs involved in these epigenetic modifications could lead to senescence and may have anti-cancer activity. CDKs can be inhibited by using adenoviral vectors carrying CKIs (CDK inhibitors such as p16, p21, p15, and p27)[40]. Further studies are needed to determine the potential of this approach as an anticancer strategy.

### Secreted proteins in OIS

A major consequence of oncogene activation is the secretion of dozens of proteins, including cytokines and chemokines[41]. Some of these secreted proteins and their receptors are known to be regulators of OIS. For example, CXCR2 (interleukin-8 receptor type-B) was identified as an important regulator of OIS, which can lead to growth inhibition[42]. In addition, Wajapeyee and colleagues[43] performed a genome-wide RNA interference screening and found that the secreted protein, IGFBP7, plays a central role in BRAFV600E-mediated senescence and apoptosis. Expression of BRAFV600E in primary cells leads to synthesis and secretion of IGFBP7, which acts through autocrine/paracrine pathways to inhibit BRAF-MEK-ERK signaling and to induce senescence and apoptosis. Nickoloff and colleagues reported that the tumor-suppressive secreted protein, maspin is up-regulated in senescent tumor cells. Maspin expression is also increased in aging skin keratinocytes *in vivo*. The upregulation of maspin in senescent keratinocytes was found to result in a secreted anti-angiogenic activity detectable using an *in vitro* assay. However, the pool of proteins secreted in response to oncogenes is complex, and some components are actually tumor-promoting. For example, it has been reported that the secreted protein Trefoil factor 1 (TFF1) allows human prostate epithelial cells to escape OIS caused by activation of the Ras oncogene or by reduced expression of the tumor suppressor PTEN[44]. Yang and colleagues[45] revealed that pre-neoplastic epithelial ovarian cells express GRO1 (a cytokine recognized by CXCR2), which is secreted in response to signaling by the RAS oncogene and has the potential to induce senescence in ovarian fibroblasts *in vitro*. Furthermore, these senescent ovarian fibroblasts promoted tumor growth when co-injected with pre-neoplastic epithelial cells into mice. Senescent cells also secrete high levels of IL-6, IL-8, VEGF, and MMPs, which can stimulate the migration and invasion of pre-malignant epithelial cells[46–49]. These studies indicate that senescent tumor cells have the ability to secrete factors that inhibit the growth of their non-senescent neighbors. However, senescent tumor cells may also secrete factors that promote proliferation of tumor cells that reside in their microenvironment. Recent studies have presented the following paradox: while a senescent response is generally associated with tumor suppression, some senescent cells can produce a second-wave of secreted proteins that facilitate and drive cancer development. A clear picture of factors contributing to this paradox will require a deeper understanding of how the genes encoding secreted proteins are up-regulated as a consequence of oncogene activation. It may be possible to selectively inhibit some of the senescence-induced secretory proteins (*eg*, VEGF or MMPs) to abrogate tumor beneficial effects, which could be a strategy to harness the power of intrinsic tumor-suppressive mechanisms for improving cancer therapies.

### Autophagy in OIS

Autophagy is a crucial cellular process involved in maintaining cellular homeostasis by helping cells cope with metabolic stress and limiting oxidative damage. Defective autophagy has been linked to various human diseases including cancer, neurodegeneration, and aging. Interestingly, both autophagic flux and expression of regulators of autophagy are increased in OIS cells[50], and de-regulation of H-Ras activity can lead to caspase-independent cell death with features of autophagy. Modulation of key autophagic components such as Ulk3, Atg5, or Atg7 has been shown to alter cellular senescence. This effect may occur through feedback control of the PI3K-Akt-mTOR pathway, which acts to limit oncogenic signaling and enables cell cycle exit[51]. These studies suggest that the pathways involved in autophagy and senescence could be functionally linked. Autophagy has apparently conflicting roles in the development and maintenance of cancer. On the one hand, activators of autophagy likely inhibit transformation and prevent cancer by limiting cellular damage. On the other hand, autophagy plays an important role in the growth and survival of pancreatic cancer cells[52]. Although autophagy is induced in response to oncogene activation, this cellular process can also be induced in response to a variety of other stresses such as starvation or hypoxia. It remains to be determined whether the autophagy process is the same in response to different activators. Induction of Ulk3 has been shown to be sufficient to stimulate autophagy and OIS[53]. The induction of Ulk3 by OIS is associated with induction of a set of autophagy-related genes that is distinct from that induced by starvation or hypoxia, indicating that the autophagic response induced in OIS might be a distinct form of autophagy that facilitates the process of OIS. Defining what aspects of autophagy are required for maintaining the senescent phenotype and for suppressing tumor formation are important questions for future investigation.

### MicroRNAs in OIS

MicroRNAs are a class of evolutionarily conserved non-coding RNAs that regulate the expression of protein-encoding genes[54, 55]. In recent years, numerous miRNAs have been identified and implicated in human cancer[56–58]. Not surprisingly, miRNAs also play important roles in the regulation of

senescence and oncogenesis. For example, miR-17-92 was reported to inhibit oncogenic RAS-induced senescence and to promote oncogenesis[59], including evasion of apoptosis[58]. Overexpression of miR-380 cooperates with active H-RAS oncoproteins to transform primary cells, block oncogene-induced senescence, and form tumors[60]. Using genome-wide siRNA and miRNA screening, Borgdorff and colleagues showed that 28 miRNAs (miR-17-5p, miR-130b, *etc*) were involved in preventing $RAS^{G12V}$-induced senescence in human mammary epithelial cells (HMECs)[61]. Similarly, two miRNAs (miR-372 and miR-373) have been shown to rescue Ras-induced senescence in human fibroblasts and have been found to be overexpressed in testicular germ cell tumors[62]. Importantly, these miRNAs have also been linked to cancer development. For example, miR-17-5p is overexpressed in pancreatic cancer[63], breast cancer[64], hepatocellular cancer[65], and thyroid cancer[66], while miR-130b is overexpressed in gastric cancer[67]. These observations demonstrate the roles of miRNAs in oncogenic RAS-induced senescence and apoptosis, and suggest that regulation of senescence by miRNAs might be part of a universal mechanism of miRNA-mediated growth control. Therefore, induction of senescence by miRNA-based therapy might be a promising approach for the prevention and treatment of cancer. Recent therapeutic applications of miRNAs include the following two major strategies: 1) For oncogenic miRNAs that are overexpressed in tumors and promote cell proliferation, the therapeutic approach would be to suppress miRNA expression. This could be accomplished by using anti-miRNA oligonucleotides, miRNA masking, and small molecule inhibitors of miRNAs. 2) For tumor-suppressor miRNAs (TS-miRNAs), which are often lost in tumors, the therapeutic strategy would be to restore expression of TS-miRNAs by exogenous transfection of designated miRNA mimics. Some miRNA-based therapeutic molecule delivery methods have been developed and applied in clinical trials, including viral and non-viral vector systems.

## Therapy-induced senescence (TIS), a double-edged sword?

As mentioned above, the progression to malignancy involves bypassing or inhibiting crucial mediators of cellular senescence. Nevertheless, this does not mean that malignant cells have completely lost their capacity to undergo senescence. Given the intrinsic tumor-suppressive potential of senescence, investigation of the effectiveness of senescence-inducing interventions for the treatment of cancer should be interesting and potentially useful. Therapy-induced senescence (TIS) is another form of cellular senescence that has been described recently. Although TIS is caused by genotoxic agents such as irradiation and chemotherapeutic drugs, it shares many similarities to OIS (*eg*, common markers) (Figure 4).

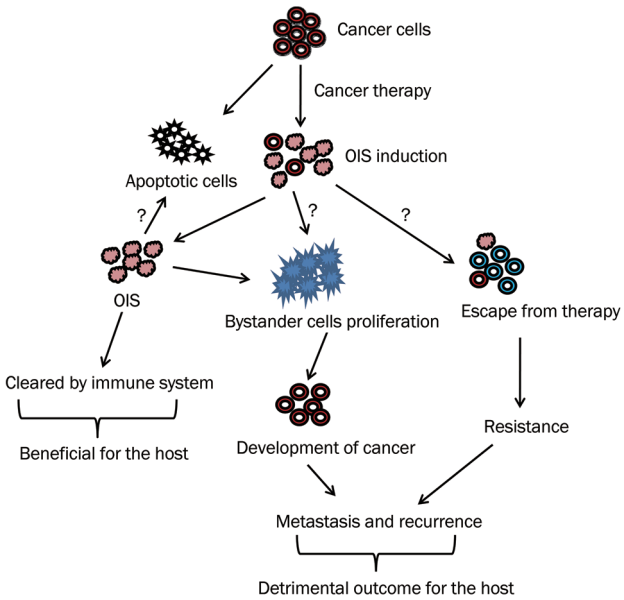


**Figure 4.** TIS, a double-edged sword? In response to therapeutic intervention, cancer cells can rapidly undergo apoptosis or enter TIS. These senescent cells can be cleared by the immune system, which is beneficial for the host. In contrast, some cancer cells in a senescence-like state can remain 'dormant' or possess a secretory phenotype. They therefore possess a dangerous potential for tumor relapse, which is considered a detrimental outcome for the host.

### Induction of senescence *in vitro* and *in vivo* by chemotherapy

A variety of anticancer agents can induce senescence-like morphological changes and SA-β-gal expression in tumor cells. These drugs include the topoisomerase I inhibitor camptothecin[68], the topoisomerase II inhibitor doxorubicin[69], the DNA damaging agents cisplatin and doxorubicin[70], γ-irradiation[71], and the anti-metabolite cytarabine[72]. These observations suggest that different drugs may activate senescence through different signaling pathways. DNA damage response pathways have been shown to play a critical role in OIS, RS, and TIS. For instance, the DNA methyltransferase inhibitor, 5-azacytidine, has been shown to cause senescence in DU145 and LNCaP prostate cancer cells within 7 d after treatment[73]. Sirtinol, an inhibitor of histone DNA acetylase, induced senescence in MCF7 breast and H1299 lung cancer cells after 24 h of exposure to this agent[74]. Recently, the involvement of the c-Jun N-terminal kinase p38 (MAPK 14) and the extracellular signal-regulated kinase (MAPK 1) pathways in TIS have also been reported[75, 76].

TIS has also been observed *in vivo*. Two recent reports[77, 78] have addressed the pro-senescence efficacy of restoring the tumor suppressive function of p53. Most of the sarcomas, lymphomas and liver carcinomas that developed in the absence of p53 regressed after p53 restoration. These reports support the idea that drugs that restore p53 function in tumors may provide an effective means of using senescence to restrict tumor growth. Several p53-restoring agents are currently being developed, such as MI-219 and Tenovin-6. In addition, Alimonti and colleagues reported that the PTEN inhibitor, VO-OHpic, induced a novel type of cellular senescence in mouse models of prostate cancer[79]. Wouters, BG and colleagues reported that tumor cells with altered levels of the

CDK inhibitor and growth arrest gene CIP1 produced similar results in clonogenic assays following γ-irradiation but appeared to be more radio-sensitive in the absence of p21 *in vivo*. This suggests that genetic protection from γ-irradiation-induced growth arrest may result in a higher rate of remission if apoptosis is still available[80]. Using newly sectioned specimens from frozen breast tumors of patients treated with the chemotherapeutic agents doxorubicin, 5-fluorouracil and cyclophophamide, Poele and colleagues[81] observed SA-β-gal staining in tumor cells but not in normal tissue. They further found that SA-β-gal staining in breast cancer was associated with low p53 staining and high p16 staining, suggesting that chemotherapy-induced senescence is a specific response of tumor cells. In a similar study, 2 out of 3 tumor biopsies from patients treated with carboplatin/paclitaxel were positive for markers of cellular senescence, whereas no significant SA-β-gal activity was found in 3 tumor samples obtained from untreated patients[82]. These results suggest that clinical benefits might be achieved by neoadjuvant chemotherapy for various cancer entities as the tumor lesions present at the time of surgery may not only be largely senescent thus reducing tumor size, but such therapy could also limit the growth potential of the remaining masses.

### Escape of tumor cells from TIS

It is conceivable that some cancer cells in a senescence-like state might remain 'dormant' or possess tumor stem cell characteristics, therefore representing a dangerous potential for tumor relapse. If drug-inducible senescence is indeed of clinical importance, then mechanisms that allow tumor cells to overcome this terminal arrest might contribute to anticancer drug resistance and tumor relapse. In fact, some *in vitro* experiments have already demonstrated that senescent cells can re-enter the mitotic cycle upon acquisition of additional senescence-compromising mutations[83–85]. *In vivo* observations also suggest that escaping from drug-induced senescence is responsible, at least in part, for treatment failure. For example, Braig and colleagues[86] observed in mice harboring drug-induced senescent tumors that loss of genes critical for the induction and maintenance of cellular senescence was facilitated by a heterozygotic state for the genes in question; however, mice heterozygous at those alleles also appeared to be particularly prone to overcoming drug-induced arrest.

### Clinical applications of cellular senescence-based therapy: is it a parable?

TIS has several features that may be beneficial for the management and treatment of cancer. First, senescence stimulates a persistent terminal growth arrest and senescent cells may persist in a stable state even *in vivo*. For example, senescent melanocytes have been identified in benign nevi that remain dormant for years[6]. It has also been reported that a subset of senescent prostate cancer cells persisted for at least 6 weeks after establishment of xenografts with doxorubicin-induced senescent prostate cancer cells[87]. Second, induction of senescence in tumor cells can stimulate an immune response, which increases susceptibility to cytotoxicity through lymphokine-activated killer cells[88]. It has been observed in a mouse liver carcinoma model that re-expression of a functional p53 induced senescence, resulting in tumor regression[89, 90]. This response may also be instrumental in the improved survival observed in a mouse lymphoma model in which senescence was induced by chemotherapy and BCL2[90]. Third, the observation that senescence can be induced by lower concentrations of chemotherapeutic agents suggests another potential benefit of TIS for cancer treatment. Schwarze and colleagues[73] tested a range of concentrations of doxorubicin, 5-azacytidine, and docetaxel for the ability to induce senescence and found that, at lower concentrations, the senescent phenotype was predominant in most prostate cancer cells, whereas higher concentrations led to DNA damage and were associated with apoptosis. These studies demonstrated that induction of senescence in tumors may be achieved with lower concentrations of therapeutic agents, which may help limit drug-related toxic effects.

Cellular senescence is generally considered to be irreversible in most cases, thus making it an attractive therapeutic target for diseases like cancer. Nevertheless, we must pay close attention to the potential problems that might arise from senescence-inducing therapies. The reversibility of senescence, particularly in fibroblasts, cannot yet be ruled out, as the factors involved in maintenance of senescence may stop being expressed[83, 84]. This possibility remains to be further clarified experimentally. In addition, the occurrence of cellular senescence may result in resistance to cell death programs such as apoptosis, autophagic cell death or necrosis. For example, senescent fibroblasts are resistant to the apoptotic effects of serum starvation[91] and hydrogen peroxide[92]. Pro-apoptotic signaling via ceramide and TNF-α can be blocked in the senescent fibroblasts. However, whether TIS causes resistance of cancer cells to apoptosis has not been clearly demonstrated. Additionally, as mentioned above, senescent cells have a robust secretory phenotype, which results in the production of pro-inflammatory cytokines and chemokines. These may also stimulate malignant phenotypes in nearby tumor cells[93]. For example, Chang and colleagues[94] found that chemotherapeutic agent-induced senescence of HCT116 cells not only led to up-regulation of growth inhibitors but also increased the levels of secreted factors with tumor-promoting activity. Such secreted factors included extracellular matrix components, Cyr61 and prosaposin (anti-apoptotic factors), transforming growth factor α (TGFα), and several proteases that could potentially contribute to metastatic growth. Coppe and colleagues[47] also found that senescent fibroblasts secrete pro-inflammatory immune cytokines, including IL-6 and IL-8, which have the potential to promote bystander cell proliferation and may account for the development of some cancers. In this regard, it is important to gain a deeper understanding of the mechanisms responsible for the clearance of senescent tumor cell.

## Conclusions and perspectives

Senescence-inducing agents, when combined with other clas-

sic therapeutic approaches, may prove to be more effective in the treatment of cancer. Thus, gaining a better understanding of the importance and significance of cellular senescence and exploring how to modulate this cellular process to treat cancer have become areas of extensive research. The advantages of enhancing senescence include terminal growth arrest, low toxicity-related side effects, and immune stimulation. However, under certain conditions, acutely-induced senescence has been shown to be a reversible program. Moreover, cellular senescence may contribute to resistance to the cytotoxic effects of cancer therapies. Senescent cells have the potential to promote the proliferation of bystander cells and may thus account for the development of certain types of cancer. To make the best use of the intrinsic tumor-suppressive potential of cancer cells, further studies are needed to determine whether senescence is indeed relevant to cancer development and therapeutic responses. Future studies should focus on searching for and developing robust senescence-inducing agents, identifying more reliable senescence markers, discovering new regulators of cellular senescence, and designing new therapeutic strategies that force transformed cancer cells to enter the senescence program and promote clearance of these senescent cells.

## Acknowledgements

This article was supported by the US Public Health Service R01CA135038 and the National Natural Sciences Foundation of China 81072146.

## References

1 Campisi J, d'Adda di Fagagna F. Cellular senescence: when bad things happen to good cells. Nat Rev Mol Cell Biol 2007; 8: 729–40.
2 Hayflick L, Moorhead PS. The serial cultivation of human diploid cell strains. Exp Cell Res 1961; 25: 585–621.
3 Dimri GP, Lee X, Basile G, Acosta M, Scott G, Roskelley C, *et al*. A biomarker that identifies senescent human cells in culture and in aging skin *in vivo*. Proc Natl Acad Sci U S A 1995; 92: 9363–7.
4 Serrano M, Lin AW, McCurrach ME, Beach D, Lowe SW. Oncogenic ras provokes premature cell senescence associated with accumulation of p53 and p16INK4a. Cell 1997; 88: 593–602.
5 Narita M, Krizhanovsky V, Nunez S, Chicas A, Hearn SA, Myers MP, *et al*. A novel role for high-mobility group a proteins in cellular senescence and heterochromatin formation. Cell 2006; 126: 503–14.
6 Michaloglou C, Vredeveld LC, Soengas MS, Denoyelle C, Kuilman T, van der Horst CM, *et al*. BRAFE600-associated senescence-like cell cycle arrest of human naevi. Nature 2005; 436: 720–4.
7 Chandeck C, Mooi WJ. Oncogene-induced cellular senescence. Adv Anat Pathol 2010; 17: 42–8.
8 Braig M, Schmitt CA. Oncogene-induced senescence: putting the brakes on tumor development. Cancer Res 2006; 66: 2881–4.
9 Courtois-Cox S, Jones SL, Cichowski K. Many roads lead to oncogene-induced senescence. Oncogene 2008; 27: 2801–9.
10 Banito A, Rashid ST, Acosta JC, Li S, Pereira CF, Geti I, *et al*. Senescence impairs successful reprogramming to pluripotent stem cells. Genes Dev 2009; 23: 2134–9.
11 Kawamura T, Suzuki J, Wang YV, Menendez S, Morera LB, Raya A, *et al*. Linking the p53 tumour suppressor pathway to somatic cell reprogramming. Nature 2009; 460: 1140–4.
12 Utikal J, Polo JM, Stadtfeld M, Maherali N, Kulalert W, Walsh RM, *et al*. Immortalization eliminates a roadblock during cellular reprogramming into iPS cells. Nature 2009; 460: 1145–8.
13 Wang X, Wong SC, Pan J, Tsao SW, Fung KH, Kwong DL, *et al*. Evidence of cisplatin-induced senescent-like growth arrest in nasopharyngeal carcinoma cells. Cancer Res 1998; 58: 5019–22.
14 Di Leonardo A, Linke SP, Clarkin K, Wahl GM. DNA damage triggers a prolonged p53-dependent $G_1$ arrest and long-term induction of Cip1 in normal human fibroblasts. Genes Dev 1994; 8: 2540–51.
15 Cesinaro AM, Migaldi M, Ferrari G, Castagnetti G, Dotti A, De Gaetani C, *et al*. Expression of p53 and Bcl-2 in clinically localized prostate cancer before and after neo-adjuvant hormonal therapy. Oncol Res 2000; 12: 43–9.
16 Bryan TM, Englezou A, Gupta J, Bacchetti S, Reddel RR. Telomere elongation in immortal human cells without detectable telomerase activity. EMBO J 1995; 14: 4240–8.
17 Hayflick L. The limited *in vitro* lifetime of human diploid cell strains. Exp Cell Res 1965; 37: 614–36.
18 Vaziri H, Benchimol S. Reconstitution of telomerase activity in normal human cells leads to elongation of telomeres and extended replicative life span. Curr Biol 1998; 8: 279–82.
19 Shay JW, Bacchetti S. A survey of telomerase activity in human cancer. Eur J Cancer 1997; 33: 787–91.
20 Muntoni A, Reddel RR. The first molecular details of ALT in human tumor cells. Hum Mol Genet 2005; 14 : R191–6.
21 Harley CB. Telomerase and cancer therapeutics. Nat Rev Cancer 2008; 8: 167–79.
22 Pascolo E, Wenz C, Lingner J, Hauel N, Priepke H, Kauffmann I, *et al*. Mechanism of human telomerase inhibition by BIBR1532, a synthetic, non-nucleosidic drug candidate. J Biol Chem 2002; 277: 15566–72.
23 Colangelo D, Ghiglia A, Ghezzi A, Ravera M, Rosenberg E, Spada F, *et al*. Water-soluble benzoheterocycle triosmium clusters as potential inhibitors of telomerase enzyme. J Inorg Biochem 2005; 99: 505–12.
24 Strahl C, Blackburn EH. The effects of nucleoside analogs on telomerase and telomeres in Tetrahymena. Nucleic Acids Res 1994; 22: 893–900.
25 Kim MO, Moon DO, Kang SH, Heo MS, Choi YH, Jung JH, *et al*. Pectenotoxin-2 represses telomerase activity in human leukemia cells through suppression of hTERT gene expression and Akt-dependent hTERT phosphorylation. FEBS Lett 2008; 582: 3263–9.
26 Ugel S, Scarselli E, Iezzi M, Mennuni C, Pannellini T, Calvaruso F, *et al*. Autoimmune B-cell lymphopenia after successful adoptive therapy with telomerase-specific T lymphocytes. Blood 2010; 115: 1374–84.
27 Wei S, Sedivy JM. Expression of catalytically active telomerase does not prevent premature senescence caused by overexpression of oncogenic Ha-Ras in normal human fibroblasts. Cancer Res 1999; 59: 1539–43.
28 Di Micco R, Fumagalli M, Cicalese A, Piccinin S, Gasparini P, Luise C, *et al*. Oncogene-induced senescence is a DNA damage response triggered by DNA hyper-replication. Nature 2006; 444: 638–42.
29 Wynford-Thomas D. p53: guardian of cellular senescence. J Pathol 1996; 180: 118–21.
30 Blaydes JP, Wynford-Thomas D. The proliferation of normal human fibroblasts is dependent upon negative regulation of p53 function by mdm2. Oncogene 1998; 16: 3317–22.
31 Polsky D, Bastian BC, Hazan C, Melzer K, Pack J, Houghton A, *et al*. HDM2 protein overexpression, but not gene amplification, is related to tumorigenesis of cutaneous melanoma. Cancer Res 2001; 61: 7642–6.
32 Rowland BD, Bernards R, Peeper DS. The KLF4 tumour suppressor is a transcriptional repressor of p53 that acts as a context-dependent oncogene. Nat Cell Biol 2005; 7: 1074–82.

33 Takeuchi S, Takahashi A, Motoi N, Yoshimoto S, Tajima T, Yamakoshi K, *et al*. Intrinsic cooperation between p16INK4a and p21$^{Waf1/Cip1}$ in the onset of cellular senescence and tumor suppression *in vivo*. Cancer Res 2010; 70: 9381–90.
34 Zhao B, Benson EK, Qiao R, Wang X, Kim S, Manfredi JJ, *et al*. Cellular senescence and organismal ageing in the absence of p21$^{CIP1/WAF1}$ in ku80$^{-/-}$ mice. EMBO Rep 2009; 10: 71–8.
35 Kuroda Y, Aishima S, Taketomi A, Nishihara Y, Iguchi T, Taguchi K, *et al*. 14-3-3sigma negatively regulates the cell cycle, and its down-regulation is associated with poor outcome in intrahepatic cholangiocarcinoma. Hum Pathol 2007; 38: 1014–22.
36 Jackson JG, Pereira-Smith OM. p53 is preferentially recruited to the promoters of growth arrest genes p21 and GADD45 during replicative senescence of normal human fibroblasts. Cancer Res 2006; 66: 8356–60.
37 Haddad MM, Xu W, Schwahn DJ, Liao F, Medrano EE. Activation of a cAMP pathway and induction of melanogenesis correlate with association of p16(INK4) and p27(KIP1) to CDKs, loss of E2F-binding activity, and premature senescence of human melanocytes. Exp Cell Res 1999; 253: 561–72.
38 Liu Y, El-Naggar S, Clem B, Chesney J, Dean DC. The Rb/E2F pathway and Ras activation regulate RecQ helicase gene expression. Biochem J 2008; 412: 299–306.
39 Amati B, Alevizopoulos K, Vlach J. Myc and the cell cycle. Front Biosci 1998; 3: d250–68.
40 Carnero A. Targeting the cell cycle for cancer therapy. Br J Cancer 2002; 87: 129–33.
41 Campisi J. Senescent cells, tumor suppression, and organismal aging: good citizens, bad neighbors. Cell 2002; 120: 513–22.
42 Acosta JC, O'Loghlen A, Banito A, Guijarro MV, Augert A, Raguz S, *et al*. Chemokine signaling via the CXCR2 receptor reinforces senescence. Cell 2008; 133: 1006–18.
43 Wajapeyee N, Serra RW, Zhu X, Mahalingam M, Green MR. Oncogenic BRAF induces senescence and apoptosis through pathways mediated by the secreted protein IGFBP7. Cell 2008; 132: 363–74.
44 Radiloff DR, Wakeman TP, Feng J, Schilling S, Seto E, Wang XF. Trefoil factor 1 acts to suppress senescence induced by oncogene activation during the cellular transformation process. Proc Natl Acad Sci U S A 2011; 108: 6591–6.
45 Yang G, Rosen DG, Zhang Z, Bast RC Jr, Mills GB, Colacino JA, *et al*. The chemokine growth-regulated oncogene 1 (Gro-1) links RAS signaling to the senescence of stromal fibroblasts and ovarian tumorigenesis. Proc Natl Acad Sci U S A 2006; 103: 16472–7.
46 Coppe JP, Kauser K, Campisi J, Beausejour CM. Secretion of vascular endothelial growth factor by primary human fibroblasts at senescence. J Biol Chem 2006; 281: 29568–74.
47 Coppe JP, Patil CK, Rodier F, Sun Y, Munoz DP, Goldstein J, *et al*. Senescence-associated secretory phenotypes reveal cell-nonautonomous functions of oncogenic RAS and the p53 tumor suppressor. PLoS Biol 2008; 6: 2853–68.
48 Ksiazek K, Jorres A, Witowski J. Senescence induces a proangiogenic switch in human peritoneal mesothelial cells. Rejuvenation Res 2008; 11: 681–3.
49 Parrinello S, Coppe JP, Krtolica A, Campisi J. Stromal-epithelial interactions in aging and cancer: senescent fibroblasts alter epithelial cell differentiation. J Cell Sci 2005; 118: 485–96.
50 Patschan S, Chen J, Polotskaia A, Mendelev N, Cheng J, Patschan D, *et al*. Lipid mediators of autophagy in stress-induced premature senescence of endothelial cells. Am J Physiol Heart Circ Physiol 2008; 294: H1119–29.
51 Elgendy M, Sheridan C, Brumatti G, Martin SJ. Oncogenic ras-induced expression of noxa and beclin-1 promotes autophagic cell death and limits clonogenic survival. Mol Cell 2011; 42: 23–35.
52 Yang S, Wang X, Contino G, Liesa M, Sahin E, Ying H, *et al*. Pancreatic cancers require autophagy for tumor growth. Genes Dev 2011; 25: 717–29.
53 Young AR, Narita M, Ferreira M, Kirschner K, Sadaie M, Darot JF, *et al*. Autophagy mediates the mitotic senescence transition. Genes Dev 2009; 23: 798–803.
54 Bartel DP. MicroRNAs: genomics, biogenesis, mechanism, and function. Cell 2004; 116: 281–97.
55 Bartel DP. MicroRNAs: target recognition and regulatory functions. Cell 2009; 136: 215–33.
56 Shi XB, Tepper CG, deVere White RW. Cancerous miRNAs and their regulation. Cell Cycle 2008; 7: 1529–38.
57 Dillhoff M, Wojcik SE, Bloomston M. MicroRNAs in solid tumors. J Surg Res 2009; 154: 349–54.
58 Croce CM. Causes and consequences of microRNA dysregulation in cancer. Nat Rev Genet 2009; 10: 704–14.
59 Hong L, Lai M, Chen M, Xie C, Liao R, Kang YJ, *et al*. The miR-17-92 cluster of microRNAs confers tumorigenicity by inhibiting oncogene-induced senescence. Cancer Res 2010; 70: 8547–57.
60 Swarbrick A, Woods SL, Shaw A, Balakrishnan A, Phua Y, Nguyen A, *et al*. miR-380-5p represses p53 to control cellular survival and is associated with poor outcome in MYCN-amplified neuroblastoma. Nat Med 2010; 16: 1134–40.
61 Borgdorff V, Lleonart ME, Bishop CL, Fessart D, Bergin AH, Overhoff MG, *et al*. Multiple microRNAs rescue from Ras-induced senescence by inhibiting p21$^{Waf1/Cip1}$. Oncogene 2010; 29: 2262–71.
62 Voorhoeve PM, le Sage C, Schrier M, Gillis AJ, Stoop H, Nagel R, *et al*. A genetic screen implicates miRNA-372 and miRNA-373 as oncogenes in testicular germ cell tumors. Cell 2006; 124: 1169–81.
63 Yu J, Ohuchida K, Mizumoto K, Fujita H, Nakata K, Tanaka M. MicroRNA miR-17-5p is overexpressed in pancreatic cancer, associated with a poor prognosis, and involved in cancer cell proliferation and invasion. Cancer Biol Ther 2010; 10: 748–57.
64 O'Day E, Lal A. MicroRNAs and their target gene networks in breast cancer. Breast Cancer Res 2010; 12: 201.
65 Yang F, Yin Y, Wang F, Wang Y, Zhang L, Tang Y, *et al*. miR-17-5p Promotes migration of human hepatocellular carcinoma cells through the p38 mitogen-activated protein kinase-heat shock protein 27 pathway. Hepatology 2010; 51: 1614–23.
66 Takakura S, Mitsutake N, Nakashima M, Namba H, Saenko VA, Rogounovitch TI, *et al*. Oncogenic role of miR-17-92 cluster in anaplastic thyroid cancer cells. Cancer Sci 2008; 99: 1147–54.
67 Yao Y, Suo AL, Li ZF, Liu LY, Tian T, Ni L, *et al*. MicroRNA profiling of human gastric cancer. Mol Med Report 2009; 2: 963–70.
68 Hayward RL, Macpherson JS, Cummings J, Monia BP, Smyth JF, Jodrell DI. Antisense Bcl-xl down-regulation switches the response to topoisomerase I inhibition from senescence to apoptosis in colorectal cancer cells, enhancing global cytotoxicity. Clin Cancer Res 2003; 9: 2856–65.
69 Elmore LW, Rehder CW, Di X, McChesney PA, Jackson-Cook CK, Gewitz DA, *et al*. Adriamycin-induced senescence in breast tumor cells involves functional p53 and telomere dysfunction. J Biol Chem 2002; 277: 35509–15.
70 Chang BD, Broude EV, Dokmanovic M, Zhu H, Ruth A, Xuan Y, *et al*. A senescence-like phenotype distinguishes tumor cells that undergo terminal proliferation arrest after exposure to anticancer agents. Cancer Res 1999; 59: 3761–7.
71 Mirzayans R, Scott A, Cameron M, Murray D. Induction of accelerated senescence by gamma radiation in human solid tumor-derived cell

lines expressing wild-type TP53. Radiat Res 2005; 163: 53–62.
72 Rosenbeck L, Kiel PJ. Images in clinical medicine. Palmar-plantar rash with cytarabine therapy. N Engl J Med 2011; 364: e5.
73 Schwarze SR, Fu VX, Desotelle JA, Kenowski ML, Jarrard DF. The identification of senescence-specific genes during the induction of senescence in prostate cancer cells. Neoplasia 2005; 7: 816–23.
74 Ota H, Tokunaga E, Chang K, Hikasa M, Iijima K, Eto M, *et al*. Sirt1 inhibitor, Sirtinol, induces senescence-like growth arrest with attenuated Ras-MAPK signaling in human cancer cells. Oncogene 2006; 25: 176–85.
75 Hong EH, Lee SJ, Kim JS, Lee KH, Um HD, Kim JH, *et al*. Ionizing radiation induces cellular senescence of articular chondrocytes via negative regulation of SIRT1 by p38 kinase. J Biol Chem 2010; 285: 1283–95.
76 Chen JY, Hwang CC, Chen WY, Lee JC, Fu TF, Fang K, *et al*. Additive effects of C(2)-ceramide on paclitaxel-induced premature senescence of human lung cancer cells. Life Sci 2010; 87: 350–7.
77 Martinelli P, Bonetti P, Sironi C, Pruneri G, Fumagalli C, Raviele PR, *et al*. The lymphoma-associated NPM-ALK oncogene elicits a p16INKa/pRb-dependent tumour-suppressive pathway. Blood 2011; 117: 6617–26.
78 Chao SK, Lin J, Brouwer-Visser J, Smith AB 3rd, Horwitz SB, McDaid HM. Resistance to discodermolide, a microtubule-stabilizing agent and senescence inducer, is 4E-BP1-dependent. Proc Natl Acad Sci U S A 2011; 108: 391–6.
79 Alimonti A, Nardella C, Chen Z, Clohessy JG, Carracedo A, Trotman LC, *et al*. A novel type of cellular senescence that can be enhanced in mouse models and human tumor xenografts to suppress prostate tumorigenesis. J Clin Invest 2010; 120: 681–93.
80 Wouters BG, Giaccia AJ, Denko NC, Brown JM. Loss of $p21^{Waf1/Cip1}$ sensitizes tumors to radiation by an apoptosis-independent mechanism. Cancer Res 1997; 57: 4703–6.
81 te Poele RH, Okorokov AL, Jardine L, Cummings J, Joel SP. DNA damage is able to induce senescence in tumor cells *in vitro* and *in vivo*. Cancer Res 2002; 62: 1876–83.
82 Roberson RS, Kussick SJ, Vallieres E, Chen SY, Wu DY. Escape from therapy-induced accelerated cellular senescence in p53-null lung cancer cells and in human lung cancers. Cancer Res 2005; 65: 2795–803.
83 Beausejour CM, Krtolica A, Galimi F, Narita M, Lowe SW, Yaswen P, *et al*. Reversal of human cellular senescence: roles of the p53 and p16 pathways. EMBO J 2003; 22: 4212–22.
84 Dirac AM, Bernards R. Reversal of senescence in mouse fibroblasts through lentiviral suppression of p53. J Biol Chem 2003; 278: 11731–4.
85 Sage J, Miller AL, Perez-Mancera PA, Wysocki JM, Jacks T. Acute mutation of retinoblastoma gene function is sufficient for cell cycle re-entry. Nature 2003; 424: 223–8.
86 Braig M, Lee S, Loddenkemper C, Rudolph C, Peters AH, Schlegelberger B, *et al*. Oncogene-induced senescence as an initial barrier in lymphoma development. Nature 2005; 436: 660–5.
87 Ewald J, Desotelle J, Almassi N, Jarrard D. Drug-induced senescence bystander proliferation in prostate cancer cells *in vitro* and *in vivo*. Br J Cancer 2008; 98: 1244–9.
88 Petti C, Molla A, Vegetti C, Ferrone S, Anichini A, Sensi M. Coexpression of NRASQ61R and BRAFV600E in human melanoma cells activates senescence and increases susceptibility to cell-mediated cytotoxicity. Cancer Res 2006; 66: 6503–11.
89 Xue W, Zender L, Miething C, Dickins RA, Hernando E, Krizhanovsky V, *et al*. Senescence and tumour clearance is triggered by p53 restoration in murine liver carcinomas. Nature 2007; 445: 656–60.
90 Schmitt CA, Fridman JS, Yang M, Lee S, Baranov E, Hoffman RM, *et al*. A senescence program controlled by p53 and p16INK4a contributes to the outcome of cancer therapy. Cell 2002; 109: 335–46.
91 Wang E. Senescent human fibroblasts resist programmed cell death, and failure to suppress bcl2 is involved. Cancer Res 1995; 55: 2284–92.
92 Sasaki M, Kumazaki T, Takano H, Nishiyama M, Mitsui Y. Senescent cells are resistant to death despite low Bcl-2 level. Mech Ageing Dev 2001; 122: 1695–706.
93 Sun X, Cheng G, Hao M, Zheng J, Zhou X, Zhang J, *et al*. CXCL12/CXCR4/CXCR7 chemokine axis and cancer progression. Cancer Metastasis Rev 2010; 29: 709–22.
94 Chang BD, Swift ME, Shen M, Fang J, Broude EV, Roninson IB. Molecular determinants of terminal growth arrest induced in tumor cells by a chemotherapeutic agent. Proc Natl Acad Sci U S A 2002; 99: 389–94.

Acta Pharmacologica Sinica (2011) 32: 1208–1214
 1671-4083/11 $32.00
www.nature.com/aps

Original Article

# Comparison between cerebral state index and bispectral index as measures of electroencephalographic effects of sevoflurane using combined sigmoidal $E_{max}$ model

Dong Woo HAN[1, 2], Olinto-Jose LINARES-PERDOMO[3], Jong Seok LEE[1, 2], Jun Ho KIM[1], Steven E KERN[3, 4, 5, *]

*Department of [1]Anesthesiology and Pain Medicine and [2]Anesthesia and Pain Research Institute, Yonsei University College of Medicine, Seoul, Korea; Department of [3]Anesthesiology and [4]Pharmaceutics/Pharmaceutical Chemistry and [5]Bioengineering, University of Utah, Salt Lake City, UT 84108, USA*

**Aim:** The cerebral state index (CSI) was recently introduced as an electroencephalographic monitor for measuring the depth of anesthesia. We compared the performance of CSI to the bispectral index (BIS) as electroencephalographic measures of sevoflurane effect using two combined sigmoidal $E_{max}$ models.
**Methods:** Twenty adult patients scheduled for laparotomy were studied. After induction of general anesthesia, sevoflurane concentrations were progressively increased and then decreased over 70 min. An analysis of the BIS and CSI with the sevoflurane effect-site concentration was conducted using two combined sigmoidal $E_{max}$ models.
**Results:** The BIS and CSI decreased over the initial concentration range of sevoflurane and then reached a plateau in most patients. A further increase in sevoflurane concentration produced a secondary plateau in the pharmacodynamic response. The CSI was more strongly correlated with effect-site sevoflurane concentration ($R^2$=0.95±0.04) than the BIS was ($R^2$=0.87±0.07) ($P$<0.05). The individual $E_{max}$ and $C_{eff50}$ (effect-site concentration associated with 50% decrease from baseline to plateau) values for the upper and lower plateaus were significantly greater for BIS (12.7±7.3, 1.6±0.4, and 4.2±0.5, respectively) than for CSI (3.4±2.2, 1.2±0.4, and 3.8±0.5, respectively) ($P$<0.05). The remaining pharmacodynamic parameters for the BIS and CSI were similar.
**Conclusion:** The overall performance of the BIS and CSI during sevoflurane anesthesia was similar despite major differences in their algorithms. However, the CSI was more consistent and more sensitive to changes in sevoflurane concentration, whereas the measured BIS seemed to respond faster. The newly developed combined $E_{max}$ model adequately described the clinical data, including the pharmacodynamic plateau.

**Keywords:** general anesthesia; bispectral index; cerebral state index; electroencephalogram; pharmacodynamic modeling; sevoflurane

*Acta Pharmacologica Sinica* (2011) 32: 1208–1214; doi: 10.1038/aps.2011.99; published online 5 Sep 2011

## Introduction

The electroencephalogram (EEG) is commonly used to measure an anesthetic drug's effect on the central nervous system. Several processed EEG monitors have been developed to extract and process the information because it is challenging to analyze the real-time, raw electroencephalographic signal during anesthesia. The most extensively validated device used for this purpose is the bispectral index (BIS) monitor (Aspect Medical System, Newton, MA, USA). The cerebral state index (CSI), which is obtained by a cerebral state monitor (CSM™ Danmeter, Odense, Denmark), was recently introduced as a measure of the hypnotic component of anesthesia, and its usefulness has been previously evaluated[1–7]. However, there are no reports regarding the dose-response relationship between sevoflurane concentration and its effect in adults measured with CSI.

The administration of inhalational anesthetic drugs produces dose-response changes on EEG devices. When increasing or decreasing the anesthetic depth level, delays between the end-tidal concentration and the effect-site concentration occur. Pharmacokinetic-pharmacodynamic modeling can quantify these delays by incorporating the plasma-effect site equilibration rate constant ($K_{e0}$)[8]. A classical sigmoidal $E_{max}$ model has been commonly used to describe the dose-response

*To whom correspondence should be addressed.
E-mail Steven.Kern@utah.edu
Received 2011-03-14 Accepted 2011-06-23

relationship between anesthetic drugs and electroencephalographic data because of the advantage of its high flexibility. However, as anesthetic doses increase, two pronounced pharmacodynamic plateaus appear in the dose-response curves of the processed EEG devices[9-11]. These biphasic dose-response curves suggest that the classical sigmoidal $E_{max}$ model cannot reflect these data, and thus a new pharmacodynamic model needs to be developed.

The aim of this study is to quantify and compare the pharmacodynamic profile of sevoflurane's effect measured with the CSI and the BIS using a new model that combines two sigmoidal $E_{max}$ models.

## Materials and methods

### Patients and anesthesia

After obtaining approval of the Institutional Review Board, informed written consent was obtained from all patients. Twenty patients (8 men and 12 women), American Society of Anesthesiologists physical status I, ages 30 to 65 years old, were prospectively studied. All patients were scheduled for open subtotal gastrectomy under general anesthesia and did not receive any premedication. The patients' exclusion criteria were preoperative use of medication acting on the central nervous system or of opioids, excessive weight, a history of cardiac, pulmonary, hepatic, renal, or cerebrovascular disease, and use of any premedication. All subjects were fasted for at least 8 h before anesthesia.

After arrival at the operating room, standard monitors (*ie*, electrocardiogram, oxygen saturation, intermittent non-invasive blood pressure, and gas analysis) were applied. The EEG was continuously recorded using the BIS and the CSI monitor simultaneously for all patients. For the BIS electrodes, the skin of the forehead was prepared with alcohol swabbing, and monitoring electrodes were positioned as recommended by the manufacturer. We placed the BIS sensor with electrode 1 at the center of the forehead, approximately 5 cm above the nose, electrode 2 lateral to electrode 1, electrode 3 on temple between the corner of the eye and hairline, and electrode 4 right above the eyebrow. For the CSI electrodes, the skin of the forehead and mastoid process were firmly rubbed with abrasive paper, and one drop of sodium chloride was applied to the skin before placing the electrodes. One CSI electrode was placed at the midline of the forehead, one more laterally on the forehead, and one on the mastoid process behind the ear. After an initial control for electrode impedance, the monitor calculated its index from the raw EEG signals. Both monitors provided numerical indices from 0 to 100. Anesthesia was induced with 1.5 mg/kg propofol with a remifentanil infusion at 0.2 μg/kg per min. Rocuronium 0.6 mg/kg was administered to facilitate orotracheal intubation. Anesthesia was maintained with sevoflurane and remifentanil infusion at 0.2 μg/kg per min. Complete neuromuscular block was achieved by repeated injection of 0.2 mg/kg rocuronium and monitored by using neuromuscular monitoring, *ie*, train-of-four. The tidal volume was set at 8 mL/kg, and the respiratory rate was adjusted to maintain an end-tidal carbon dioxide partial pressure of 35–40 mmHg. The oral temperature was monitored continuously and was maintained at normothermia (36.0–36.5 °C) by using a warm blanket.

### Study measurements

To rule out a residual propofol effect and to ensure a condition of constant surgical stimulation, the study measurements were performed during the opening of the peritoneum, a minimum of 45 min after the induction of anesthesia. The sevoflurane agent was administered using a sevoflurane vaporizer, and the sevoflurane was added to the inspired gas mixture. The end-tidal sevoflurane concentrations (*ie*, expired sevoflurane concentrations) were continuously measured with a Capnomac anesthetic gas analyzer (Datex, Copenhagen, Denmark) by sampling gas from the circuit. Sampling was performed as close to the patient as possible to minimize the effects of circuit dead space. It was assumed that the end-tidal sevoflurane concentration reflected its plasma concentration. The fresh gas flow was set at 6 L/min (4 L/min air and 2 L/min $O_2$). To obtain concentration-response curves, the sevoflurane end-tidal concentrations were steadily increased and then decreased according to the following paradigm: starting at an end-tidal sevoflurane concentration of 1%, the sevoflurane vaporizer was increased stepwise by 0.5% every 2.5 min up to a maximum value of 8.0%. Subsequently, the sevoflurane vapor setting was decreased stepwise by 0.5% every 2.5 min again, until the end-tidal sevoflurane concentration had decreased to 1.0%, or a BIS value of 60 had been reached. The BIS and CSI values were recorded simultaneously during the study period as the sevoflurane end-tidal concentration changed. If necessary, phenylephrine was intermittently given for hemodynamic stability. After the final suture was placed, sevoflurane was discontinued, and the patients were allowed to awaken from anesthesia. All patients were examined for unintended wakefulness by an interview on postoperative d 1.

### Pharmacodynamic model

Using a program called NONMEM VI, we modeled a relationship between the end-tidal concentrations of sevoflurane as an independent parameter and the BIS and CSI as dependent parameters. The model parameters were estimated by maximizing the likelihood between the measured and the predicted EEG parameters. To eliminate hysteresis between the end-tidal concentrations of sevoflurane and BIS and CSI values, an effect-site compartment was introduced into the model. Sevoflurane effect-site concentrations were obtained by simultaneous pharmacokinetic and pharmacodynamic modeling[8]. The effect site was assumed to be linked to the plasma compartment by a traditional first-order process, and the effect-site concentrations over time were calculated as the convolutions of the predicted plasma concentrations over time, with the disposition function of the effect site. The convolution was based on a "connect the dots" approach, previously used by Schnider *et al*[12]. The sevoflurane effect-site concentration was estimated using a differential equation as follows:

$$dC_{eff}/dt=(C_{et}-C_{eff})\times k_{e0}$$

where $C_{et}$ was the end-tidal concentration, $C_{eff}$ was the effect-site concentration of sevoflurane, and $k_{e0}$ was the first-order rate constant determining the equilibration between the two. The $k_{e0}$ was estimated by minimizing the area of the hysteresis loop of either EEG index's data *versus* the effect-site concentration. One individual $k_{e0}$ value was calculated for each patient on the basis of his or her particular inhalation anesthetic ramp.

Because of the bimodal shape of the concentration *versus* effect curves for all study subjects, the relationship between $C_{eff}$ and the electroencephalographic effect $E$ (BIS or CSI) was modeled using two combined sigmoid $E_{max}$ models ($E_1$ and $E_2$):

$$E_1=E_{01}+(E_{max1}-E_{01})\times C_{eff}^{\lambda 1}/(C_{eff501}^{\lambda 1}+C_{eff}^{\lambda 1})$$
$$E_2=E_{02}+(E_{max2}-E_{02})\times C_{eff}^{\lambda 2}/(C_{eff502}^{\lambda 2}+C_{eff}^{\lambda 2})$$
$$E=E_1+E_2$$

The combined sigmoidal curve was made up of total sum of two separate $E_{max}$ curves, indicated by $E_1$ and $E_2$. Both sigmoidal curves had their own parameters for $E_1$ and $E_2$. The effect ($E$) was the measured BIS and CSI value, $E_{01}$ and $E_{02}$ were the baseline values, $E_{max1}$ and $E_{max2}$ were the maximum values, $\lambda_1$ and $\lambda_2$ were the steepnesses of the concentration-response relation curves for $E_1$ and $E_2$, respectively, and $C_{eff}$ was the calculated effect-site concentration of sevoflurane. $C_{eff501}$ and $C_{eff502}$ were the effect-site concentrations associated with a 50% decrease from $E_{01}$ and $E_{02}$ to $E_{max1}$ and $E_{max2}$, respectively. $E_1$ was expected to represent the EEG effect of sevoflurane concentrations from the baseline value to the first plateau value, as $E_2$ was constant in that period. $E_2$ was expected to represent the EEG effect of sevoflurane from the first plateau value to the maximum value when $E_1$ was constant.

The interindividual variability for $E_1$ and $E_2$ was assumed to have a log-normal distribution. The interindividual variabilities in $E_{01}$, $E_{02}$, $E_{max2}$, $C_{eff501}$, $C_{eff502}$, and $k_{e0}$ were modeled using an exponential error model. Residual intraindividual variability was modeled using an additive error model. The FOCE with INTERACTION estimation method was used for analysis.

### Covariate analysis

In our modeling approach, the base population model was first developed, which did not include any covariates. The effects of age, weight, height, and sex were then explored. The Bayesian estimates of the individual pharmacodynamic parameters were plotted against the covariates. Covariates were added one at a time and were kept in the model if they improved the goodness of the fit, judged by a reduction in the log likelihood ratio greater than 4 for each added degree of freedom, with $P<0.05$.

### Statistical analysis

Minimizing the squared error between the measured and the predicted concentration necessarily maximizes the coefficient of determination ($R^2$), which can be considered as an objection function:

$$R^2=1-SSE/SST=1-\Sigma(yi-\hat{y}i)^2/\Sigma(yi-\ddot{y}i)^2$$

The sum of squared errors ($SSE$) represents the sum of squares of the differences between the observed measurement, $yi$, for a given time and the corresponding model prediction, $\hat{y}i$. The total sum of squares ($SST$) indicates the sum of squares of the differences between each actual measurement, $yi$, and the average of all measurements, $\ddot{y}i$. The $R^2$ values and pharmacodynamic parameters were compared between the two indices using Student's $t$ test or the Wilcoxon test where appropriate. All tests were two-tailed, with statistical significance defined as $P<0.05$. Data are presented as mean and standard deviation (SD). Statistical analysis was performed using Sigma Stat 2.03 and Sigma Plot 2000 (SPSS Inc, Erkrath, Germany) and SPSS (version 12) computer software.

## Results

Twenty patients, 8 men and 12 women, age 52±9 years old, weight 60±8 kg, and height 166±8 cm, were enrolled in this study. There were no problems with the skin adherence of the electrodes. The systolic blood pressure was maintained above 90 mmHg during the study period in all patients. No patients reported postoperative recall of intraoperative awareness. The mean duration of the measurements was 59.2±8.4 min. The end-tidal sevoflurane concentration ranged from 0.96%±0.15% to 5.30%±0.46%.

Figure 1 shows the observed value and predicted value of the CSI *vs* time (A) and the effect-site sevoflurane concentration (B) from one patient. Figure 2 shows the time course of the measured BIS (A) and CSI (B) obtained from all patients in the study. The hysteresis loop between the BIS, CSI, and end-tidal sevoflurane concentration is illustrated in Figure 3. Decreased BIS and CSI values adequately reflected the increase in the sevoflurane effect-site concentrations, and sevoflurane revealed a pronounced plateau, leading to a biphasic dose-response curve in most cases of the BIS and CSI (Figure 4A and 4C). In one patient who was included in our results, an unexpectedly prolonged paradoxical BIS elevation was observed when the effect-site concentration of sevoflurane was high (>3.5%), but the CSI values were similar to those of the population group. The observed values and individually predicted values of the BIS and CSI against the calculated effect-site sevoflurane concentration are shown, and a combined sigmoidal $E_{max}$ model was fitted to the data from all patients (Figure 4). The goodness of the model's fit was analyzed by the relationship between the observed values and the individually predicted values, and a smaller scatter was observed for the CSI than for the BIS (Figure 5). The correlation of the CSI to the effect-site sevoflurane concentration ($R^2$=0.95±0.04) was significantly better than that of the BIS to the effect-site sevoflurane concentration ($R^2$=0.87±0.07) ($P<0.05$).

The pharmacodynamic parameters are displayed in Table 1. The $E_{max1}$ value was fixed at 0 in our study because $E_{02}$ can represent a part of a pharmacodynamic plateau, and a more stable model can be produced without overparametrization. The $K_{e0}$ value of the individual fits derived from the BIS was 0.36±0.48

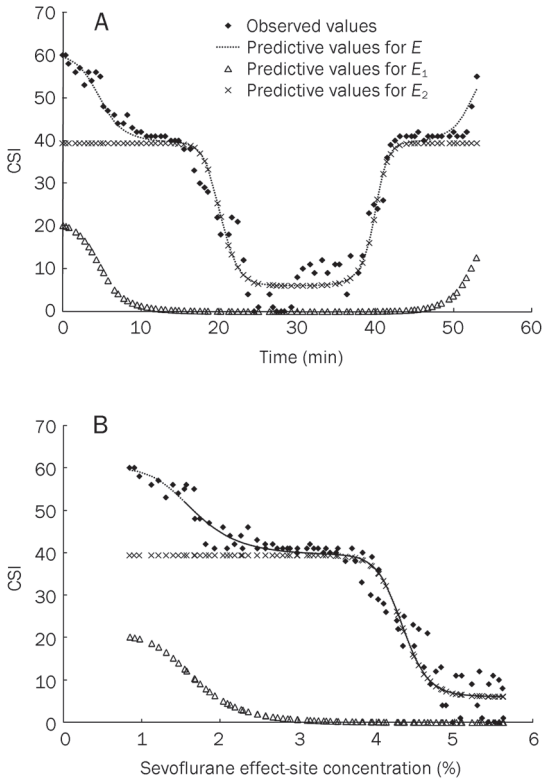


**Figure 1.** Observed value and predicted value of CSI *vs* time (A) and effect-site sevoflurane concentration (B) from one patient. The individual prediction value ($E$) is the sum of the two sigmoidal $E_{max}$ models ($E_1$ and $E_2$). $E_1$ represents the effect of sevoflurane concentrations from the baseline value to plateau value, while $E_2$ remains constant. $E_2$ represents the effect at sevoflurane concentrations from the plateau value to the maximal value while $E_1$ remains constant.

min$^{-1}$, and that from the CSI was 0.22±0.16 min$^{-1}$ ($P$>0.05). Both the $C_{eff501}$ and $C_{eff502}$ values of the BIS were greater than those of the CSI ($P$<0.05). The individual $E_{max2}$ value for the CSI (3.4±2.2) was significantly lower than that for the BIS (12.7±7.3) ($P$<0.05). The intraindividual variabilities (residual error σ) for the BIS and CSI were 5.7 and 4.3, respectively. During the covariate model selection, none were found to be significant for improving the model's fit to the data.

**Table 1.** Comparison of pharmacokinetic and pharmacodynamic parameters between BIS and CSI.

| | Bispectral index (BIS) | Cerebral state index (CSI) |
|---|---|---|
| $K_{e0}$ (min$^{-1}$) | 0.36±0.48 | 0.22±0.16 |
| $E_{01}$ | 20.6±3.7 | 21.1±7.7 |
| $C_{eff501}$ | 1.6±0.4[b] | 1.2±0.4 |
| $\lambda_1$ | 8.2 | 5.7 |
| $E_{02}$ | 38.7±3.3 | 40.6±1.8 |
| $E_{max2}$ | 12.7±7.3[b] | 3.4±2.2 |
| $C_{eff502}$ | 4.2±0.5[b] | 3.8±0.5 |
| $\lambda_2$ | 30.0 | 26.5 |
| MDPE (%)/MDAPE (%) | -1.13/8.05 | -0.87/6.53 |

Data are presented as mean±SD. $E_1$ and $E_2$=the electroencephalographic effect at sevoflurane concentrations from start point to plateau point and from plateau point to the maximal point; $K_{e0}$= first-order rate constant determining the efflux from the effect-site; $E_{01}$ and $E_{02}$=the baseline value for $E_1$ and $E_2$; $\lambda_1$ and $\lambda_2$=the steepness of the concentration-response relation curve for $E_1$ and $E_2$; $C_{eff501}$ and $C_{eff502}$=the effect-site concentration associated with 50% decrease from $E_{01}$ to 0 and from $E_{02}$ to $E_{max2}$; $E_{max2}$=the maximum value for $E_2$; MDPE=median prediction error; MDAPE=median absolute prediction error. [b]$P$<0.05 for BIS *vs* CSI. $E_{max1}$=0.

## Discussion

This study demonstrated that the CSI has only minor differences in dose-response relations, compared with the BIS, as a measure of the electroencephalographic effects of sevoflurane, despite major differences in their algorithms. The overall BIS and CSI progressively decreased with the increasing sevoflurane concentration, but the prominent pharmacodynamic plateau was observed in most cases, necessitating the use of this new $E_{max}$ model. The newly developed combined sigmoidal $E_{max}$ model adequately described the pharmacodynamic parameters in the processed EEG data, including the pharmacodynamic plateau.

The CSI uses an algorithm different from that used for the BIS, which has four subparameters derived from the time domain analysis (burst-ratio) and frequency domain analysis (α-ratio, β-ratio, and β-ratio-α-ratio) of the EEG. Some comparative studies between the BIS and CSI have shown similar

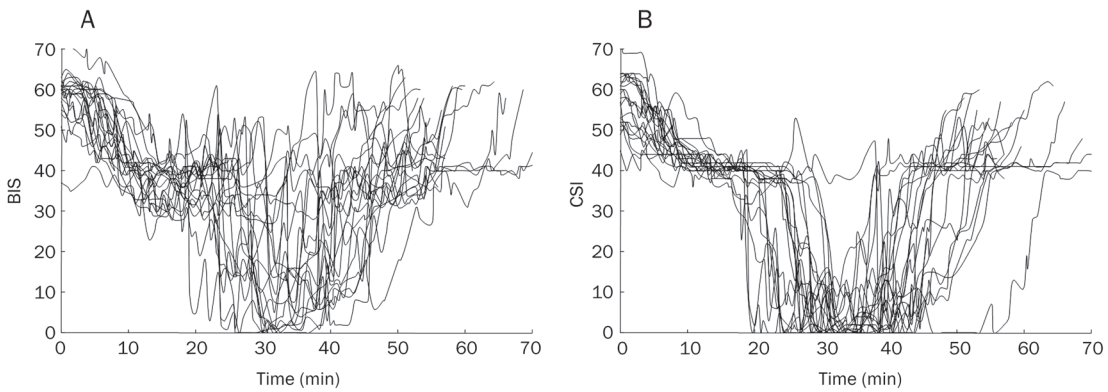


**Figure 2.** Time course of the measured BIS (A) and CSI (B) obtained from each patient.

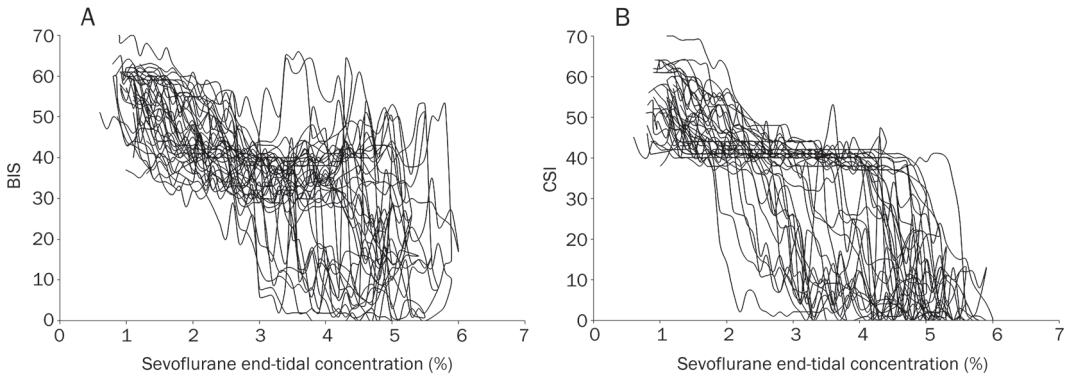


**Figure 3.** Relationship between the individually measured BIS and CSI values *vs* the measured sevoflurane end-tidal concentrations. The hysteresis in the relationship is shown in both plots.

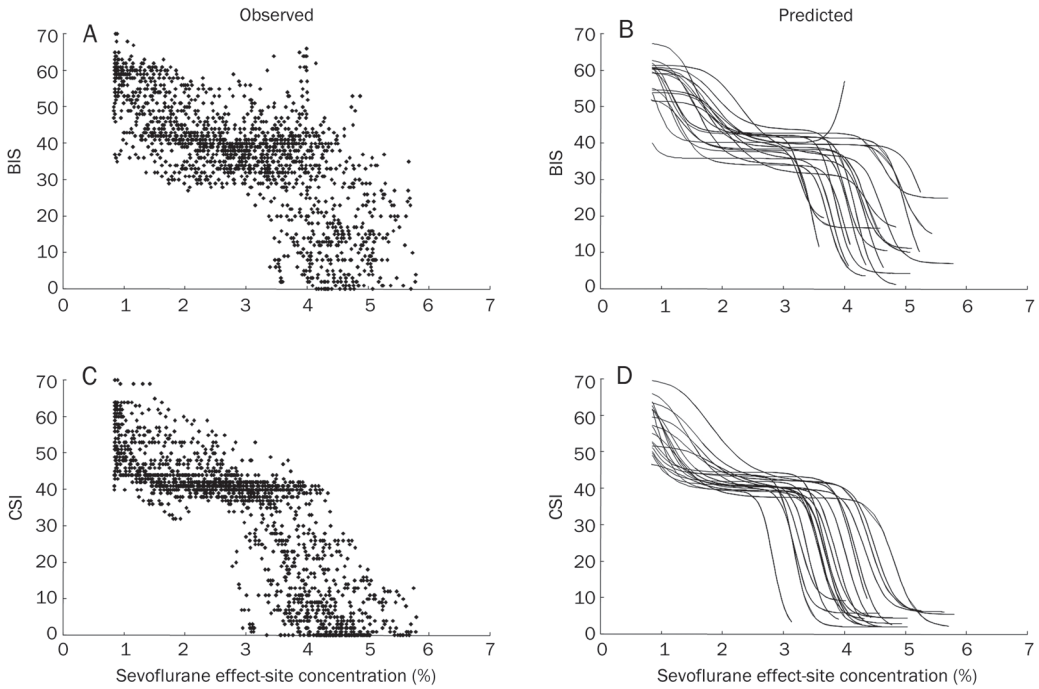


**Figure 4.** Observed BIS values (A) and individually predicted values (B) for all patients *vs* the calculated sevoflurane effect-site concentrations. Observed CSI values (C) and individually predicted values (D) for all patients *vs* the calculated sevoflurane effect-site concentrations.

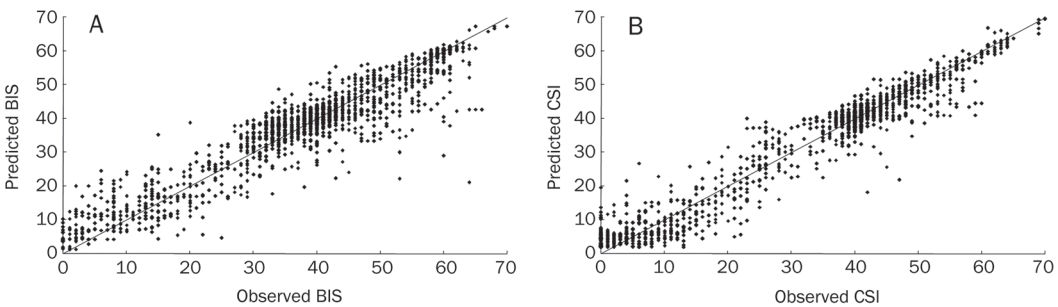


**Figure 5.** Relationship between the observed and individually predicted values of the BIS (A) and CSI (B). The solid line represents the line of identity.

values with both monitors during administration of propofol and inhalational agents[1–3, 5–7]. However, our study is the first clinical investigation of pharmacodynamic modeling using the CSI for adult patients. Pharmacokinetic-pharmacodynamic modeling is required before using new EEG devices as tools to guide anesthetic administration and to quantify the drug concentration versus the effect relationship[13]. This approach can quantify the relationship between the effect-site concentration and measured effect with these monitors, as well as the speed of onset and offset of the anesthetic's action.

When using a processed parameter from the EEG, the larger the $k_{e0}$ estimated value is, the faster the on and offset times for the response measured with the monitor are. The $k_{e0}$ in this study represents not only sevoflurane's end-tidal to brain equilibration time, but also the time delay of the index used to measure the sevoflurane effect[2]. The $k_{e0}$ was faster with the BIS than with the CSI, although the two values were not statistically different. Our results were similar to those reported in children whose $K_{e0}$ value in the BIS was also greater than in the CSI, although the actual $K_{e0}$ values of children are larger than those of adults[2, 14]. Our mean individual $K_{e0}$ value for the BIS was 0.36 $min^{-1}$, which is comparable to previously reported range (0.22–0.48 $min^{-1}$)[15–18]. While it was expected that the administration of additional remifentanil might lead to an increase in $k_{e0}$[17], the infusion dose of remifentanil did not seem to have much influence on the $k_{e0}$ value. The BIS has higher interindividual variability in the coefficients of variation of the $E_{max2}$ than the CSI. This finding suggests that the BIS may be a less consistent indicator for deep levels of anesthetic than the CSI. Both $C_{eff501}$ and $C_{eff502}$ values of the BIS are greater than those of the CSI, meaning that the CSI shows higher sensitivity to changes in sevoflurane concentrations in the periods before and after the pharmacodynamic plateau.

Patient covariates may have some influence on the dynamic profile of sevoflurane's effect, although this influence has not been previously investigated. The $C_{eff50}$ and $k_{e0}$ were expected to decrease with increasing age because age reduces the requirements of sevoflurane and increases the blood-brain equilibration times[14]. However, in our population, the covariate of age did not improve the goodness of fit. Thus, a study population with a broader age distribution would be required to clarify whether the pharmacodynamic parameters are dependent on age.

We chose the $R^2$ value as an indicator of the relationship between the EEG signal and sevoflurane concentration. The $R^2$ value of the CSI, with values approaching 1, suggests that the changes in electroencephalographic effect can be entirely explained by changes in anesthetic concentration at its postulated effect site. The $R^2$ value of the BIS of 0.87 is likely influenced by an unexpected case, which greatly deviated from the mean population group but was not excluded.

The pharmacodynamic plateau appears at the time of transition to burst suppression on the BIS monitor[19]. At the first attempt, the minimization of NONMEM was not successful for either the BIS data or CSI data using the classical sigmoidal $E_{max}$ model, which could not adequately quantify the dose-response relationship (data not shown). Some studies have explained the EEG data showing a pharmacodynamic plateau with $E_{max}$ models that are divided into two periods, before and after the onset of burst suppression[9, 10]. The pharmacodynamic plateau appeared when the BIS value was approximately 40 during sevoflurane anesthesia[10]. Our model may represent the pharmacodynamic plateau with the $E_{02}$ value, as it was designed with the $E_{max1}$ value fixed at 0. The mean individual predictive $E_{02}$ value of 38.7 for the BIS, close to 40 as shown in other studies, suggests that the transition point into burst suppression can be properly described with our model. The pharmacodynamic plateau in the BIS may be more prominent with anesthetics when the duration of one sequence for increasing or decreasing concentrations of the anesthetic agent is short, which is more clinically applicable[9–11].

Limitations of our study include that the $\lambda_1$ and $C_{eff501}$ of the BIS and CSI are likely to be different from data collected on induction or data including low sevoflurane concentrations, as our experiment precluded the use of less than 1% sevoflurane end-tidal concentrations. The $C_{eff501}$ and $\lambda_1$ may correspond to the $C_{eff50}$ and $\lambda$ in data that exclude the burst suppression or deep anesthetic condition. The $C_{eff501}$ and $\lambda_1$ of the BIS in our study were somewhat greater than the $C_{eff50}$ and $\lambda$ in previously published research[16, 18]. However, our results may be more common from a clinical point of view.

In conclusion, the overall performance of both monitors during sevoflurane anesthesia was similar, despite major differences in their algorithms. However, the CSI was more consistent and more sensitive to changes in sevoflurane concentration, whereas the measured BIS seemed to respond more quickly. The newly developed combined sigmoidal $E_{max}$ model adequately described the pharmacodynamic parameters in the processed EEG data, including the pharmacodynamic plateau. This model could be further investigated for pharmacodynamic data, including the burst suppression plateau.

## Acknowledgements

This work was supported in part by the 2007 Yonsei University Research Fund. The authors thank Tae Dong KWEON, MD (Department of Anesthesiology and Pain Medicine and Anesthesia and Pain Research Institute, Yonsei University College of Medicine, Seoul, Korea), for his assistance with the data collection and design of the research protocol. This work was performed at Gangnam Severance Hospital, Yonsei University College of Medicine, Seoul, Korea.

## Author contribution

Dong Woo HAN and Jong Seok LEE designed research; Jun Ho KIM performed research; Dong Woo HAN, Olinto-Jose LINARES-PERDOMO, and Steven E KERN analyzed data; and Dong Woo HAN wrote the paper.

## References

1 Anderson RE, Jakobsson JG. Cerebral state monitor, a new small handheld EEG monitor for determining depth of anaesthesia: a

clinical comparison with the bispectral index during day-surgery. Eur J Anaesthesiol 2006; 23: 208–12.
2 Fuentes R, Cortínez LI, Struys MM, Delfino A, Muñoz H. The dynamic relationship between end-tidal sevoflurane concentrations, bispectral index, and cerebral state index in children. Anesth Analg 2008; 107: 1573–8.
3 Hoymork SC, Hval K, Jensen EW, Raeder J. Can the cerebral state monitor replace the bispectral index in monitoring hypnotic effect during propofol/remifentanil anaesthesia? Acta Anaesthesiol Scand 2007; 51: 210–6.
4 Anderson RE, Jakobsson JG. Cerebral state index response to incision: a clinical study in day-surgical patients. Acta Anaesthesiol Scand 2006; 50: 749–53.
5 Cortínez LI, Delfino AE, Fuentes R, Muñoz HR. Performance of the cerebral state index during increasing levels of propofol anesthesia: a comparison with the bispectral index. Anesth Analg 2007; 104: 605–10.
6 Jensen EW, Litvan H, Revuelta M, Rodriguez BE, Caminal P, Martinez P, *et al.* Cerebral state index during propofol anesthesia: a comparison with the bispectral index and the A-line ARX index. Anesthesiology 2006; 105: 28–36.
7 Zhong T, Guo QL, Pang YD, Peng LF, Li CL. Comparative evaluation of the cerebral state index and the bispectral index during target-controlled infusion of propofol. Br J Anaesth 2005; 95: 798–802.
8 Sheiner LB, Stanski DR, Vozeh S, Miller RD, Ham J. Simultaneous modeling of pharmacokinetics and pharmacodynamics: application to *d*-tubocurarine. Clin Pharmacol Ther 1979; 25: 358–71.
9 Kreuer S, Bruhn J, Larsen R, Grundmann U, Shafer SL, Wilhelm W. Application of bispectral index and narcotrend index to the measurement of the electroencephalographic effects of isoflurane with and without burst suppression. Anesthesiology 2004; 101: 847–54.
10 Kreuer S, Bruhn J, Walter E, Larsen R, Apfel CC, Grundmann U, *et al*. Comparative pharmacodynamic modeling using bispectral and narcotrend-index with and without a pharmacodynamic plateau during sevoflurane anesthesia. Anesth Analg 2008; 106: 1171–81.
11 Kreuer S, Bruhn J, Ellerkmann R, Ziegeler S, Kubulus D, Wilhelm W. Failure of two commercial indexes and spectral parameters to reflect the pharmacodynamic effect of desflurane on EEG. J Clin Monit Comput 2008; 22: 149–58.
12 Schnider TW, Minto CF, Shafer SL, Gambus PL, Andresen C, Goodale DB, *et al.* The influence of age on propofol pharmacodynamics. Anesthesiology 1999; 90: 1502–16.
13 Billard V, Gambus PL, Chamoun N, Stanski DR, Shafer SL. A comparison of spectral edge, delta power, and bispectral index as EEG measures of alfentanil, propofol, and midazolam drug effect. Clin Pharmacol Ther 1997; 61: 45–58.
14 Cortínez LI, Trocóniz IF, Fuentes R, Gambús P, Hsu YW, Altermatt F, *et al.* The influence of age on the dynamic relationship between end-tidal sevoflurane concentrations and bispectral index. Anesth Analg 2008; 107: 1566–72.
15 Ellerkmann RK, Liermann VM, Alves TM, Wenningmann I, Kreuer S, Wilhelm W, *et al.* Spectral entropy and bispectral index as measures of the electroencephalographic effects of sevoflurane. Anesthesiology 2004; 101: 1275–82.
16 Soehle M, Ellerkmann RK, Grube M, Kuech M, Wirz S, Hoeft A, *et al.* Comparison between bispectral index and patient state index as measures of the electroencephalographic effects of sevoflurane. Anesthesiology 2008; 109: 799–805.
17 Olofsen E, Sleigh JW, Dahan A. The influence of remifentanil on the dynamic relationship between sevoflurane and surrogate anesthetic effect measures derived from the EEG. Anesthesiology 2002; 96: 555–64.
18 Mourisse J, Lerou J, Struys M, Zwarts M, Booij L. Multi-level approach to anaesthetic effects produced by sevoflurane or propofol in humans: 1. BIS and blink reflex. Br J Anaesth 2007; 98: 737–45.
19 Bruhn J, Bouillon TW, Shafer SL. Onset of propofol-induced burst suppression may be correctly detected as deepening of anaesthesia by approximate entropy but not by bispectral index. Br J Anaesth 2001; 87: 505–7.

Acta Pharmacologica Sinica (2011) 32: 1215–1224
 1671-4083/11 $32.00
www.nature.com/aps

Original Article

# Pharmacological mechanisms underlying the antinociceptive and tolerance effects of the 6,14-bridged oripavine compound 030418

Quan WEN, Gang YU, Yu-lei LI, Ling-di YAN*, Ze-hui GONG*

*Department of Medicine Evaluation, Beijing Institute of Pharmacology and Toxicology, Beijing 100850, China*

**Aim:** To investigate possible pharmacological mechanisms underlying the antinociceptive effect of and tolerance to *N*-methyl-7α-[(*R*)-1-hydroxy-1-methyl-3-(thien-3-yl)-propyl]-6,14-endo-ethanotetrahydronororipavine (030418), a derivative of thienorphine.
**Methods:** The binding affinity and efficacy of 030418 were determined using receptor binding and guanosine 5′-O-(3-[$^{35}$S]thio)triphosphate ([$^{35}$S]GTPγS) assays in CHO-μ, CHO-κ, CHO-δ, and CHO-ORL1 cell membranes. The analgesic activity of and tolerance to 030418 were evaluated in thermal nociceptive tests in mice. The effects of 030418 on opioid receptors were further investigated using *in vivo* pharmacological antagonist blockade and *in vitro* tissue preparations.
**Results:** The compound 030418 displayed high binding affinity to all subtypes of opioid receptors with $K_i$ values in the nanomolar range. In [$^{35}$S]GTPγS binding assay, the maximal stimulation of 030418 to μ-, κ-, δ-receptors and the ORL1 receptor was 89%, 86%, 67% and 91%, respectively. In hot-plate test, the antinociceptive effect of 030418 was more potent and longer than morphine. The nonselective opioid receptor antagonist naloxone could completely block 030418-induced antinociception, while both the μ-opioid receptor antagonist β-FNA and the κ-opioid receptor antagonist nor-BNI attenuated 030418-induced antinociception. In contrast, the ORL1 receptor antagonist J-113397 enhanced the antinociceptive effect of 030418. Additionally, chronic treatment with 030418 resulted in a dramatic development of tolerance that could not be effectively prevented by J-113397. In guinea pig ileum preparation, the existing action of 030418 could be removed with difficulty after prolonged washing.
**Conclusion:** The compound 030418 is a novel agonist of opioid receptors with high efficiency, long-lasting effect and liability to tolerance, which may be closely correlated with the methyl group at the $N_{17}$ position and the high hydrophobicity of the $C_7$-thiophene group in its chemical structure.

**Keywords:** 030418; opioid receptor; oripavine; antinociception; drug tolerance

*Acta Pharmacologica Sinica* (2011) 32: 1215–1224; doi: 10.1038/aps.2011.83; published online 22 Aug 2011

## Introduction

Although opioid-derived alkaloids, particularly morphine, are the standard analgesic drugs of choice in the treatment of moderate to severe pain, these compounds cause various adverse reactions[1, 2]. This observation implies that developing other analgesic drugs that exhibit high potency and fewer side effects as alternatives to morphine is still a challenge that remains for pharmacologists and medicinal chemists[3]. The 6,14-bridged oripavines, which were originally derived from the Diels-Alder adducts of thebaine in the 1960s by Bentley and Hardy[4, 5], have been studied extensively to yield a rich source of resultant high-affinity opioid ligands[6]. Among these ligands, a number of important opioid drugs have emerged, such as etorphine/dihydroetorphine, diprenorphine, and particularly buprenorphine. In fact, buprenorphine is still used as an analgesic and is an effective alternative to methadone in the treatment of opiate dependence[7–10].

Many compounds obtained from the structural modification of buprenorphine have also been extensively developed[6, 11, 12]. Inspired by these reports, *N*-cyclopropylmethyl-7α-[(*R*)-1-hydroxy-1-methyl-3-(thien-3-yl)-propyl]-6,14-endo-ethanotetrahydronororipavine (thienorphine, Figure 1) was synthesized in our institute[13]. Previous studies have found that thienorphine has a higher potency, longer duration of action, and better oral bioavailability than buprenorphine[14, 15]. Therefore, thienorphine has a pharmacological profile that indicates its use as a potential treatment for opiate abuse. However, thienorphine has been demonstrated to be a partial κ-opioid receptor agonist with low efficacy at the μ-opioid receptor[16],

* To whom correspondence should be addressed.
E-mail yanlingdi@hotmail.com (Ling-di YAN);
gongzeh@yahoo.com.cn (Ze-hui GONG)
Received 2011-03-12 Accepted 2011-05-18

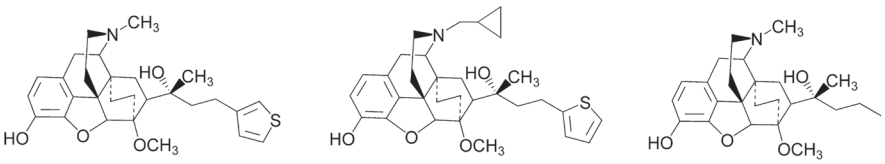


**Figure 1.** Chemical structures of the 6,14-bridged oripavine compounds 030418, thienorphine, and dihydroetorphine.

which might cause poor compliance in addicts.

To obtain more highly efficacious compounds, a series of thienorphine derivatives that possess a thiophene group at the $C_7$ position have been further synthesized and assessed[17]. In primary animal experiments, one of these derivatives, *N*-methyl-7α-[(*R*)-1-hydroxy-1-methyl-3-(thien-3-yl)-propyl]-6,14-endo-ethanotetrahydronororipavine (030418, Figure 1), seemed to show powerful antinociceptive effects. In addition, 030418 exhibited a very low dependence liability in naloxone precipitated withdrawal, conditioned place preference in mice and a self-administration model in rats (unpublished data). Although 6,14-bridged oripavines that possess the complex substituents at the $C_7$ position have been previously reported to have high binding affinities for opioid receptors[18, 19], the pharmacological mechanisms of 030418, which also belongs to the 6,14-bridged oripavine compounds, have not been studied. The present study systematically examined the binding affinity, stimulating potency, and efficacy of 030418 to the μ-, κ-, δ-opioid receptors and the opioid receptor-like 1 receptor (ORL1 receptor) using receptor binding and a [$^{35}$S]GTPγS assay in Chinese hamster ovary (CHO) cell membrane homogenates. In addition, the antinociceptive effects of and tolerance to 030418 and the gold standard morphine were comparatively evaluated in thermal stimuli-induced nociceptive tests in mice. The pharmacological properties of 030418 on opioid receptors were further investigated using *in vivo* pharmacological blockade of opioid receptor antagonists and *in vitro* guinea pig ileum preparations. These investigations illustrate the pharmacological properties and mechanisms of the antinociceptive effect of and tolerance to 030418.

## Materials and methods

### Materials

Compounds including 030418 hydrochloride (purity ≥99%) and thienorphine hydrochloride were synthesized at our institute. Morphine hydrochloride, dihydroetorphine hydrochloride, and buprenorphine hydrochloride were purchased from Qinghai Pharmaceutical Factory (Xining, China). DAMGO, (±)U50488, SNC80, N/OFQ, naloxone, nor-BNI, and GDP were purchased from Sigma Chemical Co (St Louis, MO, USA), while J-113397 and β-FNA were purchased from Tocris Bioscience (Bristol, UK). [$^3$H]diprenorphine (1.85 TBq/mmol) and [$^{35}$S]GTPγS (46.25 TBq/mmol) were obtained from PerkinElmer Inc (Boston, MA, USA), and [$^3$H]nociceptin/OFQ (5.70 TBq/mmol) was obtained from Amersham Corp (Buckinghamshire, UK). GTPγS was purchased from Biolog Life Science Institute (Bremen, Germany). $F_{12}$ medium, fetal bovine serum, and G418 were obtained from Gibco (Grand Island, NY, USA) and GF/C filters from Whatman (Maidstone, UK).

### Animals

Male and female Kunming mice (18–22 g, 7 weeks of age) and male Hartley guinea pigs (350–400 g, 3 months of age) were supplied by the Beijing Animal Center and maintained on a 12-h light/dark cycle (lights on between 7:00 AM and 7:00 PM). Animals were allowed access to food and water *ad libitum*. All experimental procedures were conducted in accordance with the Guidelines for the Use of Experimental Animals and were approved by the local ethical committee and the Institutional Review Committee on Animal Care and Use.

### CHO cell line and membrane preparation

CHO cells stably expressing the rat μ-, human κ-, and human δ-opioid receptors and the human ORL1 receptor have previously been established in our laboratory. These cells were cultured in $F_{12}$ medium supplemented with 100 units/mL penicillin, 100 μg/mL streptomycin, 200 μg/mL Geneticin (G418), and 10% fetal bovine serum at 37 °C in a humidified atmosphere consisting of 95% air and 5% $CO_2$. Cell membranes were prepared using a modified procedure of Zhu *et al*[20]. Briefly, the cells were harvested and centrifuged at 500×*g* for 5 min and the cell pellet was then suspended in Lysis buffer (5 mmol/L Tris, 5 mmol/L EDTA, 5 mmol/L EGTA, and 0.1 mmol/L phenylmethylsulfonyl fluoride, pH 7.4). The cells were passed through a 29-gauge 3/8 syringe needle five times and then centrifuged. The pellet was resuspended in Tris-HCl buffer (50 mmol/L Tris, pH 7.4) and centrifuged again, whereupon this process was repeated. Subsequently, the membrane pellet was resuspended in Tris-HCl buffer (50 mmol/L Tris, pH 7.4). The protein concentration was determined using the Bradford method[21] with bovine serum albumin as the standard. All the above procedures were performed at 4 °C.

### Receptor binding assay

Competitive inhibition of [$^3$H]diprenorphine (1 nmol/L) binding to the μ-, κ-, and δ-opioid receptors or [$^3$H]nociceptin/OFQ (0.5 nmol/L) binding to the ORL1 receptor was performed in the absence or presence of various concentrations of 030418 or thienorphine. Binding was carried out in 50 mmol/L Tris-HCl buffer (pH 7.4) at 37 °C for 30 min in duplicate in a final volume of 0.5 mL with 20–40 μg of membrane protein.

Naloxone (5 μmol/L) and N/OFQ (5 μmol/L) were used to define nonspecific binding. Subsequently, bound and free [$^3$H]diprenorphine or [$^3$H]nociceptin/OFQ were separated by filtration under reduced pressure with GF/C filters presoaked with 0.2% polyethyleneimine. The radioactivity on the filters was determined by liquid scintillation counting (LS6500, Beckmen Inc, USA). Each experiment was performed in duplicate and repeated at least three times. The competitive binding data were fitted to sigmoidal curves for the determination of $IC_{50}$ values. The $K_i$ values of each drug were derived from the $IC_{50}$ values using the following equation: $K_i=IC_{50}/[1+[^3H]\text{ligand}/K_d]$. Based on our previous experiments, the $K_d$ values of [$^3$H]diprenorphine to the μ-, κ-, and δ-opioid receptors and [$^3$H]nociceptin/OFQ to the ORL1 receptor were 0.56 nmol/L, 0.55 nmol/L, 0.46 nmol/L, and 0.29 nmol/L, respectively.

### [$^{35}$S]GTPγS binding assay

Membrane protein (15–50 μg) was incubated with different concentrations of 030418, thienorphine, or dihydroetorphine ($10^{-13}$ to $10^{-5}$ mol/L) in buffer A (100 mmol/L Tris, 100 mmol/L NaCl, and 5 mmol/L $MgCl_2$, pH 7.4) containing [$^{35}$S]GTPγS (200 pmol/L) and GDP (20–40 μmol/L) in a total volume of 0.5 mL at 30 °C for 60 min. Nonspecific binding was defined by incubation in the presence of 20 μmol/L GTPγS. Bound and free [$^{35}$S]GTPγS was separated by filtration with GF/C filters under reduced pressure and rinsed three times with ice-cold buffer B (50 mmol/L Tris-HCl, 50 mmol/L NaCl, and 5 mmol/L $MgCl_2$, pH 7.4). The radioactivity on the filters was determined by liquid scintillation counting. The maximal stimulation of each of the selective agonists DAMGO (μ), (±)U50488 (κ), SNC80 (δ), and N/OFQ (ORL1) was defined as the 100% effect in this experiment. Each experiment was performed in duplicate and repeated at least three times. The concentration-response data were fitted to sigmoidal curves for the determination of $EC_{50}$ values and the maximal effects ($E_{max}$).

### Tail-flick test

The mouse tail-flick test was adapted for measuring the latency of the tail-flick response[22]. Mice were gently held by hand with their tail positioned in an apparatus (Tail-flick Analgesia Meter, Columbia instruments, OH, USA) for radiant heat stimulation on the surface of the tail. The intensity of the heat stimulus was adjusted so that the animal flicked its tail after 3 to 5 s for a baseline reading. The inhibition of the tail-flick response was expressed as a percentage of maximal possible effect (%MPE), which was calculated as $\%MPE=[(T_1-T_0)/(T_2-T_0)]\times100\%$, where $T_0$ and $T_1$ were the tail-flick latencies before and after the treatments, respectively, and $T_2$ was the cut-off time, which was set at 10 s to avoid injury of the tail.

### Hot-plate test

The mouse hot-plate test, as previously reported[23], was used to assess the antinociceptive effects of the compounds. Female mice were individually placed on the surface of a hot plate (Hugo Sachs Elektronik-Harvard Apparatus GmbH, March-Hugstetten, Germany) maintained at 55±0.5 °C. The latency time for hind-paw licking was recorded as the nociceptive response. Mice with a baseline latency shorter than 5 s or longer than 30 s were eliminated. The antinociceptive data are also presented as %MPE calculated using the equation $\%MPE=[(T_1-T_0)/(T_2-T_0)]\times100\%$, where $T_0$ and $T_1$ were the latency times of hind-paw licking before and after treatment, respectively, and $T_2$ was the cutoff time, which was set at 60 s to avoid injury of the animal's paw.

### Dosage regimen and injection procedure in thermal nociception

To establish the dose-response curves in acute thermal nociception tests, mice ($n$=8–10 per group) received sc injections of 030418 alone (1.6–4.0 μg/kg for the tail-flick and 1.4–5.7 μg/kg for the hot-plate test). To compare the effects of 030418 with those of other opioid drugs, morphine (0.7–9.9 mg/kg sc for tail-flick and 1.3–10.0 mg/kg sc for hot-plate) and dihydroetorphine (0.25–0.9 μg/kg sc for tail-flick and 1.3–2.9 μg/kg sc for hot-plate) dose-response curves for thermal antinociception were determined using parameters similar to those described above. The animals were tested for response latency 30 min after administration of 030418, morphine, or dihydroetorphine.

To determine the duration of antinociceptive action during the hot-plate test, mice were administered 030418 (6.0 μg/kg, sc), dihydroetorphine (3.0 μg/kg, sc), or morphine (10 mg/kg, sc) and tested at 0.5, 1, 1.5, 2, 3, 4, 6, 8, 10, and 12 h after injection. The doses of 030418, dihydroetorphine, and morphine were chosen because they produced the greatest level of antinociception of the doses tested.

To determine the effects of different opioid receptor antagonists on the analgesic effects produced by 030418 during the hot-plate test, the animals were pretreated with the nonselective opioid antagonist naloxone (1 mg/kg, sc), the μ-opioid receptor antagonist β-FNA (10 μg/mouse, icv), and the κ-opioid receptor antagonist nor-BNI (3.7 μg/mouse, icv) before sc injection of 030418 (4.0 μg/kg, approximate $ED_{80}$). Animals were also pretreated with the ORL1 receptor antagonist J-113397 (4.0 μg/mouse, icv) before sc injection of 030418 (2.0 μg/kg, approximate $ED_{60}$). In the experiments, the opioid receptor antagonists naloxone, β-FNA, nor-BNI, and J-113397 were respectively administered 15 min, 24 h, 24 h, and 15 min prior to the agonists. The dosage and time intervals of these antagonists were based on previous experiments and reports[24–26]. The doses of the other opioid agonists were administered as follows: morphine (6.0 mg/kg, sc), DAMGO (50 ng/mouse, icv), (±)U50488 (50 μg/mouse, icv), and buprenorphine (1.7 mg/kg, sc). Animals were tested for response latency 15 min after icv injection of DAMGO and (±)U50488 or 30 min after sc injection of 030418, morphine, and buprenorphine. The control groups were given a corresponding volume of vehicle injection.

To establish a chronic analgesic tolerance model during the hot-plate test, animals received sc injections of high doses of 030418 (18.0 μg/kg, once daily), morphine (30.0 mg/kg, thrice daily), or vehicle for 7 consecutive days. The dosage regimen

was used for the induction of drug tolerance, as previously reported by our laboratory[27]. The antinociceptive effects were measured 30 min after administration of the opioid drugs every day to monitor the development of tolerance. In this chronic tolerance model, mice were pretreated with the ORL1 receptor antagonist J-113397 (4.0 μg/mouse, icv) or vehicle 15 min before the last injection of morphine or 030418 on d 7, and the animals were tested at different times after the administration of morphine (30.0 mg/kg, sc) or 030418 (18.0 μg/kg, sc) on d 1 and d 7, respectively.

### Isolated tissue bioassay

The longitudinal muscle of guinea pigs was gently separated from the underlying circular muscle of the ileum using the method described by Paton and Vizi[28] and placed under 1 g tension in a 5 mL organ bath containing Krebs-Henseleit solution (118 mmol/L NaCl, 4.7 mmol/L KCl, 2.5 mmol/L $CaCl_2$, 1.2 mmol/L $MgSO_4$, 1.2 mmol/L $KH_2PO_4$, 25 mmol/L $NaHCO_3$, and 10 mmol/L glucose). The bath was maintained at 37 °C and continuously bubbled with a mixture of 95% $O_2$ and 5% $CO_2$. Muscle contractions were recorded using an isometric transducer coupled to a multichannel polygraph. The data acquired from the samples stimulated by acetylcholine chloride (1.0 μmol/L) was recorded as the ileum muscle contraction response. A single 030418 (0.1 mmol/L), morphine (5 mmol/L), dihydroetorphine (0.2 mmol/L), or vehicle was added to the organ bath containing the tissue preparations ($n$=3–4 samples per group). The response of ileum muscle contractions to opioid drugs was expressed as %inhibition, which was calculated as %inhibition=[1–(muscle contractions after treatment)/(muscle contractions before treatment)]×100%. The tissue preparations were measured at different times during prolonged washing, and the time-course curves were generated.

### Statistical analysis

All the data in this study are expressed as mean±SEM. The $ED_{50}$ values with 95% confidence limits in the antinociceptive assays were calculated using the method described by Bliss[29]. The competition binding data and concentration-response data in [$^{35}$S]GTPγS assays were fitted by nonlinear regression analysis using the Origin 6.0 program (Northampton, MA, USA). The effects of the opioid receptor agonists and antagonists in the hot-plate tests were analyzed using one-way ANOVA followed by the SNK test. The time-course of the drug effects was analyzed using two-way ANOVA for repeated measures followed by Bonferroni-corrected Student's $t$ test. All statistical analyses were performed using SPSS 13.0 (SPSS Inc, Chicago, IL, USA), and $P$<0.05 was the level of statistical significance.

## Results

### Binding affinity of 030418 to opioid receptors and the ORL1 receptor

As shown in Table 1, 030418 showed high binding affinities to all four subtypes of opioid receptors with $K_i$ values for inhibiting [$^3$H]diprenorphine or [$^3$H]nociceptin/OFQ binding in the nanomolar range. The ratio of the $K_i$ values was 1:0.7:0.6:1.7 for μ:κ:δ:ORL1. Similarly, thienorphine also exhibited no selectivity for all four subtypes of receptors. Nevertheless, the $K_i$ value for the inhibition of [$^3$H]nociceptin/OFQ binding to the ORL1 receptor by thienorphine was approximately 22-fold higher than that of 030418.

**Table 1.** Apparent $K_i$ values (nmol/L) of 030418 and thienorphine for μ-, κ-, δ-opioid receptors and the ORL1 receptor. Competitive inhibition of [$^3$H]diprenorphine or [$^3$H]nociceptin/OFQ by 030418 and thienorphine was performed in membranes from CHO-μ, CHO-κ, CHO-δ, and CHO-ORL1 cells as described in Materials and methods. Each value represents mean±SEM from at least three independent experiments performed in duplicate.

| Compound | $K_i$ (nmol/L) | | | |
|---|---|---|---|---|
| | μ | κ | δ | ORL1 |
| 030418 | 0.91±0.05 | 0.60±0.28 | 0.58±0.21 | 1.6±0.4 |
| Thienorphine | 1.4±0.1 | 0.34±0.15 | 0.63±0.48 | 36.5±3.0 |

### Potency and efficacy of 030418 in the [$^{35}$S]GTPγS binding assay

As controls for each receptor, the subtype selective, highly efficacious agonists DAMGO (μ), (±)U50488 (κ), SNC80 (δ), and N/OFQ (ORL1) increased the binding of [$^{35}$S]GTPγS in a concentration-dependent manner and produced maximal stimulations of 174%, 204%, 162%, and 287% over the basal level, respectively. The $EC_{50}$ values and maximal effects ($E_{max}$) are shown in Figure 2 and Table 2. The compound 030418 produced a maximal stimulation of 89% on the μ-opioid receptor, 86% on the κ-opioid receptor, 67% on the δ-opioid receptor, and 91% on the ORL1 receptor. The $EC_{50}$ values of 030418 for the μ-, κ-, and δ-opioid receptors and the ORL1 receptor were 0.10, 0.15, 0.38, and 15 nmol/L, respectively. Comparatively, thienorphine only partially activated the μ- and κ- receptors and showed a maximal response of 28% and 65%, respectively. The $EC_{50}$ values for thienorphine were in the nanomolar range, but this compound was inactive at the δ-opioid receptor and the ORL1 receptor. In addition, dihydroetorphine exhibited full agonism at the μ-, κ-, and δ-opioid receptors and moderate, low-potency agonism at the ORL1 receptor.

### Antinociceptive effect of 030418

According to the data shown in Figure 3, 030418 presented full opioid agonist characteristics with typical sigmoid dose-response curves in thermal stimuli-induced nociceptive models. In the mouse tail-flick test and hot-plate test, the antinociceptive $ED_{50}$ (95% confidence limits) values of 030418 were calculated to be 2.39 μg/kg sc (2.26–2.52) and 2.90 μg/kg sc (2.42–3.37), respectively. In comparison, the $ED_{50}$ (95% confidence limits) values of the gold standard morphine were 3.74 mg/kg sc (2.42–5.05) and 3.20 mg/kg sc (3.02–3.39), respectively. The $ED_{50}$ (95% confidence limits) values of another pure full agonist, dihydroetorphine, were 0.66 μg/kg sc (0.61–0.72)

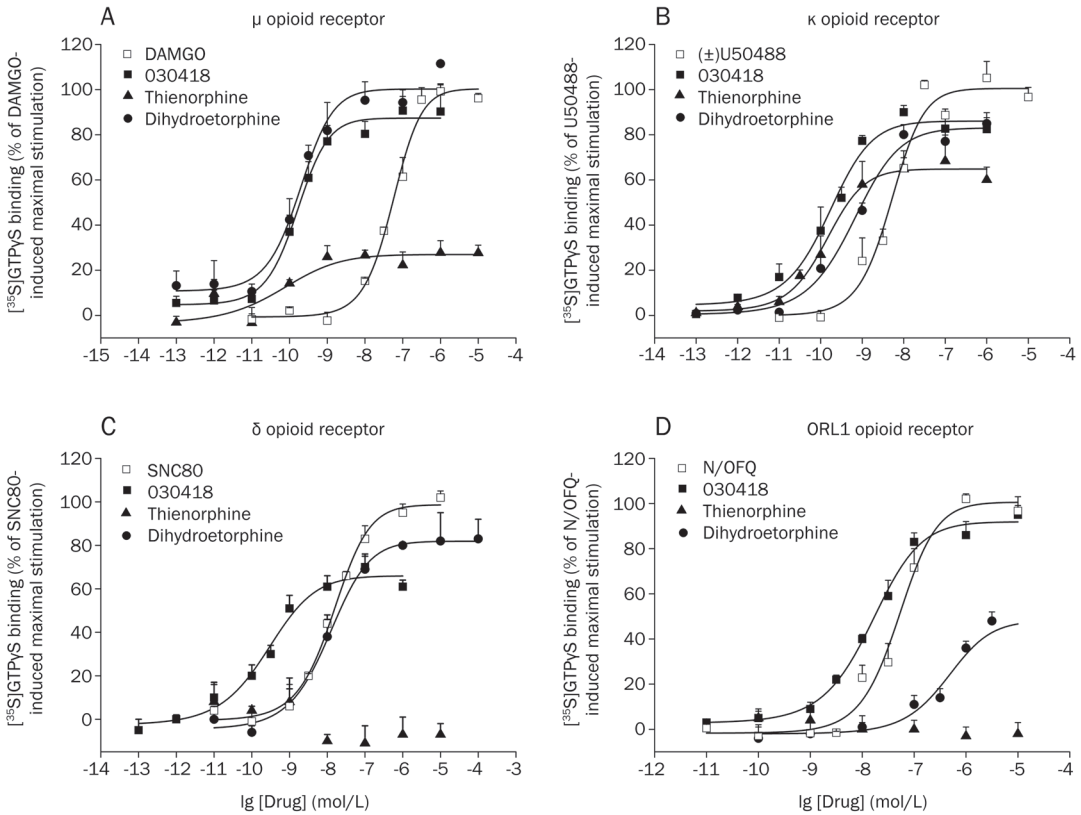


**Figure 2.** Stimulation of [$^{35}$S]GTPγS binding to membranes of CHO-μ (A), CHO-κ (B), CHO-δ (C), and CHO-ORL1 (D) cells by 030418, thienorphine, dihydroetorphine, and a selective full agonist for each subtype of opioid receptors. [$^{35}$S]GTPγS binding was performed as described in the Materials and methods. [$^{35}$S]GTPγS binding data were normalized to the percentage of maximal efficacy induced by each selective full agonist. Each value represents the mean±SEM from at least three independent experiments performed in duplicate. The $EC_{50}$ values and maximal effects ($E_{max}$) are shown in Table 2.

**Table 2.** $EC_{50}$ values (nmol/L) and $E_{max}$ (%) of 030418, thienorphine, and dihydroetorphine in stimulating [$^{35}$S]GTPγS binding to membranes of CHO-μ-, CHO-κ, CHO-δ, and CHO-ORL1 cells. Maximal stimulation of binding was defined using the selective agonists DAMGO (μ), (±)U50488 (κ), SNC80 (δ), and N/OFQ (ORL1). Data were derived from the curves in Figure 2. Each value represents mean±SEM from at least three independent experiments performed in duplicate.

| Compound | μ | | κ | | δ | | ORL1 | |
|---|---|---|---|---|---|---|---|---|
| | $EC_{50}$ (nmol/L) | $E_{max}$ (%) | $EC_{50}$ (nmol/L) | $E_{max}$ (%) | $EC_{50}$ (nmol/L) | $E_{max}$ (%) | $EC_{50}$ (nmol/L) | $E_{max}$ (%) |
| DAMGO | 65.8±13.7 | 100 | | | | | | |
| (±)U50488 | | | 4.8±1.0 | 100 | | | | |
| SNC80 | | | | | 13.2±2.2 | 100 | | |
| N/OFQ | | | | | | | 42.9±13.3 | 100 |
| 030418 | 0.10±0.03 | 89±8 | 0.15±0.08 | 86±5 | 0.38±0.10 | 67±5 | 15.0±2.0 | 91±5 |
| Thienorphine | 0.07±0.03 | 28±4 | 0.13±0.03 | 65±8 | NS | | NS | |
| Dihydroetorphine | 0.18±0.04 | 98±9 | 0.60±0.15 | 83±4 | 7.7±1.9 | 81±6 | 457±110 | 50±4 |

NS, no stimulation up to 10 μmol/L.

and 1.71 μg/kg sc (1.62–1.80), respectively. As shown in Figure 4, the maximally effective dose of 030418 (6.0 μg/kg, sc) had the longest duration of the antinociceptive effect in the mouse hot-plate test compared to that of dihydroetorphine (3.0 μg/kg, sc) and morphine (10.0 mg/kg, sc). This dose of 030418 maintained the maximal antinociceptive activity for at least 2 h after administration and was ineffective 10 h after administration.

### Effects of opioid receptor antagonists on antinociception of 030418

In the mouse hot-plate test, 030418 (4.0 μg/kg, sc), morphine

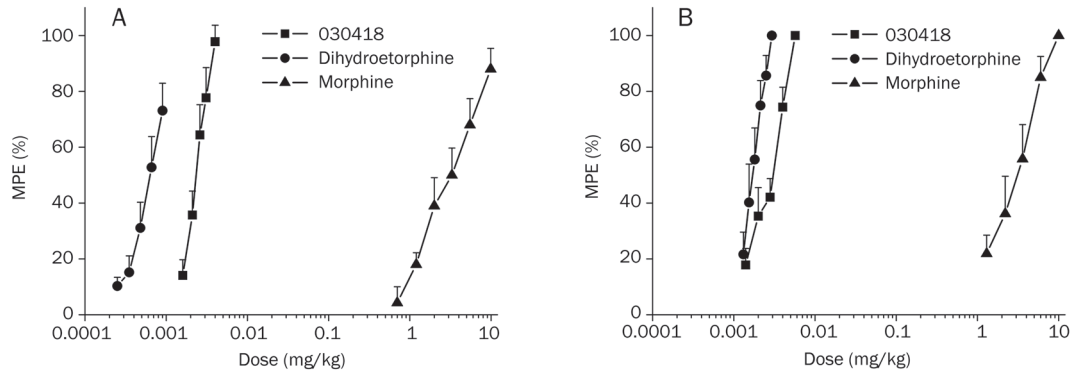


**Figure 3.** Dose-response curves of the antinociceptive effects produced by sc administration of 030418, dihydroetorphine, and morphine in mice. (A) Antinociceptive effects of 030418 (1.6–4.0 μg/kg, sc), dihydroetorphine (0.25–0.9 μg/kg, sc), and morphine (0.7–9.9 mg/kg, sc) in the tail-flick test; (B) Antinociceptive effects of 030418 (1.4–5.7 μg/kg, sc), dihydroetorphine (1.3–2.9 μg/kg, sc), and morphine (1.3–10.0 mg/kg, sc) in the hot-plate test. The data are expressed as %MPE, and each point represents the mean±SEM (*n*=8–10 mice).

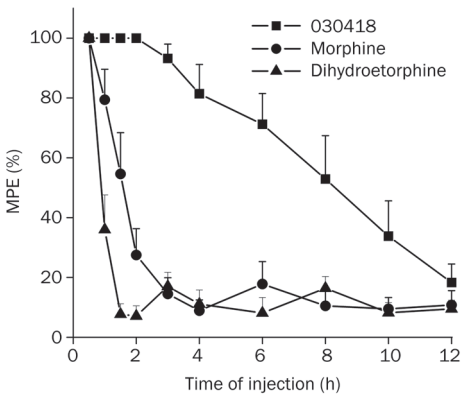


**Figure 4.** Time-course of the antinociceptive effects produced by the administration of 030418 (6.0 μg/kg sc), dihydroetorphine (3.0 μg/kg sc), and morphine (10.0 mg/kg sc) in the mouse hot-plate test. The data are expressed as %MPE, and each point represents the mean±SEM (*n*=8–10 mice).

(6.0 mg/kg, sc), DAMGO (50 ng/mouse, icv), and (±)U50488 (50 μg/mouse, icv) produced a %MPE of approximately 80%. The antinociceptive effects of 030418 and morphine could both be blocked by the nonselective opioid receptor antagonist naloxone (Figure 5A). The selective opioid antagonists β-FNA (10 μg/mouse, icv) and nor-BNI (3.7 μg/mouse, icv) could partially block the DAMGO- and (±)U50488-induced antinociception, respectively (Figure 5B and 5C). Pretreatment with the same doses of β-FNA and nor-BNI decreased the antinociceptive response to 030418 (4.0 μg/kg, sc) to 26% and 50%, respectively. As shown in Figure 5D, moderate doses of 030418 (2.0 μg/kg, sc) and buprenorphine (1.7 mg/kg, sc) respectively produced 64% and 33% of MPE in the hot-plate test. Co-administration of the ORL1 receptor antagonist J-113397 (4.0 μg/mouse, icv) enhanced the %MPE of 030418 to 90% and that of buprenorphine to 56%. In addition, these opioid antagonists administered alone did not alter the latency time in the hot-plate test because the mice that received these compounds exhibited similar levels of %MPE relative to vehicle control mice (data not shown).

### Development of 030418 tolerance and the effect of pretreatment with J-113397

The development of tolerance to 030418 and morphine across 7 d in the mouse hot-plate test is shown in Figure 6A. Many previous studies have used high doses of opioid drugs to induce and study tolerance[27, 30, 31]. As expected, repeated treatment with morphine (30 mg/kg, sc, thrice daily) induced the rapid development of analgesic tolerance. The mice started to develop tolerance on d 4 of morphine injection and had only 45.7% %MPE on d 7. The 18 μg/kg dose of 030418 also produced a significant decrease in %MPE over time. Compared with d 1, 030418 produced a significant reduction in %MPE on d 4, 5, 6, and 7. Moreover, the decrease in antinociception observed after repeated administration of 030418 was more dramatic than that of morphine.

Subsequently, the effects of the ORL1 receptor antagonist J-113397 on analgesic tolerance to morphine and 030418 were further investigated. As mentioned above, repeated treatments with morphine led to tolerance on d 7, and a single pretreatment with J-113397 (4.0 μg/mouse, icv) before the injection of morphine could significantly attenuate the analgesic tolerance to morphine (Figure 6B). In contrast, 030418 tolerance on d 7 was not significantly affected by coadministration of J-113397 over the entire 8-h session (Figure 6C).

### Prolonged washing of 030418 from the guinea pig ileum preparation

In the isolated guinea pig ileum preparation, stimulation induced by acetylcholine chloride (1.0 μmol/L) produces ileum muscle contraction, which can be inhibited by the action of an opioid drug added into the organ bath. The final concentrations of 0.1 mmol/L 030418, 5 mmol/L morphine, or 0.2 mmol/L dihydroetorphine were chosen in the experiments because they could produce an approximately 80% inhibition. As shown in Figure 7, 030418, morphine and dihydro-

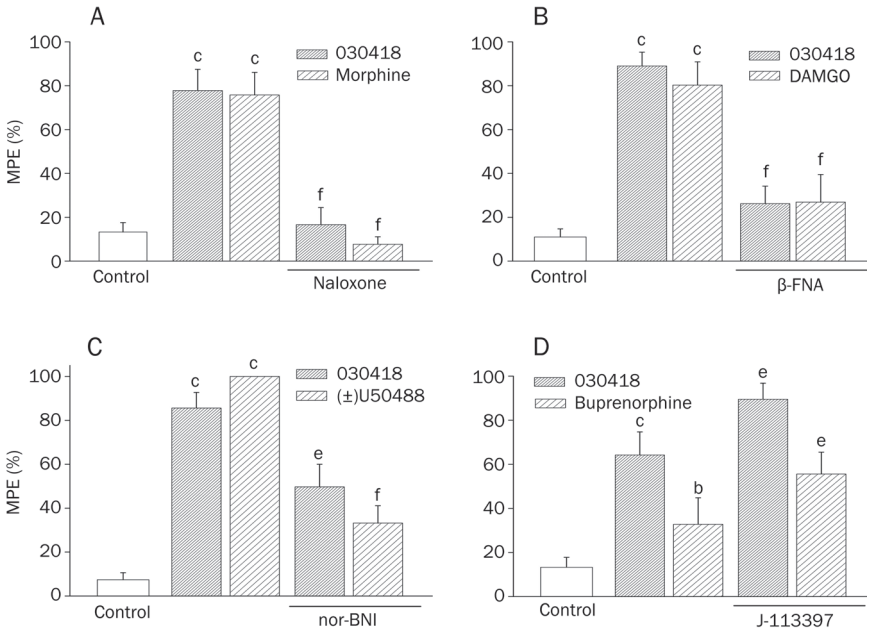


**Figure 5.** Effects of the nonselective opioid receptor antagonist naloxone (A), selective μ-opioid receptor antagonist β-FNA (B), selective κ-opioid receptor antagonist nor-BNI (C), and selective ORL1 receptor antagonist J-113397 (D) on the antinociception activity of 030418 in the mouse hot-plate tests. 030418 (4.0 μg/kg ABC; 2.0 μg/kg D, sc), morphine (6.0 mg/kg, sc), DAMGO (50 ng/mouse, icv), (±)U50488 (50 μg/mouse, icv), buprenorphine (1.7 mg/kg, sc), or vehicle control were administered before testing. The mice were pretreated with naloxone (1 mg/kg, sc), β-FNA (10 μg/mouse, icv), nor-BNI (3.7 μg/mouse, icv), or J-113397 (4.0 μg/mouse, icv) at 15 min, 24 h, 24 h, or 15 min, respectively, before administration of the corresponding agonists. The data are expressed as %MPE, and each point represents the mean±SEM ($n$=8–10 mice). $^{b}P<0.05$, $^{c}P<0.01$ *vs* control; $^{e}P<0.05$, $^{f}P<0.01$ *vs* corresponding agonists.

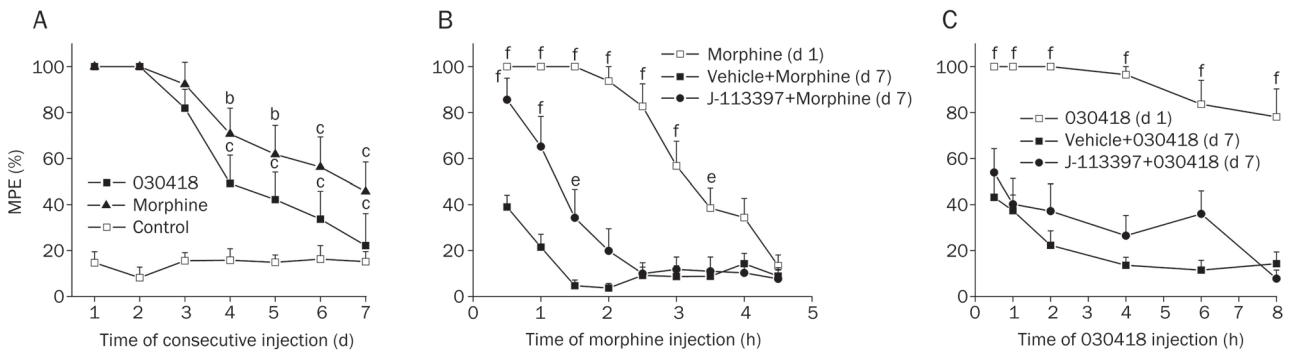


**Figure 6.** Effects of pretreatment with the selective ORL1 receptor antagonist J-113397 on morphine or 030418 tolerance in the mouse hot-plate test. (A) Analgesic tolerance to morphine, 030418, or vehicle control; (B) Time-course of morphine-induced antinociception without (vehicle) or with J-113397 in the tolerance model; (C) Time course of 030418-induced antinociception without (vehicle) or with J-113397 in the tolerance model. The mice repeatedly received sc injections of morphine (30.0 mg/kg, thrice daily), 030418 (18.0 μg/kg, once daily), or vehicle control. J-113397 (4.0 μg/mouse icv) or vehicle was administered 15 min before the last injection of morphine or 030418 on d 7. The data are expressed as %MPE, and each point represents the mean±SEM ($n$=8–10 mice). $^{b}P<0.05$, $^{c}P<0.01$ *vs* first injection on d 1. $^{e}P<0.05$, $^{f}P<0.01$ *vs* vehicle+corresponding agonists at the same time on d 7.

etorphine all significantly inhibited ileum muscle contraction stimulated by acetylcholine chloride (1.0 μmol/L) at time zero. During prolonged washing, the action of morphine and dihydroetorphine could be easily removed within 5 min, which was a relatively rapid process. In comparison, the course of prolonged washing of 030418 was much slower, and the inhibitory effect of 030418 remained at 24% until 45 min after the attempted washout. Moreover, the time course curve of 030418 was biphasic with an initial rapid phase followed by a slower phase.

## Discussion

The 6,14-bridged oripavines, which possess a $C_6$-methoxy group part of the ring system and a long alkyl chain at the

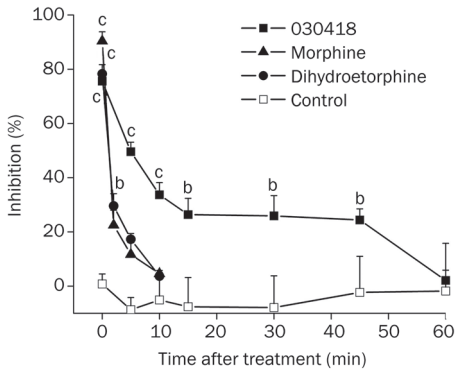


**Figure 7.** Time course of inhibition induced by 030418 (0.1 mmol/L), morphine (5 mmol/L), dihydroetorphine (0.2 mmol/L), or vehicle control on guinea pig ileum muscle contraction during prolonged washing. Ileum muscle contractions stimulated by acetylcholine chloride (1.0 μmol/L) were recorded as the sample responses. The data are expressed as %inhibition, and each point represents the mean±SEM ($n$=3–4 samples). $^bP<0.05$, $^cP<0.01$ *vs* control at the same time.

$C_7$ substituent, have been reported to have high affinity to opioid receptors[6]. As expected, the receptor binding assay revealed that 030418, a novel 6,14-bridged oripavine compound, displayed nonselective binding affinities to the μ-, κ-, and δ-opioid receptors and the ORL1 receptor with $K_i$ values in the nanomolar range, as did thienorphine. Moreover, our observation that thienorphine highly bound to the μ-, κ-, and δ-opioid receptors is in accord with previous reports[15, 16].

Consistent with Li *et al*[16], thienorphine exhibited partial agonist activity at the κ-opioid receptor and at the μ-opioid receptor (to a lesser extent) but not at the δ-opioid receptor *in vitro*. In contrast, 030418, which has a methyl group at the $N_{17}$ substituent, was more efficacious in stimulating [$^{35}$S]GTPγS binding at the μ-, κ-, and δ-opioid receptors and the ORL1 receptor than its parent congener, thienorphine. This compound was also equally as efficacious as dihydroetorphine at all subtypes of the receptors except at the ORL1 receptor. Several structure-activity relationship (SAR) studies have shown that the 6,14-bridged oripavines with a cyclopropylmethyl group at $N_{17}$, such as diprenorphine, buprenorphine, and naltrexone, might possess some morphine-antagonist characteristics. Replacing this group with a methyl group has been found to greatly increase the efficacy of compounds, particularly at the μ- and κ-opioid receptors[11, 12]. We also considered that the mixed ORL1/μ-opioid receptor activity of 030418 may have an attractive profile for the treatment of pain and addiction, similar to SR16435 and buprenorphine[32, 33]. However, explaining the nonselective agonism of 030418 at opioid receptors will be difficult, and further studies are required to provide insights into the SAR of 030418 and the 6,14-bridged oripavine scaffold.

In the mouse tail-flick test and hot-plate test, the antinociceptive potency of 030418 was similar to that of the typical full agonist dihydroetorphine. Moreover, the $ED_{50}$ value of 030418 was in the microgram range and was calculated as approximately 1100–1500 times that of the standard morphine hydrochloride. Experimental data regarding the potency of dihydroetorphine and morphine were consistent with those of Aceto *et al*[34]. In addition, 030418 had more potent and powerful antinociceptive effects *in vivo* than its parent compound thienorphine, which has previously been demonstrated to be a partial opioid agonist, with an $ED_{50}$ value in the milligram range in the mouse antinociceptive tests[15]. Compared with morphine, 030418 shows a rather long-lasting duration of the antinociceptive effect in the hot-plate test, which is similar to thienorphine. This similarity could occur because 030418 and thienorphine may have tight lipophilic interactions with the binding pocket of opioid receptors given the high liposolubility of the $C_7$ substituent. This feature may lead to the persistent occupation of the opioid receptors by 030418. Several early reports have also demonstrated that 6,14-bridged oripavine compounds have very powerful binding interactions with opioid receptors and thus slow receptor kinetics, which causes a long-lasting effect[35–37].

Using pharmacological blockade in the hot-plate tests, the antinociception mediated by 030418 could be fully reversed by systemic administration of the classic opioid receptor antagonist naloxone, suggesting that the antinociceptive effect of 030418, similar to morphine, is likely related to the opioid receptor system. In addition, icv pretreatment with either β-FNA (μ-opioid receptor antagonist) or nor-BNI (κ-opioid receptor antagonist) was found to decrease 030418-induced antinociception. These results indicate that the activation of supraspinal μ- and κ-opioid receptors appears to be involved in the antinociceptive effect of 030418. The μ-opioid receptor is generally considered to represent the major molecular gate for opioid analgesia, and the activation of the κ-opioid receptor also evokes an analgesic action[38]. More interestingly, icv pretreatment with J-113397 (ORL1 receptor antagonist) could enhance antinociception induced by a moderate dose of 030418. In summary, the experimental results demonstrate that systemic administration of 030418 can simultaneously activate the μ- and κ-opioid receptor and the ORL-1 receptor *in vivo*.

Although 030418 showed remarkable antinociceptive effects, high doses of this compound unfortunately produced significant and rapid development of analgesic tolerance. In chronically administered animal models, 030418 produced a 78% decrease in %MPE on d 7 relative to d 1; in comparison, morphine produced a 54% decrease in %MPE. Although repeated administration of opioid agonists unavoidably produces analgesic tolerance associated with adaptive changes on opioid receptors and complex molecular events in cellular signaling pathways[39], our observation of the dramatic development of tolerance to 030418, which activates both the ORL1 and the μ-opioid receptors, seems contradictory to earlier reports. These studies have hypothesized that a compound that contains both μ-opioid receptor and ORL1 receptor agonist activities has reduced tolerance development[32, 33]. Thus, we next investigated the effect of pretreatment with the selective ORL1 antagonist J-113397 on 030418 tolerance. The experimental

results suggested that pharmacological blockade with J-113397 significantly prevented analgesic tolerance to morphine on d 7, which confirms earlier findings[30, 31]. In contrast, pretreatment with J-113397 could not effectively alter the development of tolerance to 030418. These findings highlight the complicated relationship between ORL1 receptor activation and μ-opioid receptor mediated tolerance. Therefore, additional studies are necessary to explain the issue.

Previous [$^{35}$S]GTPγS assays have revealed the high efficacy of 030418 at μ- and κ-opioid receptors; therefore, the inhibition by 030418 on muscle contraction in the guinea pig ileum (a tissue with enriched populations of functional μ- and κ-opioid receptors) seen in this study may have been primarily mediated through opioid receptor activity. Notably, the action of 030418 could be removed (with difficulty, compared to morphine and dihydroetorphine) by repeated, prolonged washing. This finding, taken together with the observation that 030418 had high binding affinity to opioid receptors, clearly indicates that 030418 has slow receptor dissociation kinetics. Considering that the only difference between 030418 and dihydroetorphine exists in the $C_7$ substituent structure (Figure 1), the persistent binding affinity of 030418 to the opioid receptors may result from the high hydrophobicity caused by the structure of the $C_7$-thiophene group. Similar examples of slow receptor dissociations of buprenorphine and BU74 have been observed and have been explained by powerful lipophilic binding interactions with the opioid receptors[37, 40]. The pharmacological property of slow receptor dissociation kinetics may account for the long duration of the agonist effect of 030418 *in vivo*. Additionally, the persistent occupation of the opioid receptors, particularly the μ-opioid receptors, can easily lead to the development of tolerance to 030418 by either receptor phosphorylation or a combination of receptor phosphorylation and desensitization. Woolf and Linderman[41] have believed that the ligand receptor dissociation rate constant and the conformational selectivity factor, which roughly corresponds to a drug's efficacy, positively conspire to regulate receptor phosphorylation.

In conclusion, the present study demonstrates that 030418, a 6,14-bridged oripavine compound, is a nonselective, high-affinity, and full opioid receptor agonist *in vitro*. This compound has highly potent and long-lasting antinociceptive effects, and tolerance to 030418 rapidly develops *in vivo*. The pharmacological properties of 030418 closely correlate with a high activity of the methyl group at the $N_{17}$ position and high hydrophobicity of the $C_7$-thiophene group in the 030418 chemical structure. The results of this study indicate that 030418 may be a candidate for development in the management of acute pain or as a 'universal' opioid ligand to be used as a pharmacological tool. Although more efforts are needed to discover the possible mechanisms of the unique effects of 030418, the current findings help to further understand the SAR of 6,14-bridged oripavines and provide insights into the design of ideal opioid drugs.

## Acknowledgements

This work was supported by the National High Technology Research and Development Program of China (No 2005AA233040) and the National S&T Major Project of Original New Drug Research of China (No 2009ZXJ09004-079). We acknowledge Dr Bo-hua ZHONG and his group for supplying samples of 030418 and thienorphine for these experiments. We also thank Dr Zheng YONG and Dr Yan GAO for excellent expert technical assistance.

## Author contribution

Ze-hui GONG and Ling-di YAN designed the research; Quan WEN and Yu-lei LI performed the research; Quan WEN and Gang YU analyzed the data; and Quan WEN wrote the paper.

## References

1 Cherny NJ, Chang V, Frager G, Ingham JM, Tiseo PJ, Popp B, *et al*. Opioid pharmacotherapy in the management of cancer pain: a survey of strategies used by pain physicians for the selection of analgesic drugs and routes of administration. Cancer 1995; 76: 1283–93.
2 Koob GF, Le Moal M. Drug abuse: hedonic homeostatic dysregulation. Science 1997; 278: 52–8.
3 Berger AC, Whistler JL. How to design an opioid drug that causes reduced tolerance and dependence. Ann Neurol 2010; 67: 559–69.
4 Bentley KW, Hardy DG. Novel analgesics and molecular rearrangements in the morphine-thebaine group. I. Ketones derived from 6,14-endo-ethenotetrahydrothebaine. J Am Chem Soc 1967; 89: 3267–73.
5 Bentley KW, Hardy DG. Novel analgesics and molecular rearrangements in the morphine-thebaine group. III. Alcohols of the 6,14-endo-ethenotetrahydrooripavine series and derived analogs of N-allylnormorphine and -norcodeine. J Am Chem Soc 1967; 89: 3281–92.
6 Lewis JW, Husbands SM. The orvinols and related opioids — high affinity ligands with diverse efficacy profiles. Curr Pharm Des 2004; 10: 717–32.
7 Cowan A, Lewis JW, MacFarlane IR. Agonist and antagonist properties of buprenorphine, a new antinociceptive agent. Br J Pharmacol 1977; 60: 537–45.
8 Mello NK, Mendelson JH, Lukas SE, Gastfriend DR, Teoh SK, Holman BL. Buprenorphine treatment of opiate and cocaine abuse: clinical and preclinical studies. Harv Rev Psychiatry 1993; 1: 168–83.
9 Picard PR, Tramer MR, McQuay HJ, Moore RA. Analgesic efficacy of peripheral opioids (all except intra-articular): a qualitative systematic review of randomised controlled trials. Pain 1997; 72: 309–18.
10 Barnett PG, Rodgers JH, Bloch DA. A metaanalysis comparing buprenorphine to methadone for treatment of opiate dependence. Addiction 2001; 96: 683–90.
11 Park HS, Lee HY, Kim YH, Park JK, Zvartau EE, Lee H. A highly selective kappa-opioid receptor agonist with low addictive potential and dependence liability. Bioorg Med Chem Lett 2006; 16: 3609–13.
12 Rennison D, Neal AP, Cami-Kobeci G, Aceto MD, Martinez-Bermejo F, Lewis JW, *et al*. Cinnamoyl derivatives of 7α-aminomethyl-6,14-endo-ethanotetrahydrothebaine and 7α-aminomethyl-6,14-endoethano-tetrahydrooripavine and related opioid ligands. J Med Chem 2007; 50: 5176–82.
13 Liu CH, Liu H, Han XY, Wu B, Zhong BH, Gong ZH. Synthesis and characterization of thienorphine and its glucuronide conjugate. Synth Commun 2005; 35: 701–10.

14 Zhao WL, Gong ZH, Liang JH. A new buprenorphine analogy, thienorphine, inhibits morphine-induced behavioral sensitization in mice. Acta Pharmacol Sin 2004; 25: 1413–8.
15 Yu G, Yue YJ, Cui MX, Gong ZH. Thienorphine is a potent long-acting partial opioid agonist: a comparative study with buprenorphine. J Pharmacol Exp Ther 2006; 318: 282–7.
16 Li JX, Becker GL, Traynor JR, Gong ZH, France CP. Thienorphine: receptor binding and behavioral effects in rhesus monkeys. J Pharmacol Exp Ther 2006; 321: 227–36.
17 Yu G, Liu YS, Yan LD, Wen Q, Gong ZH. Structure-activity relationships analysis of thienorphine and its derivatives. Yao Xue Xue Bao 2009; 44: 726–30.
18 Loew GH, Berkowitz DS. Intramolecular hydrogen bonding and conformational studies of bridged thebaine and oripavine opiate narcotic agonists and antagonists. J Med Chem 1979; 22: 603–7.
19 Sebastian A, Bidlack JM, Jiang Q, Deecher D, Teitler M, Glick SD, *et al*. 14 beta-[(*p*-nitrocinnamoyl)amino]morphinones, 14 beta-[(*p*-nitrocinnamoyl)amino]-7,8-dihydro-morphinones, and their codeinone analogues: synthesis and receptor activity. J Med Chem 1993; 36: 3154–60.
20 Zhu J, Luo LY, Chen C, Liu-Chen LY. Activation of the cloned human kappa-opioid receptor by agonists enhances [$^{35}$S]GTPgammaS binding to membranes: determination of potencies and efficacies of ligands. J Pharmacol Exp Ther 1997; 282: 676–68.
21 Bradford MM. A rapid and sensitive method for the quantitation of microgram quantities of protein utilizing the principle of protein-dye binding. Anal Biochem 1976; 72: 248–54.
22 D'Amour FE, Smith DL. A method for determining loss of pain sensation. J Pharmacol Exp Ther 1941; 72: 74–9.
23 Eddy NB, Leimbach D. Synthetic analgesics. II. Dithienylbutenyl- and dithienylbutylamines. J Pharmacol Exp Ther 1953; 107: 385–93.
24 Horan P, Taylor J, Yamamura HI, Porreca F. Extremely long-lasting antagonistic actions of nor-binaltorphimine (nor-BNI) in the mouse tail-flick test. J Pharmacol Exp Ther 1992; 260: 1237–43.
25 Craft RM, Henley SR, Haaseth RC, Hruby VJ, Porreca F. Opioid antinociception in a rat model of visceral pain: systemic versus local drug administration. J Pharmacol Exp Ther 1995; 275: 1535–42.
26 Lutfy K, Eitan S, Bryant CD, Yang YC, Saliminejad N, Walwyn W, *et al*. Buprenorphine-induced antinociception is mediated by mu-opioid receptors and compromised by concomitant activation of opioid receptor-like receptors. J Neurosci 2003; 23: 10331–7.
27 Wu N, Lu XQ, Yan HT, Su RB, Wang JF, Liu Y, *et al*. Aquaporin 4 deficiency modulates morphine pharmacological actions. Neurosci Lett 2008; 448: 221–5.
28 Paton WD, Vizi ES. The inhibitory action of noradrenaline and adrenaline on acetylcholine output by guinea-pig ileum longitudinal muscle strip. Br J Pharmacol 1969; 35: 10–28.
29 Bliss CI. Statistics in biology. New York: McGraw-Hill Book Company; 1967.
30 Ueda H, Inoue M, Takeshima H, Iwasawa Y. Enhanced spinal nociceptin receptor expression develops morphine tolerance and dependence. J Neurosci 2000; 20: 7640–7.
31 Chung S, Pohl S, Zeng J, Civelli O, Reinscheid RK. Endogenous orphanin FQ/nociceptin is involved in the development of morphine tolerance. J Pharmacol Exp Ther 2006; 318: 262–7.
32 Khroyan TV, Zaveri NT, Polgar WE, Orduna J, Olsen C, Jiang F, *et al*. SR 16435 [1-(1-(bicyclo[3.3.1]nonan-9-yl)piperidin-4-yl)indolin-2-one], a novel mixed nociceptin/orphanin FQ/mu-opioid receptor partial agonist: analgesic and rewarding properties in mice. J Pharmacol Exp Ther 2007; 320: 934–43.
33 Spagnolo B, Calo G, Polgar WE, Jiang F, Olsen CM, Berzetei-Gurske I, *et al*. Activities of mixed NOP and mu-opioid receptor ligands. Br J Pharmacol 2008; 153: 609–19.
34 Aceto MD, Harris LS, Bowman ER. Etorphines: mu-opioid receptor-selective antinociception and low physical dependence capacity. Eur J Pharmacol 1997; 338: 215–23.
35 Boas RA, Villiger JW. Clinical actions of fentanyl and buprenorphine. The significance of receptor binding. Br J Anaesth 1985; 57: 192–6.
36 Neilan CL, Husbands SM, Breeden S, Ko MC, Aceto MD, Lewis JW, *et al*. Characterization of the complex morphinan derivative BU72 as a high efficacy, long-lasting mu-opioid receptor agonist. Eur J Pharmacol 2004; 499: 107–16.
37 Husbands SM, Neilan CL, Broadbear J, Grundt P, Breeden S, Aceto MD, *et al*. BU74, a complex oripavine derivative with potent kappa opioid receptor agonism and delayed opioid antagonism. Eur J Pharmacol 2005; 509: 117–25.
38 Pasternak GW. Pharmacological mechanisms of opioid analgesics. Clin Neuropharmacol 1993; 16: 1–18.
39 Kieffer BL, Evans CJ. Opioid tolerance — in search of the holy grail. Cell 2002; 108: 587–90.
40 Hambrook JM, Rance MJ. The interaction of buprenorphine with the opiate receptor: lipophilicity as a determining factor in drug-receptor kinetics. In: Kosterlitz HW, editor. Opiates and endogenous opioid peptides. Amsterdam: Elsevier; 1976. p 295–301.
41 Woolf PJ, Linderman JJ. Untangling ligand induced activation and desensitization of G-protein coupled receptors. Biophys J 2003; 84: 3–13.

Acta Pharmacologica Sinica (2011) 32: 1225–1232

www.nature.com/aps

Original Article

# Neurobehavioral and genotoxic parameters of antipsychotic agent aripiprazole in mice

Jaqueline Nascimento PICADA[1, *], Bruna de Jesus Neto DOS SANTOS[2], Franciele CELSO[2], Jéssica Dias MONTEIRO[2], Kelly Morais DA ROSA[2], Leandro Rosa CAMACHO[3], Luciana Rodrigues VIEIRA[1], Taís Madelon FREITAS[1], Tatiana Grasiela DA SILVA[2], Viviane Minuzzo PONTES[2], Patrícia PEREIRA[2]

*[1]Laboratório de Genética Toxicológica, Programa de Pós-Graduação em Genética e Toxicologia Aplicada, Universidade Luterana do Brasil, ULBRA, Bairro São José, Canoas, RS, CEP: 92425-900, Brazil; [2]Laboratório de Farmacologia e Toxicologia, Programa de Pós-Graduação em Genética e Toxicologia Aplicada, ULBRA, Canoas, RS, Brazil; [3]Laboratório de Bioinformática Estrutural, Programa de Pós-Graduação em Genética e Toxicologia Aplicada, ULBRA, Canoas, RS, Brazil*

**Aim:** Aripiprazole is an antipsychotic agent to treat schizophrenia, which acts through dopamine $D_2$ partial agonism, serotonin 5-$HT_{1A}$ partial agonism and 5-$HT_{2A}$ antagonism. This study was designed to evaluate the neurobehavioral effects and genotoxic/mutagenic activities of the agent, as well as its effects on lipoperoxidation.
**Methods:** Open field and inhibitory avoidance tasks were used. Thirty min before performing the behavioral tasks, adult male CF-1 mice were administered aripiprazole (1, 3 or 10 mg/kg, ip) once for the acute treatment, or the same doses for 5 d for the subchronic treatment. Genotoxic effects were assessed using comet assay in the blood and brain tissues. Mutagenic effects were evaluated using bone marrow micronucleus test. Lipoperoxidation was assessed with thiobarbituric acid reactive substances (TBARS).
**Results:** Acute and subchronic treatments significantly decreased the number of crossing and rearing in the open field task. Acute treatment significantly increased the step-down latency for both the short- and long-term memory in the inhibitory avoidance task. Subchronic treatments with aripiprazole (3 and 10 mg/kg) caused significant DNA strain-break damage in peripheral blood but not in the brain. Mutagenic effect was not detected in the acute and subchronic treatments. Nor TBARS levels in the liver were affected.
**Conclusion:** Aripiprazole improved memory, but could impair motor activities in mice. The drug increased DNA damage in blood, but did not show mutagenic effects, suggesting that it might affect long-term genomic stability.

**Keywords:** antipsychotic agent; aripiprazole; locomotion; memory; genotoxic/mutagenic activities; DNA damage; lipoperoxidation

*Acta Pharmacologica Sinica* (2011) 32: 1225–1232; doi: 10.1038/aps.2011.77; published online 15 Aug 2011

## Introduction

Cognitive deficits (attention, executive function, short- and long-term memory) are symptoms observed in patients with schizophrenia[1, 2]. Several studies have assessed physiopathologic aspects linked to schizophrenia, such as declarative and nondeclarative memory functions, to identify areas of impairment *versus* preservation[3]. Similarly, some investigations have evaluated the effect of antipsychotic drugs on cognitive parameters in humans and animals[4, 5]. Research suggests that schizophrenic patients treated with atypical antipsychotics may perform better in cognitive tasks when compared to patients treated with typical antipsychotics[2, 6].

Aripiprazole, 7-{4-[4-(2,3-dichlorophenyl)-1-piperazinyl] butyloxy}-3,3-dihydro-carbostycil (Figure 1), is an atypical antipsychotic drug with distinct properties compared to other efficient antipsychotics[4]. The drug was developed recently, and it presents a unique pharmacological profile that includes dopamine $D_2$ partial agonism, serotonin 5-$HT_{1A}$ partial agonism, and 5-$HT_{2A}$ antagonism[5, 6]. Clinical trials have found that aripiprazole was effective in treating the positive, negative, and cognitive symptoms of schizophrenia[7]. Numerous large scale clinical studies have shown that aripiprazole has a favorable safety and tolerability profile with a relatively low potential for parkinsonism, prolactin elevation, weight gain, QTc prolongation, sedation, tardive dyslinesia, changes in

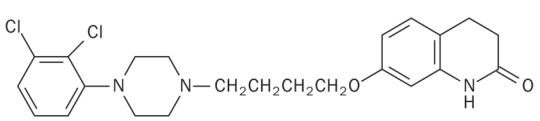


**Figure 1.** Structure of aripiprazole.

* To whom correspondence should be addressed.
E-mail jnpicada@cpovo.net
Received 2011-02-06 Accepted 2011-05-09

plasma lipid levels, and glucose level elevation[8].

In the experimental context, Nagai *et al*[9] showed that aripiprazole that was administered as either a single dose or as consecutive doses (for 7 d) ameliorated phencyclidine-induced impairment of recognition memory in mice. However, another study showed that aripiprazole impaired the passive-avoidance response at doses near its anti-dopamine $ED_{50}$ (7.7 mg/kg, as defined by apomorphine stereotypy). At doses lower than those that affected the passive-avoidance response, aripiprazole was unable to reverse the MK-801-induced impairment in the same task[4]. Therefore, further investigations are necessary to elucidate the effect of aripiprazole on memory.

The aim of the present study was to investigate the effects of aripiprazole on memory and on locomotor and exploratory activities with the inhibitory avoidance and open field tasks as behavioral models. Some drugs that affect memory can induce damage in biomolecules, such as lipids and DNA. Therefore, possible cytotoxic and genotoxic effects were evaluated by measuring lipid peroxidation in the liver and DNA strand breaks in both the peripheral blood and brain tissues after behavioral tasks. Mutagenic effects of aripiprazole were also assessed using the micronucleus frequency in the bone marrow of mice.

## Materials and methods

### Animals

Male SR-1 mice (163 animals, 2–3 months of age; 30–40 g) from our breeding colony were used. The mice were housed in plastic cages with *ad libitum* access to water and food, under a 12-h light/dark cycle (lights on at 8:00 AM), and at a constant temperature of 23.0 °C. All experimental procedures were performed in accordance with the NIH Guide for the Care and Use of Laboratory Animals and the Brazilian Society for Neuroscience and Behavior (SBNeC) recommendations for animal care. This work was approved by the Ethical Committee of ULBRA.

### Drugs and pharmacological procedures

Abilify™ (Brystol) was used as a source of aripiprazole. Four pills of 20 mg aripiprazole were powdered in a ceramic pestle, and two extractions by steam route were performed with 20% ethanol and ethanol pro analysi (PA). An infrared technique was used to analyze the samples, and the resulting spectrum was compared with the spectrum from the monography.

Aripiprazole was dissolved in saline solution and 5% Tween. The animals were divided in groups and received saline, 5% Tween or 1, 3, or 10 mg/kg doses of aripiprazole. The animals were given only one intraperitoneal (ip) injection (acute treatment) or one injection per day for 5 d (subchronic treatment) as a 0.1 mL/10 g body weight dose. The doses were chosen based on previous reports about the behavioral effects of aripiprazole[4]. To study the effect that aripiprazole has on memory, the animals received injections 30 min before training in the inhibitory avoidance task.

### Neurobehavioral experiments

#### *Open field behavior*

The animals were exposed to a 40 cm×50 cm×60 cm open field that was divided into 12 equal squares. The animals were placed in the rear left square, and they were allowed to freely explore the field for 5 min. The animals received the injections 30 min before the test. Crossing of the black lines, rearings performed, and latency to start locomotion were counted and used as measurements of locomotion, exploration and motivation[10].

#### *Inhibitory avoidance task*

Inhibitory avoidance in rodents is a widely used animal model of aversive learning and memory. A 50 cm×25 cm×25 cm plastic box with a frontal glass wall that had a floor that consisted of parallel 10-mm caliber bronze bars spaced 1 cm from one another was used. The left end of the grid was equipped with a 9-cm wide and 1.5-cm high platform. The mice were placed gently on the platform facing the rear wall, and their latency to step down with all four paws onto the grid was measured. In the training session, after stepping down, the animals received a 0.3-mA, 2-s scrambled foot shock and were immediately withdrawn from the cage. In the test session, either 1.5 h short-term memory (STM) or 24 h long-term memory (LTM) later, the procedure was repeated, but the foot shock was not given. Test session step-down latency was used as a measure of retention. A 180-s upper bound was set up for this measure[10].

### Genotoxic/mutagenic assays

#### *Comet assay*

The alkaline comet assay in peripheral blood and brain tissues was performed as previously described[11] but with minor modifications[12, 13]. Blood samples were collected from a tail blood vessel 3 h and 24 h after the first administration (acute treatment) and 3 h after the last administration (subchronic treatment). The animals were killed by cervical dislocation, and forebrain samples were immediately collected. Each piece of forebrain was finely minced and placed in 0.5 mL of cold phosphate-buffered saline (PBS) to obtain a cell suspension. Brain and blood cell suspensions (5 μL) were embedded in 95 μL of 0.75% low melting point agarose (Gibco BRL) and spread on agarose-precoated microscope slides. After solidification, the slides were placed in lysis buffer (2.5 mol/L NaCl, 100 mmol/L EDTA and 10 mmol/L Tris, pH 10.0) with freshly added 1% Triton X-100 (Sigma) and 10% DMSO for 48 h at 4 °C. The slides were subsequently incubated in freshly prepared alkaline buffer (300 mmol/L NaOH and 1 mmol/L EDTA, pH>13) for 20 min, at 4 °C. An electric current of 300 mA and 25 V (0.90 V/cm) was applied for 15 min to perform DNA electrophoresis. The slides were then neutralized (0.4 mol/L Tris, pH 7.5), stained with silver and analyzed using a microscope. Images of 100 randomly selected cells (50 cells from each of two replicate slides) were analyzed from each animal. The cells were also visually scored according to tail

size into five classes, ranging from undamaged (0) to maximally damaged (4), resulting in a single DNA damage score for each animal and consequently for each studied group. Therefore, the damage index (DI) can range from 0 (completely undamaged, 100 cells×0) to 400 (with maximum damage, 100 cells×4)[14].

### *Micronucleus assay*

The micronucleus assay was performed according to the US Environmental Protection Agency Gene-Tox Program[15]. Bone marrow from both femurs was collected after acute and subchronic treatments. The tissue was suspended in fetal calf serum, and smears on the clean glass slides were prepared as described in a previous report[16]. The slides were air-dried, fixed in methanol, stained in 10% Giemsa and coded for a blind analysis. To avoid false negative results and to obtain a measure of toxicity on bone marrow, the ratio of polychromatic erythrocytes to normochromatic erythrocytes (PCE:NCE) was scored in 1000 cells. The incidence of micronuclei (MN) was observed in 2000 PCE for each animal[17].

### Lipid peroxidation assay

Thiobarbituric acid reactive substances (TBARS) were used as a marker of lipid peroxidation. After subchronic treatment, the livers were removed, weighed, immediately frozen in liquid nitrogen and stored at -80 °C for ulterior analyses. The frozen tissue was homogenized in 10 volumes (*w/v*) of phosphate buffer solution (KCl 140 mmol/L, phosphate 20 mmol/L, pH 7.4) in ULTRA-Turrax (IKA-WERK) and centrifuged at 704×*g* for 10 min. Lipoperoxidation was measured using the TBARS on homogenized tissues, as described by Esterbauer and Cheeseman[18]. The amount of aldehyde products generated by lipid peroxidation was quantified by the thiobarbituric acid reaction using 3 mg of protein per sample. The results were expressed as nanomoles per milligram of protein. Proteins were determined by the method described by Lowry[19].

### Statistical analysis

Data from the open field test were expressed as the mean±SEM. These data were analyzed using one-way ANOVA followed by Duncan's test. The analyses of the step-down inhibitory avoidance task were non-parametric because this procedure involved a cutoff score. The data were expressed as medians (interquartile ranges) and analyzed using the Kruskal-Wallis test, followed by the Mann-Whitney test when necessary. Data from the comet assay, micronucleus test and lipid peroxidation assay are expressed as the mean±SD, and statistical significance was determined by one-way ANOVA followed by Tukey's test. In all comparisons, $P<0.05$ was considered to indicate statistical significance.

## Results

### Neurobehavioral parameters

Figure 2 shows the behavioral patterns of mice given saline or aripiprazole (1, 3, or 10 mg/kg) during a 5-min exploration period in an open field after acute treatment. The number of crossings and rearings was lower in the groups that received aripiprazole compared to the control group ($P<0.05$); however, it was not lower than the Tween group, suggesting that aripiprazole affected the locomotion or exploration of the animals in this task. The latency to start locomotion was different only in the group that received aripiprazole 1 mg/kg ($P<0.05$).

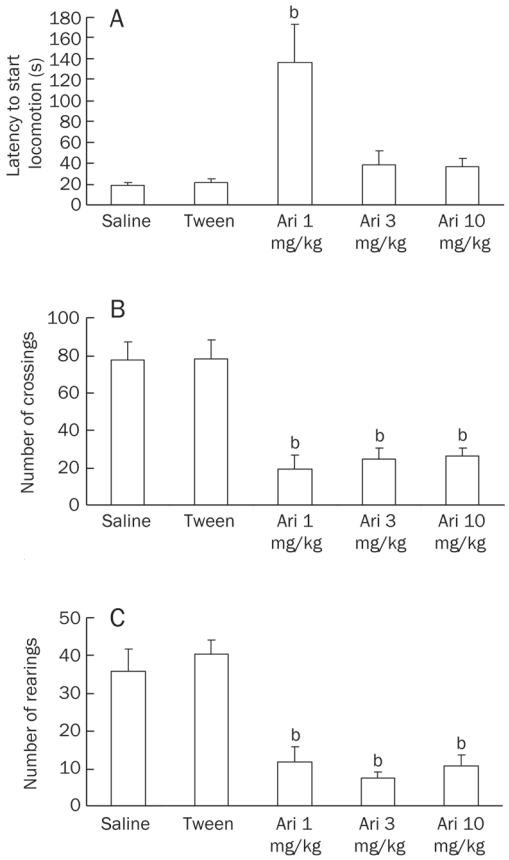


**Figure 2.** Effect of aripiprazole (1, 3, or 10 mg/kg) pretest administration on the following: (A) latency to start locomotion, (B) number of crossings performed and (C) number of rearings performed during a 5-min exploration period of an open field. Animals received an ip injection of saline, Tween or aripiprazole 30 min prior to the locomotory behavior test in the open field (acute treatment). Data are expressed as the mean±SEM. $n=10$ animals per group. $^bP<0.05$ compared to the saline group; ANOVA/Duncan's test.

Figure 3 shows the effect of aripiprazole on the open field task after a 5-d treatment. Aripiprazole decreased the crossings performed in all doses tested ($P<0.05$), although it did not affect rearings ($P=0.086$) and latency to start locomotion ($P=0.182$).

Short- and long-term memory retention of inhibitory avoidance was evaluated in different animals that received aripiprazole (Figure 4). There were no significant differences in training performed among the groups ($P=0.819$). For both the STM and LTM, aripiprazole increased the step-down latency in all doses tested ($P<0.05$), which indicates that the drug has the potential to improve the memory of animals in this task after acute treatment.

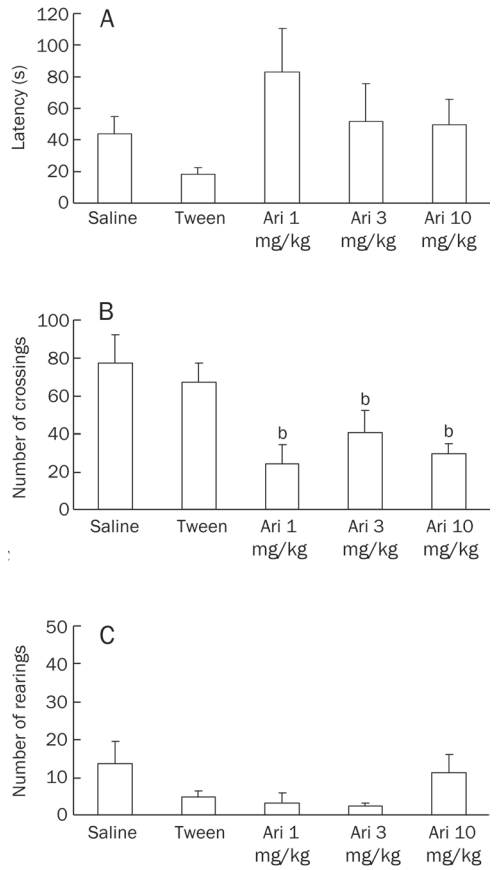


**Figure 3.** Effect of repeated aripiprazole (1, 3, or 10 mg/kg) administration on the following: (A) latency to start locomotion, (B) number of crossings performed and (C) number of rearings performed during a 5-min exploration period of an open field. Animals received an ip injection of saline, Tween, or aripiprazole for 5 d (subchronic treatment). Behavioral parameters were recorded 30 min after the last administration. Data are expressed as the mean±SEM. $n$=8–10 animals per group. $^{b}P<0.05$ compared to the saline group; ANOVA/Duncan's test.

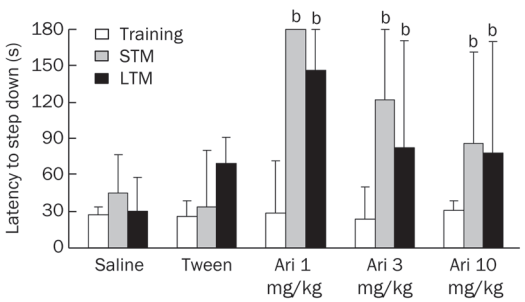


**Figure 4.** Effect of pretraining administration (ip) of saline, Tween or aripiprazole (1, 3, or 10 mg/kg) on STM (1.5 h after training) and LTM (24 h after training) in inhibitory avoidance. $n$=11–15 animals per group. $^{b}P<0.05$ compared to the saline group; Kruskal-Wallis/Mann-Whitney test.

### Genotoxic parameters

For the acute treatment, aripiprazole did not induce DNA damage in the blood and in brain tissues collected 3 h (blood) and 24 h (blood and brain) after administration (data not shown). However, doses administered for 5 d led to an increase in DI in the peripheral blood of the treated groups compared to the saline or Tween groups (Table 1). In the brain, DI values obtained from groups treated with aripiprazole were not significantly different from those of the controls groups.

**Table 1.** DNA damage after subchronic treatment with aripiprazole in mice.

| Groups | Blood DI* (mean±SD) | Brain DI (mean±SD) |
|---|---|---|
| Saline | 39±5 | 207±60 |
| Tween | 39±4 | 190±34 |
| Aripiprazole 1 mg/kg | 47±3 | 132±32 |
| Aripiprazole 3 mg/kg | 51±5$^{c}$ | 161±62 |
| Aripiprazole 10 mg/kg | 58±7$^{c}$ | 174±54 |
| Positive control# | 77±27$^{c}$ | 389±6$^{c}$ |

$n$=5 animals per group. *DI (damage index) can range from 0 (completely undamaged. 100 cells×0) to 400 (with maximum damage 100 cells×4). #Positive control: blood or brain cells from the saline group treated *ex vivo* with hydrogen peroxide 0.20 mmol/L. $^{c}P<0.01$ statistically significant difference from the saline and tween groups (ANOVA Tukey's test).

The frequency of micronuclei in the aripiprazole-treated groups was similar to the values obtained for the saline or Tween groups in both the acute and subchronic treatments (Table 2). There was no toxicity in the bone marrow because the PCE:NCE ratio did not decrease significantly in either of the two treatments (data not shown).

**Table 2.** Frequency of micronucleus in bone marrow of mice after acute and subchronic treatments with aripiprazole.

| Groups | Acute treatment MNPCE in 2000 PCE mean±SD | Subchronic treatment MNPCE in 2000 PCE mean±SD |
|---|---|---|
| Saline | 1.14±0.38 | 1.15±0.37 |
| Tween | 1.20±0.45 | 1.86±1.60 |
| Aripiprazole 1 mg/kg | 1.80±1.79 | 1.43±1.90 |
| Aripiprazole 3 mg/kg | 2.25±1.50 | 1.40±0.89 |
| Aripiprazole 10 mg/kg | 1.40±0.89 | 2.86±2.49 |
| Positive control | 10.0±5.29$^{c}$ | – |

$n$=5 animals per group. Positive control: cyclophosphamide (25 mg/kg). MNPCE: micronucleated polychromatic erythrocytes (PCE). $^{c}P<0.01$: statistically significant difference from the saline group (ANOVA Tukey's test).

### Lipoperoxidation

Table 3 shows the results of lipid peroxidation evaluated in

**Table 3.** TBARS (thiobarbituric acid reactive substances) values (nmol/mg protein) in liver of mice after subchronic treatment with aripiprazole.

| Saline | Tween | Aripiprazole 1 mg/kg | Aripiprazole 3 mg/kg | Aripiprazole 10 mg/kg |
|---|---|---|---|---|
| 0.72±0.23 | 0.65±0.13 | 0.62±0.26 | 0.53±0.13 | 0.42±0.17 |

*n*=7 animals per group.

the liver tissue after subchronic treatment. Aripiprazole did not increase lipid damage in this tissue.

## Discussion

### Neurobehavioral parameters

This work reports the effects of aripiprazole on memory and locomotor activity in mice using the inhibitory avoidance and open field tasks. The experiments showed that this antipsychotic drug was able to decrease the crossings and rearings measured 30 min after only one administration (Figure 2). However, when the animals received aripiprazole for 5 d, a decrease was observed only in the crossing parameter (Figure 3), suggesting that the drug can affect both the locomotor and exploratory activities when administered as an acute dose. The group of animals treated with one dose of aripiprazole (1 mg/kg) exhibited a significant increase in latency time in beginning locomotion in the open field task, which reveals a decrease in motivation. This effect was not observed after 5 d of treatment.

Some works studied the effect of aripiprazole on locomotion and exploration in animals. Used alone, aripiprazole (2.5 and 5 mg/kg) decreased the locomotor activity measured during a 60-min period in mice[20]. In the same study, aripiprazole antagonized amphetamine- (2 mg/kg) or ethanol-induced (1.75 g/kg) locomotor stimulation[21]. Therefore, aripiprazole attenuated LY-341495-induced hyperactivity, a metabotropic glutamate receptor antagonist[20].

Another study reported that aripiprazole was able to decrease total locomotor activity in a dose-dependent manner, causing marked locomotor suppression 1 h after oral treatment with 0.3 and 1 mg/kg doses[4]. In the same work, aripiprazole was administered for 7 d, and the locomotor activity was recorded 24 h after the last treatment. Contrasting with the single treatment, repeated treatment with aripiprazole had no effect on locomotor activity.

Here, we observed that a single aripiprazole dose (1, 3, or 10 mg/kg) affected both locomotor and exploratory activities, but after a 5-d treatment, only the crossing parameter was altered. The difference between the behavioral results obtained in the present study and those by Nagai *et al*[9] can be associated with the aripiprazole doses and the animal species used in these treatments.

Phencyclidine [1-(1-phenylcyclohexyl) piperidine hydrochloride (PCP)], a noncompetitive *N*-methyl-*D*-aspartate receptor antagonist, impairs the animals' performance in the novel object recognition task. In another study, the single or repeated treatment with aripiprazole, but not haloperidol, revealed that aripiprazole was able to ameliorate the cognitive impairment induced by treatment with PCP. This effect was blocked by co-treatment with dopamine $D_1$ and 5-$HT_{1A}$ antagonist receptors, suggesting that behavior triggered by aripiprazole can be associated with dopamine $D_1$ and serotonin 5-$HT_{1A}$ receptors[9].

Enomoto *et al*[5] showed that aripiprazole did not affect animal performance in the Morris water maze and radial-arm maze tests. The authors also observed that the drug showed no ameliorating effect on MK-801-induced impairment of learning and memory in these tasks, which indicated that there was no activity at the NMDA glutamate receptors.

However, 10 mg/kg of aripiprazole, but not 1 or 3 mg/kg, impaired the passive-avoidance response[4]. These results disagree with what was observed in our study, which shows a memory improvement caused by aripiprazole administration. This can be associated with the differences in the tasks and the administration route (we used the ip route to administer the drugs).

The inhibitory avoidance task reveals how averse an animal may become when faced with some negative stimuli, and it involves associative behavior because the animal has to avoid the shock to the paws. Here, we reported that aripiprazole caused significant changes in STM and LTM in the inhibitory avoidance task, with an improvement in the performance of the animals (longer latency to climb down the platform) when compared to the control group. The inhibitory avoidance task has been used to hypothesize that several biochemical mechanisms may influence memory[22, 23]. This task is heavily dependent on the hippocampus, where a sequence of molecular events takes place. However, the task is also governed by the events occurring in the entorhinal and parietal cortex because it is also intensely modulated by the basolateral nucleus of the amygdala and influenced by a different sequences of molecular events[24]. Aripiprazole presents a novel action mechanism, and it is able to modulate several different receptors[25]. The action mechanism of aripiprazole has not been fully clarified, which may hinder the interpretation of the data obtained in the present study. Serotonin 5-$HT_{1A}$ and 5-$HT_{2A}$ receptors are suggested to play important roles in cognitive functions[4]. Therefore, the effects on memory shown here might be involved in the actions of aripiprazole on those receptors.

### Genotoxic parameters

The comet assay was used to detect recent DNA damage, such as single and double strand breaks, alkali-labile sites, DNA-DNA and DNA-protein crosslinks[26]. Three hours after the last administration in subchronic treatment, blood and brain samples were collected from the same animals that had been tested in the open-field task to conduct the comet assay. An increase in DNA damage in the blood was observed, indicating a genotoxic effect (Table 1). Class 1 damage was the most frequent among the aripiprazole-damaged cells, which is considered a reparable minimal damage (Figure 5).

The micronucleus test was used to detect clastogenic/

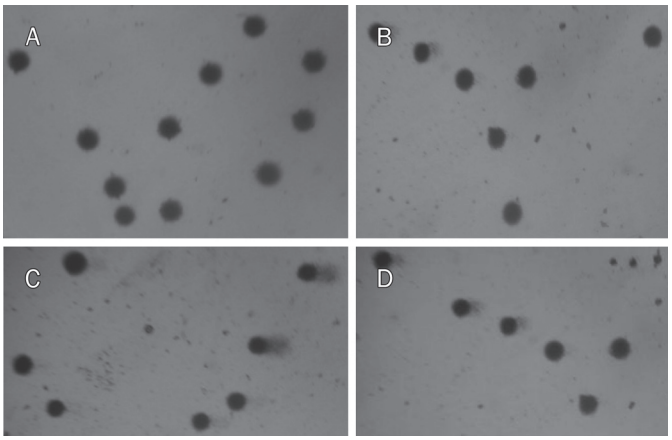


**Figure 5.** Representative images of comets in blood and brain tissues. (A) Blood comets from the control group; (B) Blood comets from the aripiprazole treated group; (C) Brain comets from the control group; (D) Brain comets from the aripiprazole treated group.

aneugenic activities, which leads to an increasing frequency of micronuclei, and suggests mutagenic effects at the chromosomal level[15, 26]. Aripiprazole has shown positive results in mutagenicity assays[27]. Here, an increase in the frequency of micronuclei in the PCE of bone marrow was observed, although it was not in a dose-dependent manner and had no statistically significant values (Table 2).

In the brain tissue, aripiprazole did not induce DNA damage in any of the treatments (Table 1), although it caused impairment of neurobehavioral performance. Conversely, DNA damage levels in the aripiprazole-treated groups were lower than in the control groups, though not significantly (Figure 5). Thus, aripiprazole showed weak systemic genotoxicity, inducing DNA damage in the blood and a tendency to protect brain tissue.

This result corroborates previous studies demonstrating the beneficial effects of aripiprazole on neuronal functions. Antipsychotic drugs, such as aripiprazole, consistently increased N-acetylaspartate (NAA) levels, pointing to a usual therapeutic response of increased neuronal viability[28]. Another study has suggested that aripiprazole inhibits glutamate release from rat prefrontocortical nerve terminals, probably by the activation of dopamine $D_2$ and 5-$HT_{1A}$ receptors, which subsequently results in the reduction in nerve terminal excitability and downstream activation of voltage-dependent $Ca^{2+}$ channels through a signaling cascade involving PKA. These actions of aripiprazole may contribute to its neuroprotective effect in excitotoxic injury[29]. In SH-SY5Y human neuroblastoma cells, aripiprazole increased the levels of brain-derived neurotrophic factor (BDNF)-mediated signaling, suggesting that aripiprazole offers neuroprotective effects on human neuronal cells[30].

### Lipoperoxidation

It is known that aripiprazole is metabolized in the liver by cytochrome P450 3A4 (CYP3A4) and CYP2D6 to dehydroaripiprazole, an active metabolite[31, 32]. In this sense, aripiprazole was not able to increase the TBARS values, suggesting no induction of lipid peroxidation.

TBARS is a measure of major oxidative degradation products, such as lipid hydroperoxides from unsaturated fatty acids of the membrane, which have been implicated in psychiatric diseases, including schizophrenia[33–35]. In the rat brain, aripiprazole has been shown to diminish TBARS in the prefrontal cortex, and it did not alter protein carbonyl content when compared to the control group, indicating that the compound does not induce oxidative damage[36]. Our results corroborate those findings, suggesting protective effects of aripiprazole on lipids. A small decrease was observed in the TBARS values, but this lacked statistical significance (Table 3). Furthermore, 2.5 mg/kg aripiprazole administered for 28 d has been shown to decrease lipid peroxidation in the brain cortex and plasma in depression-induced rats by chronic mild stress, indicating a protective effect of this drug on oxidative stress[37]. In another study, aripiprazole increased succinate dehydrogenase activity in the prefrontal cortex, suggesting that it may reverse a possible reduction in metabolism involved in the pathophysiology of neuropsychiatry disorders[38].

In conclusion, aripiprazole improved STM and LTM in the inhibitory avoidance task. These findings are in accordance with studies that have shown that atypical antipsychotics may improve cognitive tasks[2, 6]. Aripiprazole decreased baseline DNA damage in brain tissue, which suggests a neuroprotective effect, and no cytotoxic or mutagenic effects were detected. However, this drug showed a potential to impair motor activity. In addition, the reparable DNA damage in the blood in the subchronic treatment suggests that aripiprazole might affect genomic stability. Therefore, further studies are necessary to assess the molecular mechanisms of aripiprazole on motor, exploratory, and genotoxic activities in chronic treatments to guarantee its safe use.

## Acknowledgements

This work was supported by CNPq (Conselho Nacional de Desenvolvimento Científico e Tecnológico) and FAPERGS (Fundação de Amparo à Pesquisa do Estado do Rio Grande do Sul), Brazil.

## Author contribution

Jaqueline Nascimento PICADA analyzed the data on genotoxic parameters and wrote the paper. Bruna de Jesus Neto DOS SANTOS performed behavioral tests. Franciele CELSO performed genotoxic tests. Jéssica Dias MONTEIRO performed behavioral tests. Kelly Morais DA ROSA performed behavioral tests. Leandro Rosa CAMACHO performed the extraction of aripiprazole from Abilify™ (Brystol). Luciana Rodrigues VIEIRA performed TBARS. Taís Madelon FREITAS performed genotoxic testes. Tatiana Grasiela DA SILVA performed genotoxic tests. Viviane Minuzzo PONTES performed behavioral tests. Patrícia PEREIRA analyzed the data

on behavioral parameters and wrote the paper.

## References

1 Harvey PD, Green MF, Keefe RS, Velligan DI. Cognitive functioning in schezophrenia: a consenses on its role in the definition and evaluation of effective treatments for the illness. J Cli Psychiatry 2004; 65: 361–72.
2 Velligan DI, Kern RS, Gold JM. Cognitive rehabilitation for schizophrenia and the putative role of motivation and expectancies. Schizophr Bull 2006; 32: 474–85.
3 Kern RS, Hartzell AM, Izaguirre B, Hamilton AH. Declarative and nondeclarative memory in schizophrenia: what is impaired? What is spared? J Clin Exp Neuropsychol 2010; 32: 1017–27.
4 Ishiyama T, Tokuda K, Ishibashi T, Ito A, Ohno Y. Lurasidone (SM-13496), a novel atypical antipsychotic drug, reverses MK-801-induced impairment of learning and memory in the rat passive-avoidance test. Eur J Pharmacol 2007; 572: 160–70.
5 Enomoto T, Ishibashi T, Tokuda K, Ishiyama T, Toma S, Ito A. Lurasidone reverses MK-801-induced impairment of learning and memory in the Morris water maze and radial-arm maze tests in rats. Behav Brain Res 2008; 186: 197–207.
6 Kern KS, Green MF, Lornblatt BA, Owen JR, McQuade RD, Larson WH, *et al*. The neurocognitive effects of aripiprazole: an open-label comparison with olanzapine. Psychopharmacology 2006; 187: 312–20.
7 Kane JM, Larson WH, Saha AR, McQuade RD, Ingenito GG, Zimbroff DL. Efficacy and safety of aripiprazole and haloperidol *versus* placebo in patients with schizophrenia and schizoaffective disorder. J Clin Psychiatry 2002; 63: 763–11.
8 Miller DD, Eudicone JM, Pikalov A, Kim E. Comparative assessment of the incidence and severity of tardive dyskinesia in patients receiving aripiprazole or haloperidol for treatment of schizophrenia: a *post hoc* analysis. J Clin Psychiatry 2007; 68: 1901–6.
9 Nagai T, Murai R, Matsui K, Komei H, Noda Y, Furukawa H, *et al*. Aripiprazole ameliorates phencyclidine-induced impairment of recognition memory through dopamine $D_1$ and serotonin 5-$HT_{1A}$ receptors. Psychopharmacology 2009; 202: 315–28.
10 Pereira P, Tysca D, Oliveira P, da Silva Brum LF, Picada JN, Ardenghi P. Neurobehavioral and genotoxic aspects of rosmarinic acid. Pharmacol Res 2005; 52: 199–203.
11 Tice RR, Agurell E, Anderson D, Burlinson B, Hartmann A, Kobayashi Y, *et al*. Single cell gel/comet assay: guidelines for *in vitro* and *in vivo* genetic toxicology testing. Environ Mol Mutagen 2000; 35: 206–21.
12 Picada JN, Flores DG, Zettler CG, Marroni NP, Roesler R, Henriques JAP. DNA damage in brain cells of mice treated with an oxidized form of apomorphine. Mol Brain Res 2003; 114: 80–5.
13 Pereira P, Oliveira P, Ardenghi P, Rotta LN, Henriques JAP, Picada JN. Neuropharmacological analysis of caffeic acid in rats. Basic Clin Pharmacol Toxicol 2006; 99: 374–8.
14 Pereira P, Gianesini J, da Silva Barbosa C, Cassol GF, Von Borowski RG, Kahl VF, *et al*. Neurobehavioral and genotoxic parameters of duloxetine in mice using the inhibitory avoidance task and comet assay as experimental models. Pharmacol Res 2009; 59: 57–61.
15 Mavournin KH, Blakey DH, Cimino MC, Salamone MF, Heddle JA. The *in vivo* micronucleus assay in mammalian bone marrow and peripheral blood. A report of the US Environmental Protection Agency Gene-Tox Program. Mutat Res 1990; 239: 29–80.
16 Picada JN, da Silva KV, Erdtmann B, Henriques AT, Henriques JAP. Genotoxic effects of structurally related beta-carboline alkaloids. Mutat Res 1997; 379: 135–49.
17 Rodrigues CR, Dias JH, Semedo JG, da Silva J, Ferraz AB, Picada JN. Mutagenic and genotoxic effects of *Baccharis dracunculifolia* (DC). J Ethnopharmacol 2009; 124: 321–4.
18 Esterbauer H, Cheeseman KH. Determination of aldehydic lipid peroxidation products: malonaldehyde and 4-hydroxynonenal. Methods Enzymol 1990; 186: 407–21.
19 Lowry H, Rosebrough MJ, Farr AL. Protein measurement with the foline reagent. J Biol Chem 1951; 193: 265–75.
20 Bespalov A, Jongen-Rêlo AL, Van Gaalen M, Harich S, Schoemaker H, Gross G. Habituation deficits induced by metabotropic glutamate receptor 2/3 receptor blockade in mice: reversal by antipsychotic drugs. J Pharmacol Exp Ther 2007; 320: 944–50.
21 Jerlhag E. The antipsychotic aripiprazole antagonizes the ethanol- and amphetamine-induced locomotor stimulation in mice. Alcohol 2008; 42: 123–7.
22 Izquierdo I, Medina JH. Memory formation: the sequence of biochemical events in the hippocampus and its connections to activity in other brain structures. Neurobiol Learn Mem 1997; 68: 285–316.
23 Rossato JL, Bonini JS, Coitinho AS, Vianna MR, Medina JH, Cammarota M, *et al*. Retrograde amnésia induced by drugs acting on different molecular systems. Behav Neurosci 2004; 118: 563–8.
24 Rossato JI, Zinn CG, Furini C, Bevilaqua LR, Medina JH, Cammarota M, *et al*. A link between the hippocampal and the striatal memory systems of the brain. An Acad Bras Cienc 2006; 78: 515–23.
25 Kessler RM. Aripiprazole: what is the role of dopamine $D_2$ receptor partial agonism? Am J Psychiatry 2007; 164: 1310–2.
26 Hartmann A, Agurell E, Beevers C, Brendler–Schwaab S, Burlinson B, Clay P, *et al*. Recommendations for conducting the *in vivo* alkaline Comet assay. Mutagenesis 2003; 18: 45–51.
27 Brambilla G, Mattioli F, Martelli A. Genotoxic and carcinogenic effects of antipsychotics and antidepressants. Toxicology 2009; 261: 77–88.
28 McLoughlin GA, Ma D, Tsang TM, Jones DN, Cilia J, Hill MD, *et al*. Analyzing the effects of psychotropic drugs on metabolite profiles in rat brain using $^1$H NMR spectroscopy. J Proteome Res 2009; 8: 1943–52.
29 Yang TT, Wang SJ. Aripiprazole and its human metabolite OPC14857 reduce, through a presynaptic mechanism, glutamate release in rat prefrontal cortex: possible relevance to neuroprotective interventions in schizophrenia. Synapse 2008; 62: 804–18.
30 Park SW, Lee JG, Ha EK, Choi SM, Cho HY, Seo MK, *et al*. Differential effects of aripiprazole and haloperidol on BDNF-mediated signal changes in SH-SY5Y cells. Eur Neuropsychopharmacol 2009; 19: 356–62.
31 Urichuk L, Prior TI, Dursun S, Baker G. Metabolism of atypical antipsychotics: involvement of cytochrome P450 enzymes and relevance for drug-drug interactions. Curr Drug Metab 2008; 9: 410–8.
32 Waade RB, Christensen H, Rudberg I, Refsum H, Hermann M. Influence of comedication on serum concentrations of aripiprazole and dehydroaripiprazole. Ther Drug Monit 2009; 31: 233–8.
33 Halliwell B. Role of free radicals in the neurodegenerative diseases, therapeutic implications for antioxidant treatment. Drugs Aging 2001; 18: 685–716.
34 Arvindakshan M, Sitasawad S, Debsikdar V, Ghate M, Evans D, Horrobin DF, *et al*. Essential polyunsaturated fatty acid and lipid peroxide levels in never-medicated and medicated schizophrenia patients. Biol Psychiatry 2003; 53: 56–64.
35 Gama CS, Salvador M, Andreazza AC, Lobato MI, Berk M, Kapczinski F, *et al*. Elevated serum thiobarbituric acid reactive substances in clinically symptomatic schizophrenic males. Neurosci Lett 2008; 433: 270–3.
36 Martins MR, Petronilho FC, Gomes KM, Dal-Pizzol F, Streck EL, Quevedo J. Antipsychotic-induced oxidative stress in rat brain.

Neurotox Res 2008; 13: 63–9.

37 Eren I, Nazıroglu M, Demirdas A. Protective effects of lamotrigine, aripiprazole and escitalopram on depression-induced oxidative stress in rat brain. Neurochem Res 2007; 32: 1188–95.

38 Streck EL, Rezin GT, Barbosa LM, Assis LC, Grandi E, Quevedo J. Effect of antipsychotics on succinate dehydrogenase and cytochrome oxidase activities in rat brain. Naunyn Schmiedeberg Arch Pharmacol 2007; 376: 127–33.

Acta Pharmacologica Sinica (2011) 32: 1233–1238
 1671-4083/11 $32.00
www.nature.com/aps

Original Article

# Involvement of cholinergic system in suppression of formalin-induced inflammatory pain by cobratoxin

Gao-na SHI[1], Yan-li LIU[1], Hai-ming LIN[1], Shi-lin YANG[1], Yu-lin Feng[2], Paul F REID[3], Zheng-hong QIN[1, *]

*[1]Department of Pharmacology, Soochow University School of Pharmacy, Suzhou 215123, China; [2]Jiangxi University of Chinese Traditional Medicine, Nanchang 330004, China; [3]ReceptoPharm Inc, Fortlaudale, Florida 33336, USA*

**Aim:** To investigate the analgesic effect of cobratoxin (CTX), a long-chain α-neurotoxin from Thailand cobra venom, in a rat model of formalin-induced inflammatory pain.
**Methods:** Inflammatory pain was induced in SD rats via injecting 5% formalin (50 μL) into the plantar surface of their right hind paw. CTX and other agents were ip administered before formalin injection. The time that the animals spent for licking the injected paw was counted every 5 min for 1 h.
**Results:** CTX (25, 34, and 45 μg/kg) exhibited a dose-dependent analgesic effect during the phase 1 (0–15 min) and phase 2 (20–60 min) response induced by formalin. Pretreatment with naloxone (0.5 or 2.5 mg/kg) did not block the analgesic effect of CTX. Pretreatment with atropine at 5 mg/kg, but not at 2.5 mg/kg, antagonized the analgesic effect of CTX. Treatment with the nonselective nAChR antagonist mecamylamine (3 mg/kg) inhibited the analgesic effects of CTX in Phase 1 and Phase 2 responses, while with the selective α7-nAChR antagonist methyllycaconitine (3 mg/kg) antagonized the effect of CTX only in the Phase 1 response. Treatment with the α7-nAChR agonist PNU282987 (3 mg/kg) significantly reduced the formalin-induced phase 2 pain response, but only slightly reduced the Phase 1 pain response.
**Conclusion:** The results suggest that CTX exerts an antinociceptive effect in formalin-induced inflammatory pain, which appears to be mediated by mAChR and α7-nAChR.

**Keywords:** cobratoxin; formalin; inflammatory pain; cholinergic receptors; α7-nAChR

*Acta Pharmacologica Sinica* (2011) 32: 1233–1238; doi: 10.1038/aps.2011.65; published online 15 Aug 2011

## Introduction

Snake venoms and several neurotoxins isolated from venoms have demonstrated potent analgesic activity in animal models of pain. A previous study reported that *crotalus dirissus terrificus* venom administered subcutaneously inhibited the migration of polymorphonuclear cells to the peritoneal cavity before and after plantar side injection of carrageenan into the mouse right hind paw[1, 2]. Cobrotoxin[3], a short-chain postsynaptic α-neurotoxin isolated from *Naja naja atra*, is reported to have analgesic activity and is commercially available in China for this purpose[4]. Cobratoxin (CTX), a neurotoxin isolated from *Naja naja kaouthia*, is a high-affinity ligand for the alpha 7 nicotinic receptor subtype (α7-nAchR)[5, 6], which can conduct $Ca^{2+}$ ions and thereby directly impact neurotransmitter release[7].

Our previous studies found that CTX exhibited a dose-dependent analgesic action in mice as determined by hot-plate and acetic acid writhing tests. The peak effect of analgesia was seen 3 h after CTX administration. Furthermore, naloxone failed to block the analgesic effects of CTX, but atropine did antagonize the analgesia mediated by CTX in the mouse acetic acid writhing test, indicating that the cholinergic, but not opioid system, appears to be involved in the antinociceptive action of CTX[8]. It is not currently known whether CTX inhibits inflammatory pain. The present study evaluated analgesic effects of CTX in a rat model of inflammatory pain induced by formalin.

Injection of formalin into rat paws is a valid and reliable model of inflammation-mediated nociception. Intradermal injection of formalin into the paw induces a biphasic nociceptive response evidenced by flinching, licking or biting of the affected paw. Two phases of the response can be observed: an early phase starting immediately after injection and lasting for 0–15 min and a late phase from 20 to 60 min after injection. It is now known that the first phase is due to the direct action of formalin on nociceptors, whereas the second phase is mediated by a combination of peripheral input and spinal

* To whom correspondence should be addressed.
E-mail zhqin5@hotmail.com
Received 2011-02-28 Accepted 2011-04-21

cord sensitization[9–11]. This makes the formalin test a well-accepted animal model for studying pain[9]. The formalin test is a chemically induced tonic pain model in which the biphasic changes of nociception are considered a molecular basis for neuropathic pain, particularly during the second phase of the test, during which most clinically used drugs against neuropathic pain are active. Opioid analgesics such as codeine and nalbuphine appear to be antinociceptive for both phases[12, 13]. In contrast, NSAIDs such as diclofenac and lumiracoxib suppress pain only in the second phase[14–16]. The present study examined the effects of CTX from *Naja naja kaouthia* on the nociceptive response by intradermal administration of formalin and the involvement of the opioid and cholinergic systems in its analgesic effects.

## Materials and methods

### Animals

Male Sprague-Dawley rats weighing 180 to 220 g were purchased from the Experimental Animal Center of Soochow University and housed in a climatically controlled room (temperature 18–22 °C; humidity 40%–80%; 12 h light/dark cycle with lights on at 7:00 AM) with food and water available *ad lib*. Animals were acclimated to the housing conditions and handled for 3–4 d before experiments. All experiments were performed between 08:00 AM and 16:00 PM. All experimental procedures were conducted according to the NIH Guidelines for the Care and Use of Laboratory Animals (NIH Publication No 80–23, revised 1996). The experimental procedures were approved by the Committee on Animal Care and Use of Soochow University.

### Drug injections

CTX was obtained from ReceptoPharm Inc (Fortlaudale, Florida, USA) and dissolved in 0.9 % saline. The doses of CTX used were 25, 34, and 45 μg/kg, and these were administered ip at a volume of 2 mL/kg 3 h prior to formalin injection. Naloxone, atropine, mecamylamine, methyllycaconitine and PNU282987 were obtained from Sigma (St Louis, MO, USA), dissolved in 0.9% saline and administered ip at a volume of 2 mL/kg. Some mice received an ip injection of naloxone (0.25 and 5 mg/kg) or atropine (0.25 and 5 mg/kg) 2.5 h prior to formalin injection, and some were injected with mecamylamine (3 mg/kg) or methyllycaconitine (3 mg/kg) 1 h before the formalin injection. PNU282987 (3 mg/kg) was administered 30 min prior to formalin injection. The time intervals used for agonist and antagonist administration were adapted from previous studies[8]. For control rats, 0.9% saline solution was injected at a volume of 2 mL/kg.

### Formalin test

For all experiments, animals were habituated to the formalin test environment by placing them in the test apparatus (Plexiglass chamber 16 cm×15 cm×15 cm) for 2 h prior to the injection of formalin. Subjects were then given an ip injection of either CTX or saline, followed by an sc injection of 5% formalin (volume of 50 μL) into the plantar surface of the right hind paw 3 h later. Immediately after the formalin injection, licking time was recorded in 5-min intervals for 1 h.

During each experiment, the time that the animal spent in licking the injected paw was recorded every 5 min for 1 h, and results are shown as the total time spent on licking in each phase. Phase 1 was defined as the period of time beginning immediately after the formalin injection and lasting for 15 min. Phase 2 was defined as beginning 20 min post-formalin injection and lasting until 1 h post-injection. Behaviors during each phase are presented as the sum of the total seconds spent on licking during that phase.

### Statistical analysis

All data were analyzed using a one-way ANOVA. *Post hoc* comparisons were performed using Student's *t*-test. $P<0.05$ was considered statistically significant. Calculations were performed using the SPSS 10.0 statistical package.

## Results

### Formalin response

Intradermal injection of 5% formalin 50 μL into the right hind paw produced a consistent licking response in rats. A biphasic nociceptive behavior occurred immediately in Phase 1 and then diminished gradually (0–15 min), followed by a quiescent period (16–19 min), and then occurred again in Phase 2 (20–60 min) (Figure 1).

### Antinociceptive effects of CTX on formalin-induced inflammatory pain

As shown in Figure 1, formalin-evoked biphasic nociceptive responses induced an early, short-lasting response (Phase 1, 0–15 min post-injection) followed by a late, prolonged response (Phase 2, approximately 20–60 min post-injection). Licking time evoked by formalin in both Phase 1 and Phase 2 were reduced in a dose-dependent manner by pretreatment with CTX (20, 34, and 45 μg/kg, ip). Licking time in Phase 1 decreased from 118.60±12.96 s (saline) to 100.40±16.00 s (CTX 20 μg/kg, $P>0.05$), 86.21±11.14 s (CTX 34 μg/kg, $P<0.05$), and 65.41±15.09 s (CTX 45 μg/kg, $P<0.05$). Licking time in Phase 2 decreased from 497.20±62.08 s (saline) to 425.20±35.31 s (CTX 20 μg/kg, $P>0.05$), 319.41±28.72 s (CTX 34 μg/kg, $P<0.05$), and

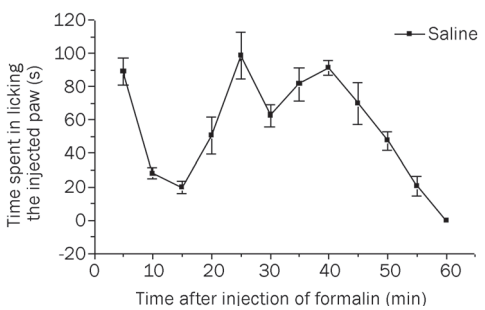


**Figure 1.** Formalin-induced pain response in rats. Injection of formalin into the plantar surface of the right hind paw produced a typical pattern of licking behavior. The licking time was recorded in 5-min intervals for 1 h. Licking time is shown as the mean±SEM from 10 rats per group.

295.01±38.30 s (CTX 45 μg/kg, $P<0.05$). No side effect was observed in rats after injection of CTX (Figure 2).

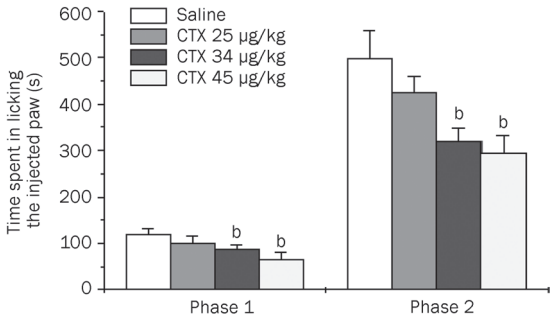


**Figure 2.** Effects of CTX on formalin-induced licking responses. Rats received CTX (25, 34, or 45 μg/kg, ip) or saline vehicle, followed by intradermal injection of formalin 3 h later. Licking time is shown as the mean±SEM from 10 rats per group. Phase 1 was defined as the licking response 0–15 min after formalin, and Phase 2 was established as the licking response 20–60 min after formalin. $^bP<0.05$ compared with the saline group.

### Naloxone did not affect the analgesic effects of CTX on formalin-induced pain

Naloxone (0.5 and 2.5 mg/kg, ip) alone had no significant effect on the formalin-induced nociceptive response in either Phase 1 or Phase 2, compared with the saline-treated group. CTX (34 μg/kg, ip) combined with naloxone (0.5 and 2.5 mg/kg, ip) produced significant analgesic effects similar to CTX alone. There was no significant difference between these groups, indicating that naloxone failed to affect the analgesic effects of CTX (Figure 3).

### Atropine inhibited the analgesic effects of CTX on formalin-induced pain

As shown in Figure 4, atropine (0.25 and 5 mg/kg) had no significant effect on formalin-induced pain response. When CTX (34 μg/kg) was combined with a small dose of atropine (0.25 mg/kg), licking time in Phases 1 and 2 slightly increased from 94.38±12.99 s to 120.00±10.64 s (Phase 1, $P>0.05$) and 338.22±34.24 s to 364.25±65.17 s (Phase 2, $P>0.05$), respectively (Figure 4B). When CTX (34 μg/kg) was combined with a larger dose of atropine (5 mg/kg), licking time in Phases 1 and 2 increased from 94.38±12.99 to 124.40±24.40 s (Phase 1, $P<0.05$) and 124.40±24.40 s to 460.00±89.20 s (Phase 2, $P<0.05$) (Figure 4B). These results indicate that a large dose of atropine could antagonize the analgesic and anti-inflammatory effects exerted by CTX.

### Mecamylamine inhibited the analgesic effects of CTX on formalin-induced pain

As shown in Figure 5, mecamylamine (3 mg/kg) had a significant effect on the CTX (34 μg/kg, ip)-mediated attenuation of formalin-induced pain response. Licking time in Phase 1 increased from 16.71±3.84 s (CTX 34 μg/kg alone) to

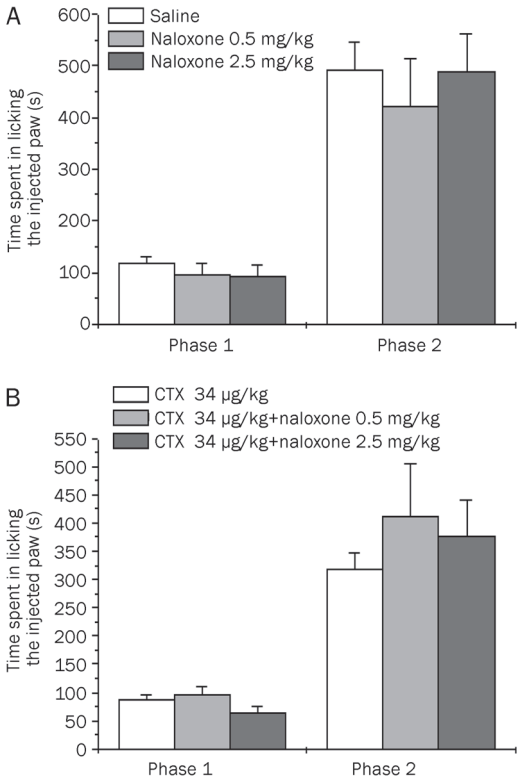


**Figure 3.** Effects of naloxone on CTX-induced attenuation of the licking response induced by formalin. (A) Effects of systemic naloxone on the formalin-induced pain response. Rats were pretreated with naloxone (0.25, 5 mg/kg, ip) and formalin was injected 2.5 h later. (B) Effects of naloxone on CTX-induced attenuation of the licking response after formalin injection. Thirty minutes after injection of CTX (34 μg/kg, ip), naloxone (0.25, 5 mg/kg, ip) or saline was injected, followed by formalin injection 2.5 h later. Licking time is shown as the mean±SEM from 10 rats per group.

41.20±3.84 s (CTX 34 μg/kg plus mecamylamine 3 mg/kg, $P<0.05$). Licking time in Phase 2 increased from 94.77±26.09 s (CTX 34 μg/kg alone) to 215.96±35.79 s (CTX 34 μg/kg plus mecamylamine 3 mg/kg, $P<0.05$, Figure 5). These data suggest that mecamylamine could antagonize the analgesic effects exerted by CTX.

### Methyllycaconitine inhibited the analgesic effects of CTX on formalin-induced pain in Phase 1

As shown in Figure 6, methyllycaconitine (3 mg/kg) combined with CTX (34 μg/kg, ip) had a significant effect on licking time in Phase 1 compared with CTX (34 μg/kg, ip) alone. Licking time in Phase 1 increased from 16.71±3.84 s (CTX 34 μg/kg) to 47.12±9.92 s (CTX 34 μg/kg and methyllycaconitine 3 mg/kg, $P<0.05$). However, there was no significant effect on the CTX-mediated reduction in licking time in Phase 2 (Figure 6), indicating that other nAChRs or mAchRs may have participated in the analgesic effects of CTX.

### PNU282987 inhibited the pain response induced by formalin

PNU282987 had an effect on the formalin-induced nociceptive

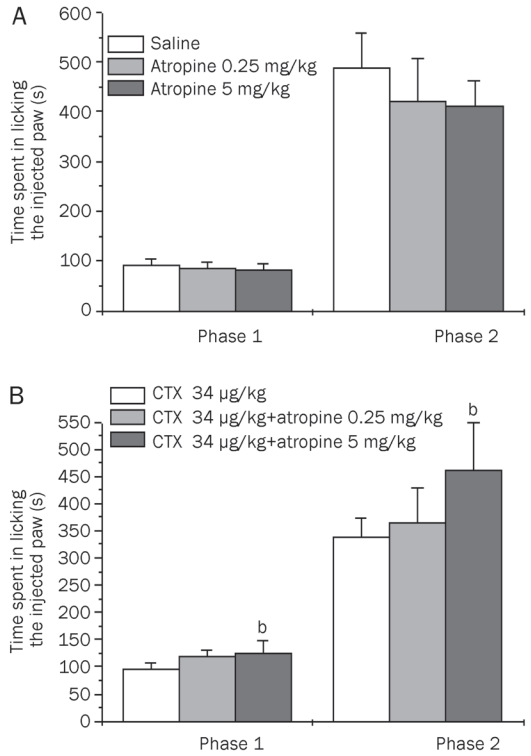


**Figure 4.** Effects of atropine on CTX-induced attenuation of the licking response after formalin injection. (A) Effects of systemic atropine on formalin-induced pain response. Rats were pretreated with atropine (0.25 and 5 mg/kg, ip) and formalin was injected 2.5 h later. (B) Effects of atropine on CTX-induced attenuation of licking responses after formalin treatment. Thirty minutes after CTX injection (34 μg/kg, ip), atropine (0.25 and 5 mg/kg, ip) or saline was injected, followed by formalin 2.5 h later. Licking time is shown as the mean±SEM from 10 rats per group. $^{b}P<0.05$ compared with the CTX (34 μg/kg) alone group.

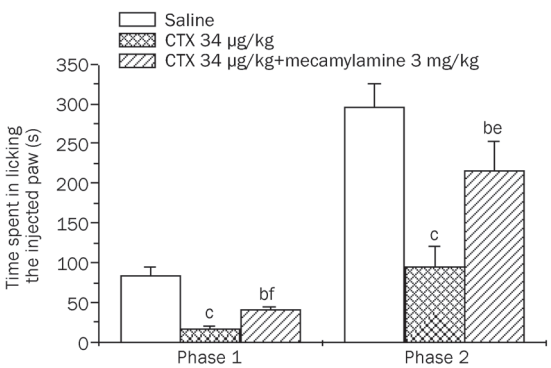


**Figure 5.** Effects of mecamylamine on CTX-induced attenuation of the licking response after formalin injection. Mecamylamine (3 mg/kg, ip) or saline was administered 2 h after CTX injection (34 μg/kg, ip), followed by formalin 1 h later. Licking time is shown as the mean±SEM from 10 rats per group. $^{b}P<0.05$, $^{c}P<0.01$ compared with the saline group; $^{e}P<0.05$, $^{f}P<0.01$ compared with the CTX (34 μg/kg) alone group.

response (Figure 7). Licking time in Phase 1 slightly decreased from 82.85±11.35 s (saline) to 65.90±16.79 s (PNU282987

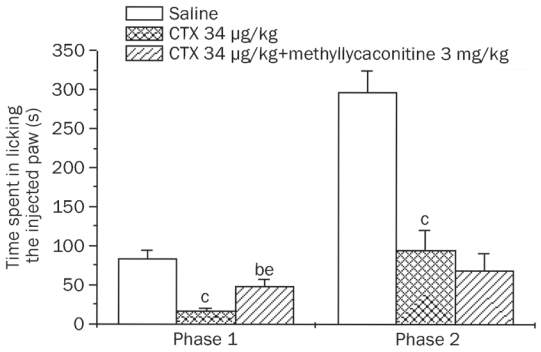


**Figure 6.** Effects of methyllycaconitine on CTX-induced attenuation of the licking response after formalin injection. Methyllycaconitine (3 mg/kg, ip) or saline was administered 2 h after CTX injection (34 μg/kg, ip), followed by formalin 1 h later. Licking time is shown as the mean±SEM from 10 rats per group. $^{b}P<0.05$, $^{c}P<0.01$ compared with the saline group. $^{e}P<0.05$ compared with the CTX (34 μg/kg) alone group.

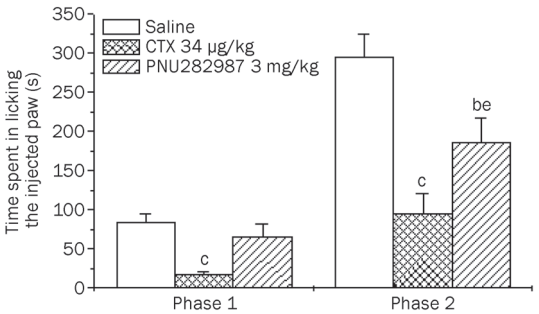


**Figure 7.** Effects of PNU282987 on the formalin-induced licking response. Rats received PNU282987 (3 mg/kg, ip), CTX 34 μg/kg or saline vehicle, followed by intradermal injection of formalin 1.5 h later. Licking time is shown as the mean±SEM from 10 rats per group. $^{b}P<0.05$, $^{c}P<0.01$, compared with the saline group; $^{e}P<0.05$ compared with the CTX (34 μg/kg) alone group.

3 mg/kg, $P>0.05$). Licking time in Phase 2 decreased from 295.77±28.39 s (saline) to 186.60±30.49 s (PNU282987 3 mg/kg, $P<0.05$). These data indicate that CTX may exert its analgesic action against inflammatory pain by activating nicotinic receptors, including α7-nAChR.

## Discussion

The mechanism underlying formalin-induced pain behavior involves a complex series of events including peripheral and central biphasic responses. The first phase of the response is driven directly by formalin stimulating to peripheral nociceptors, thereby producing an acute barrage of activity in the dorsal horn. The second phase is thought to be the consequence of ongoing afferent input maintained by inflammatory mediators acting on peripheral nociceptors[17–19] and functional changes in central pain processing[20].

In the present study, we evaluated the antinociceptive effects of CTX on formalin-induced inflammatory pain. Our results show that CTX exhibited a dose-dependent analgesic

action on formalin-induced biphasic nociceptive behaviors. Naloxone had no impact on CTX-mediated analgesic effects. In contrast, atropine at 5 mg/kg (ip) antagonized the analgesia mediated by CTX. The non-selective nAChR antagonist mecamylamine attenuated the analgesic effects of CTX. These findings indicate that CTX is effective for attenuating nociception induced by inflammation. Chen *et al* reported that dose-dependent antinociceptive effects of CTX were observed in mice in the acetic acid and hot-plate model, and atropine but not naloxone antagonized the analgesic action of CTX[8]. The present results are consistent with this study, and together they indicate that the antinociceptive and anti-inflammatory effects of CTX have no association with the opioid system but do involve the cholinergic system.

These data show that atropine antagonized the analgesic and anti-inflammatory effects of CTX on formalin-induced pain in Phase 1 and Phase 2. Atropine is a competitive nonselective antagonist of central and peripheral muscarinic acetylcholine receptors (mAChR). Wang *et al* have shown that a subtle relationship exists between nicotinic and muscarinic receptors in triggering central cholinergic function[21–23]. They also demonstrated that activation of α7 receptors can modulate Muscatine receptors in rat superior cervical ganglion neurons[24] and that α-neurotoxins may be considered potent nAChR antagonists, making them efficient paralyzing agents[25]. Therefore, it is possible that the activation of muscarinic receptors, which leads to antinociceptive effects, may occur after α7 receptors are inhibited by CTX.

It has been proposed that CTX preferentially targets the alpha 7 and alpha 1 nAChRs in nerve and muscle tissue, respectively, and function by preventing the activation of these acetylcholine receptors in pre- and post-synaptic membranes. The involvement of alpha 7 nicotinic receptors in nicotinic analgesia has been assessed in mice. Choline, a α7 receptor agonist, has dose-dependent antinociceptive effects on formalin tests in mice. Methyllycaconitine significantly blocked the effects of choline. These studies suggested that activation of alpha 7 receptors in the central nervous system elicits antinociceptive effects in an acute thermal pain model[26]. In the present study, we found that mecamylamine blocked CTX-mediated analgesic effects in Phase 1 and Phase 2, while methyllycaconitine inhibited CTX's analgesic action in Phase 1. Moreover, PNU282987 mimicked the effects of CTX in formalin-induced inflammatory pain responses, suggesting that CTX might induce activation of α7-nAChR through indirect mechanisms *in vivo*. However, methyllycaconitine did not block the formalin-induced Phase 2 nociceptive response. These results indicate that, in addition to α7-nAchR, other mAchRs or nAChRs are also involved in CTX's analgesic action.

In summary, the present study demonstrated that ip injection of CTX, a long-chain α-neurotoxin from *Naja naja kaouthia*, could dose-dependently decrease formalin-induced inflammatory pain in rats and that this activity is mediated by activation of the cholinergic but not the opioid system.

## Acknowledgements

This work was supported by Pre-research Funding of Soochow University (No Q3132821).

## Author contribution

Zheng-hong QIN and Yan-li LIU designed the research; Yan-li LIU, Gao-na SHI, and Hai-ming LIN performed the research; Paul F REID contributed new analytical tools and reagents; Yan-li LIU, Gao-na SHI, Shi-lin YANG, and Yu-lin FENG analyzed data; Yan-li LIU, Gao-na SHI, Zheng-hong QIN, and Paul F REID wrote the paper.

## References

1 Nunes FP, Sampaio SC, Santoro ML, Sousa-e-Silva MC. Long-lasting anti-inflammatory properties of Crotalus durissus terrificus snake venom in mice. Toxicon 2007; 49: 1090–8.
2 Farsky SH, Antunes E, Mello SB. Pro and antiinflammatory properties of toxins from animal venoms. Curr drug targets inflamm Allergy 2005; 4: 401–11.
3 Yang CC. Cobrotoxin: structure and function. J Na Toxins 1999; 8: 221–33.
4 Grasset E. The cobra neurotoxin, pharmacology and clinical applications in the treatment of pain. Med Hyg (Geneve) 1952; 10: 55–8.
5 Servent D, Anti-Delbeke S, Gaillard C, Corringer PJ, Changeux JP, Menenz A. Molecular characterization of the specificity of interactions of various neurotoxins on two distinct nicotinic acetylcholine receptors. Eur J Pharmacol 2000; 393: 197–204.
6 Dajas-Bailador F, Costa G, Dajas F, Emmett. Effects of α-bungarotoxin, α-cobratoxin and fasciculin on the nicotine-evoked release of dopamine in the rat striatum *in vivo*. Neurochem Intl 1998; 33: 307–12.
7 Lena C, Changeux JP. Role of $Ca^{2+}$ ions in nicotinic facilitation of GABA release in mouse thalamus. J Neurosci 1997; 17: 576–85.
8 Chen ZX, Zhan HL, Gu ZL, Chen BW, Han R, Reid PF, *et al*. A long-form α-neurotoxin from cobra venom produces potent opioid independent analgesia1. Acta Pharmacol Sin 2006; 27: 402–8.
9 Tjolsen A, Berge OG, Hunskaar S, Rosland JH, Hole K. The formalin test: an evaluation of the method. Pain 1992; 51: 5–17.
10 Dubuisson D, Dennis SG. The formalin test: a quantitative study of the analgesic effects of morphine, meperidine, and brain stem stimulation in rats and cats. Pain 1977; 4: 161–74.
11 Wheeler-Aceto H, Cowan A. Standardization of the rat paw formalin test for the evaluation of analgesics. Psychopharmacology 1991; 104: 35–44.
12 Ortiz MI, Castro-Olguın J, Pena-Samaniego N, Castaneda-Hernandez G. Probable activation of the opioid receptor-nitric oxide-cyclic GMP-$K^+$ channels pathway by codeine. Pharmacol Biochem Behav 2005; 82: 695–703.
13 Castaneda-Hernandez G. Possible activation of ATP sensitive $K^+$ channels by nalbuphine on the formalin test. Eur J Pain 2006; 10(supp1): S88.
14 Malmberg AB, Yaksh TL. Antinociceptive actions of spinal nonsteroidal anti-inflammatory agents on the formalin test in the rat. J Pharmacol Exp Ther 1992; 263: 136–46.
15 Ortiz MI, Granados-Soto V, Castaneda-Hernandez G. The NO-cGMP-$K^+$ channel pathway participates in the antinociceptive effect of diclofenac, but not of indomethacin. Pharmacol Biochem Behav 2003; 76: 187–95.
16 Lozano-Cuenca J, Castaneda-Hernandez G, Granados-Soto V. Peripheral and spinal mechanisms of antinociceptive action of

lumiracoxib. Eur J Pharmacol 2005; 513: 81–91.
17 Dickenson AH, Sullivan AF. Peripheral origins and central modulation of subcutaneous formalin-induced activity of rat dorsal horn neurones. Neurosci Lett 1987; 83: 207–11.
18 Mccall WD, Tanner KD, Levine JD. Formalin induces biphasic activity in C-fibers in the rat. Neurosci Lett 1996; 208: 45–8.
19 Pitcher GM, Henry JL. Second phase of formalin-induced excitation of spinal dorsal horn neurons in spinalized rats is reversed by sciatic nerve block. Eur J Neurosci 2002; 15: 1509–15.
20 Coderre TJ, Vaccarino AL, Melzack R. Central nervous system plasticity in the tonic pain response to subcutaneous formalin injection. Brain Res 1990; 535: 155–8.
21 Wang H. Modulation by nicotine on muscarinic receptor-effector systems. Acta Pharmacol Sin 1997; 18: 193–7.
22 Wang H, Cui WY, Liu CG. Regulatory effects of acutely repeated nicotine treatment towards central muscarinic receptors. Life Sci 1996; 59: 1415–21.
23 Wang H, Cui WY, Liu CH. Modulation by nicotine on binding of cerebral muscarinic receptors with muscarinic agonist and antagonist. Acta Pharmacol Sin 1996; 17: 497–9.
24 Yin X, Cui W, Hu G, Wang H. Desensitization of alpha7 nicotinic receptors potentiated the inhibitory effect on M-current induced by stimulation of muscarinic receptors in rat superior cervical ganglion neurons. J Neural Transm 2005; 112: 1133–48.
25 Dutertre S, Lewis RJ. Toxin insights into nicotinic acetylcholine receptors. Biochem Pharmacol 2006; 72: 661–70.
26 Wang Y, Su DM, Wang RH, Liu Y, Wang H. Antinociceptive effects of choline against acute and inflammatory pain. Neuroscience 2005; 132: 49–56.

Acta Pharmacologica Sinica (2011) 32: 1239–1245
 1671-4083/11 $32.00
www.nature.com/aps

Original Article

# Ghrelin promotes differentiation of human embryonic stem cells into cardiomyocytes

Jin YANG[1, 3, #], Guo-qiang LIU[1, 3, #], Rui WEI[1, 3], Wen-fang HOU[1, 3], Mei-juan GAO[1, 3], Ming-xia ZHU[2, 3], Hai-ning WANG[1, 3], Gui-an CHEN[2, 3, *], Tian-pei HONG[1, 3, *]

*[1]Department of Endocrinology and Metabolism, Peking University Third Hospital, Beijing 100191, China; [2]Reproductive Medical Center, Peking University Third Hospital, Beijing 100191, China; [3]Clinical Stem Cell Research Center, Peking University Third Hospital, Beijing 100191, China*

**Aim:** Ghrelin is involved in regulating the differentiation of mesoderm-derived precursor cells. The aim of this study was to investigate whether ghrelin modulated the differentiation of human embryonic stem (hES) cells into cardiomyocytes and, if so, whether the effect was mediated by growth hormone secretagogue receptor 1α (GHS-R1α).
**Methods:** Cardiomyocyte differentiation from hES cells was performed according to an embryoid body (EB)-based protocol. The cumulative percentage of beating EBs was calculated. The expression of cardiac-specific markers including cardiac troponin I (cTnI) and α-myosin heavy chain (α-MHC) was detected using RT-PCR, real-time PCR and Western blot. The dispersed beating EBs were examined using immunofluorescent staining.
**Results:** The percentage of beating EBs and the expression of cTnI were significantly increased after ghrelin (0.1 and 1 nmol/L) added into the differentiation medium. From 6 to 18 d of differentiation, the increased expression of cTnI and α-MHC by ghrelin (1 nmol/L) was time-dependent, and in line with the alteration of the percentages of beating EBs. Furthermore, the dispersed beating EBs were double-positively immunostained with antibodies against cTnI and α-actinin. However, blockage of GHS-R1α with its specific antagonist *D*-[lys$^3$]-GHRP-6 (1 μmol/L) did not alter the effects of ghrelin on cardiomyocyte differentiation.
**Conclusion:** Our data show that ghrelin enhances the generation of cardiomyocytes from hES cells, which is not mediated via GHS-R1α.

**Keywords:** cardiomyocytes; differentiation; ghrelin; embryonic stem cells

*Acta Pharmacologica Sinica* (2011) 32: 1239–1245; doi: 10.1038/aps.2011.79; published online 1 Aug 2011

## Introduction

It is well known that human embryonic stem (hES) cells, one of the most promising pluripotent stem cell source for the treatment of many incurable diseases, can differentiate into the majority of cell types including cardiomyocytes[1–3]. In 2001, Kehat and the colleagues firstly reported a spontaneous embryoid body (EB)-based protocol of hES cell differentiation into cardiomyocytes[2]. In that study, the spontaneously beating areas appeared in only 8.1% of EBs, indicating the efficiency of differentiation was typically low. It is therefore preferable to use specific differentiation agents to elevate the efficiency of cardiomyocyte differentiation from hES cells. To date, however, only a few factors, such as bone morphogenetic proteins (BMPs)[4–6], fibroblast growth factors (FGFs)[7] or members of Wnt family[8], have been shown to enhance cardiomyocyte differentiation from hES cells. Therefore, identifying new cardiogenic factors is absolutely necessary to establish a more efficient cardiomyocyte differentiation protocol of hES cells.

Ghrelin, a 28-amino-acid peptide identified as the first endogenous ligand for the growth hormone secretagogue receptor (GHS-R)[9], is found mainly in stomach and hypothalamus where it exercises biological activities such as regulating food intake and stimulating the release of growth hormone (GH)[9–12]. It has been recently reported that ghrelin is also synthesized and secreted by cardiomyocytes[13] and that ghrelin treatment inhibits cell death and apoptosis and promotes cell proliferation in cardiomyocytes[14]. In addition, several studies have shown that ghrelin is involved in regulating the differentiation of mesoderm-derived precursor cells including premyocyte[15, 16], osteoblast[17], and preadipocyte[18, 19] either *in vivo* or *in vitro*. However, whether ghrelin has a potential role in the differentiation of cardiomyocytes derived from stem

# These authors contributed equally to this work.
* To whom correspondence should be addressed.
E-mail tpho66@bjmu.edu.cn (Tian-pei HONG);
chenguian@bjmu.edu.cn (Gui-an CHEN)
Received 2011-03-01 Accepted 2011-05-18

cells remains to be clarified.

In the present study, we investigated whether ghrelin affected the differentiation of hES cells into cardiomyocytes and, if so, whether GHS-R1α mediated the effect of ghrelin. Our data show for the first time that ghrelin significantly enhances the generation of beating cardiomyocytes from hES cells, which is likely mediated via an unidentified subtype of ghrelin receptor rather than GHS-R1α. Therefore, our study might provide an insight to create an effective strategy for promoting differentiation of hES cells into cardiomyocytes.

## Materials and methods

### Regents

KnockOut™ Dulbecco's modified Eagle's medium (DMEM), KnockOut™ serum replacement (SR), nonessential amino acids solution (NEAA), *L*-glutamine, β-mercaptoethanol, collagenase IV and DMEM/F12 medium were purchased from Invitrogen (Carlsbad, CA, USA). Fetal bovine serum (FBS) was obtained from Hyclone (Logan, UT, USA). Dispase, gelatin, penicillin, streptomycin and *D*-[lys$^3$]-GHRP-6 (*D*-lys$^3$ growth hormone release peptide-6) were purchased from Sigma (St Louis, MO, USA). Basic fibroblast growth factor (bFGF) was purchased from PeproTech (Rocky Hill, NJ, USA). Collagenase B was purchased from Roche (Basel, Switzerland). Human ghrelin was purchased from Phoenix (Burlingame, CA, USA). Paraformaldehyde, phosphate buffered saline (PBS), triton X-100, 4′,6-diamidino-2-phenylindole (DAPI) and normal goat serum were purchased from Zhongshan Biotechnology Company (Beijing, China). Rabbit anti-cardiac troponin I (cTnI) antibody and rabbit anti-α-MHC antibody were purchased from Sigma. Mouse anti-Oct4 antibody and mouse anti-α-actinin antibody were obtained from Chemicon (Temecula, CA, USA). Mouse anti-β-actin antibody, tetramethyl rhodamine isothiocyanate (TRITC)-conjugated goat anti-rabbit IgG and fluorescein isothiocyanate (FITC)-conjugated goat anti-mouse IgG were purchased from Zhongshan Biotechnology Company. IRDye 800CW conjugated goat anti-rabbit IgG and goat anti-mouse IgG were purchased from LI-COR Biosciences (Lincoln, NE, USA). The primers for RT-PCR and real-time RT-PCR were obtained from Beijing Aoke Biotechnology Company (Beijing, China).

### Culture and differentiation of hES cells

The hES cell line PKU1.1, established by the Reproductive Medical Center of Peking University Third Hospital, was cultured as described previously[20]. Briefly, undifferentiated hES cells were propagated on irradiated mouse embryonic fibroblast (MEF) feeder layers in KnockOut™ DMEM supplemented with 20% (*v/v*) KnockOut™ SR, 1% (*v/v*) NEAA, 2 mmol/L *L*-glutamine, 4 ng/mL bFGF, 0.1 mmol/L β-mercaptoethanol, 50 IU/mL penicillin, and 50 mg/mL streptomycin. The cells were passaged every 5–7 d by incubation in 1 mg/mL collagenase IV.

For differentiation, the hES cells were dispersed into small clumps by incubation with 1 mg/mL dispase and were then transferred to ultra low attachment 6-well plates (Corning, NY, USA) for 5-d suspension culture to form EBs in the differentiation medium DMEM/F12 medium containing 20% (*v/v*) FBS, 2 mmol/L *L*-glutamine, 1% (*v/v*) NEAA and 0.1 mmol/L β-mercaptoethanol. The medium was changed every day. Human ghrelin was simultaneously added to the differentiation medium at the final concentrations of 0.1 or 1 nmol/L in the presence or absence of 1 μmol/L *D*-[lys$^3$]-GHRP-6, a specific antagonist of GHS-R1α. The formed EBs were then transferred to and plated on 0.1% gelatin-precoated 96-well plates (Corning) with one EB per well, and cultured for additional 13 d in the same medium which was changed every 2 d. The plates with attached EB cultures were carefully observed under a phase contrast microscope for the appearance of rhythmic beating areas within EBs, which indicated the cardiomyocyte differentiation. The control group was cultured in the aforementioned medium without ghrelin and/or *D*-[lys$^3$]-GHRP-6 throughout the whole differentiation procedure. The numbers of beating EBs and total EBs were counted, and the cumulative percentages of beating EBs were calculated. Four independent experiments were done in each group and at least 100 EBs were included in each experiment.

### Immunofluorescent and cytochemical staining

The hES cells were fixed in 4% (*v/v*) paraformaldehyde for 20 min at room temperature (RT) and blocked for 30 min at RT with 10% normal goat serum, followed by incubation with mouse anti-Oct4 antibody (1:100) at 4 °C overnight. For immunostaining of differentiated cells, the beating areas within EBs were dissected and dispersed into single cells using 1 mg/mL collagenase B. Dispersed cells were plated on 0.1% gelatin-precoated glass coverslips, cultured for additional 2 d and then immunostained with rabbit anti-cTnI (1:100) and mouse anti-α-actinin (1:200) antibodies. After washing, the cells were incubated with the diluted secondary antibodies, TRITC-conjugated goat anti-rabbit IgG or FITC-conjugated goat anti-mouse IgG, at RT for 30 min, followed by washing and stained with DAPI. Images were captured under a fluorescent microscope (Nikon, Kanagawa, Japan) or a confocal laser microscope (Carl Zeiss, Oberkochen, Germany). Negative controls were performed by using corresponding isotype sera to replace the primary antibodies.

For cytochemical staining of alkaline phosphatase, the hES cells were fixed by 4% paraformaldehyde and analysis was determined by cytochemical techniques using 5-bromo-4-chloro-3-indolyl phosphate (BCIP)/nitrotetrazolium blue chloride (NBT) (Vector Labs, Burlingame, CA, USA) as substrates. Images were captured under a phase contrast microscope (Nikon).

### RT-PCR and real-time RT-PCR

Total RNA samples were prepared from undifferentiated hES cells and differentiated EBs with RNeasy Mini Kit (Qiagen, Hilden, Germany) according to the manufacturer's instructions. Total RNA was reversely transcribed into cDNA using First Strand cDNA Synthesis Kit (Fermentas, Burlington, Ontario, Canada). For analysis of GHS-R1α, reverse transcrip-

tion reactions were conducted by using 1 nmol/L specific antisense primer (5′-CCCAGAAGTCTGAACACTGCCACC-3′)[21]. The cDNA was then amplified by PCR using *Taq* Plus PCR Master Mix (Qiagen) or by real-time PCR with an iQ5 real-time PCR detection system (Bio-Rad, Hercules, CA, USA) as described previously[3, 22]. In real-time RT-PCR analysis, the expression level of each gene at every checkpoint was normalized to the maximal level observed, which was set as 100%. Three tests were performed for each sample at the same time. The primer sequences and PCR conditions used in this study are listed in Table 1.

**Table 1.** Primer sequence, annealing temperature and product size of RT-PCR and real-time RT-PCR analyses.

| Gene | Primer sequence | Annealing temperature (°C) | Product size (bp) |
|---|---|---|---|
| RT-PCR | | | |
| cTnI | Forward: 5′-CCCTGCACCAGCCCCAATCAGA-3′<br>Reverse: 5′-CGAAGCCCAGCCCGGTCAACT-3′ | 66 | 233 |
| α-MHC | Forward: 5′-GGGCGGGGAAGACTGTGAAC-3′<br>Reverse: 5′-CCCAGCACGTCAAAGGCACT-3′ | 66 | 481 |
| Oct4 | Forward: 5′-GAAGTTAGGTGGGCAGCTTG-3′<br>Reverse: 5′-AGCTTCCTCCACCCACTTCT-3′ | 66 | 376 |
| Nanog | Forward: 5′-ATACCTCAGCCTCCAGCAGA-3′<br>Reverse: 5′-CAGGACTGGATGTTCTGGGT-3′ | 62 | 294 |
| GHS-R1α | Forward: 5′-CTGCGCTCAGGGACCAGAACCA-3′<br>Reverse: 5′-GTTGATGGCAGCACTGAGGTAGAA-3′ | 61 | 205 |
| GAPDH | Forward: 5′-ACAGTCAGCCGCATCTTCTT-3′<br>Reverse: 5′-CTGGAAGATGGTGATGGGAT-3′ | 60 | 289 |
| Real-time RT-PCR | | | |
| cTnI | Forward: 5′-ACACCGAGAAGGAAAACCG-3′<br>Reverse: 5′-GAAGGCTCAGCTCTCAAACT-3′ | 58 | 101 |
| α-MHC | Forward: 5′-CAGAGGAGAAAGCTGGCGTC-3′<br>Reverse: 5′-TTGTCAGCATCTTCGGTGCC-3′ | 64 | 121 |
| GAPDH | Forward: 5′-TGCACCACCAACTGCTTAGC-3′<br>Reverse: 5′-GGCATGGACTGTGGTCATGAG-3′ | 64 | 87 |

### Western blot

Cell lysates were extracted from the EBs on d 6, 12, and 18 of differentiation. The proteins were separated by 10% SDS-PAGE, and were electrophoretically transferred to polyvinylidene difluoride membranes. Blots were then done by overnight incubation with rabbit anti-cTnI (1:500), rabbit anti-α-MHC (1:1000) and mouse anti-β-actin (1:5000), followed by a reaction with IRDye 800CW conjugated goat anti-rabbit IgG and goat anti-mouse IgG (1:10 000) for 1 h. Immunocomplexes were visualized with the Odyssey infrared imaging system (LI-COR, Lincoln, NE, USA).

### Statistical analysis

Data are presented as mean±SEM. Statistical analysis was assessed by SPSS statistical package (SYSTAT Software Inc, Chicago, IL, USA) with standard Student's *t*-test. $P<0.05$ was considered to be statistically significant.

## Results

### Differentiation of hES cells into beating EBs

The hES cell line PKU1.1 used in this study had undergone 72 passages, and thus the features of the cells were assessed again here. The karyotype analysis showed that these cells maintained their normal diploid female 46 XX karyotype (data not shown). The hES cells were morphologically characterized by flat and compact colony with small cells having a high nucleus/cytoplasm ratio and prominent nucleoli (Figure 1A). The expression of Oct4 and alkaline phosphatase was observed in hES cell colony (Figure 1B–1E), suggesting that the pluripotent state of hES cells was well maintained in our culture system.

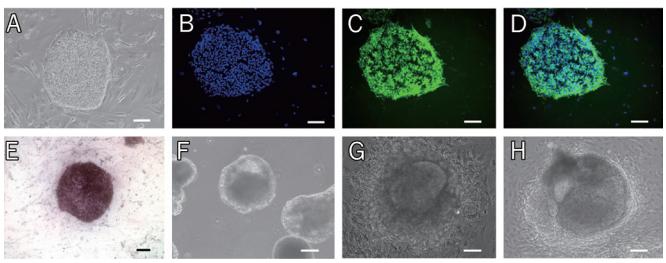


**Figure 1.** Characterization of hES cells and their differentiation into beating EBs. (A) Undifferentiated hES cell colony under a phase contrast microscope. (B-D) Immunofluorescent staining for Oct4 expression in hES cells: (B) DAPI in blue; (C) Oct4 in green; (D) Merge. (E) Cytochemical staining for alkaline phosphatase in hES cells. (F) Generation of mature EBs characterized by cystic cavities after suspension culture for 5 d. (G) The EBs in adherent culture for further differentiation. (H) Beating EBs observed after d 6 of differentiation culture. Magnification bars represent 100 μm.

After 5-d suspension culture of hES cells with the differentiation medium, mature EBs as shown by the appearance of cystic cavities were observed (Figure 1F). The EBs were then plated in adherent culture condition for further differentiation. Within 24 h, the EBs attached to the bottom of the plates and the monolayer cells spread out from the EBs (Figure 1G). The three-dimensional beating areas within the attached EBs began to appear in very small proportion of EBs from 1 d after plating (d 6 of differentiation). These beating areas, located in the cell mass but not the monolayer cells, were observed and recorded (Figure 1H).

### Effects of ghrelin on derivation of beating EBs from hES cells

The cumulative percentages of beating EBs among total EBs increased gradually after plating on adherent culture plates until d 18 of differentiation and then maintained at that level. The percentages of beating EBs on d 18 of differentiation were 12.2% and 18.6% respectively in the groups treated with 0.1 and 1 nmol/L ghrelin, which were markedly higher than 9.5% in the control group (Figure 2A). On d 12 and 18 of differen-

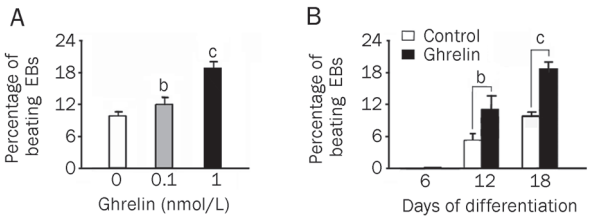


**Figure 2.** Effects of ghrelin on the generation of beating EBs. (A) Dose-effects of ghrelin on the percentage of beating EBs as evaluated on d 18 of differentiation. (B) Time-kinetic effects of 1 nmol/L ghrelin on the percentages of beating EBs as evaluated on d 6, 12 and 18 of differentiation. Each value represents the mean±SEM. $n$=4. $^bP$<0.05, $^cP$<0.01 *vs* control group.

tiation, the percentages of beating EBs were 4.9% and 9.5% respectively in control group, which were markedly increased to 11.1% and 18.6% by treatment with 1 nmol/L ghrelin (Figure 2B). These results indicated that ghrelin increased the percentage of beating EBs derived from hES cells in a dose- and time-dependent manner.

### Effects of ghrelin on the expression of cardiac-specific markers in the differentiated EBs

In RT-PCR analysis, genes encoding cTnI and α-myosin heavy chain (α-MHC), two cardiac structural proteins, were expressed in the EBs on d 18 of differentiation. The mRNA levels of both cTnI and α-MHC were upregulated by 1 nmol/L ghrelin. On the other hand, the pluripotential markers Oct4 and Nanog, which were highly expressed in the undifferentiated hES cells, were markedly reduced in the differentiated EBs (Figure 3A). Real-time RT-PCR analysis showed that cTnI mRNA level was significantly upregulated by 0.1 and 1 nmol/L ghrelin (Figure 3B). Furthermore, the mRNA levels of cTnI and α-MHC, which were gradually increased from d 6 to d 18 of differentiation in control group, were much higher in the group treated with 1 nmol/L ghrelin on d 12 and 18 of differentiation (Figure 3C and 3D). Western blot analysis also showed that the protein levels of cTnI and α-MHC were upregulated by 1 nmol/L ghrelin (Figure 3E and 3F). It was noteworthy that the time-kinetic effects on the mRNA and protein levels of the cardiac-specific markers were in agreement with that on the percentages of beating EBs (Figure 2B and 3C-3F).

For further identification of cardiomyocyte differentiation, the dispersed cells grown on glass coverslips were assessed by immunofluorescent staining. These cells were double-positively immunostained with antibodies against both cTnI and α-actinin. Moreover, the alignment of α-actinin staining displayed organized sarcomeric striation pattern (Figure 3G). These results indicated that the beating areas within the differentiated EBs consisted of cardiomyocytes.

### Effects of GHS-R1α blockage on the cardiomyocyte differentiation of hES cells induced by ghrelin

RT-PCR analysis showed that GHS-R1α mRNA was barely detectable in the undifferentiated hES cells and was gradually increased in the EBs from d 6 to d 18 of differentiation (Figure 4A). Therefore, the possible role of GHS-R1α in the cardiomyocyte differentiation was tested by adding its specific antagonist *D*-[lys$^3$]-GHRP-6. On d 18 of differentiation, the promoting effects of 1 nmol/L ghrelin on the percentage of beating EBs and the mRNA expression of cTnI were not blocked by 1 μmol/L *D*-[lys$^3$]-GHRP-6 (Figure 4B and 4C), indicating that the induction of cardiomyocyte differentiation of hES cells caused by ghrelin was not mediated via GHS-R1α.

## Discussion

Ghrelin is a newly identified gut-brain peptide and has been demonstrated to have a wide range of functions including stimulation of GH release, control of energy metabolism and regulation of pancreatic hormone release[9, 11, 12, 23]. Recently, it has been demonstrated that ghrelin also has a cardioprotective activity via several mechanisms. Ghrelin inhibited apoptosis induced by high glucose and high free fatty acid in isolated mouse and rat cardiomyocytes[14]. In pressure-overload chronic heart failure rats, left ventricular remodeling and dysfunction were improved by treatment with ghrelin[24]. A pilot clinical study also showed that treatment with ghrelin improved left ventricular function and exercise capacity in the patients with severe chronic heart failure[25]. However, little is known about the role of ghrelin in the heart development during embryogenesis or in the differentiation of cardiomyocytes from stem cells.

The EB-based differentiation strategy, which imitates the early development of embryo, is a basic method to initiate cardiomyocyte differentiation of hES cells[2]. The role of ghrelin in cardiomyogenesis was investigated on the basis of this strategy in the present study. Our data showed that the percentage of beating EBs and the expression of cardiac-specific markers cTnI and α-MHC in the differentiated EBs were increased by treatment with ghrelin. These results suggested that ghrelin was a potent differentiation-promoting factor for hES cell-derived cardiomyocytes.

Numerous studies have shown that ghrelin directly regulates the differentiation of several mesoderm-derived precursor cells. Ghrelin promoted proliferation and differentiation in osteoblastic cell lines and cultured primary osteoblasts *in vitro*[17]. An *in vivo* study showed that administration of ghrelin stimulated osteogenesis of intramembranous bone and improved the repair of calvarial bone defect in rats[26]. Ghrelin was shown to promote differentiation of isolated rat primary preadipocytes. In GH-deficient dwarf (*dw/dw*) rats, the infusion of ghrelin induced adipogenesis in bone marrow by a direct action[19]. Ghrelin also increased the differentiation of premyocytes into myocytes in a mouse premyocyte cell line C2C12[16]. Taken together, all the results suggest that ghrelin is a differentiation-regulating factor for mesoderm-derived tissue cells.

To elucidate whether ghrelin is involved in derivation of cardiomyocyte which is also derived from mesoderm, the cardiomyocyte differentiation of hES cells was used in the present

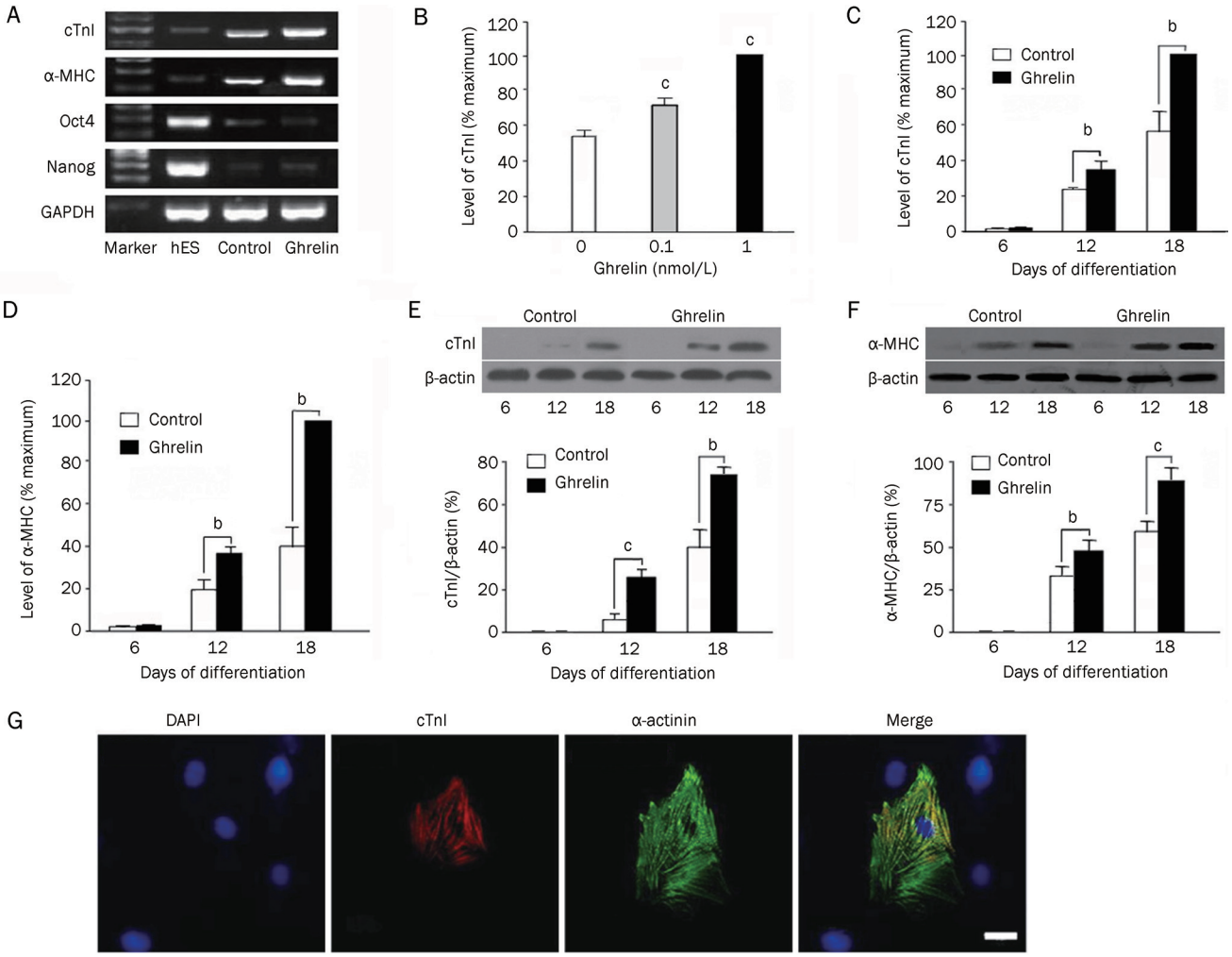


**Figure 3.** Effects of ghrelin on the expression of cardiac-specific markers in differentiated EBs. (A) RT-PCR analysis for mRNA level in the undifferentiated hES cells and the EBs treated with or without 1 nmol/L ghrelin on d 18 of differentiation. (B) Dose-effects of ghrelin on cTnI mRNA expression as evaluated by real-time RT-PCR analysis on d 18 of differentiation. (C, D) Time-kinetic effects of 1 nmol/L ghrelin on the mRNA expression of cardiac-specific markers as evaluated by real-time RT-PCR analysis in the EBs on d 6, 12 and 18 of differentiation: (C) cTnI; (D) α-MHC. The maximum expression levels which were expressed as 100% were used to normalize the expression levels at other time points. (E, F) Time-kinetic effects of 1 nmol/L ghrelin on the protein expression of cardiac-specific markers as evaluated by Western blot analysis in the EBs on d 6, 12 and 18 of differentiation: (E) cTnI; (F) α-MHC. The histograms show the percentage of target protein expression to β-actin, which served as an internal standard. Each value represents the mean±SEM. $^{b}P<0.05$, $^{c}P<0.01$ *vs* control group. $n=4$. (G) Confocal images of immunofluorescent staining for cTnI (red) and α-actinin (green) in the dispersed cells from the beating areas within EBs. Magnification bar represents 20 μm.

study. Because of unlimited proliferation capacity and multipotency, hES cells may be one of the most attractive stem cell source used in the field of regenerative medicine in the future. However, an efficient *in vitro* cardiomyocyte differentiation protocol must be established before hES cells could be clinically available in treating heart diseases. Up to now, only a few factors have been demonstrated to have a role in promoting cardiomyocyte differentiation from hES cells. In 2006, a study reported that the expression of cardiac-specific markers including cTnI and α-MHC was promoted by the combination of BMP-4 and activin A in the N2/B27-chemically defined medium used in hES cell differentiation[4]. However, the ratio of beating EBs was not analyzed in that study. Another study assessed cardiomyocyte differentiation from two hES cell lines in low FBS-containing medium in the presence of BMP-2, in which the cumulative percentages of beating EBs were only 8.75% and 6.94% respectively by d 28 of differentiation[6]. In our study, both real-time RT-PCR and Western blot analyses revealed that the expression of cTnI and α-MHC in the ghrelin-treated group was markedly higher than that in control group. Furthermore, our data showed that the percentages of beating EBs on d 12 and 18 of differentiation were 4.9% and 9.5% respectively in control group, which were increased to 11.1% and 18.6% by treatment with 1 nmol/L ghrelin. It was worth noting that the increment in the percentages of beating EBs was in accordance with the alteration in the expression

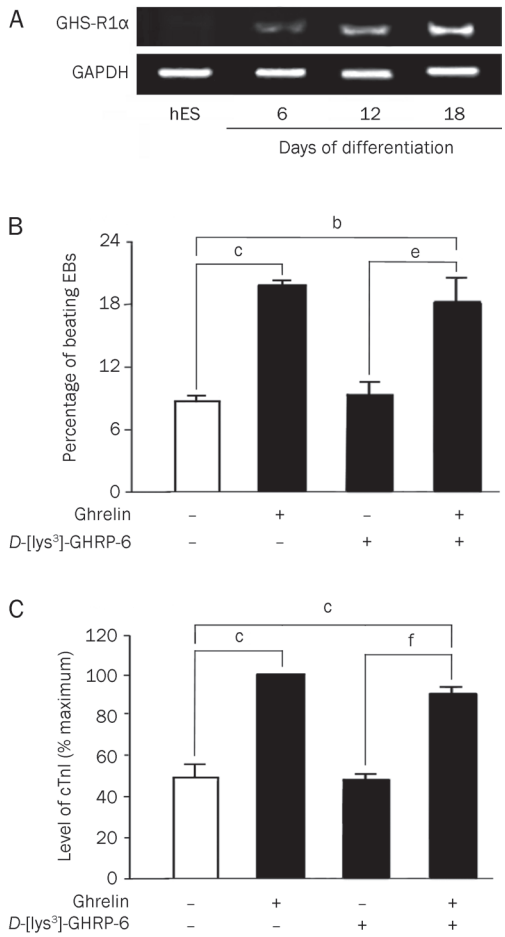


**Figure 4.** Effects of GHS-R1α blockage on the cardiomyocyte differentiation of hES cells induced by ghrelin. (A) RT-PCR analysis for GHS-R1α expression in the undifferentiated hES cells and the EBs on d 6, 12, and 18 of differentiation. (B) Effects of 1 nmol/L ghrelin on the percentages of beating EBs as evaluated on d 18 of differentiation in the presence or absence of a specific GHS-R1α antagonist *D*-[lys$^3$]-GHRP-6 (1 μmol/L). (C) Effects of 1 nmol/L ghrelin with or without 1 μmol/L *D*-[lys$^3$]-GHRP-6 on cTnI expression as evaluated by real-time RT-PCR analysis in the EBs on d 18 of differentiation. Each value represents the mean±SEM. $n$=4. $^bP$<0.05, $^cP$<0.01 *vs* control group; $^eP$<0.05, $^fP$<0.01 *vs* *D*-[lys$^3$]-GHRP-6 group.

of cTnI and α-MHC. Our data suggest that ghrelin markedly enhances the yield of cardiomyocyte differentiation from hES cells.

GHS-R1α is the functional ghrelin receptor and ghrelin exerts its biological functions via activation of the receptor subtype[9]. In the present study, GHS-R1α was expressed in the differentiated EBs. However, GHS-R1α blockage by *D*-[lys$^3$]-GHRP-6 did not alter the promoting effects of ghrelin on the percentage of beating EBs and the expression of cTnI, suggesting that the induction of cardiomyocyte differentiation of hES cells resulted from ghrelin stimulation was likely mediated via an unidentified subtype of ghrelin receptor rather than GHS-R1α. Moreover, our preliminary study showed that mitogen-activated protein kinase (MAPK) pathway was involved in the action of ghrelin (data not shown). Clearly, additional studies are needed to investigate the role of the MAPK signaling in the cardiomyocyte differentiation induced by ghrelin.

In conclusion, the present study show for the first time that ghrelin significantly enhances the generation of beating EBs and the expression of cardiac-specific markers in the differentiated EBs generated from hES cells, indicating that ghrelin promotes the differentiation of hES cells into myocardial cells. Therefore, ghrelin may serve as a useful factor for an effective method in the induction of cardiomyocyte differentiation from hES cells, which may contribute to cardiomyocyte-based regenerative medicine.

## Acknowledgements

This work was supported by grants from the Chinese National 863 Program (2006AA02A112), the National Natural Sciences Foundation of China (No 30771032, 30700879, 81070701, and 81000315), and the Specialized Research Fund for the Doctoral Program of Higher Education (20100001110083). We thank Dr Hong-mei PENG for setting up our hES cell line PKU1.1 for this research; Li CHEN and Zheng MA for their excellent technical assistance; and Hai-yan YU, Gen-hong MAO, and Tian-ran SONG for their invaluable assistance.

## Author contribution

Jin YANG and Guo-qiang LIU performed most experiments; Jin YANG, Guo-qiang LIU and Tian-pei HONG wrote the manuscript; Rui WEI, Wen-fang HOU, Mei-juan GAO, Ming-xia ZHU and Hai-ning WANG contributed to cell culture and provided technical support; Gui-an CHEN and Tian-pei HONG designed the study.

## References

1 Thomson JA, Itskovitz-Eldor J, Shapiro SS, Waknitz MA, Swiergiel JJ, Marshall VS, *et al*. Embryonic stem cell lines derived from human blastocysts. Science 1998; 282: 1145–7.
2 Kehat I, Kenyagin-Karsenti D, Snir M, Segev H, Gepstein A, Livne E, *et al*. Human embryonic stem cells can differentiate into myocytes with structural and functional properties of cardiomyocytes. J Clin Invest 2001; 108: 407–14.
3 Xu C, Police S, Rao N, Carpenter MK. Characterization and enrichment of cardiomyocytes derived from human embryonic stem cells. Circ Res 2002; 91: 501–8.
4 Yao S, Chen S, Clark J, Hao E, Beattie GM, Hayek A, *et al*. Long-term self-renewal and directed differentiation of human embryonic stem cells in chemically defined conditions. Proc Natl Acad Sci U S A 2006; 103: 6907–12.
5 Laflamme MA, Chen KY, Naumova AV, Muskheli V, Fugate JA, Dupras SK, *et al*. Cardiomyocytes derived from human embryonic stem cells in pro-survival factors enhance function of infarcted rat hearts. Nat Biotechnol 2007; 25: 1015–24.
6 Pal R, Khanna A. Similar pattern in cardiac differentiation of human embryonic stem cell lines, BG01V and ReliCellhES1, under low serum concentration supplemented with bone morphogenetic protein–2. Differentiation 2007; 75: 112–22.
7 Yook JY, Kim MJ, Son MJ, Lee S, Nam Y, Han YM, *et al*. Combinatorial

ALK/Smad and bFGF signals stimulate the differentiation of hESCs into the cardiac lineage. Stem Cells Dev 2011. doi:10.1089/scd.2010.0392.

8 Tran TH, Wang X, Browne C, Zhang Y, Schinke M, Izumo S, *et al*. Wnt3a-induced mesoderm formation and cardiomyogenesis in human embryonic stem cells. Stem Cells 2009; 27: 1869–78.

9 Kojima M, Hosoda H, Date Y, Nakazato M, Matsuo H, Kangawa K. Ghrelin is a growth-hormone-releasing acylated peptide from stomach. Nature 1999; 402: 656–60.

10 Gnanapavan S, Kola B, Bustin SA, Morris DG, McGee P, Fairclough P, *et al*. The tissue distribution of the mRNA of ghrelin and subtypes of its receptor, GHS-R, in humans. J Clin Endocrinol Metab 2002; 87: 2988–91.

11 Ariyasu H, Takaya K, Tagami T, Ogawa Y, Hosoda K, Kamizu T, *et al*. Stomach is a major source of circulating ghrelin, and feeding state determines plasma ghrelin-like immunoreactivity levels in humans. J Clin Endocrinol Metab 2001; 86: 4753–8.

12 Takaya K, Ariyasu H, Kanamoto N, Iwakura H, Yoshimoto A, Harada M, *et al*. Ghrelin strongly stimulates growth hormone release in humans. J Clin Endocrinol Metab 2000; 85: 4908–11.

13 Iglesias MJ, Piñeiro R, Blanco M, Gallego R, Diéguez C, Gualillo O, *et al*. Growth hormone releasing peptide (ghrelin) is synthesized and secreted by cardiomyocytes. Cardiovasc Res 2004; 62: 481–8.

14 Kui L, Weiwei Z, Ling L, Daikun H, Guoming Z, Linuo Z, *et al*. Ghrelin inhibits apoptosis induced by high glucose and sodium palmitate in adult rat cardiomyocytes through the PI3K-Akt signaling pathway. Regul Pept 2009; 155: 62–9.

15 Zhang W, Zhao L, Mulholland MW. Ghrelin stimulates myocyte development. Cell Physiol Biochem 2007; 20: 659–64.

16 Filigheddu N, Gnocchi VF, Coscia M, Cappelli M, Porporato PE, Taulli R, *et al*. Ghrelin and des-acyl ghrelin promote differentiation and fusion of C2C12 skeletal muscle cells. Mol Biol Cell 2007; 18: 986–94.

17 Fukushima N, Hanada R, Teranishi H, Fukue Y, Tachibana T, Ishikawa H, *et al*. Ghrelin directly regulates bone formation. J Bone Miner Res 2005; 20: 790–8.

18 Choi K, Roh SG, Hong YH, Shrestha YB, Hishikawa D, Chen C, *et al*. The role of ghrelin and growth hormone secretagogues receptor on rat adipogenesis. Endocrinology 2003; 144: 754–9.

19 Thompson NM, Gill DA, Davies R, Loveridge N, Houston PA, Robinson IC, *et al*. Ghrelin and des-octanoyl ghrelin promote adipogenesis directly *in vivo* by a mechanism independent of the type 1a growth hormone secretagogue receptor. Endocrinology 2004; 145: 234–42.

20 Hongmei P, Guian C. Serum-free medium cultivation to improve efficacy in establishment of human embryonic stem cell lines. Hum Reprod 2006; 21: 217–22.

21 Gaytan F, Morales C, Barreiro ML, Jeffery P, Chopin LK, Herington AC, *et al*. Expression of growth hormone secretagogue receptor type 1a, the functional ghrelin receptor, in human ovarian surface epithelium, mullerian duct derivatives, and ovarian tumors. J Clin Endocrinol Metab 2005; 90: 1798–804.

22 Zhang L, Hu J, Hong TP, Liu YN, Wu YH, Li LS. Monoclonal side population progenitors isolated from human fetal pancreas. Biochem Biophys Res Commun 2005; 333: 603–8.

23 Lee HM, Wang G, Englander EW, Kojima M, Greeley GH Jr. Ghrelin, a new gastrointestinal endocrine peptide that stimulates insulin secretion: enteric distribution, ontogeny, influence of endocrine, and dietary manipulations. Endocrinology 2002; 143: 185–90.

24 Xu XB, Pang JJ, Cao JM, Ni C, Xu RK, Peng XZ, *et al*. GH-releasing peptides improve cardiac dysfunction and cachexia and suppress stress-related hormones and cardiomyocyte apoptosis in rats with heart failure. Am J Physiol Heart Circ Physiol 2005; 289: H1643–51.

25 Nagaya N, Moriya J, Yasumura Y, Uematsu M, Ono F, Shimizu W, *et al*. Effects of ghrelin administration on left ventricular function, exercise capacity, and muscle wasting in patients with chronic heart failure. Circulation 2004; 110: 3674–9.

26 Deng F, Ling J, Ma J, Liu C, Zhang WZ. Stimulation of intramembranous bone repair in rats by ghrelin. Exp Physiol 2008; 93: 872–9.

Acta Pharmacologica Sinica (2011) 32: 1246–1252
 1671-4083/11 $32.00
www.nature.com/aps

Original Article

# Effects of Rhein lysinate on $H_2O_2$-induced cellular senescence of human umbilical vascular endothelial cells

Ya-jun LIN[1, #], Yong-zhan ZHEN[2, #], Jie WEI[1], Bo LIU[1], Zong-yuan YU[1], Gang HU[1, #, *]

[1]*The Key Laboratory of Geriatrics, Beijing Hospital & Beijing Institute of Geriatrics, Ministry of Health, Beijing 100730, China;* [2]*Hebei United University, Tangshan 063000, China*

**Aim:** To observe the effect of Rhein lysinate (RHL) on cellular senescence of human umbilical vascular endothelial cells (HUVECs) and elucidate its action mechanism.
**Methods:** Cell viability was determined using MTT assay. The expression levels of Sirt1 mRNA and protein were measured by RT-PCR and Western blot, respectively. Senescence associated (SA)-β-galactosidase activity was detected to evaluate cell senescence. Apoptosis and cell cycle progression were determined using flow cytometry.
**Results:** Treatment with RHL (10 μmol/L) for 48 h significantly increased the proliferation of HUVECs. In contrast, treatment with $H_2O_2$ (25, 50 and 100 μmol/L) for 6 d dose-dependently increased β-galactosidase positive cells. Spontaneous cell senescence appeared as the cell passage increased. Pre-treatment with RHL (10 μmol/L) reversed $H_2O_2$ or increased cell passage-induced cell senescence. $H_2O_2$ (100 μmol/L) significantly arrested HUVECs at $G_1$ phase (73.8% *vs* 64.6% in the vehicle group), which was blocked by RHL (10 μmol/L). RHL (5 and 10 μmol/L) enhanced both mRNA transcription and protein expression of Sirt1. $H_2O_2$ (100 μmol/L) significantly decreased Sirt1 expression, and induced up-regulation of p53 acetylation and $p16^{INK4a}$, which were blocked by pre-treatment with RHL (10 μmol/L). Interference with siRNA for Sirt1 abolished the effect of RHL. $H_2O_2$ (100 μmol/L) did not induce HUVEC apoptosis. The expression of apoptosis-associated proteins, such as p53, p21, Bcl-2, and Bax, did not significantly change in the presence of $H_2O_2$ (100 μmol/L) or RHL (10 μmol/L).
**Conclusion:** RHL protected HUVECs against cellular senescence induced by $H_2O_2$, via up-regulation of Sirt1 expression and down-regulation of the expression of acetyl-p53 and $p16^{INK4a}$.

**Keywords:** Rhein lysinate; $H_2O_2$; cell cycle; senescence; Sirt1; human umbilical vascular endothelial cells (HUVECs); RNA interference

*Acta Pharmacologica Sinica* (2011) 32: 1246–1252; doi: 10.1038/aps.2011.101; published online 12 Sep 2011

## Introduction

Aging is considered to be a major risk factor for developing atherosclerosis and is also associated with reducing the regenerative capacity of the endothelium and causing endothelial senescence[1]. Atherosclerosis is a very common condition associated with increased cardiovascular risk, and endothelial dysfunction is thought to promote its development[2]. However, the underlying mechanisms remain to be determined. Moreover, atherosclerosis is also associated with an increase in endothelial cell turnover, and endothelial cell apoptosis plays a pivotal role in developing atherosclerotic plaques[3].

The silent information regulator 2 (Sir2) is an NAD-dependent deacetylase. It is well known that an overexpression of Sir2, or its homologue, can extend the lifespan of a wide range of lower eukaryotes, including yeasts, worms and flies[4]. In mammals, Sir2 is represented by seven homologues (Sirt1~7), of which Sirt1 is the most closely related to the yeast Sir2 and has been studied extensively.

Recent studies have demonstrated that Sirt1 plays an important role in regulating cell survival by inhibiting apoptosis induced by stress[5–7]. Researchers speculate that Sirt1 could also regulate cell aging because it has been reported that apoptosis and senescence in vascular endothelial cells are closely related to atherosclerosis progression.

In this study, we investigated the ability of Sirt1 to interfere with apoptosis and cellular senescence in human umbilical vascular endothelial cells (HUVECs) and explored the effect of Rhein lysinate (RHL) on Sirt1's function.

Rhein (4,5-dihydroxy-anthraquinone-2-carboxylic acid) is

# The authors contributed equally to this work.
* To whom correspondence should be addressed.
E-mail huganglys2010@126.com
Received 2011-01-18 Accepted 2011-05-27

one of the major bioactive constituents of the rhubarb rhizome (R palmatum L or R tanguticum Maxim)[8]. In previous studies, Rhein was found to have a variety of bioactivities, such as inhibiting IL-1 induced chondrocyte activation[9], decreasing hypertrophy in mesangial cells[10], inhibiting tumor cell proliferation, and inducing tumor cell apoptosis[11]. In our previous study, we also found that a dose of more than 20 μmol/L RHL could inhibit tumor cell proliferation, and it acted synergistically with Taxol when combined, both *in vitro* and *in vivo*[12]. However, less than 20 μmol/L RHL can also improve cell viability. Therefore, we investigated the effect of RHL on cell viability in HUVECs and explored its mechanisms.

## Materials and methods

### Reagents

RHL, the salt of Rhein and lysine, was made in our department with 95% purity. Its structural formula was shown in our previous article. Gelatin, 3-(4,5-dimethylthiazol-2-yl)-2,5-diphenyl-tetrazolium bromide (MTT), dimethyl sulfoxide (DMSO), collagenase I, and heparin were obtained from Sigma Aldrich (Shanghai, China); endothelial cell growth factor (ECGF) was purchased from Roche (Shanghai, China); and trypsin was purchased from Gibco (Grand Island, NY, USA). Sirt1 and acetyl-p53 (lys382) antibody were purchased from Upstate (New York, USA); antibodies against p53, p21, $p16^{INK4a}$, Bcl-2, Bax, and β-Actin were purchased from Santa Cruz Technology (Santa Cruz, CA, USA); and secondary antibodies against rabbit or mouse were purchased from Cell Signaling Technology (Danvers, MA, USA). Pre-stained Protein Marker p7708V was purchased from New England Biolabs Ltd (Pickering, Ontario, Canada). Western Blotting Luminol Reagent and PVDF membrane were purchased from Millipore (Billerica, MA, USA).

### Cell culture and determining cell viability

HUVECs isolated from newborn umbilical cord were grown in M199 supplemented with 20% fetal bovine serum (FBS) (Hyclone, Logan, UT, USA) at 37 °C under 5% $CO_2$ in a humidified atmosphere. Cells were incubated with different concentrations of RHL (0, 5, 10, 15, and 20 μmol/L) at 37 °C for 48 h. Moreover cells were incubated with 10 μmol/L RHL for 0, 6, 12, 24, and 48 h. Cell viability was assessed by MTT method.

### Reverse transcription-PCR

The mRNA level of Sirt1 in HUVECs was measured by RT-PCR. Total RNA in HUVECs was isolated with TRIzol (Invitrogen, Carlsbad, CA, USA). After treatment with Rnase-free Dnase for 30 min, the total RNA (50 ng/μL) was reverse transcribed with oligo d(T) primers. The Sirt1 transcription level relative to GAPDH was determined by means of RT-PCR. The following primers were used: Sirt1 forward (F) 5′-CCTGACTTCAGATCAAGAGACGGT-3′, reverse (R) 5′-CTGATTAAAAATGTCTCCACGAAC AG-3′; GAPDH F 5′-ACCACAGTCCATGCCATCAC-3′, R 5′-TCCACCAC-CCTGTTGCTGTA-3′[13]. Amplification was performed on an Eppendorf thermocycler for 30 cycles with denaturing at 94 °C for 30 s, annealing at 58 °C for 40 s, and extension at 72 °C for 1.5 min.

### Immunoblot analysis

Cells were lysed on ice for 30 min in lysis buffer [50 mmol/L HCl, pH 7.6, 150 mmol/L NaCl, 1% NP-40, 0.1% sodium dodecyl sulfate (SDS), 1 mmol/L dithiothreitol, 1 mmol/L sodium vanadate, 1 mmol/L phenylmethylsulfonyl fluoride, 10 μg/mL aprotinin, 10 μg/mL leupeptin, and 10 mmol/L sodium fluoride]. Equal amounts of protein were separated by SDS-polyacrylamide gel electrophoresis and then transferred to nitrocellulose filters. First, the membrane was inoculated in a blocking buffer containing BSA (1%) and Tween 20 (0.1%, *v/v*) in PBS (PBS/Tween 20) at room temperature for 1 h. Then, it was inoculated overnight at 4 °C with the proper primary antibodies. Finally, it was inoculated with the proper secondary antibodies at room temperature for 2 h. Each membrane was developed using an enhanced ChemiImager5500 chemiluminescence system (Alpha Innotech Corporation, Miami, FL, USA).

### RNA interference

Synthetic Sirt1 small interfering RNA (siRNA) was purchased from GenePharma Co, Ltd (Shanghai, China). The 21-nt siRNA sequence targeting Sirt1 corresponded to the coding region 5′-GCAACAGCAUCUUGCCUGAUUUGUA-3′ and 5′-UACAAAUCAGGCAAGAUGCUGUUGC-3′. The scrambled control siRNA sequences were 5′-UUCUCCGAACGUGU-CACGUTT-3′ and 5′-ACGUGACACGUUCGGAGAATT-3′. After 10 μmol/L RHL treatment for 24 h, these siRNA were transfected into HUVECs using the HiPerFect Transfection Reagent (QIAGEN, Shanghai, China). After siRNA transfection for 24 h, the cells were incubated with 100 μmol/L $H_2O_2$ for 6 d. Then, the cells were stained using galactosidase (β-gal).

### Galactosidase (β-gal) staining

HUVECs were treated with or without different concentrations of $H_2O_2$, RHL or $H_2O_2$ plus RHL. After that, the cells were washed twice with phosphate-buffered saline (PBS) and then fixed for 5 min with PBS containing 2% formaldehyde and 0.2% glutaraldehyde. The cells were then incubated at 37 °C for 10 h with a staining solution (40 mmol/L citric acid, sodium phosphate, pH 6.0, 1 mg/mL 5-bromo-4-chloro-3-isolyl-β-*D*-galactoside (X-gal, sigma), 5 mmol/L potassium ferrocyanide, 5 mmol/L potassium ferricyanide, 150 mmol/L NaCl, and 2 mmol/L $MgCl_2$). Senescence-associated (SA)-β-gal-positive cells were observed by microscopy, and over 400 cells were counted in three independent fields[14].

### Annexin V FITC/PI assay

Annexin V-FITC/PI double staining was achieved using an Annexin V-FITC/PI apoptosis detection kit. HUVECs were treated with or without 100 μmol/L $H_2O_2$, 10 μmol/L RHL, or both for 48 h. The cells were washed with PBS and collected by trypsinization. The cells were then treated according to the instructions in the Annexin V-FITC/PI apoptosis detection kit

(Bao Sai, Beijing), which indicate the following:

- The Annexin V-FITC$^-$/PI$^-$ population reflects normal healthy cells.
- The Annexin V-FITC$^+$/PI$^-$ cells show early apoptosis.
- The Annexin V-FITC$^+$/PI$^+$ cells are in late apoptosis or necrosis.
- The Annexin V-FITC$^-$/PI$^+$ cells are necrotic.
- The percentage of normal, early apoptotic, late apoptotic, and necrotic cells were calculated using FACS Calibur and Cell Quest software (Becton-Dickinson, Franklin Lakes, NJ, USA)[15].

### Cell cycle assay

To determine the effect of $H_2O_2$ and RHL on cell cycle progression, HUVECs were grown for 48 h (one-cell cycle) with or without 100 μmol/L $H_2O_2$, 10 μmol/L RHL, or both. The cells were washed with PBS and collected by trypsinization. The cells were fixed with 70% ethanol and treated with 5 mg/mL (Rnase) for 30 min. After staining with 50 mmol/L propidium iodide, the cells were subjected to flow cytometric analysis with FACS Calibur and Cell Quest software (Becton-Dickinson).

### Statistical analysis

Statistical analysis was performed between the control group and the different treatment groups. Comparisons of the means were conducted by one-way ANOVA. All values were expressed as the mean±SD, and $P<0.05$ was considered to be statistically significant.

## Results

### Low levels of RHL improve HUVEC proliferation and enhance Sirt1 transcription and expression

Our previous study indicated that low levels of RHL (less than 20 μmol/L) could improve cell proliferation in MCF-7 breast cancer cells. The same effect of RHL on HUVECs was also observed in a time-dependent manner; however, only 10 μmol/L RHL could significantly promote HUVEC proliferation (Figure 1A, 1B). In the following study, RHL (5 and 10 μmol/L) enhanced Sirt1 transcription and expression in a dose-dependent manner compared to the vehicle (Figure 2).

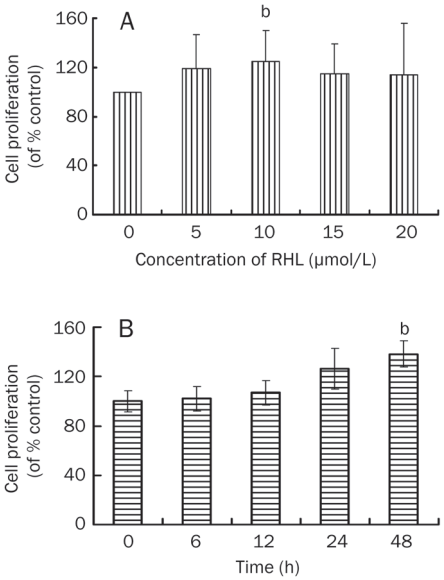


**Figure 1.** Rhein lysinate at low concentrations promoted the proliferation of HUVECs. HUVECs were treated with various concentrations of RHL at 37 °C for 48 h (A), and then cells were incubated with 10 μmol/L RHL for 0, 6, 12, 24, and 48 h (B). The effects on cell proliferation were examined by MTT assay, and cell proliferation was calculated as the percentage of control. $n$=3. Mean±SD. $^bP<0.05$ *vs* control.

### Establishing senescence model in HUVECs and Sirt1 can delay HUVEC cellular senescence progress

To investigate the effect of Sirt1 on senescence in HUVECs, we first established the senescence model in HUVECs. Four main groups were respectively treated with 0, 25, 50, or 100 μmol/L $H_2O_2$, and senescent cells were found to increase with

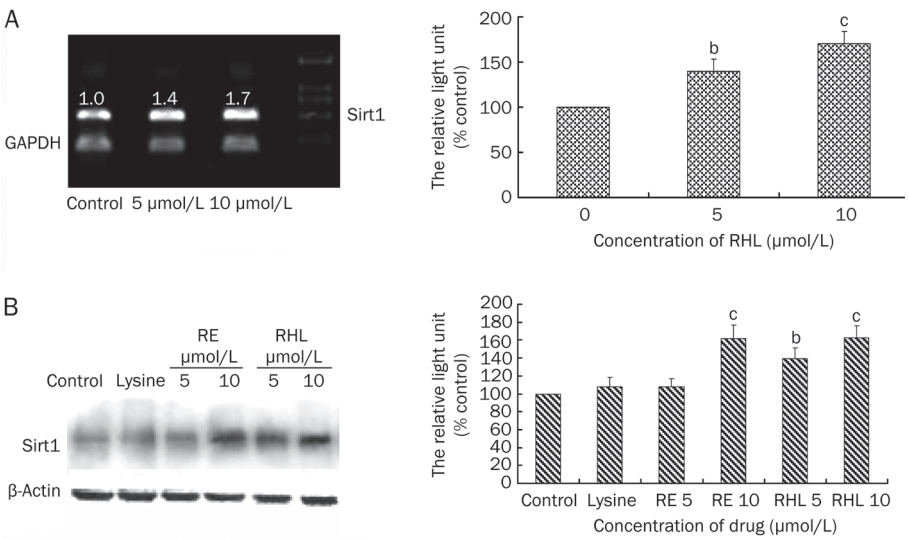


**Figure 2.** Rhein lysinate at low concentrations increased Sirt1 transcription and expression. HUVECs were treated with 5 or 10 μmol/L RHL at 37 °C for 48 h. Sirt1 transcription was examined by RT-PCR (A), and Sirt1 expression was examined by Western blot (B). RE=resveratrol (positive control); RHL=Rhein lysinate. $n$=3. Mean±SD. $^bP<0.05$, $^cP<0.01$ *vs* control.

increasing dosages of $H_2O_2$ (Figure 3A); however, the expression of Sirt1 decreased (Figure 4A). In the meantime, we also observed that the number of senescent cells increased with increasing cell passage (Figure 3B), and the expression of Sirt1 decreased (Figure 4B). Furthermore, 10 μmol/L RHL could antagonize cell senescence induced by $H_2O_2$ and the increased passage of HUVECs (Figure 3C, 3D); moreover, siRNA (Sirt1) antagonized the effect of RHL (Figure 3E, 3F).

### RHL has no effect on the apoptosis signaling pathway

$H_2O_2$ inhibited HUVEC survival with $IC_{50}$ of about 100 μmol/L. To determine whether or not $H_2O_2$ inhibits HUVEC survival by inducing apoptosis, we investigated the effect of $H_2O_2$ on apoptosis. $H_2O_2$ 100 μmol/L induced HUVECs senescence but could not induce HUVEC apoptosis (Table 1). Furthermore, we examined the associated protein expression in the apoptosis signaling pathway. It indicated that the protein expression associated with apoptosis, such as p53, p21, Bcl-2, and Bax, did not change in the $H_2O_2$ 100 μmol/L or RHL 10 μmol/L treatment groups ($P$>0.05, Figure 5A).

**Table 1.** The effect of RHL on necrosis HUVECs induced by $H_2O_2$. $n$=3. Mean±SD. $^bP$<0.05, $^cP$<0.01 *vs* control. $^eP$<0.05, $^fP$<0.01 *vs* $H_2O_2$ 100 μmol/L.

| Concentration (μmol/L) | Normal cells (%) | Necrotic cells (%) | Early apoptotic cells (%) | Late apoptotic cells (%) |
|---|---|---|---|---|
| Control | 80.9±6.7 | 7.4±0.7 | 6.6±0.6 | 5.1±0.8 |
| RHL 10 | 83.2±6.5 | 6.2±0.8 | 4.0±0.5 | 6.6±0.5 |
| $H_2O_2$ 100 | 60.4±4.8$^c$ | 21.4±1.2$^c$ | 8.8±0.7 | 9.4±1.0 |
| RHL+$H_2O_2$ | 71.0±4.1$^{be}$ | 15.6±1.4$^{bf}$ | 6.8±0.9 | 6.6±0.6 |

### $H_2O_2$ induced $G_1$ arrest in HUVECs, and RHL prevented against $H_2O_2$-induced $G_1$ arrest

Cell cycle plays an important role in cellular senescence. Senescence occurs during the $G_1$ period. Treatment with 100 μmol/L $H_2O_2$ arrested HUVECs at $G_1$ phase. The proportion of cells in the $G_1$ phase was approximately 73.8%. However, it was about 64.6% in the vehicle group. RHL 10 μmol/L reversed the $G_1$ arrest effects of $H_2O_2$. The proportion of cells in $G_1$ phase decreased to 63.1% (Table 2). $H_2O_2$ 100 μmol/L induced the p53 acetylation and $p16^{INK4a}$ up-regulation and treatment with 10 μmol/L RHL prevented this process (Figure 5B).

## Discussion

In our previous study, we found that high concentrations of RHL (more than 20 μmol/L) could inhibit cell proliferation in a dose-dependent manner[12]. In the meantime, we also found that low concentrations of RHL (less than 20 μmol/L) could improve cell proliferation and alleviate the cytotoxicity induced by Taxol (data was not shown). However, how RHL improves cell proliferation is unclear. In this study, we also observed that RHL improved HUVEC proliferation at low concentrations (less than 20 μmol/L), especially at 10 μmol/L (Figure 1). As is well known, increased cellular senescence is associated with decreased cell proliferation *in vivo* because senescent cells cannot divide[16]. Therefore, it can be concluded that by delaying cell senescence, low concentrations of RHL can improve HUVEC proliferation.

**Table 2.** The effect of RHL on cell cycle arrest of HUVECs induced by $H_2O_2$. $n$=3. Mean±SD. $^bP$<0.05, $^cP$<0.01 *vs* control. $^eP$<0.05, $^fP$<0.01 $H_2O_2$ 100 μmol/L.

| Concentration (μmol/L) | $G_0/G_1$ (%) | S (%) | $G_2$/M (%) |
|---|---|---|---|
| Control | 64.6±4.6 | 22.4±2.3 | 13.1±1.7 |
| RHL 10 | 62.0±4.5 | 25.2±2.8 | 12.8±1.5 |
| $H_2O_2$ 100 | 73.8±5.5$^b$ | 13.3±1.2$^c$ | 12.9±1.3 |
| RHL+$H_2O_2$ | 63.1±5.1$^e$ | 24.5±2.6$^f$ | 12.4±2.2 |

Cellular senescence is a process by which cells irreversibly exit the cell cycle and cease to divide in response to a variety of stresses, including oxidative stress[17]. It was reported that oxidative stress damages DNA, leading to activation of the tumor suppressor p53, a key regulator of the cell cycle and cellular senescence. It has also been reported that p53 acetylation promotes expression of growth-suppressive genes and induces cellular senescence[18, 19]. In this study, we established the cell senescence model using $H_2O_2$-treated HUVECs. We found that $H_2O_2$ could induce HUVEC senescence in a dose-dependent manner (Figure 3A). We also found cell spontaneous senescence appeared with an increase in cell passage (Figure 3B), and that HUVECs could only survive to the fifth generation without epidermal growth factor (EGF) supplementation. The characteristics of HUVECs made it easier to establish this model of cell senescence. As we investigated the HUVEC senescence mechanism, we observed that the expression of Sirt1 decreased in a dose-dependent manner following treatment with various concentrations of $H_2O_2$, that the expression of Sirt1 decreased with the increase in cell passage (Figure 4), and that 10 μmol/L RHL could antagonize cell senescence induced by $H_2O_2$ and the increase in the passage of HUVECs (Figure 3C, 3D); moreover, siRNA (Sirt1) could antagonize the effect of RHL (Figure 3E, 3F). Therefore, it can be concluded that RHL prevented cellular senescence induced by $H_2O_2$ treatment, as well as the increase of cell passage, through enhancing Sirt1 expression (Figure 3C–3F).

Endothelial senescence causes endothelial dysfunction, promotes atherogenesis and contributes to age-related vascular disorders. Sirt1 is a key sensor system for regulating endothelial cell survival, proliferation, and senescence. The protective activities of Sirt1 may be achieved at least in part by fine tuning the acetylation/deacetylation of key proteins[20]. In this study, we also observed that the p53 acetylation level was inversely related to the expression of Sirt1 in $H_2O_2$-induced

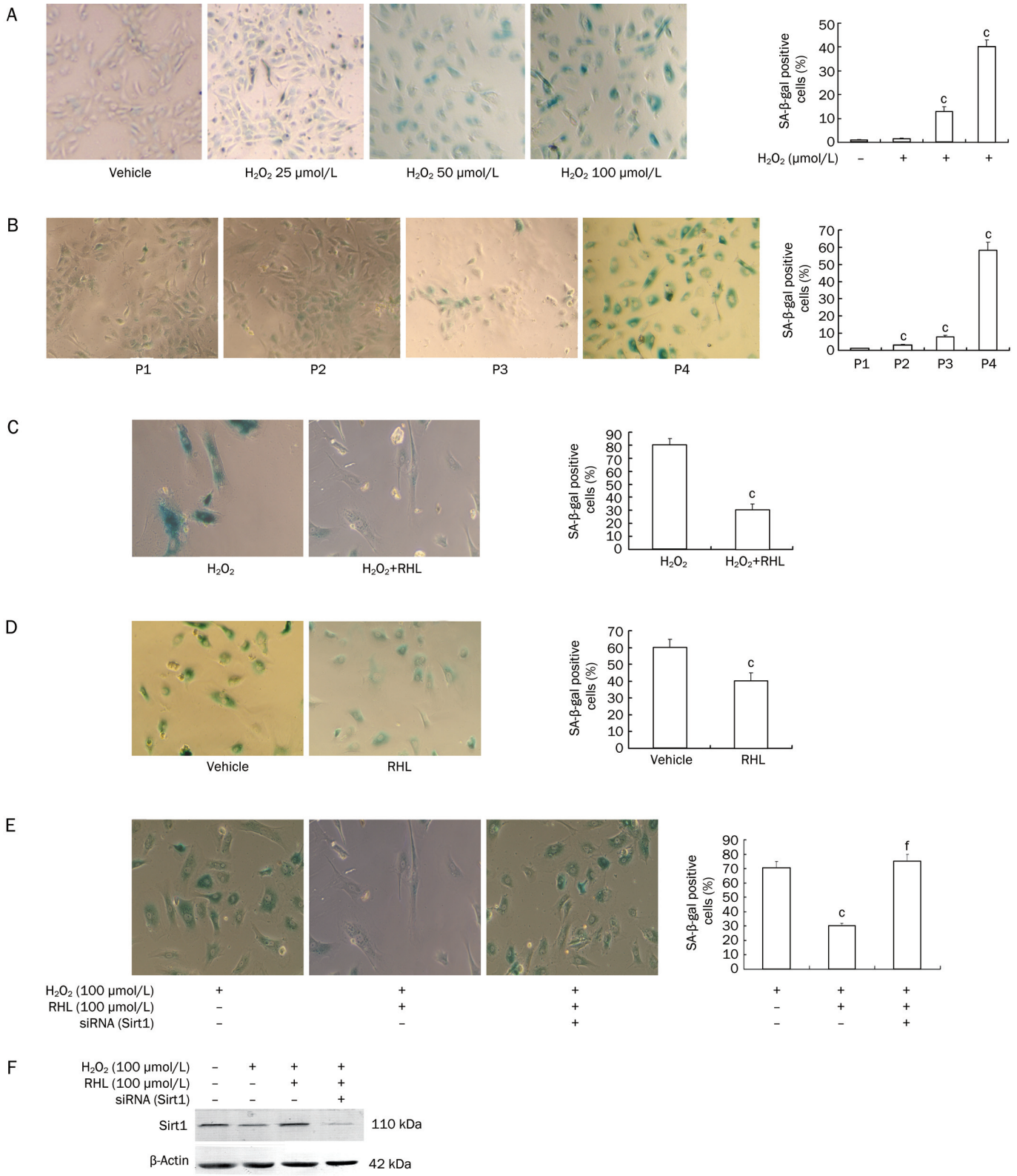


**Figure 3.** SA-β-gal activity of different passages of HUVECs treated with various concentrations of $H_2O_2$. (A) HUVECs were treated with 0, 25, 50, and 100 μmol/L $H_2O_2$ at 37 °C for 3 d and then placed in a medium with the same concentration of $H_2O_2$ for further 3 d. $^cP<0.01$ *vs* vehicle. (B) P1, P2, P3, and P4 represent the different passages of HUVECs. HUVECs were cultured for 3 d and then propagated. $^cP<0.01$ *vs* P1. (C) HUVECs were pre-treated with 10 μmol/L RHL at 37 °C for 24 h, followed by 100 μmol/L $H_2O_2$ treatment. $^cP<0.01$ *vs* $H_2O_2$. (D) P3 generation HUVECs were treated with 10 μmol/L RHL at 37 °C for 6 d. $^cP<0.01$ *vs* vehicle. (E) HUVECs were treated with 10 μmol/L RHL at 37 °C for 24 h, followed by siRNA (Sirt1) for 24 h and incubation with 100 μmol/L $H_2O_2$ for 6 d. $^cP<0.01$ *vs* $H_2O_2$. $^fP<0.01$ *vs* RHL+$H_2O_2$. (F) The expression of Sirt1 in the various groups. $n$=3. Mean±SD.

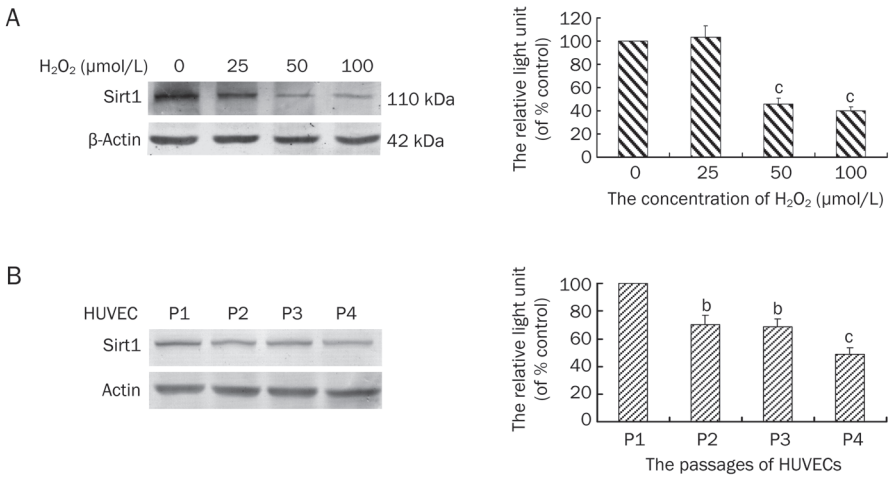


**Figure 4.** Effects of various concentrations of $H_2O_2$ on Sirt1 expression, and Sirt1 expression at different cell passages. (A) HUVECs were treated with 0, 25, 50, and 100 μmol/L $H_2O_2$ at 37 °C for 3 d and then placed in a medium with the same concentration of $H_2O_2$ for 3 more days. The Sirt1 expression was examined by Western blot. (B) P1, P2, P3, and P4 represented different passages of HUVECs. HUVECs were cultured for 3 days and then propagated. After incubation, Sirt1 expression was also determined, as in (A). $n$=3. Mean±SD. $^bP$<0.05, $^cP$<0.01 *vs* control.

cellular senescence. However, the expression of p53 did not change (Figure 5).

The p53 pathway is known to respond to a wide variety of stress signals, including telomere shortening, hypoxia, mitotic spindle damage, heat or cold shock, unfolded proteins, improper ribosomal biogenesis, nutritional deprivation, and mutational activation of some oncogenes. It is a single core module that governs the three potent tumor suppression mechanisms: growth arrest, senescence, and apoptosis[20].

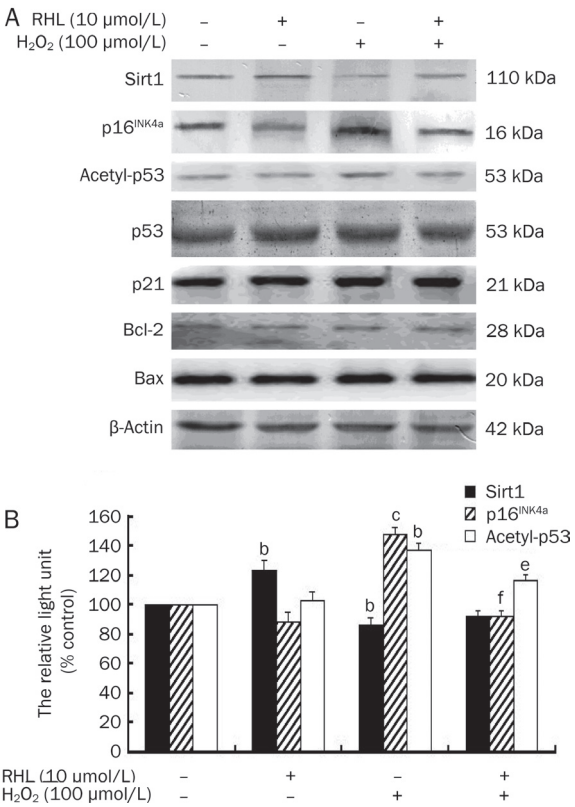


**Figure 5.** (A) Effect of RHL on the expression of Sirt1 and its downstream proteins. (B) Relative density of the protein levels. HUVECs were treated with 100 μmol/L $H_2O_2$ and/or RHL 10 μmol/L at 37 °C for 3 d and then placed in a medium with the same concentration of $H_2O_2$ for 3 more days. The expression of Sirt1, p53, p21, $p16^{INK4a}$, Bcl-2, Bax, and β-Actin was determined by Western blot. $n$=3. Mean±SD. $^bP$<0.05, $^cP$<0.01 *vs* control. $^eP$<0.05, $^fP$<0.01 *vs* $H_2O_2$ 100 μmol/L.

In this study, we explored whether apoptosis inhibited cell proliferation. Although 500 μmol/L $H_2O_2$ has been shown to induce cell apoptosis in PC12 cells (rat pheochromocytoma cell line)[21], HUVEC apoptosis was not affected by $H_2O_2$ (less than 100 μmol/L) treatment as measured by flow cytometry (Table 1) and Western blot (Figure 5). However, in the cell cycle analysis, we found that 100 μmol/L $H_2O_2$ induced $G_1$ period block, 10 μmol/L RHL prevented $G_1$ period block (Table 2), and that $G_1$ period block is the feature of cell senescence[22]. Therefore, we can conclude that the senescence induced by $H_2O_2$ was not due to apoptosis but to $G_1$ period block, and that RHL can interrupt the $G_1$ period block induced by $H_2O_2$.

Most normal mammalian cells have a finite lifespan, which is thought to constitute a protective mechanism against unlimited proliferation. This phenomenon, called senescence, is driven by telomere attrition, which triggers tumor suppressors to induce factors, including $p16^{INK4a}$ [23]. In this study, we also found that 10 μmol/L RHL could antagonize $p16^{INK4a}$ upregulation induced by 100 μmol/L $H_2O_2$. It can be inferred that $H_2O_2$ could partially induce HUVEC $G_1$ period block by increasing $p16^{INK4a}$ expression and that RHL could antagonize this phenomenon by the same signaling pathway. However, the effect of $H_2O_2$ and RHL on cyclin needs further investigation.

In conclusion, the decrease in Sirt1 expression inhibited cell proliferation induced by $H_2O_2$, as well as the spontaneous cell senescence with increased cell passage. Subsequently p53 was acetylated, and $p16^{INK4a}$ was upregulated, which caused $G_1$ period block and aging. However, RHL resisted this process. In addition, during HUVEC senescence, it was $G_1$ period block, not apoptosis, that played an important role, and RHL interrupted the $G_1$ period block induced by $H_2O_2$.

## Acknowledgements

This study was supported by a grant from the National Natu-

ral Science Foundation of China (No 81001439).

## Author contribution

Gang HU designed research; Ya-jun LIN, Bo LIU, and Zong-yuan YU performed research; Jie WEI and Yong-zhan ZHEN contributed new analytical tools and reagents; Ya-jun LIN and Yong-zhan ZHEN analyzed data; Ya-jun LIN and Gang HU wrote the paper.

## References

1 Brandes RP, Fleming I, Busse R. Endothelial aging. Cardiovasc Res 2005; 66: 286–94.
2 Muller G, Morawietz H. Nitric oxide, NAD(P)H oxidase, and atherosclerosis. Antioxid Redox Signal 2009; 11: 1711–31.
3 Ikushima M, Rakugi H, Ishikawa K, Maekawa Y, Yamamoto K, Ohta J, *et al*. Anti-apoptotic and anti-senescence effects of Klotho on vascular endothelial cells. Biochem Biophys Res Commun 2006; 339: 827–32.
4 Huang J, Gan Q, Han L, Li J, Zhang H, Sun Y, *et al*. Sirt1 overexpression antagonizes cellular senescence with activated ERK/S6k1 signaling in human diploid fibroblasts. PLoS One 2008; 3: e1710.
5 Brunet A, Sweeney LB, Sturgill JF, Chua KF, Greer PL, Lin Y, *et al*. Stress dependent regulation of FOXO transcription factors by the Sirt1 deacetylase. Science 2004; 303: 2011–5.
6 Langley E, Pearson M, Faretta M, Bauer UM, Frye RA, Minucci S, *et al*. Human Sir2 deacetylates p53 and antagonizes PML/p53-induced cellular senescence. EMBO J 2002; 21: 2383–96.
7 Wang C, Chen L, Hou X, Li Z, Kabra N, Ma Y, *et al*. Interactions between E2F1 and Sirt1 regulate apoptotic response to DNA damage. Nat Cell Biol 2006; 8: 1025–31.
8 Huang Q, Lu G, Shen HM, Chung MC, Ong CN. Anti-cancer properties of anthraquinones from rhubarb. Med Res Rev 2007; 27: 609–30.
9 Martin G, Bogdanowicz P, Domagala F, Ficheux H, Pujol JP. Articular chondrocytes cultured in hypoxia: their response to interleukin-1beta and rhein, the active metabolite of diacerhein. Biorheology 2004; 41: 549–61.
10 Tan ZH, Shen YJ, Zhao JN, Li HY, Zhang J. Effects of rhein on the function of human mesangial cells in high glucose environment. Yao Xue Xue Bao 2004; 39: 881–6.
11 Lin ML, Chen SS, Lu YC, Liang RY, Ho YT, Yang CY, *et al*. Rhein induces apoptosis through induction of endoplasmic reticulum stress and $Ca^{2+}$-dependent mitochondrial death pathway in human nasopharyngeal carcinoma cells. Anticancer Res 2007; 27: 3313–22.
12 Lin YJ, Zhen YS. Rhein lysinate suppresses the growth of breast cancer cells and potentiates the inhibitory effect of Taxol in athymic mice. Anticancer Drugs 2009; 20: 65–72.
13 Ota H, Eto M, Kano MR, Ogawa S, Iijima K, Akishita M, *et al*. Cilostazol inhibits oxidative stress-induced premature senescence via upregulation of Sirt1 in human endothelial cells. Arterioscler Thromb Vasc Biol 2008; 28: 1634–9.
14 Dimri GP, Lee X, Basile G, Acosta M, Scott G, Roskelley C, *et al*. A biomarker that identifies senescent human cells in culture and in aging skin *in vivo*. Proc Natl Acad Sci U S A 1995; 92: 9363–7.
15 Fang JH, Wang XH, Xu ZR, Jiang FG. Neuroprotective effects of bis(7)-tacrine against glutamate-induced retinal ganglion cells damage. BMC Neurosci 2010; 11; 31.
16 Gruber HE, Ingram JA, Davis DE, Hanley EN Jr. Increased cellular senescence is associated with decreased cell proliferation *in vivo* in the degenerating human annulus. Spine J 2009; 9: 210–5.
17 Ben-Porath I, Weinberg RA. The signals and pathways activating cellular senescence. Int J Biochem Cell Biol 2005; 37: 961–76.
18 Luo J, Li M, Tang Y, Laszkowska M, Roeder RG, Gu W. Acetylation of p53 augments its site-specific DNA binding both *in vitro* and *in vivo*. Proc Natl Acad Sci U S A 2004; 101: 2259–64.
19 Furukawa A, Tada-Oikawa S, Kawanishi S, Oikawa S. $H_2O_2$ accelerates cellular senescence by accumulation of acetylated p53 via decrease in the function of Sirt1 by $NAD^+$ depletion. Cell Physiol Biochem 2007; 20: 45–54.
20 Zu Y, Liu L, Lee MY, Xu C, Liang Y, Man RY, *et al*. Sirt1 promotes proliferation and prevents senescence through targeting LKB1 in primary porcine aortic endothelial cells. Circ Res 2010; 106: 1384–93.
21 Cai L, Wang H, Li Q, Qian Y, Yao W. Salidroside inhibits $H_2O_2$-induced apoptosis in PC12 cells by preventing cytochrome *c* release and inactivating of caspase cascade. Acta Biochim Biophys Sin 2008; 40: 796–802.
22 Dai CY, Enders GH. p16 INK4a can initiate an autonomous senescence program. Oncogene 2000; 19: 1613–22.
23 Michaloglou C, Vredeveld LC, Soengas MS, Denoyelle C, Kuilman T, van der Horst CM, *et al*. BRAFE600-associated senescence-like cell cycle arrest of human naevi. Nature 2005; 436: 720–4.

Acta Pharmacologica Sinica (2011) 32: 1253–1258
 1671-4083/11 $32.00
www.nature.com/aps

Original Article

# The inhibition of lipoprotein-associated phospholipase A2 exerts beneficial effects against atherosclerosis in LDLR-deficient mice

Miao-miao HU[1, #], Jie ZHANG[1, #], Wen-yi WANG[1], Wen-yu WU[1], Yan-ling MA[1], Wei-hai CHEN[2, 3], Yi-ping WANG[1, *]

*[1]Department of Pharmacology I, the State Key Laboratory of Drug Research, Shanghai Institute of Materia Medica, Chinese Academy of Sciences, Shanghai 201203, China; [2]Key Laboratory of Cognition and Personality (SWU), Ministry of Education, Southwest University, Chongqing 400715, China; [3]School of Psychology, Southwest University, Chongqing 400715, China*

**Aim:** To investigate the effects of darapladib, a specific inhibitor of lipoprotein-associated phospholipase A2 (lp-PLA2), on inflammation and atherosclerotic formation in the low density lipoprotein receptor (LDLR)-deficient mice.

**Methods:** Six-week-old LDLR-deficient mice were fed an atherogenic high-fat diet for 17 weeks and then randomly divided into two groups. One group was administered darapladib (50 mg·kg$^{-1}$·d$^{-1}$; *po*) for 6 weeks. The other group was administered saline as a control. Serum lipid levels were measured using the corresponding kits, and three inflammatory markers — interleukin-6 (IL-6), C reactive protein (hs-CRP), and platelet activating factor (PAF) — were determined using ELISA. Atherosclerotic plaque areas were stained with Sudan IV, and inflammatory gene expression at the lesions was evaluated using quantitative real-time PCR.

**Results:** The body weight and serum lipid level between the two groups were similar at the end of the dietary period. The serum lp-PLA2 activity, hs-CRP and IL-6 levels, however, were significantly reduced in the darpladib group. The inhibition of lp-PLA2 did not alter the serum PAF level. Furthermore, the plaque area, from the aortic arch to the abdominal aorta, was significantly reduced in the darpladib group. Additionally, the expression of inflammatory genes monocyte chemotactic protein-1 (MCP-1) and vascular cell adhesion molecule-1 (VCAM-1) was significantly reduced at the lesions in the darapladib group.

**Conclusion:** Inhibition of lp-PLA2 by darapladib decreases the inflammatory burden and atherosclerotic plaque formation in LDLR-deficient mice, which may be a new strategy for the treatment of atherosclerosis.

**Keywords:** atherosclerosis; lp-PLA2; darapladib; LDLR-deficient mice; inflammation; high-sensitivity C-reactive protein; interleukin-6; monocyte chemotactic protein-1; vascular cell adhesion molecule-1

*Acta Pharmacologica Sinica* (2011) 32: 1253–1258; doi: 10.1038/aps.2011.127; published online 15 Aug 2011

## Introduction

Phospholipases A2 (PLA2s) constitute a superfamily of enzymes that catalyze the hydrolysis of fatty acids from the sn-2 position of glycerophospholipids to produce free fatty acids and lysophospholipids, which are both involved in signaling transduction and metabolic processes, and account for a vast number of diseases[1, 2]. PLA2s, then, are obvious candidates for pharmacological research and intervention. Of all the PLA2s, lp-PLA2 in particular has gained increasing attention as a growing number of epidemiological and experimental studies suggest that it plays an important role in diseases such as atherosclerosis, diabetes, and asthma[3–6].

Lp-PLA2, also referred to as platelet-activating factor acetylhydrolase (PAF-AH; E.C. 3.1.1.47), is a $Ca^{2+}$-independent, 45 kDa secreted protein that associates with lipoproteins and circulates within the plasma in active form[7]. Lp-PLA2 can be up-regulated by the oxidized phospholipids in oxLDL[8] and in turn acts upon those oxidized phospholipids to produce two pro-inflammatory mediators, lysophosphatidylcholines (lysoPCs) and oxidized nonesterified fatty acids (oxNEFAs)[9]. Research suggests that the regulatory roles of these two products, especially lysoPCs, are in the promotion of atherosclerotic plaque formation. For instance, lysoPCs have the capacity to recruit leukocytes to lesions, activate leukocytes to initiate immune responses, and promote foam cell formation[10–12].

The role of lp-PLA2 in the processing of oxLDL, inflammation, and atherogenesis suggests that the inhibition of this

# Both authors contributed equally to this work.
* To whom correspondence should be addressed.
E-mail ypwang@mail.shcnc.ac.cn
Received 2011-04-01 Accepted 2011-05-27

enzyme could play a positive role in the treatment of cardiovascular events. Indeed, earlier studies have reported that a specific lp-PLA2 inhibitor, darapladib, attenuates the inflammatory burden in patients with stable coronary artery disease and prevents necrotic core expansion, a key determinant of plaque rupture[13, 14]. In animal assays, the inhibition of lp-PLA2 by darapladib reduced complex coronary atherosclerotic plaque formation in pigs with induced diabetes and hypercholesterolemia[15].

However, there has been no *in vivo* data about the effects of lp-PLA2 inhibitor on the development of atherosclerosis in mouse models. In our study, we evaluated the specific lp-PLA2 inhibitor, darapladib, in the low density lipoprotein receptor (LDLR)-deficient mice to further confirm its role in the development of atherosclerosis.

## Materials and methods

### Chemicals

Darapladib was synthesized and procured from Prof Jian-hua SHEN's lab at the Shanghai Institute of Materia Medica, Chinese Academy of Sciences, Shanghai 201203, China. TRIzol reagent was purchased from Invitrogen (Carlsbad, CA, USA). PCR-related reagents were purchased from BIO-RAD (Hercules, CA, USA). Other reagents, unless otherwise specified, were obtained from Sigma-Aldrich (St Louis, MO, USA).

### Animals

Male homozygous LDLR-deficient mice (C57/Bl6 genetic background) were obtained from the Jackson Laboratory. The animals were cared for in accordance with the institutional guidelines of the Animal Care and Use Committee of the Shanghai Institute of Materia Medica, Chinese Academy of Sciences.

The mice were fed a high-fat diet consisting of 18% hydrogenated cocoa butter, 0.15% cholesterol, 7% casein, 7% sucrose, and 3% maltodextrin for 17 weeks, beginning at 6 weeks of age. Forty mice were divided into two groups ($n$=20 per group) randomly. One group received darapladib by gavage (50 $mg \cdot kg^{-1} \cdot d^{-1}$) once daily, while the other group received the vehicle (saline). During the 6 weeks of treatment, all mice were housed in a room with a 12-h light/dark cycle and were allowed free access to a high-fat diet and water.

### Serum lipid analysis

Blood samples were obtained from the retro-orbital plexus of the mice prior to drug administration, and 24 h after the last round of drug administration. Serum was obtained through the centrifugation of blood at 1000×$g$ and stored at -80 °C until analysis. Total cholesterol (TC), high-density lipoprotein cholesterol (HDL-C), low-density lipoprotein cholesterol (LDL-C) and triglyceride (TG) levels were measured with an auto-analyzer (Hitachi 7100, Japan) using the corresponding kits from Wako Inc (Enid, OK, USA).

### Measurement of serum Lp-PLA2 activity

Serum lp-PLA2 activity was measured using 2-thio-PAF as the substrate. Briefly, 10 μL of plasma was added to 0.1 mol/L Tris-HCl (pH 7.2) containing 1 mmol/L EGTA, 50 μmol/L 2-thio-PAF and 10 μL of 2 mmol/L 5,5′-dithiobis (2-nitrobenzoic acid) in a total volume of 200 μL. The assay was performed using a plate reader to obtain absorbance values at 414 nm every minute. The lp-PLA2 activity was calculated from the change in absorbance per minute.

### Measurement of serum interleukin-6 (IL-6), high-sensitivity C-reactive protein (hs-CRP), and platelet activating factor (PAF)

Serum IL-6, hs-CRP, and PAF levels were determined by corresponding ELISA kits (Mingrui Biotech Inc, Shanghai, China).

### Morphology of atherosclerotic plaques

At the end of the 6-week treatment period, the mice were anesthetized and killed. Several mice were perfusion-fixed with 4.5% formaldehyde. The aortas were dissected, from the heart to approximately 3 mm distal to the iliac bifurcation. The aortas were then preserved in fresh paraformaldehyde solution for 2 weeks and Sudan IV staining was employed to analyze plaque formation along the entire length of the aortas. Briefly, the aortas were opened longitudinally and pinned upon on a black silica gel plate after removing the surrounding adventitial fatty tissue. The aorta was rinsed in 70% ethanol after 12 h of fixation in the paraformaldehyde solution, stained with 1% Sudan IV in 50% acetone/35% ethanol for approximately 10 min, and washed in 80% ethanol for 5 min. Finally, the stained aortas were photographed and analyzed using the Image Pro-Plus 6.0 software.

### Quantitative RT-PCR

After 6 weeks of treatment, the total RNA was extracted from the aortic arch and the thoracic-abdominal aortas of the two groups of mice using TRIzol reagent (Invitrogen Inc, Carlsbad, CA, USA). First-strand cDNAs were synthesized from 4 μg of total RNA using M-MLV reverse transcriptase (Promega Inc). Quantitative real-time PCR was performed using SYBR Green I as the detector dye. Relative gene expression was calculated by normalizing to the amount of mouse actin gene. The primer sequences are shown in Table 1.

### Statistical analysis

Data are presented as mean values±SD. For serum lipid and lp-PLA2 activity, comparisons were made using the one-way analysis of variance (ANOVA), followed by the *post-hoc* Dunnett test for significance. Comparisons of body weight, plaque area and gene expression were analyzed by a two-tailed Student's $t$-test. For all tests, $P<0.05$ was considered statistically significant.

## Results

### Darapladib inhibits serum lp-PLA2 activity *in vivo*

Our previous unpublished research has shown that mouse lp-PLA2 is less sensitive to darapladib than human lp-PLA2. In this study, then, we tested the dosage range of darapladib to establish the dose at which lp-PLA2 in mouse serum would be

**Table 1.** Primer sequences for quantitative real-time PCR.

| Gene | Forward (5'–3') | Reverse (5'–3') | Genebank ID |
|---|---|---|---|
| Lp-PLA2 | GAGCGTCTTCGTGCGTTTG | GCGGGTATTTTTCTCCAGTC | NM_013737 |
| MCP-1 | CCTGCTGTTCACAGTTGCC | TGTCTGGACCCATTCCTTCT | NM_011333 |
| ICAM-1 | GCTGTATGGTCCTCGGCTG | GCCCACAATGACCAGCAGTA | NM_010494 |
| VCAM-1 | TGAACCCAAACAGAGGCAGA | CGGAATCGTCCCTTTTTGTAG | NM_011693 |
| β-Actin | GGGAAATCGTGCGTGACA | CAAGAAGGAAGGCTGGAAAA | NM_007393 |

MCP-1, monocyte chemotactic protein-1; ICAM-1, Inter-Cellular Adhesion Molecule 1; VCAM-1, vascular cell adhesion molecule-1.

significantly inhibited. As shown in Figure 1, the activity of serum lp-PLA2 was inhibited by more than 60% in LDLR-deficient mice after oral administration of 50 mg/kg once daily of darapladib for 6 weeks.

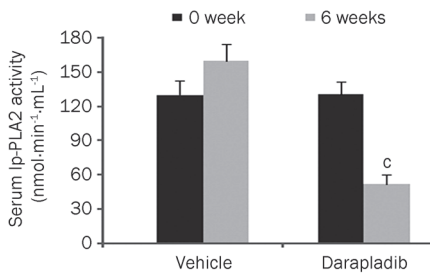


**Figure 1.** Darapladib significantly inhibits serum lp-PLA2 activity in LDLR-deficient mice. Serum lp-PLA2 activity was measured using spectrometry before and at the end of drug administration. $^{c}P<0.01$ *vs* vehicle at 6 weeks.

### Inhibition of lp-PLA2 by darapladib has no significant effects on serum lipid profile

Lipid level and body weight were evaluated in both groups. As expected, there was no significant difference in TC, TG, LDL-C, and HDL-C levels between the two groups (Table 2). Additionally, there was no significant difference in the body weight of LDLR-deficient mice in either group (Table 2).

### Inhibition of lp-PLA2 attenuates the inflammatory burden in serum

To evaluate the effects of lp-PLA2 inhibition on the inflammatory burden *in vivo*, we examined two typical inflammatory markers in the serum of LDLR-deficient mice by ELISA — hs-CRP and IL-6. As shown in Figure 2A and 2B, both hs-CRP and IL-6 were significantly reduced in the darapladib group as compared with those in the vehicle group. To determine whether inhibition of lp-PLA2 affects levels of PAF, we also examined the serum PAF. As shown in Figure 2C, plasma PAF levels between the two groups were similar.

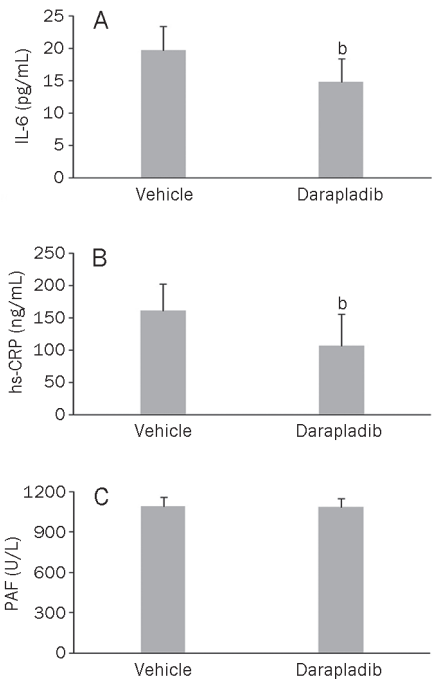


**Figure 2.** Inhibition of lp-PLA2 by darapladib decreases serum hs-CRP and IL-6 levels, but has no significant effects on the PAF level. After 6 weeks of treatment, serum hs-CRP, IL-6 and PAF levels were determined using ELISA. $^{b}P<0.05$ *vs* vehicle.

**Table 2.** Effects of inhibition of lp-PLA2 by darapladib on body weight (g), serum total cholesterol, triglyceride, HDL-C and LDL-C levels (mmol/L) in LDLR-deficient mice.

| | Body weight | Total cholesterol | Triglyceride | HDL cholesterol | LDL cholesterol |
|---|---|---|---|---|---|
| Vehicle | 41.4±4.6 | 34.70±9.24 | 4.23±1.20 | 7.04±1.22 | 30.98±5.78 |
| Darapladib | 39.5±4.7 | 35.76±7.55 | 4.36±0.48 | 6.92±0.47 | 32.00±3.44 |

### Inhibition of lp-PLA2 decreases the formation of atherosclerotic lesions

To determine the effects of the lp-PLA2 inhibitor on the development of atherosclerotic lesions in the aortic vessels of both groups of mice, we analyzed the plaque size at the proximal aorta by Sudan IV staining. As shown in Figure 3, the plaque content in the darapladib group, expressed as the occupancy of aortic luminal surface by atherosclerotic lesions, had significantly decreased compared with the plaque content in the vehicle group.

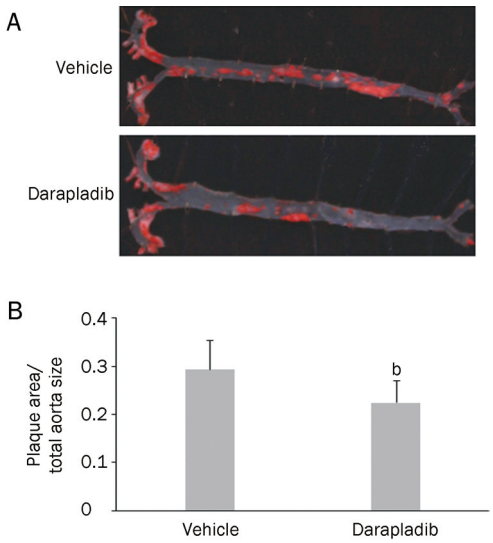


**Figure 3.** Inhibition of lp-PLA2 decreases the atherosclerotic area. (A) Representative en face atherosclerotic aorta preparations stained with Sudan IV. (B) Comparison of plaque sizes between the vehicle and darapladib groups ($n$=8 per group). $^{b}P$<0.05 *vs* vehicle.

### Inhibition of lp-PLA2 attenuates some inflammatory gene expression at plaque lesions

We additionally examined lp-PLA2, as well as the expression of several inflammatory genes in the aortic vessels, by quantitative real-time PCR. Interestingly, there was no significant difference in the expression of lp-PLA2 between the two groups (Figure 4). However, the levels of expression from the MCP-1 and the VCAM-1 genes were remarkably reduced in the darapladib group as compared to the vehicle group (Figure 4). Surprisingly, the expression of another inflammatory gene that we analyzed, ICAM-1, was comparable in the two groups (Figure 4).

## Discussion

Atherosclerosis is the most common cause of many cardiovascular diseases, such as myocardial infarction and stroke[16]. It is widely recognized that the development of atherosclerosis is associated with both the metabolism of lipids and inflammation[17]. In our study, we examined the effects of a specific lp-PLA2 inhibitor, darapladib, on inflammation and atherogenesis in well-established LDLR-deficient mice. We found that the inhibition of lp-PLA2 does not change lipid profiles. Instead, the inhibition of lp-PLA2 attenuates the *in vivo* inflammatory burden and decreases atherosclerotic plaque formation in LDLR-deficient mice.

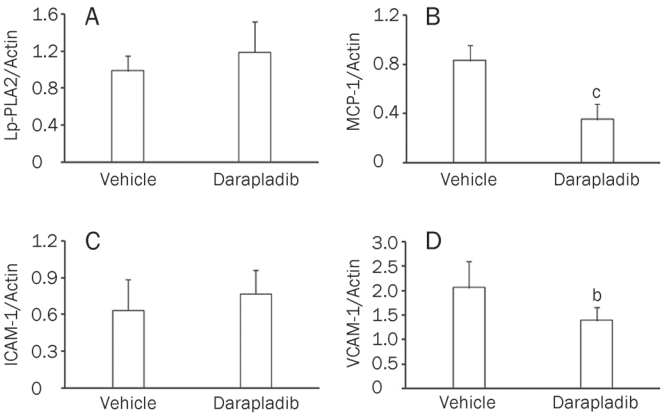


**Figure 4.** Inhibition of lp-PLA2 attenuates some inflammatory gene expression at the aortic arch and thoracic-abdominal aortas. Lp-PLA2, MCP-1, ICAM-1, and VCAM-1 gene expressions were determined using quantitative RT-PCR. $n$=5 per group. $^{b}P$<0.05, $^{c}P$<0.01 *vs* vehicle.

Specific gene-knockout mouse models are extensively used to study the pathological processes and pharmacological interventions of atherosclerosis, among which the model of the LDLR-deficient mouse is well established[18]. As the uptake of lipoprotein particles is impaired, the blood lipid profiles of these mice spontaneously rise. The high-fat diet leads to increased cholesterol, as well as atherosclerotic plaque formation[19]. As predicted, however, the treatment of these mice with the lp-PLA2 inhibitor did not alter their plasma lipoprotein profiles. The beneficial effects of the lp-PLA2 inhibitor, then, are not dependent upon the alteration of lipoprotein levels. The inhibition of lp-PLA2 has shown no marked influence on plasma lipoprotein profiles in pigs with induced diabetes and hypercholesterolemia (DM-HC) or in cardiovascular patients[13, 15, 20]. These findings are consistent with the results from our study. Interestingly, the elevation of *in vivo* lp-PLA2 activity by adenovirus-mediated gene transfer also does not alter the plasma lipoprotein profile[21].

Many epidemiological studies have suggested that lp-PLA2 is a marker for cardiovascular risk, and that the plasma levels and activity of lp-PLA2 increase during the development of atherosclerosis[22–30]. In our study, we also found that serum lp-PLA2 activity increased in the vehicle group after the mice were fed a high-fat diet for 6 weeks; such activity was significantly inhibited in the darapladib group.

Lp-PLA2 is thought to play an important regulatory role in the development of atherosclerosis due to the role of its enzyme activity in hydrolyzing bioactive lipids, such as PAF and oxidized phosphocholines (oxPCs). However, what researchers believe concerning the precise role of lp-PLA2 remains controversial. Lp-PLA2 may hydrolyze and inactivate

PAF, a well-known and typical pro-inflammatory factor that contributes to tissue damage and thrombosis formation[31]. On the other hand, lp-PLA2 may generate pro-inflammatory lipid mediators, such as oxNEFAs and lysoPCs, by hydrolyzing oxidized phospholipids in oxLDL. However, there is no evidence that lp-PLA2 hydrolyzes PAF *in vivo*. In our study, the inhibition of lp-PLA2 by darapladib did not change serum PAF levels. In addition, intravenous administration of recombinant lp-PLA2 failed to alter the PAF-mediated responses in patients with asthma or septic shock[32, 33]. Furthermore, a recent report suggested that circulating PAF is primarily cleared by transport and not by the hydrolysis of lp-PLA2 *in vivo*[34].

Conversely, there has been much *in vitro* or *in vivo* research that supports the concept of the pro-atherogenic roles of lp-PLA2. By hydrolyzing the oxidized phospholipids in oxLDL, lp-PLA2 produces two kinds of inflammatory mediators, lysoPCs and oxNEFA. These mediators initiate a high level of inflammatory response, such as cell adhesion, inflammatory gene expression, and cell death[10, 35]. In addition, *in vivo* studies have suggested that the inhibition of lp-PLA2 by darapladib decreases the inflammatory burden in humans and pigs[13–15]. In our study, we also examined the inflammatory factors in the serum and in the gene expression of some inflammatory cytokines in atherosclerotic lesions. Consistent with other *in vivo* studies, our research shows that the inflammatory burden decreased in the darapladib group compared with that in the vehicle group. Interestingly, previous research, along with our study, has suggested that the inhibition of lp-PLA2 did not affect lp-PLA2 expression. Theoretically, the inhibition of lp-PLA2 may increase lp-PLA2 expression at the vessels as with the oxPCs, which can up-regulate lp-PLA2 expression[8]. Thus, the expression of lp-PLA2 at atherosclerotic plaques needs further study. MCP-1, VCAM-1, and ICAM-1 are typical inflammatory cytokines mediating cell adhesion, a crucial step for monocyte migration into lesions[7]. LysoPCs, the product of lp-PAL2, can up-regulate MCP-1 and ICAM-1/VCAM-1 expression in the endothelial cells or vascular smooth muscle cells (VSMCs)[36]. Surprisingly, in our study, we detected the reduction of MCP-1 and VCAM-1, but not ICAM-1, expression. Regardless, our research, and the previous research of others, supports the pro-atherogenic roles of lp-PLA2 *in vivo*.

Indeed, the lp-PLA2 inhibitor has been evaluated in induced diabetes and hypercholesterolemia (DM-HC) in pigs[15]. Treatment with darapladib resulted in a considerable decrease in plaque area and a markedly reduced necrotic core area. Clinical research has also shown that the inhibition of lp-PLA2 with darapladib has arrested the expansion of the necrotic core, a key determinant of plaque vulnerability, despite not preventing plaque formation[13].

In summary, these *in vivo* studies demonstrate that the inhibition of lp-PLA2 by darapladib does not ameliorate dyslipidemia; instead, darapladib attenuates the inflammatory burden, resulting in the prevention of atherosclerosis in LDLR-deficient mice on a high-fat diet. Our study once again highlights that anti-inflammation therapy is a feasible strategy for the treatment of cardiovascular disease and lp-PLA2 is a promising target against atherosclerosis.

## Acknowledgements

This study was financially supported by a grant from the Shanghai Committee of Science and Technology, China (No 11ZR1444800), and the National Basic Research Program of China (No 2009CB930300).

## Author contribution

Yi-ping WANG and Wen-yi WANG designed the research project; Yi-ping WANG supervised the project; Jie ZHANG, Miao-miao HU performed the animal assays; Wen-yu WU, Yan-ling MA, and Wei-hai CHEN performed the *in vitro* assays; Jie ZHANG, Miao-miao HU, and Wen-yi WANG analyzed the data and wrote the manuscript; Jie ZHANG, Miao-miao HU, and Yi-ping WANG revised the manuscript.

## References

1 Burke JE, Dennis EA. Phospholipase A2 biochemistry. Cardiovasc Drugs Ther 2009; 23: 49–59.
2 Prescott SM, Zimmerman GA, Stafforini DM, McIntyre TM. Platelet-activating factor and related lipid mediators. Annu Rev Biochem 2000; 69: 419–45.
3 Stafforini DM. Biology of platelet activating factor acetyhydrolase (PAF-AH, lipoprotein associated phospholipase A2). Cardiovasc Drugs Ther 2009; 23: 73–83.
4 Kasperska-Zajac A, Brzoza Z, Rogala B. Platelet-activating factor (PAF): a review of its role in asthma and clinical efficacy of PAF antagonists in the disease therapy. Recent Pat Inflamm Allergy Drug Discov 2008; 2: 72–6.
5 Miller RG, Costacou T, Orchard TJ. Lipoprotein-associated phospholipase A2, C-reactive protein, and coronary artery disease in individuals with type 1 diabetes and macroalbuminuria. Diab Vasc Dis Res 2010; 7: 47–55.
6 Wegner M, Araszkiewicz A, Piorunska-Mikolajczak A, Zozulinska-Ziolkiewicz D, Wierusz-Wysocka B, Piorunska-Stolzmann M. The evaluation of IL-12 concentration, PAF-AH, and PLA(2) activity in patients with type 1 diabetes treated with intensive insulin therapy. Clin Biochem 2009; 42: 1621–7.
7 Zalewski A, Macphee C. Role of lipoprotein-associated phospholipase A2 in atherosclerosis: biology, epidemiology, and possible therapeutic target. Arterioscler Thromb Vasc Biol 2005; 25: 923–31.
8 Wang WY, Li J, Yang D, Xu W, Zha RP, Wang YP. OxLDL stimulates lipoprotein-associated phospholipase A2 expression in THP-1 monocytes via PI3K and p38 MAPK pathways. Cardiovasc Res 2010; 85: 845–52.
9 MacPhee CH, Moores KE, Boyd HF, Dhanak D, Ife RJ, Leach CA, *et al*. Lipoprotein-associated phospholipase A2, platelet-activating factor acetylhydrolase, generates two bioactive products during the oxidation of low-density lipoprotein: use of a novel inhibitor. Biochem J 1999; 338: 479–87.
10 Leitinger N. Oxidized phospholipids as modulators of inflammation in atherosclerosis. Curr Opin Lipidol 2003; 14: 421–30.
11 Tselepis AD, John Chapman M. Inflammation, bioactive lipids and atherosclerosis: potential roles of a lipoprotein-associated phospholipase A2, platelet activating factor-acetylhydrolase. Atheroscler Suppl 2002; 3: 57–68.
12 Rong JX, Berman JW, Taubman MB, Fisher EA. Lysophosphatidylcho-

line stimulates monocyte chemoattractant protein-1 gene expression in rat aortic smooth muscle cells. Arterioscler Thromb Vasc Biol 2002; 22: 1617–23.

13 Serruys PW, Garcia-Garcia HM, Buszman P, Erne P, Verheye S, Aschermann M, *et al*. Effects of the direct lipoprotein-associated phospholipase A(2) inhibitor darapladib on human coronary atherosclerotic plaque. Circulation 2008; 118: 1172–82.

14 Mohler ER 3rd, Ballantyne CM, Davidson MH, Hanefeld M, Ruilope LM, Johnson JL, *et al*. The effect of darapladib on plasma lipoprotein-associated phospholipase A2 activity and cardiovascular biomarkers in patients with stable coronary heart disease or coronary heart disease risk equivalent: the results of a multicenter, randomized, double-blind, placebo-controlled study. J Am Coll Cardiol 2008; 51: 1632–41.

15 Wilensky RL, Shi Y, Mohler ER 3rd, Hamamdzic D, Burgert ME, Li J, *et al*. Inhibition of lipoprotein-associated phospholipase A2 reduces complex coronary atherosclerotic plaque development. Nat Med 2008; 14: 1059–66.

16 Pinon P, Kaski JC. Inflammation, atherosclerosis and cardiovascular disease risk: PAPP-A, Lp-PLA2, and cystatin C. New insights or redundant information? Rev Esp Cardiol 2006; 59: 247–58.

17 Steinberg D. Atherogenesis in perspective: hypercholesterolemia and inflammation as partners in crime. Nat Med 2002; 8: 1211–7.

18 Zadelaar S, Kleemann R, Verschuren L, de Vries-Van der Weij J, van der Hoorn J, Princen HM, *et al*. Mouse models for atherosclerosis and pharmaceutical modifiers. Arterioscler Thromb Vasc Biol 2007; 27: 1706–21.

19 Ishibashi S, Brown MS, Goldstein JL, Gerard RD, Hammer RE, Herz J. Hypercholesterolemia in low density lipoprotein receptor knockout mice and its reversal by adenovirus-mediated gene delivery. J Clin Invest 1993; 92: 883–93.

20 Rosenson RS. Fenofibrate reduces lipoprotein associated phospholipase A2 mass and oxidative lipids in hypertriglyceridemic subjects with the metabolic syndrome. Am Heart J 2008; 155: 499.e9–16.

21 Quarck R, De Geest B, Stengel D, Mertens A, Lox M, Theilmeier G, *et al*. Adenovirus-mediated gene transfer of human platelet-activating factor-acetylhydrolase prevents injury-induced neointima formation and reduces spontaneous atherosclerosis in apolipoprotein E-deficient mice. Circulation 2001; 103: 2495–500.

22 Packard CJ, O'Reilly DS, Caslake MJ, McMahon AD, Ford I, Cooney J, *et al*. Lipoprotein-associated phospholipase A2 as an independent predictor of coronary heart disease. West of Scotland Coronary Prevention Study Group. N Engl J Med 2000; 343: 1148–55.

23 Koenig W, Khuseyinova N, Lowel H, Trischler G, Meisinger C. Lipoprotein-associated phospholipase A2 adds to risk prediction of incident coronary events by C-reactive protein in apparently healthy middle-aged men from the general population: results from the 14-year follow-up of a large cohort from southern Germany. Circulation 2004; 110: 1903–8.

24 Ballantyne CM, Hoogeveen RC, Bang H, Coresh J, Folsom AR, Heiss G, *et al*. Lipoprotein-associated phospholipase A2, high-sensitivity C-reactive protein, and risk for incident coronary heart disease in middle-aged men and women in the Atherosclerosis Risk in Communities (ARIC) study. Circulation 2004; 109: 837–42.

25 Persson M, Hedblad B, Nelson JJ, Berglund G. Elevated Lp-PLA2 levels add prognostic information to the metabolic syndrome on incidence of cardiovascular events among middle-aged nondiabetic subjects. Arterioscler Thromb Vasc Biol 2007; 27: 1411–6.

26 May HT, Horne BD, Anderson JL, Wolfert RL, Muhlestein JB, Renlund DG, *et al*. Lipoprotein-associated phospholipase A2 independently predicts the angiographic diagnosis of coronary artery disease and coronary death. Am Heart J 2006; 152: 997–1003.

27 Koenig W, Twardella D, Brenner H, Rothenbacher D. Lipoprotein-associated phospholipase A2 predicts future cardiovascular events in patients with coronary heart disease independently of traditional risk factors, markers of inflammation, renal function, and hemodynamic stress. Arterioscler Thromb Vasc Biol 2006; 26: 1586–93.

28 Gerber Y, McConnell JP, Jaffe AS, Weston SA, Killian JM, Roger VL. Lipoprotein-associated phospholipase A2 and prognosis after myocardial infarction in the community. Arterioscler Thromb Vasc Biol 2006; 26: 2517–22.

29 Caslake MJ, Packard CJ. Lipoprotein-associated phospholipase A2 as a biomarker for coronary disease and stroke. Nat Clin Pract Cardiovasc Med 2005; 2: 529–35.

30 Brilakis ES, McConnell JP, Lennon RJ, Elesber AA, Meyer JG, Berger PB. Association of lipoprotein-associated phospholipase A2 levels with coronary artery disease risk factors, angiographic coronary artery disease, and major adverse events at follow-up. Eur Heart J 2005; 26: 137–44.

31 Zalewski A, Macphee C, Nelson JJ. Lipoprotein-associated phospholipase A2: a potential therapeutic target for atherosclerosis. Curr Drug Targets Cardiovasc Haematol Disord 2005; 5: 527–32.

32 Henig NR, Aitken ML, Liu MC, Yu AS, Henderson WR Jr. Effect of recombinant human platelet-activating factor-acetylhydrolase on allergen-induced asthmatic responses. Am J Respir Crit Care Med 2000; 162: 523–7.

33 Opal S, Laterre PF, Abraham E, Francois B, Wittebole X, Lowry S, *et al*. Recombinant human platelet-activating factor acetylhydrolase for treatment of severe sepsis: results of a phase III, multicenter, randomized, double-blind, placebo-controlled, clinical trial. Crit Care Med 2004; 32: 332–41.

34 Liu J, Chen R, Marathe GK, Febbraio M, Zou W, McIntyre TM. Circulating platelet-activating factor is primarily cleared by transport, not intravascular hydrolysis by lipoprotein-associated phospholipase A2/PAF acetylhydrolase. Circ Res 2011; 108: 469–77.

35 Nonas S, Birukova AA, Fu P, Xing J, Chatchavalvanich S, Bochkov VN, *et al*. Oxidized phospholipids reduce ventilator-induced vascular leak and inflammation *in vivo*. Crit Care 2008; 12: R27.

36 Kume N, Cybulsky MI, Gimbrone MA Jr. Lysophosphatidylcholine, a component of atherogenic lipoproteins, induces mononuclear leukocyte adhesion molecules in cultured human and rabbit arterial endothelial cells. J Clin Invest 1992; 90: 1138–44.

Acta Pharmacologica Sinica (2011) 32: 1259–1265
 1671-4083/11 $32.00
www.nature.com/aps

Original Article

# Combination of fluvastatin and losartan relieves atherosclerosis and macrophage infiltration in atherosclerotic plaques in rabbits

Ya-pei YANG[1, 2, 4, #], Qiu-li DONG[1, 3, 4, #], Xu-hong ZHANG[1], Yue-hui ZHANG[1], Li ZHU[1, 4], Shu-ying LI[1, 4, 5], Zhong-zhi LIU[1], Hui XU[1, 4, 5], Nan WANG[1, 4], Hong JIANG[4], Chun-xi LIU[4], Xian-xi LIU[2, *], Bo DONG[1, 4, 5, *]

*[1]Department of Cardiology, Provincial Hospital Affiliated to Shandong University, Shandong University, Ji-nan 250021, China; [2]Institute of Biochemistry and Molecular Biology, School of Medicine, Shandong University, Ji-nan 250012, China; [3]Department of Cardiology, General Hospital of Huabei Petroleum Company, Renqiu 062552, China; [4]The Key Laboratory of Cardiovascular Remodeling and Function Research, Chinese Ministry of Education and Chinese Ministry of Health, Shandong University Qilu Hospital, Ji-nan 250012, China; [5]Shandong Provincial Key Laboratory of Diagnosis and Treatment of Cardio-cerebral Vascular Disease, Ji-nan 250021, China*

**Aim:** To investigate whether the combination of fluvastatin and losartan synergistically relieve atherosclerosis and plaque inflammation induced by a high-cholesterol diet in rabbits.
**Methods:** Atherosclerosis was induced with a high-cholesterol diet for 3 months in 36 New Zealand white rabbits. The animals were randomly divided into model group, fluvastatin (10 mg·kg$^{-1}$·d$^{-1}$) group, losartan (25 mg·kg$^{-1}$·d$^{-1}$) group, and fluvastatin plus losartan group. After the 16-week treatments, the blood samples the animals were collected, and the thoracic aortas were examined immunohistochemically. The mRNA and protein expression levels of monocyte chemotactic protein-1 (MCP-1) were measured using RT-PCR and Western blot.
**Results:** Compared to the treatment with losartan or fluvastatin alone, the combined treatment did not produce higher efficacy in reduction of blood cholesterol level. However, the combination did synergistically decrease the intimal and media thickness of thoracic aortas with significantly reduced macrophage infiltration and MCP-1 expression in the plaques.
**Conclusion:** The combined treatment with losartan and fluvastatin significantly inhibited atherosclerotic progress and reduced inflammation associated with atherosclerotic plaques.

**Keywords:** losartan; fluvastatin; cholesterol; atherosclerosis; macrophages; monocyte chemotactic protein-1 (MCP-1); inflammation; p38 MAPK; smooth muscle cells

*Acta Pharmacologica Sinica* (2011) 32: 1259–1265; doi: 10.1038/aps.2011.95; published online 12 Sep 2011

## Introduction

A growing body of evidence has suggested that blood lipid metabolism disorders and angiotensin II (Ang II) have synergistic effects on the occurrence of atherosclerosis, and the combination of dyslipidemia and the activation of the renin–angiotensin system (RAS) plays an important role in the pathogenesis of atherogenesis[1]. Oxidized low-density lipoprotein (ox-LDL) can upregulate the expression of the angiotensin II type 1 receptor (AT1R) on the surface of endothelial cells and macrophages[2–4]. Ang II facilitates LDL oxidization and uptake by endothelial cells, smooth muscle cells and macrophages[5].

Angiotensin II also increases the oxidative stress response, which leads to the production of reactive oxygen species (ROS) and the aggravation of atherosclerosis. It is common to use a combination of a statin and an angiotensin II type 1 receptor blocker (ARB) to treat hypertensive patients with lipid metabolism disorders. However, few studies have been reported in regards to the underlying molecular mechanisms. Recent studies have shown that the combination of an HMG-CoA (3-hydroxy-3-methylglutaryl-coenzyme A) reductase inhibitor and an ARB has a better effect on relieving the severity of atherosclerosis and down-regulating the expression of lectin-like oxidized low density lipoprotein receptor-1 (LOX-1) than the use of a single drug[6]. Our previous study showed that angiotensin II plays an important role in the pathogenesis

# The first two authors contributed equally to this work.
* To whom correspondence should be addressed.
E-mail dongbo1@medmail.com.cn (Bo DONG);
xianxi@sdu.edu.cn (Xian-xi LIU)
Received 2011-06-08 Accepted 2011-06-27

of atherosclerosis[7, 8]. In addition, Han *et al* and Koh *et al* also demonstrated that the combination of simvastatin and losartan has vascular protective effects[9, 10]. These studies indicated that the combination of simvastatin and losartan may play an important role in preventing the progression of coronary heart disease. However, little is known about the exact role of the combination of statins and ARBs in the formation of atherosclerotic plaques and its effect on the inflammation of plaques. With these considerations in mind, our present study was designed to develop an atherosclerosis model by feeding rabbits with high-fat food and to investigate the effects and mechanisms of the combinational use of fluvastatin and losartan on the development of atherosclerosis and inflammation within the atherosclerotic plaques.

## Materials and methods

### Atherosclerosis model

New Zealand white rabbits (weight: 1.5–1.63 kg) were provided by the Institute of Animal Science and Veterinary Medicine, Shandong Academy of Agriculture Sciences (Shandong, China). The rabbits ($n$=36) were provided with regular food for 1 week and were subsequently provided with high-cholesterol food (1% cholesterol and 5% pig oil particles) for 3 months to generate the atherosclerosis model. The 36 rabbits were randomly divided into 4 groups. The high-cholesterol group (CH) contained rabbits ($n$=9) that were provided with high-cholesterol food without other treatments. The fluvastatin group (F) contained rabbits ($n$=9) that were provided with high-cholesterol food and fluvastatin (10 $mg \cdot kg^{-1} \cdot d^{-1}$) (Novartis, Beijing, China). The losartan group (L) contained rabbits ($n$=9) that were provided with high-cholesterol food and losartan (25 $mg \cdot kg^{-1} \cdot d^{-1}$) (Merck Sharp & Dohme, Hangzhou, China). The fluvastatin and losartan combination group (F+L) contained rabbits ($n$=9) that were provided with high-cholesterol food and treated with a combination of fluvastatin (10 $mg \cdot kg^{-1} \cdot d^{-1}$) and losartan (25 $mg \cdot kg^{-1} \cdot d^{-1}$). Both drugs were administered in the food[11–13]. An additional 8 rabbits were provided with regular food to act as a negative control group for comparison with the occurrence of atherosclerotic plaques induced by high-cholesterol food.

### Total cholesterol and LDL-cholesterol analysis

Blood samples were drawn from the marginal ear vein after the 16-week treatment period. Total cholesterol (TC) and LDL-cholesterol concentrations were evaluated by enzymatic assays (Sigma Diagnostics).

### Pathological examination and immunohistochemistry

The rabbits were anesthetized by an intramuscular injection of ketamine (35 mg/kg)/xylazine (7 mg/kg) and local anesthesia of the inguinal region by lidocaine. The thoracic aorta was separated, and the upper section was stored in liquid nitrogen. The lower sections of the arteries were fixed in 4% formaldehyde and embedded in paraffin. Sections (5 μm) were cut for the analyses of macrophage infiltration, smooth muscle cells (SMCs) and MCP-1 expression. Macrophage infiltration, smooth muscle cells (SMCs) and MCP-1 protein expression were measured by immunohistochemistry. In the macrophage infiltration analysis, the sections were incubated with mouse anti-macrophage antibody (RAM11) (DAKO, USA). The SMCs and MCP-1 protein were incubated with mouse anti-human antibody (Santa Cruz, USA). The first antibody was cultured overnight at 4 °C. After extensive washing, the sections were incubated with biotin-conjugated goat anti-mouse IgG antibody. Visualization of the sections was performed with the SABC staining kit (Santa Cruz, USA). Staining for the macrophages, MCP-1 and SMCs was performed in a similar way. A customized imaging analysis system (Image-Pro Plus 5.0, Media Cybernetics, USA) was used to analyze the immunohistochemical results. The thickness of the intima and media of the thoracic aortas and positive staining in immunohistochemistry were analyzed using the imaging processing software.

### RT-PCR

The total RNA was extracted from the rabbits in each group using the Trizol kit (Invitrogen, Carlsbad, CA). The concentration of RNA was measured by an ultraviolet spectrophotometer. Reverse transcription was performed in a total volume of 20 μL. The total RNA (1.5 μL) was mixed with DEPC water (8 μL) and denatured at 72 °C for 10 min followed by incubation on ice for 5 min. The RNase inhibitor (50 U/L) (0.5 μL), reverse transcriptase (M-MLV 5U/L) (1 μL), $MgCl_2$ (25 mmol/L, 4 μL), dNTP (10 mmol/L, 2 μL), 10×buffer (2 μL) and OligodT (2.5 pmol/L, 1 μL) were added to the denatured RNA samples and incubated at 42 °C for 30 min, 99 °C for 5 min and 5 °C for 5 min. PCR was performed in a total volume of 50 μL containing 1.5 μL of reverse transcription products (cDNA), 0.5 μL of DNA polymerase (5 U/L), 5 μL of 10×buffer, 4 μL of dNTP (2.5 mmol/L), 4 μL $MgCl_2$ (25 mmol/L) and 1 μL of each forward and reverse primers. The sequences of the forward and reverse primers for the amplification of the MCP-1 gene (330 bp) were 5′-TGCTCATTCCATACAGCCTGTG-3′ and 5′-CTTTTCATGCTTAGCGGCG-3′, respectively. The sequences of the forward and reverse primers for the amplification of the GAPDH gene (476 bp) were 5′-GAGCTGAACG-GGAAACTCAC-3 and 5′-GGTCTGGGATGGAAACTGTG-3′, respectively. All of the primers were synthesized by Shanghai Sangon Biological Engineering Technology Co, LTD (Shanghai, China). The parameters for the PCR reaction were 94 °C for 4 min followed by 40 cycles of 94 °C for 30 s, 55 °C for 45 s, 72 °C for 1 min and a final extension of 72 °C for 10 min. The PCR products were electrophoresed on a 1.5% agarose gel. The PCR products of the GAPDH gene were used as an internal control, and the relative expression of the MCP-1 gene was calculated as an *OD* value of the MCP-1 PCR products/GAPDH products.

### Western blot

The aortic tissues were homogenized in a Tris-HCl buffer and centrifuged at 4000 r/min for 10 min at 4 °C. Protein concentrations were determined using a bicinchoninic acid protein

assay. The lysate proteins from the aortas were separated with 10% SDS-PAGE gels and were subsequently transferred onto nitrocellulose membranes. After being blocked with 5% non-fat milk, the membranes were incubated with primary antibodies to mouse p38 MAPK (Cell Signaling Technology) followed by the corresponding horseradish peroxidase-conjugated secondary antibodies. The bands were visualized by an MSF-300G Scanner (Microtek Lab, Nikon, Japan).

### Statistical analysis

Data were analyzed using an ANOVA procedure. A $P<0.05$ was considered statistically significant. Data were presented as the mean±SD. SPSS for Windows Version 10.0 (SPSS Inc, Chicago, IL, USA) was used for the statistical analysis.

## Results

### Blood cholesterol level

After 4 months of high-fat feeding, the administration of fluvastatin alone and the combination of fluvastatin and losartan decreased the total cholesterol and LDL-cholesterol levels ($P<0.01$). The total cholesterol and LDL-cholesterol levels were not significantly different between the losartan group and the high-cholesterol group, indicating that losartan alone had no significant effect on the total cholesterol and LDL-cholesterol levels (Figure 1A, 1B).

### The effects of fluvastatin and losartan on plaque morphology

To further study the inhibitory effects of fluvastatin and losartan on atherosclerosis, we measured the intimal thicknesses, the ratio of intima to media thickness (I/M) and the lipid content after treatment with fluvastatin and losartan. The intimal thickness and the ratios of intima to media thickness (I/M) were lower in the individual fluvastatin and losartan groups than in the high-cholesterol group ($P<0.01$, Figure 1C, 1D, Table 1). The intimal thickness and the ratio of intima to media thickness (I/M) were further decreased by the combination of the two agents ($P<0.01$) [note that the combination of fluvastatin and losartan had a greater atherosclerosis-reducing effect than fluvastatin or losartan alone (Figure 1C, 1D, Table 1)]. The lipid contents were statistically lower in the individual fluvastatin and losartan groups than in the high-cholesterol group ($P<0.01$). Furthermore, the lipid content was markedly lower in the combination group than in the individual fluvastatin and losartan groups ($P<0.01$, Figure 2A, 2B).

**Table 1.** The intimal thickness and the ratio of intima to media thickness (I/M) in the four groups. Mean±SD. $n=9$. $^{c}P<0.01$ *vs* HC group. $^{f}P<0.01$ *vs* fluvastatin group. $^{i}P<0.01$ *vs* losartan group.

| Group | The intimal thickness (μm) | The ratio of intima to media thickness (I/M) |
|---|---|---|
| HC | 536.81±87.04 | 1.37±0.15 |
| F | 281.43±28.47$^{c}$ | 0.80±0.06$^{c}$ |
| L | 316.21±38.31$^{c}$ | 0.87±0.03$^{c}$ |
| F+L | 228.70±22.96$^{fi}$ | 0.66±0.04$^{fi}$ |

### The effect of the combination of fluvastatin and losartan on decreasing macrophages in atherosclerotic plaques

To further study the effect of fluvastatin and losartan on regulating macrophages in atherosclerotic plaques, we performed immunohistochemical analysis and observed macrophage changes after treatment with fluvastatin and losartan. A large number of macrophages were present in the atherosclerotic plaques of the high-cholesterol group compared to the fluvastatin group and the losartan group, which demonstrated a small number of macrophages. This indicated that fluvastatin or losartan alone was able to reduce macrophage infiltration in the atherosclerotic plaques ($P<0.01$, Figure 2C, 3B, Table 2). The macrophages in atherosclerotic plaques were further reduced by the combination of fluvastatin and losartan, which demonstrated that the combinational treatment had a greater macrophage-reduction activity within the atherosclerotic plaques ($P<0.01$, Figure 2C, 3B, Table 2).

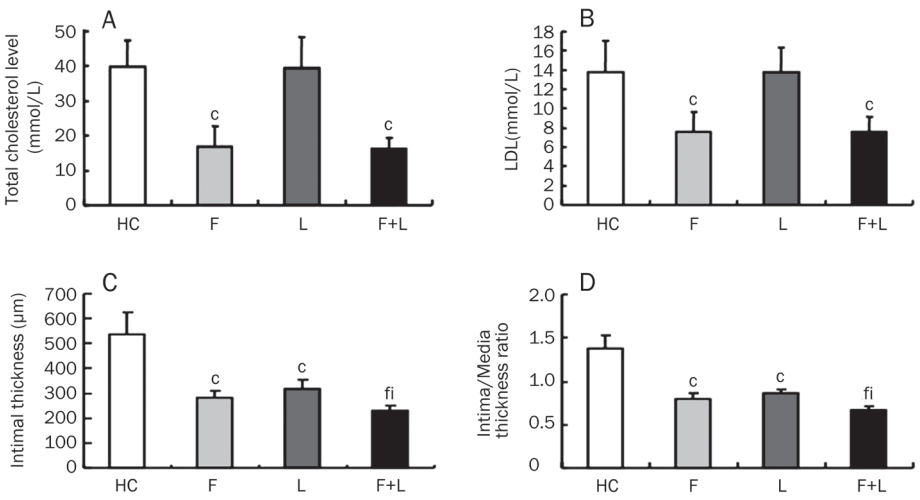


**Figure 1.** The effect of fluvastatin and losartan on plasma lipid levels and the extent of atherosclerosis. (A) The total cholesterol levels. (B) The LDL-cholesterol levels. (C) The intimal thickness in four groups. (D) The ratio of intima to media thickness (I/M) in four groups. $^{c}P<0.01$ *vs* HC-diet group; $^{f}P<0.01$ *vs* fluvastatin group; $^{i}P<0.01$ *vs* losartan group. Mean±SD. $n=9$.

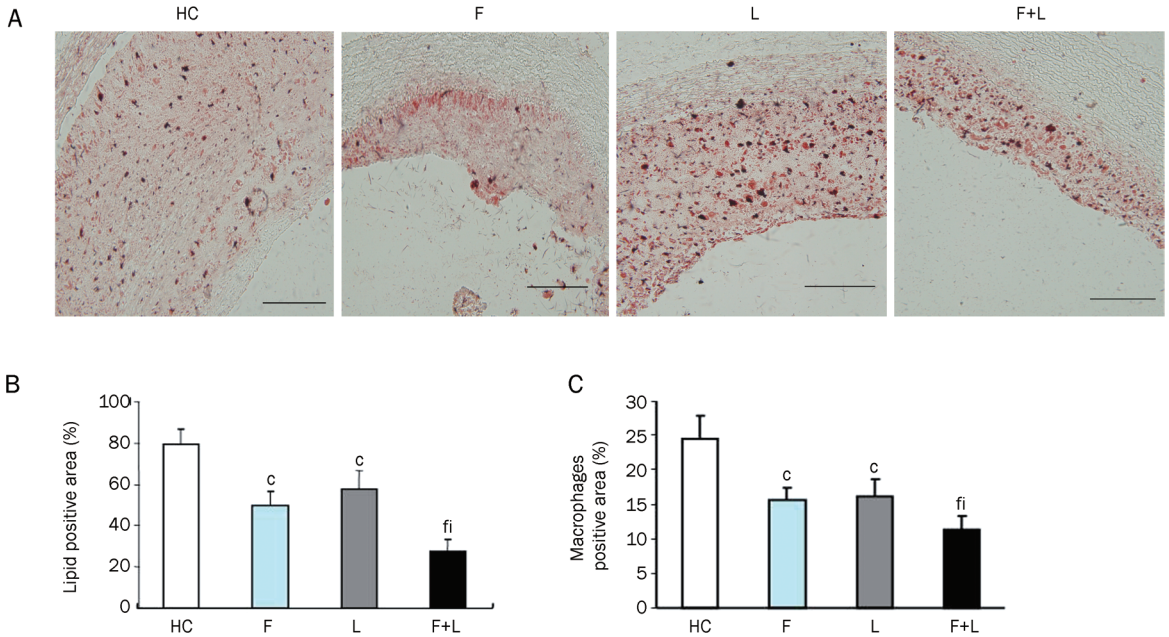


**Figure 2.** Oil Red O staining and macrophages in atherosclerotic plaques. (A) Oil Red O staining in atherosclerotic plaques in the four groups (magnification×10, scale bars equal 200 μm). (B) Quantification of the positive staining area. $^{c}P<0.01$ *vs* HC-diet group; $^{f}P<0.01$ *vs* fluvastatin group; $^{i}P<0.01$ *vs* losartan group. Data are the mean±SD. (C) Quantification of the macrophages that stained positive in the plaques. $^{c}P<0.01$ *vs* HC-diet group; $^{f}P<0.01$ *vs* fluvastatin group; $^{i}P<0.01$ *vs* losartan group. Mean±SD. $n=9$.

**Table 2.** Quantification of the macrophages that stain positive in the plaques. The results are expressed as the mean±SD. $n=9$. $^{c}P<0.01$ *vs* HC group. $^{f}P<0.01$ *vs* fluvastatin group. $^{i}P<0.01$ *vs* losartan group.

| Group | Macrophages positive (%) |
|---|---|
| HC | 24.47±3.44 |
| F | 15.66±1.66$^{c}$ |

### The effect of fluvastatin and losartan on MCP-1 expression in the four groups

To study the role of fluvastatin and losartan in the inhibition of MCP-1 expression, we performed an experiment to determine the expression of MCP-1 at both the protein and mRNA levels. The MCP-1 protein expression level was reduced by fluvastatin and losartan alone as compared to an HC-diet group ($P<0.01$). The expression of the MCP-1 protein was fur-

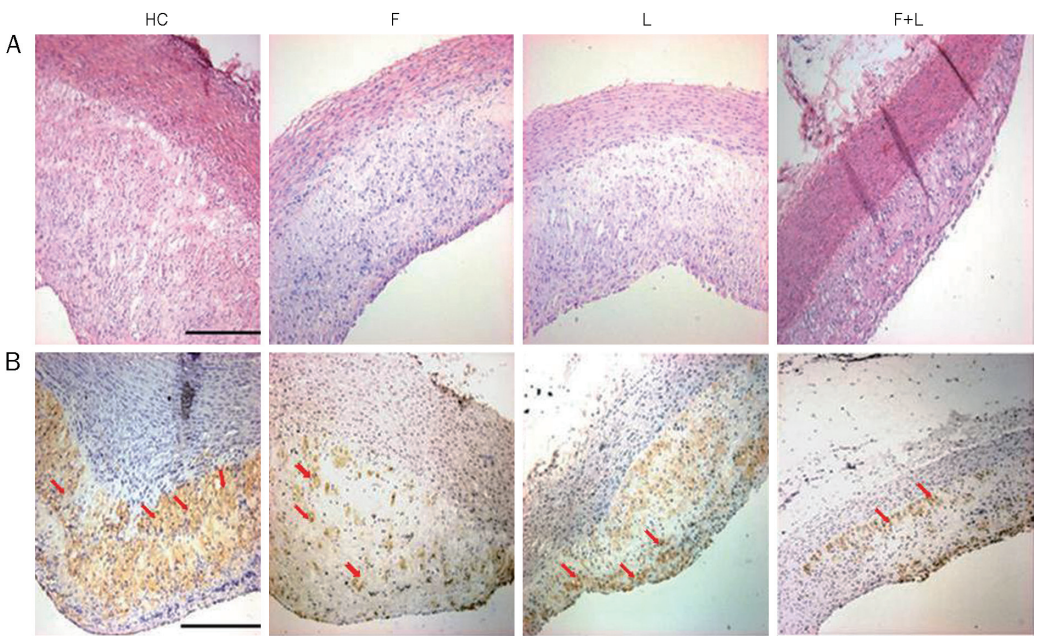


**Figure 3.** HE staining and morphological analysis in plaques in the four groups. (A) HE staining in the HC-diet group (HC), fluvastatin group (F), losartan group (L), fluvastatin and losartan group (F+L). (magnification×10, scale bars equal 200 μm). (B) Macrophage expression in the HC-diet group (HC), fluvastatin group (F), losartan group (L), fluvastatin and losartan group (F+L) in plaques by immunohistochemical staining. (magnification×10, scale bars equal 200 μm).

ther reduced by the combinational treatment with fluvastatin and losartan ($P$<0.05), which indicated that the combination of the two agents had a synergistic inhibitory effect on MCP-1 protein expression (Figure 4A, 4B). A similar inhibitory effect was observed for MCP-1 gene expression (Figure 4C, 4D).

### SMC expression in the four groups

The proliferation and migration of SMCs is one feature of early atherosclerotic lesions. To study the effect of fluvastatin or losartan on the expression of SMCs in atherosclerotic plaques, we observed α-actin-positive vascular smooth muscle cells in atherosclerotic plaques among the four groups. There were no significant differences among the four groups (Figure 5A).

### p38 MAPK protein expression in the four groups

Western blot analysis showed that p38 MAPK protein expression was present in the atherosclerotic plaques of the high-cholesterol group. Both fluvastatin and losartan alone significantly attenuated p38 MAPK expression ($P$<0.05 *vs* the HC-diet group). Furthermore, the combination of fluvastatin and losartan further reduced p38 MAPK protein expression within the plaques compared to either fluvastatin or losartan alone ($P$<0.05 *vs* fluvastatin or losartan alone) (Figure 5B, 5C).

## Discussion

In this study, we explored the effect of fluvastatin or losartan and the combinational treatment with these two drugs on the extent of atherosclerosis and inflammation of atherosclerotic plaques in our constructed animal model[14]. This atherosclerosis model was induced by feeding on a high-cholesterol diet and treating the animals with fluvastatin or losartan or a combination of the two drugs.

We have shown that after treatment of the atherosclerotic rabbits with either fluvastatin or losartan, the severity of atherosclerosis and the number of macrophages in the atherosclerotic plaques decreased. More importantly, treatment of the atherosclerotic rabbits with a combination of fluvastatin and losartan further reduced the severity of atherosclerosis and decreased the number of macrophages and MCP-1 expression compared to the administration of fluvastatin or losartan alone. These results suggested that combinational use of fluvastatin and losartan was more efficient in treating atherosclerosis and inflammation, which ultimately results in the stabilization of the plaques and decreases the occurrence of acute coronary syndrome. Our results are consistent with a previous report[15] in which the combination of pravastatin and captopril further reduced the macrophage-foam cell size and fatty streak area compared to the individual use of either pravastatin or captopril[8]. Previous studies showed that the combination of rosuvastatin and candesartan further reduced the severity of atherosclerosis and the expression of lectin-like ox-LDL receptor-1 (LOX-1), which is a receptor for oxidized low-density lipoprotein, compared to the administration of rosuvastatin or candesartan[16] separately in mice.

A growing body of evidence has indicated that lipid metabolism disorders and angiotensin II have a synergistic effect on the occurrence of atherosclerosis. Hypercholesterolemia can up-regulate the expression of AT1R and angiotensin converting enzyme at both the mRNA and protein levels, which increases production of angiotensin II[17, 18]. Angiotensin II not only enhances the transformation of LDL to ox-LDL by increasing the production of ROS but also has a direct effect on the ox-LDL receptor, LOX-1[19]. Previous studies have demonstrated that angiotensin II increased the expression of LOX-1 in a dose-dependent manner when coronary endothelial cells were incubated with different concentrations of angiotensin II. In addition, an AT1R blocker (losartan) down-regulated the expression of LOX-1 while an AT2R blocker (PD123319) did not inhibit the expression of LOX-1. These results suggest that angiotensin II-induced expression of LOX-1 is mediated by AT1R[20]. Further studies have shown that angiotensin II can activate NF-kappaB, which in turn activates the promoter of the LOX-1 gene and up-regulates the transcription of LOX-1[21]. Chen J *et al* showed that rosuvastatin and candesartan alone had inhibitory effects on LOX-1 expression in the atherosclerotic plaques, whereas a combination had a dramatic inhibitory effect on LOX-1 expression. In addition, the author demonstrated that the combination of a statin and an AT1R blocker inhibited p38 mitogen-activated protein kinase (MAPK) expression, which indicates that the antiatherosclerotic effect of combination therapy may be due to the inhibition of LOX-1 protein expression and p38 MAPK expression[15].

MCP-1 is an important chemokine and plays a critical role in monocyte aggregation. Previous studies showed that statins (*eg*, simvastatin) significantly reduced the MCP-1 level in monocytes *in vitro*[12]. In addition, angiotensin II receptor blockers (*eg*, irbesartan) can also decrease the expression of MCP-1 and relieve the extent of atherosclerotic plaques[22, 23]. However, less synergistic effects on the expression of MCP-1 were observed by the combination of statins and ARB. Our current study further explored the effects of a combination of fluvastatin and losartan on the expression of MCP-1 to identify the potential anti-inflammatory mechanisms. Our results showed that a combination of fluvastatin and losartan further reduced the expression of MCP-1 on both the gene and protein levels compared to individual treatment with either fluvastatin or losartan. Because the aggregation of inflammatory cells is a consequence of multiple factors, decreased expression of MCP-1 might only represent one of the mechanisms by which combinational treatment exerts its additive anti-inflammatory effects.

The activation of p38 MAPK by ox-LDL and angiotensin II in vascular smooth muscle cells has been reported. It was found that the activation of p38 MAPK was involved in the ox-LDL- and angiotensin II-induced up-regulation of MCP-1 in vascular endothelial cells and in hyperlipidemia-induced atherosclerosis. Our study found that while fluvastatin and losartan alone could significantly decrease p38 MAPK expression and phosphorylation, a combination of the two drugs demonstrated a synergistic effect. Our results suggest that decreased p38 MAPK expression and phosphorylation as a result of combinational treatment may play an important role

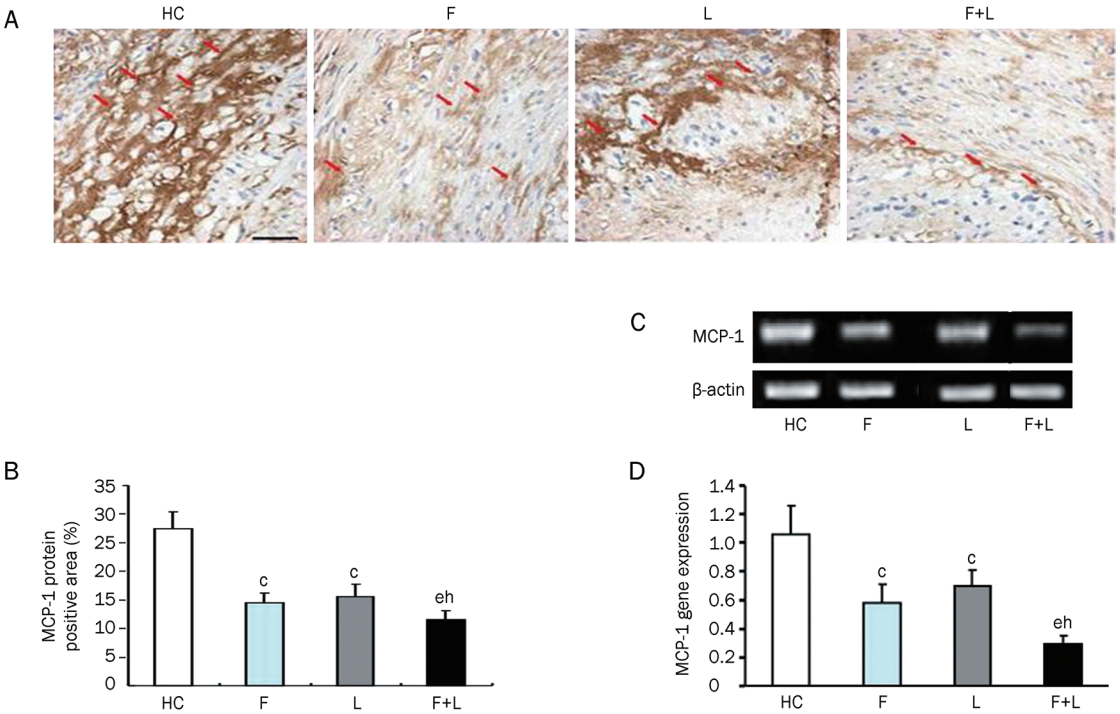


**Figure 4.** MCP-1 protein and gene expression in the four groups. (A) MCP-1 protein expression in the four groups by immunohistochemical staining (magnification×40, scale bars equal 50 μm). (B) Quantification of the MCP-1 protein level by immunohistochemical staining in the four groups. (C) MCP-1 mRNA expression levels by RT-PCR in the four groups. (D) Quantification of MCP-1 mRNA levels by RT-PCR in the four groups. $^{c}P<0.01$ *vs* HC-diet group; $^{e}P<0.05$ *vs* fluvastatin group; $^{h}P<0.05$ *vs* losartan group. Mean±SD. $n=9$.

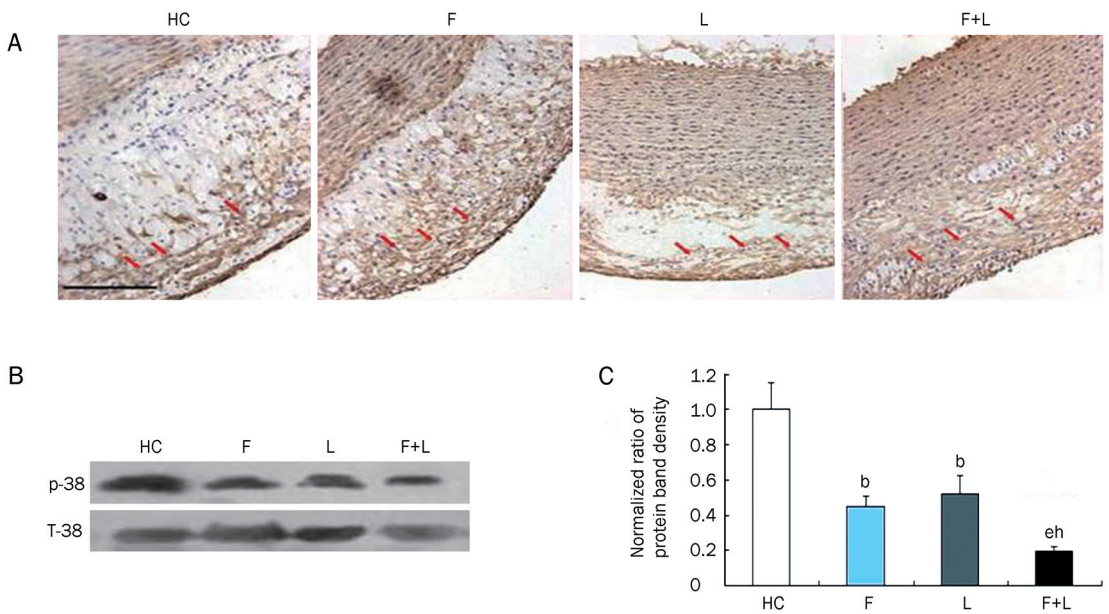


**Figure 5.** Vascular smooth muscle cells (SMCs) and p38 MAPK protein expression in the four groups. (A) SMCs expression in the four groups by immunohistochemical staining (magnification×20, scale bars equal 200 μm). There was no difference among the four groups. (B) p38 MAPK protein expression in the four groups by Western blot. (C) Quantification of p38 MAPK protein level by Western blot in the four groups. $^{b}P<0.05$ *vs* HC-diet group. $^{e}P<0.05$ *vs* fluvastatin group. $^{h}P<0.05$ *vs* losartan group. Mean±SD. $n=9$.

in inhibiting atherosclerosis.

In conclusion, our studies showed that the combination of fluvastatin and losartan further reduced the severity of atherosclerosis compared to the individual use of either fluvastatin or losartan. These results demonstrated that a synergistic anti-inflammatory effect is mediated by the combinational use of fluvastatin and losartan by inhibiting RAS and p38 MAPK expression and phosphorylation. This combination therapy may play an important role in preventing the progression of coronary heart disease.

## Acknowledgements

This work was supported by National Natural Science Foundation of China (No 81170207) and the Program of Introducing Talents of Discipline to Universities (No B07035) and Shandong Natural Science Foundation of China (Nos 03BS37 and Y2006C68). We thank Rong WANG, Yong-huan ZHANG, and Xu-ping WANG for their technical assistance.

## Author contribution

Ya-pei YANG, Qiu-li DONG, Bo DONG, Yue-hui ZHANG, and Li ZHU performed research; Xu-hong ZHANG, Zhong-zhi LIU, Hui XU, Hong JIANG, and Chun-xi LIU participated in drug administration and the construction of atherosclerosis model; Shu-ying LI and Nan WANG contributed analytic tools; Ya-pei YANG, Qiu-li DONG, and Bo DONG analyzed data; and Ya-pei YANG, Qiu-li DONG, Bo DONG, and Xian-xi LIU wrote the paper.

## References

1 Graninger M, Reiter R, Drucker C, Minar E, Jilma B. Angiotensin receptor blockade decreases markers of vascular inflammation. J Cardiovasc Pharmacol 2004; 44: 335–9.
2 Heeba G, Moselhy ME, Hassan M, Khalifa M, Gryglewski R, Malinski T. Anti-atherogenic effect of statins: role of nitric oxide, peroxynitrite and haem oxygenase-1. Br J Pharmacol 2009; 156: 1256–66.
3 Singh BM, Mehta JL. Interactions between the renin-angiotensin system and dyslipidemia. Arch Intern Med 2003; 163: 1296–304.
4 Gómez-Garre D, Muñoz-Pacheco P, González-Rubio ML, Aragoncillo P, Granados R, Fernández-Cruz A. Ezetimibe reduces plaque inflammation in a rabbit model of atherosclerosis and inhibits monocyte migration in addition to its lipid-lowering effect. Br J Pharmacol 2009; 156: 1218–27.
5 Chen HJ, Li DY, Saldeen T, Phillips MI, Mehta JL. Attenuation of tissue P-selectin and MCP-1 expression and intimal proliferation by $AT_1$ receptor blockade in hyperlipidemic rabbits. Biochem Biophys Res Commun 2001; 282: 474–9.
6 Marcu L, Fang Q, Jo JA, Papaioannou T, Dorafshar A, Reil T, *et al*. *In vivo* detection of macrophages in a rabbit atherosclerotic model by time-resolved laser-induced fluorescence spectroscopy. Atherosclerosis 2005; 181: 295–303.
7 Dong B, Zhang C, Feng JB, Zhao YX, Li SY, Yang YP, *et al*. Overexpression of ACE2 enhances plaque stability in a rabbit model of atherosclerosis. Arterioscler Thromb Vasc Biol 2008; 28: 1270–6.
8 Zhang C, Zhao YX, Zhang YH, Zhu L, Deng BP, Zhou ZL, *et al*. Angiotensin-converting enzyme 2 attenuates atherosclerotic lesions by targeting vascular cells. Proc Natl Acad Sci U S A 2010; 107: 15886–91.
9 Han SH, Koh KK, Quon MJ, Lee Y, Shin EK. The effects of simvastatin, losartan, and combined therapy on soluble CD40 ligand in hypercholesterolemic, hypertensive patients. Atherosclerosis 2007; 190: 205–11.
10 Koh KK, Quon MJ, Han SH, Chung WJ, Ahn JY, Seo YH, *et al*. Additive beneficial effects of losartan combined with simvastatin in the treatment of hypercholesterolemic, hypertensive patients. Circulation 2004; 110: 3687–92.
11 Kim Y, Park K, Kang W. Effect of fluvastatin, lovastatin, nifedipine and verapamil on the systemic exposure of nateglinide in rabbits. Biopharm Drug Dispos 2010; 31: 443–9.
12 Hu MY, Li YL, Jiang CH, Liu ZQ, Qu SL, Huang YM. Comparison of lycopene and fluvastatin effects on atherosclerosis induced by a high–fat diet in rabbits. Nutrition 2008; 24: 1030–8.
13 Ruan LM, Cai W, Chen JZ, Duan JF. Effects of losartan on expression of connexins at the early stage of atherosclerosis in rabbits. Int J Med Sci 2010; 7: 82–9.
14 Boban PT, Nambisan B, Sudhakaran PR. Dietary mucilage promotes regression of atheromatous lesions in hypercholesterolemic rabbits. Phytother Res 2009; 23: 725–30.
15 Chen J, Li D, Schaefer R, Mehta JL. Cross–talk between dyslipidemia and renin-angiotensin system and the role of LOX-1 and MAPK in atherogenesis studies with the combined use of rosuvastatin and candesartan. Atherosclerosis 2006; 184: 295–301.
16 Zhong L, Chen WQ, Ji XP, Zhang M, Zhao YX, Yao GH, *et al*. Dominant-negative mutation of monocyte chemoattractant protein-1 prevents vulnerable plaques from rupture in rabbits independent of serum lipid levels. J Cell Mol Med 2008; 12: 2362–71.
17 Sun YP, Zhu BQ, Browne AE, Pulukurthy S, Chou TM, Sudhir K, *et al*. Comparative effects of ACE inhibitors and an angiotensin receptor blocker on atherosclerosis and vascular function. J Cardiovasc Pharmacol Ther 2001; 6: 175–81.
18 Chatzizisis YS, Jonas M, Beigel R, Coskun AU, Baker AB, Stone BV, *et al*. Attenuation of inflammation and expansive remodeling by valsartan alone or in combination with simvastatin in high–risk coronary atherosclerotic plaques. Atherosclerosis 2009; 203: 387–94.
19 Ge J, Huang D, Liang C, Luo Y, Jia Q, Wang K. Upregulation of lectin-like oxidized low-density lipoprotein receptor-1 expression contributes to the vein graft atherosclerosis: modulation by losartan. Atherosclerosis 2004; 177: 263–8.
20 Xu HX, Li JJ, Li GS, Wang J, Li NX, Peng J. Decreased infiltration of macrophages and inhibited activation of nuclear factor-kappa B in blood vessels: a possible mechanism for the anti-atherogenic effects of losartan. Acta Cardiol 2007; 62: 607–13.
21 Imanishi T, Kuroi A, Ikejima H, Kobayashi K, Muragaki Y, Mochizuki S, *et al*. Effects of angiotensin converting enzyme inhibitor and angiotensin II receptor antagonist combination on nitric oxide bioavailability and atherosclerotic change in Watanabe heritable hyperlipidemic rabbits. Hypertens Res 2008; 31: 575–84.
22 Chen J, Liu Y, Liu H, Hermonat PL, Mehta JL. Molecular dissection of angiotensin II-activated human LOX-1 promoter. Arterioscler Thromb Vasc Biol 2006; 26: 1163–8.
23 Soufi M, Sattler AM, Maisch B, Schaefer JR. Molecular mechanisms involved in atherosclerosis. Herz 2002; 27: 637–48.

Acta Pharmacologica Sinica (2011) 32: 1266–1275
 1671-4083/11 $32.00
www.nature.com/aps

Original Article

# Reactive oxygen species contribute to oridonin-induced apoptosis and autophagy in human cervical carcinoma HeLa cells

Ya-hong ZHANG[1, 2], Ying-liang WU[3], Shin-ichi TASHIRO[4], Satoshi ONODERA[4], Takashi IKEJIMA[2, *]

*[1]Key Laboratory of Natural Medicine and Immuno-Engineering, Henan University, Kaifeng 475004, China; [2]China-Japan Research Institute of Medical Pharmaceutical Sciences, Shenyang Pharmaceutical University, Shenyang 110016, China; [3]Department of Pharmacology, Shenyang Pharmaceutical University, Shenyang 110016, China; [4]Department of Clinical and Biomedical Sciences, Showa Pharmaceutical University, Tokyo 194-8543, Japan*

**Aim:** To investigate the role of reactive oxygen species (ROS) in oridonin-induced apoptosis and autophagy in HeLa cells.
**Methods:** The cell viability was measured using MTT assay. Morphological changes of apoptosis and autophagy were examined using Hoechst 33258 staining and monodansylcadaverine (MDC) staining, respectively. The mitochondrial membrane potential (ΔΨm) was measured using fluorescent dye rhodamine 123. DCF-induced fluorescence was used to measure the intracellular ROS level. Protein expression was examined using Western blot.
**Results:** Treatment of HeLa cells with oridonin (20–160 μmol/L) inhibited the cell growth in time- and concentration-dependent manners. The cells treated with oridonin (80 μmol/L) for 24 h displayed marked DNA fragmentation and MDC-positive autophagosomes. In the presence of the specific autophagy inhibitor 3-MA (2 mmol/L), the oridonin-induced apoptosis was significantly enhanced. Treatment of HeLa cells with oridonin (20–120 μmol/L) induced intracellular ROS generation in a concentration-dependent manner. In the presence of the ROS scavenger NAC (5 mmol/L), the oridinin-induced ROS generation was markedly reduced. NAC (5 mmol/L) or non-thiol antioxidant catalase (1000 U/mL) significantly reduced the oridonin-induced inhibition of cell growth and apoptosis. Furthermore, oridonin significantly reduced ΔΨm, which was blocked by NAC. Oridonin markedly increased Bax expression in mitochondria, and decreased Bcl-2 expression in both the cytosol and mitochondria. Oridonin also markedly increased the phosphorylation of Bcl-2 in the cytosol. All the effects were blocked by NAC. Oridonin increased the levels of caspase-3 and caspase-8, and decreased the expression of pro-caspase 3 and pro-caspase 9, which were blocked by NAC.
**Conclusion:** ROS plays a critical role in oridonin-induced apoptosis and autophagy.

**Keywords:** oridonin; reactive oxygen species; apoptosis; autophagy; Bax; Bcl-2; caspase 3; caspase 8; HeLa cell

*Acta Pharmacologica Sinica* (2011) 32: 1266–1275; doi: 10.1038/aps.2011.92; published online 5 Sep 2011

## Introduction

Programmed cell death (PCD), an essential mechanism for development, tissue turnover and host defense in multicellular organisms, exists in two major forms: apoptotic and autophagic cell death[1]. Apoptosis, or type I PCD, is a genetically controlled cell suicide process that plays an important role in maintaining cell homeostasis of higher organisms[2]. Defective apoptosis results in a variety of diseases, such as autoimmunity, neurodegenerative disorders and many types of cancer[3]. Autophagy is also a crucial cellular homeostatic mechanism whereby eukaryotic cells degrade unnecessary proteins and prepare cytoplasmic organelles for their removal or turnover[4]. Although excessive autophagy can mediate cell death (type II PCD) under certain conditions, autophagy is largely considered to be a survival mechanism that is triggered by starvation or hormonal stimulation[5, 6]. The relationship between apoptosis and autophagy is complex and varies with both the cell type and the category of the stimulus[7, 8]. Mounting evidence suggests that there is a mechanistic overlap between apoptosis and autophagy[9, 10]. Thus, researchers have become increasingly interested in understanding the co-regulated factors of these two processes.

ROS are ions or small molecules that include singlet oxygen molecules, free radicals and peroxides, which are formed as byproducts of the normal cellular metabolism of oxygen[11]. Organisms have developed antioxidant systems that include

* To whom correspondence should be addressed.
E-mail ikejimat@vip.sina.com
Received 2011-01-24 Accepted 2011-06-15

antioxidant enzymes such as superoxide dismutase (SOD) and antioxidant molecules such as glutathione (GSH) to balance these species[12]. However, oxidative stress, a condition characterized by the dramatic increase in ROS levels and the disruption of the antioxidant balance, results in oxidative damage to cellular structures, signal transduction changes and cell death[13]. In addition, many studies have reported that ROS induce apoptosis in various cancer cells[14–16]. The mitochondrial membrane potential and the expression of Bcl-2 family proteins, which have been closely linked to mitochondrial-mediated apoptosis, were also reported to be affected by ROS[17]. Recent reports have also demonstrated that ROS participate in the regulation of autophagy in certain circumstances[18, 19]. Therefore, we are interested in the role of ROS in both apoptosis and autophagy.

Oridonin, an active diterpenoid isolated from *Rabdosia rubescens*, was found to present various pharmacological and physiological outcomes, including anti-bacterial, anti-inflammation and anti-tumor effects[20, 21]. Our previous studies showed that both apoptosis and autophagy were induced by oridonin in HeLa cells, and autophagy antagonized apoptosis by activating the PKC signaling pathway[22]. We also found that oridonin could induce ROS to mediate apoptosis in murine fibrosarcoma L929 cells and human hepatoma HepG2 cells[23, 24]. Hence, in this study, we investigated the possible regulatory mechanisms of ROS in oridonin-induced apoptosis and autophagy in HeLa cells.

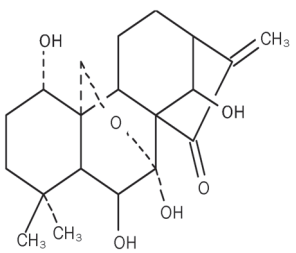


Chemical structure of oridonin.

## Materials and methods

### Materials

Oridonin was obtained from the Kunming Institute of Botany, The Chinese Academy of Sciences (Kunming, China). The purity of oridonin was confirmed by HPLC and determined to be 99.4%. Oridonin was dissolved in dimethyl sulfoxide (DMSO) to make a stock solution. The DMSO concentration was kept below 0.1% in cell culture and did not induce any detectable effect on cell growth or cell death.

Fetal bovine serum (FBS) was obtained from TBD Biotechnology Development (Tianjin, China). 3-(4,5-Dimethylthiazol-2-yl)-2,5-diphenyltetrazolium bromide (MTT), Hoechst 33258, Annexin V-FITC, propidium iodide (PI), monodansylcadaverine (MDC), 3-methyladenine (3-MA), *N*-acetyl-cysteine (NAC), 2′,7′-dichlorofluorescein diacetate (DCF-DA), catalase (CAT) and rhodamine-123 were purchased from Sigma Chemical (St Louis, MO, USA). Polyclonal antibodies to Bax, Bcl-2, phosphor-Bcl-2, caspase-3, caspase-8, caspase-9, LC3, Beclin 1, β-actin, and horseradish peroxidase-conjugated secondary antibodies were obtained from Santa Cruz Biotechnology (Santa Cruz, CA, USA).

### Cell culture

The human cervical carcinoma HeLa cell line was obtained from American Type Culture Collection (ATCC, Manassas, VA, USA). The cells were cultured in RPMI-1640 medium (GIBCO, Gaithersburg, MD, USA) supplemented with 10% fetal bovine serum (FBS), 0.03% *L*-glutamine (GIBIO, Grand Island, NY, USA), 100 U/mL penicillin and 100 μg/mL streptomycin and maintained at 37 °C with 5% $CO_2$ in a humidified atmosphere.

### Cell growth inhibition assay

The inhibition of cell growth was measured by MTT assay as described previously[25]. The cells were dispensed in 96-well flat bottom microtiter plates (NUNC, Roskilde, Denmark) at a density of $1.5\times10^4$ cells per well. After 24 h of incubation, they were treated with various concentrations of oridonin or 5 mmol/L NAC 1 h prior to 80 μmol/L oridonin for the indicated time periods. Next, MTT (5 mg/L) was added to each well for 3 h, and the resulting crystals were dissolved in DMSO. Optical density was measured by MTT assay using a plate microreader (TECAN SPECTRA, Wetzlar, Germany). The percentage of cell growth inhibition was calculated as follows:

$$\text{Cell inhibition ratio (\%)} = \frac{A_{492\ \text{control}} - A_{492\ \text{sample}}}{A_{492\ \text{control}} - A_{492\ \text{blank}}} \times 100$$

### Observation of nuclear damage by Hoechst 33258 staining

HeLa cells ($5\times10^5$/well) were cultured in 6-well culture plates. After 24 h of incubation, the cells were treated with or without 80 μmol/L oridonin for 24 h. The cells were then incubated with 5 mmol/L Hoechst 33258 at 37 °C for 30 min, and the nuclear changes of fluorescence were observed by OLYMPUS IX70 reverse fluorescence microscopy (Olympus, Tokyo, Japan) at excitation wavelength 350 nm with emission filter 460 nm[26].

### Analysis of autophagy and apoptosis by flow cytometry

HeLa cells were dispensed in 25 mL culture bottles at a density of $1\times10^6$ per bottle. After 24 h of incubation, they were treated with or without 3-MA and NAC at the given concentrations 1 h prior to the administration of oridonin for 24 h. The cells were harvested by trypsin and rinsed with PBS. To measure autophagy, monodansylcadaverine (MDC) was used as a marker for autophagic vacuoles[27]; collected cells were suspended with 0.05 mmol/L MDC at 37 °C for 60 min. Staining with Annexin V/PI was used to measure apoptosis. The cells were fixed with 100 μL binding buffer and treated with 2 μL Annexin V-FITC solution (20 mg/L) at 4 °C for 20 min; they

were then added 1 mL PI solution (50 mg/L) for 5 min. For measuring apoptosis with PI staining, the collected cells were fixed with 500 μL PBS and 10 mL 70% ethanol at 4 °C for 18 h, and then after being washed twice with PBS, the cells were suspended with 1 mL PI solution (PI 50 mg/L and RNase A 1 g/L)[26]. Next, the samples were analyzed using a FACScan flow cytometer (Becton Dickinson, Franklin Lakes, NJ, USA).

### Flow cytometric analysis of intracellular ROS production

HeLa cells were dispensed in 25 mL culture bottles at a density of $1\times10^6$ per bottle. After 24 h of incubation, they were treated with various concentrations of oridonin or 3-MA and NAC at the given concentrations 1 h prior to 80 μmol/L oridonin for the indicated time periods. The cells were incubated with 10 μmol/L DCF-DA at 37 °C for 15 min to assess ROS-mediated oxidation of DCF-DA to the fluorescent compound DCF. Next, the cells were harvested and the pellets were suspended in 1 mL PBS. Samples were analyzed at an excitation wavelength of 480 nm and an emission wavelength of 525 nm using a FACScan flow cytometer (Becton Dickinson, Franklin Lakes, NJ, USA)[28].

### Observation of morphologic changes

HeLa cells ($5\times10^5$/well) were seeded into 6-well culture plates. After 24 h of incubation, the cells were treated with or without 5 mmol/L NAC 1 h prior to the administration of 80 μmol/L oridonin for 24 h of incubation. The cellular morphology was observed by a phase-contrast microscope (Leica, Nussloch, Germany).

### Flow cytometric analysis of ΔΨm

HeLa cells were dispensed into 25 mL culture bottles at a density of $1\times10^6$ per bottle. After 24 h of incubation, the cells were treated with or without 5 mmol/L NAC 1 h prior to the administration of 80 μmol/L oridonin for a 24-h incubation. The cells were harvested by trypsin and rinsed with PBS. For measuring ΔΨm, a cationic fluorescent dye rhodamine 123 was used as previously described[29]. The collected cells were stained with 1 μg/mL rhodamine 123 and incubated at 37 °C for 15 min. The samples were analyzed using a FACScan flow cytometer (Becton Dickinson, Franklin Lakes, NJ, USA).

### Isolation of cytosolic and mitochondrial fractions

The cell groups were harvested by trypsin, and the cell pellets were resuspended in ice-cold homogenizing buffer, (250 mmol/L sucrose, 20 mmol/L HEPES, 10 mmol/L KCl, 1 mmol/L EDTA, 1 mmol/L EGTA, 1.5 mmol/L $MgCl_2$, 1 mmol/L DTT, 1 mmol/L PMSF, 1 μg/mL aprotinin, and 1 μg/mL leupeptin). After homogenization (40 strokes), the homogenates were centrifuged at 4200×*g* at 4 °C for 30 min. The supernatant was used as the cytosolic fraction, and the pellet was resolved in lysis buffer as the mitochondrial fraction[17].

### Western blot analysis

HeLa cells ($2\times10^6$) were preincubated with or without specific inhibitors before treatment with 80 μmol/L oridonin. After 24 h, both adherent and floating cells were collected and frozen at -80 °C. Western blot analysis was carried out as follows. The cell pellets were resuspended in lysis buffer containing 50 mmol/L Hepes (pH 7.4), 1% Triton-X 100, 2 mmol/L sodium orthovanadate, 100 mmol/L sodium fluoride (NaF), 1 mmol/L edetic acid, 1 mmol/L egtazic acid (EGTA), 1 mmol/L phenylmethyl-sulfonylfluoride (PMSF), 0.1 g/L aprotinin, and 0.01 g/L leupeptin and lysed at 4 °C for 1 h. Then the cells were spun in a centrifuge at 12000×*g* for 10 min, and the protein content of the supernatant was determined by Bio-Rad protein assay reagent (Bio-Rad, Hercules, CA, USA). The proteins were separated by 12% SDS polyacrylamide gel electrophoresis and blotted onto nitrocellulose membrane. The membranes were soaked in 5% skimmed milk and incubated with primary polyclonal antibodies overnight. The proteins were visualized by an anti-rabbit IgG conjugated with peroxidase and diamino-benzidine (DAB)[30]. Protein levels were quantified by densitometry (Fluochim v2.0 Alpha; Alpha Innotech, San Leandro, CA, USA). The relative density was calculated as follows:

$$\text{Relative density}=\frac{\text{Band density of the sample}}{\text{Band density of control}}$$

### Observation of autophagy by monodansylcadaverine (MDC) staining

HeLa cells ($5\times10^5$/well) were cultured in 6-well culture plates. After 24 h of incubation, the cells were treated with or without 5 mmol/L NAC 1 h prior to the administration of 80 μmol/L oridonin for 24 h. Next, the cells were incubated with 0.05 mmol/L MDC at 37 °C for 1 h, and the change in fluorescence was observed by OLYMPUS IX70 reverse fluorescence microscopy (Olympus, Tokyo, Japan) at an excitation wave length 380 nm with an emission filter of 525 nm.

### Statistical analysis

All results and data were confirmed in at least three separate experiments. Data are expressed as mean±SD. Statistical comparisons were made by one-way ANOVA. $P<0.05$ was considered significant.

## Results

### Oridonin induced apoptosis and autophagy in HeLa cells

Oridonin inhibited HeLa cell growth in a time- and concentration-dependent manner. Concentrations of oridonin ranging from 10 to 160 μmol/L all exerted cytotoxic effects on HeLa cell growth and treatment with 80 μmol/L oridonin for 24 h resulted in almost 50% inhibition (Figure 1A). To determine whether apoptosis was induced by oridonin, the morphological changes were observed by Hoechst 33258 staining. Oridonin treated cells showed marked fragmented DNA in their nuclei, whereas the nuclei were round and homogeneously stained in the control group (Figure 1B). We also examined the effect of oridonin on autophagy by detecting MDC (a fluorescent dye of autophagosome) labeled cells. Analysis

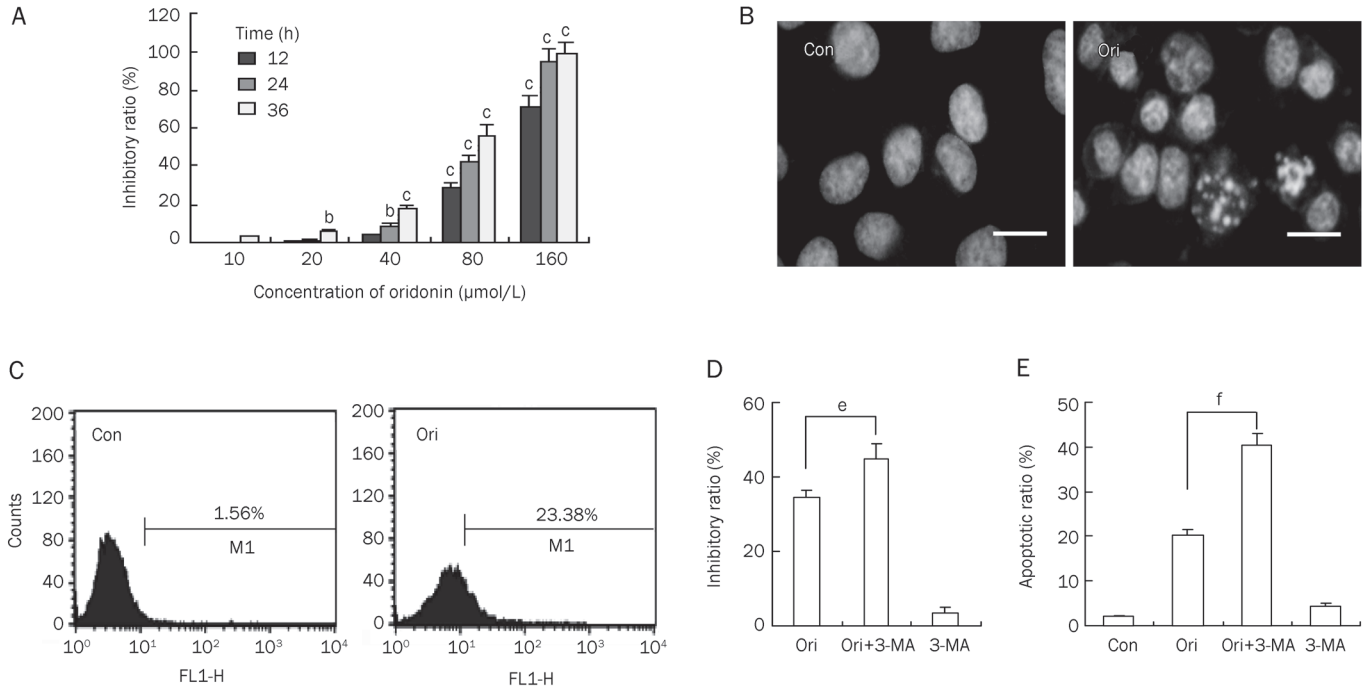


**Figure 1.** Oridonin induced apoptosis and autophagy in HeLa cells. (A) The cells were treated with various doses of oridonin for 12, 24, or 36 h. The cell growth inhibition ratio was measured by MTT assay. $n$=3. Mean±SD. $^{b}P$<0.05, $^{c}P$<0.01 *vs* control group. (B) The cells were treated with 80 μmol/L oridonin for 24 h and the changes in cellular morphology were observed by fluorescence microscopy with Hoechst 33258 staining (×400 magnification, Bar=10 μm). (C) The ratio of MDC-positive cells was measured by flow cytometric analysis after the cells were incubated with 80 μmol/L oridonin for 24 h. The FACScan histograms are shown. (D–E) The cells were treated with 80 μmol/L oridonin for 24 h in the presence or absence of 2 mmol/L 3-MA, the cell growth inhibition ratio (D) was measured by MTT assay, and the apoptotic cells were measured by flow cytometry analysis that detected Annexin V/PI staining. The apoptotic ratio (E) represents the addition of the proportion of Annexin V positive cells and the proportion of PI-positive cells. $n$=3. Mean±SD. $^{e}P$<0.05, $^{f}P$<0.01 *vs* oridonin group. Con: control, Ori: oridonin.

of flow cytometry data showed that the percentage of MDC-positive cells after oridonin treatment was 23.38% at 24 h and was considerably higher than that in the control group (Figure 1C). To further investigate the relationship of apoptosis and autophagy in oridonin-treated HeLa cells, 3-MA (a specific autophagy inhibitor) was introduced. Treatment with 3-MA prior to the addition of oridonin led to a markedly increased cell growth inhibition ratio and apoptotic ratio compared with the group treated with oridonin alone (Figure 1D and 1E). These results indicated that oridonin induced both apoptosis and autophagy in HeLa cells and that the inhibition of autophagy contributed to the up-regulation of apoptosis.

### Oridonin dose-dependently induced intracellular ROS generation in HeLa cells

To investigate whether ROS were triggered by oridonin in HeLa cells, DCF-DA, a specific ROS-detecting fluorescent dye, was used to examine the intracellular ROS level. The exposure of HeLa cells to various doses of oridonin for 24 h led to a sharp increase in DCF fluorescence compared with the control group (Figure 2). Furthermore, the ratio of DCF-positive cells was increased from 3.73% in untreated cells to 3.81%, 7.50%, 23.07%, or 41.93% in cells treated with oridonin doses of 20, 40, 80, and 120 μmol/L, respectively. When pretreated with the ROS scavenger NAC, the corresponding ratio of DCF-positive cells was markedly reduced, from 23.07% to 7.96%, compared with the group treated with 80 μmol/L oridonin alone (Figure 2). These data suggested that ROS in HeLa cells were induced by oridonin in a dose-dependent manner.

### ROS mediated oridonin-induced apoptosis in HeLa cells

To evaluate the role of ROS in oridonin-induced apoptosis, we pretreated HeLa cells with NAC before oridonin administration. Oridonin treatment induced canonical apoptotic changes including membrane blebbing and granular apoptotic bodies. In contrast, these apoptotic morphologic alterations were almost completely suppressed by pretreatment with NAC (Figure 3A). The MTT assay also demonstrated that NAC treatment significantly reduced the cell growth inhibition ratio from 33.1% for oridonin alone to 5.8% in the presence of NAC (Figure 3B). Flow cytometry analysis revealed that NAC reduced the apoptotic ratio compared with oridonin treatment alone (Figure 3C). Like NAC, treatment with an additional non-thiol antioxidant catalase (CAT), which catalyzes the conversion of hydrogen peroxide to water and oxygen, also reduced the oridonin-induced cell growth inhibition and apoptosis (Figure 3B and 3C). Together, these results demonstrated that ROS played an important role in oridonin-induced

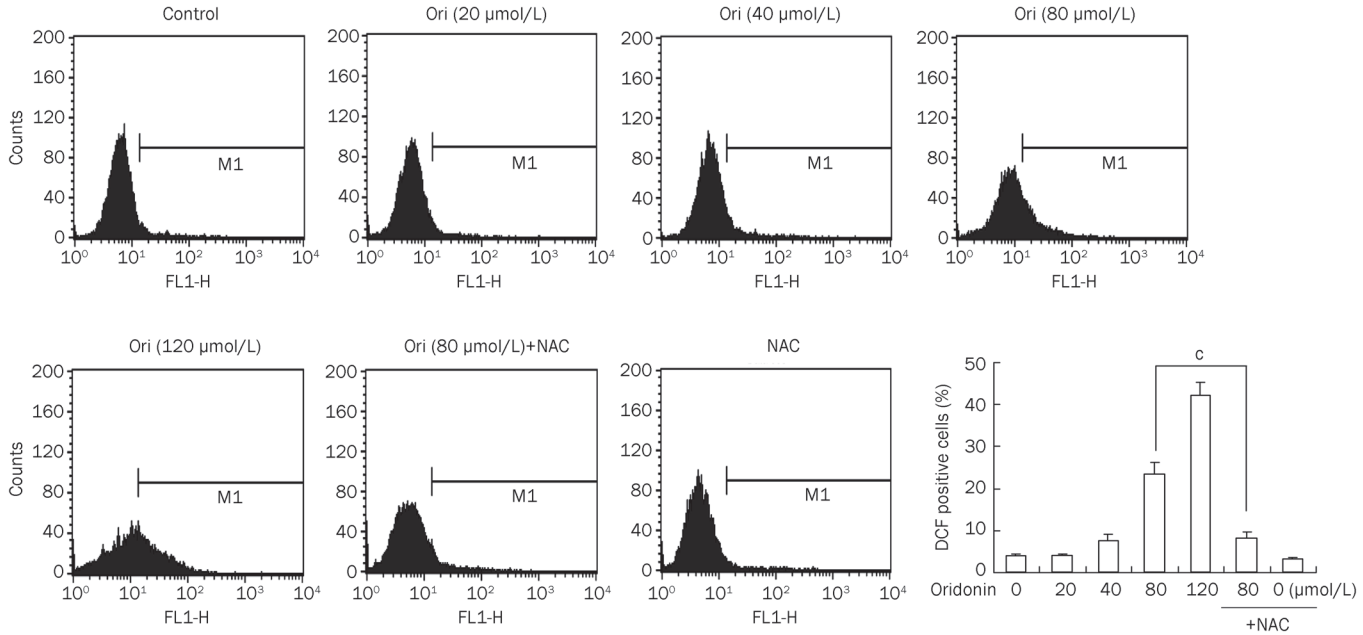


**Figure 2.** ROS production was induced by oridonin and could be inhibited by NAC in HeLa cells. The cells were treated with various doses of oridonin or coincubated with 5 mmol/L NAC and 80 μmol/L oridonin for 24 h. The DCF-positive cells were measured by flow cytometry. The corresponding linear diagram of the FACScan histograms is expressed at the base. *n*=3. Mean±SD. $^{c}P<0.01$ *vs* 80 μmol/L oridonin group.

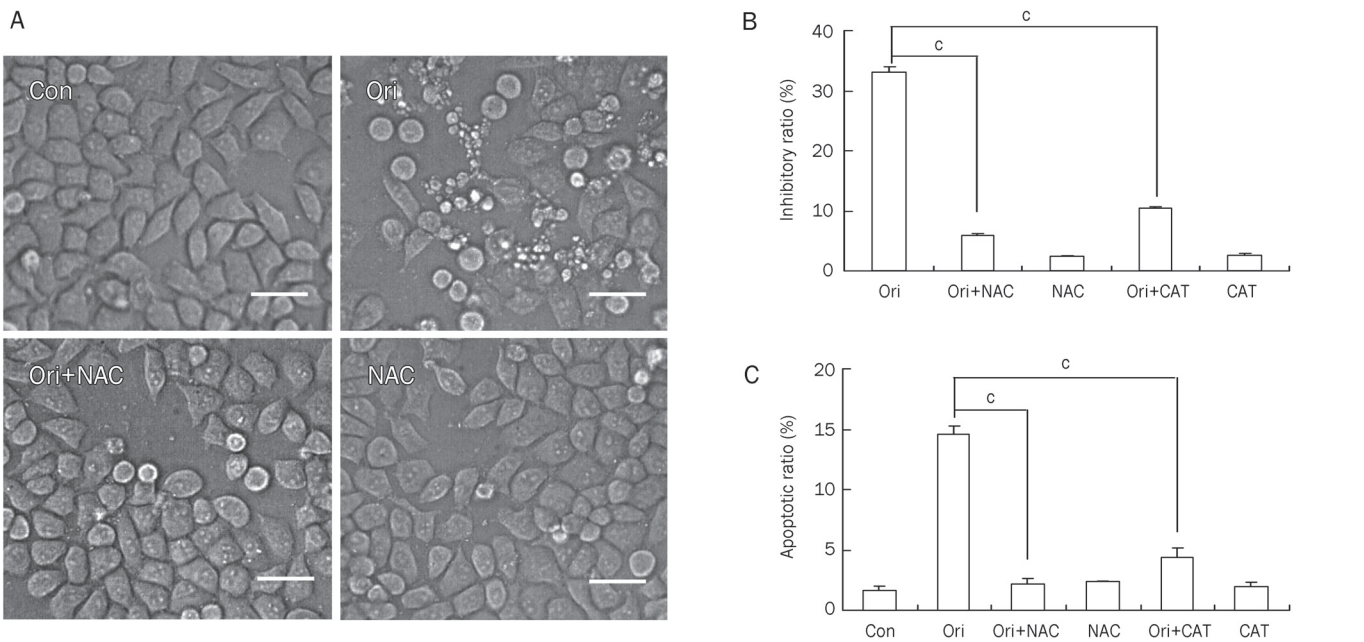


**Figure 3.** Effect of ROS on oridonin-induced apoptosis in HeLa cells. The cells were treated with 80 μmol/L oridonin for 24 h in the presence or absence of 5 mmol/L NAC or 1000 U/mL CAT. (A) The cellular morphologic changes were observed by phase contrast microscopy (×200 magnification, Bar=20 μm). The cell growth inhibitory ratio was measured by MTT assay (B), and the apoptotic ratio was measured by flow cytometric analysis stained with PI (C). *n*=3. Mean±SD. $^{c}P<0.01$ *vs* oridonin group.

apoptosis in HeLa cells.

### Inhibition of ROS rescued the loss of ΔΨm in oridonin-treated HeLa cells

Because there is a relationship between ROS generation and the disruption of the mitochondrial membrane potential, we examined whether ROS are involved in the regulation of ΔΨm in HeLa cells. The loss of the ΔΨm was reflected by a decrease in the intensity of rhodamine 123 fluorescent staining, which was used to detect the integrity of mitochondrial membrane.

Oridonin treatment alone reduced the ratio of rhodamine-positive cells from 95.72% in the control group to 77.87%. However, this decrease was reversed by NAC pretreatment which increased that ratio to 94.93% when co-incubated with oridonin (Figure 4). These findings revealed that ROS contributed to the oridonin-induced dissipation in ΔΨm in HeLa cells.

### ROS was involved in oridonin-induced Bax translocation and Bcl-2 degradation in HeLa cells

Because the results above indicated that ROS influenced the mitochondrial membrane potential, the expression of Bax and Bcl-2, which are Bcl-2 family members modulating mitochondrial-mediated apoptotic pathway, were examined using Western blot analysis. As shown in Figure 5, the expression level of Bax in the cytosol was only slightly upregulated in response to oridonin treatment, but oridonin caused a sharp increase in Bax expression in the mitochondria. This suggests that oridonin induced the translocation of Bax from the cytosol to the mitochondria in these conditions. The results also showed that oridonin attenuated the expression of Bcl-2 in both the cytosol and the mitochondria but induced the phosphorylation of Bcl-2. In the presence of NAC, oridonin-induced Bax translocation and Bcl-2 degradation were both reversed, and the expression of all proteins returned to untreated levels (Figure 5). Therefore, ROS participated in the regulation of mitochondrial-mediated apoptosis in oridonin-treated HeLa cells.

### ROS participated in oridonin-activated caspase-3, caspase-8, and caspase-9 process in HeLa cells

It is well known that the caspase protein family plays a critical role in the apoptotic process. To further elucidate the importance of ROS in apoptosis, we examined the expression of caspase-3, caspase-8, and caspase-9 by Western blot analysis. As shown in Figure 6, the cleavage of procaspase-3 and procaspase-8, as well as the decrease in procaspase-9, was observed in oridonin-treated cells. The activation of this process was inhibited by NAC administration. These results further confirmed the critical role of ROS in apoptosis in this system.

### ROS regulated oridonin-induced autophagy in HeLa cells

Because oridonin may induce autophagy and apoptosis, we examined the effect of ROS on oridonin-induced autophagy. Oridonin treatment led to a marked increase in the number of MDC-labeled fluorescent particles in the cells, which further confirmed that oridonin could induce autophagy in HeLa cells. However, when NAC was applied, the number of MDC-labeled fluorescent particles was completely suppressed (Figure 7A). Quantitative analysis by flow cytometry also showed that the percentage of MDC-positive cells by oridonin treatment was reduced by NAC or CAT treatment from 23.38% to 5.18% and 9.31%, respectively (Figure 7B). We further examined the effect of NAC on oridonin-induced autophagy through detection of the autophagic markers Beclin 1 and MAP-LC3. As expected, oridonin treatment alone enhanced both the expression level of Beclin 1 and the conversion of LC3-I to LC3-II, but these enhancements were reversed by NAC pretreatment. NAC alone had no effect on the expressions of these two marker proteins (Figure 7C). Next, the influence of autophagy inhibitor 3-MA on oridonin-induced ROS generation was evaluated. The percentage of DCF-positive cells declined from 26.22% in the oridonin-treated cells to 14.05% in 3-MA and oridonin-treated cells (Figure 7D). Together, these results indicated that ROS was also involved in regulating oridonin-induced autophagy in HeLa cells.

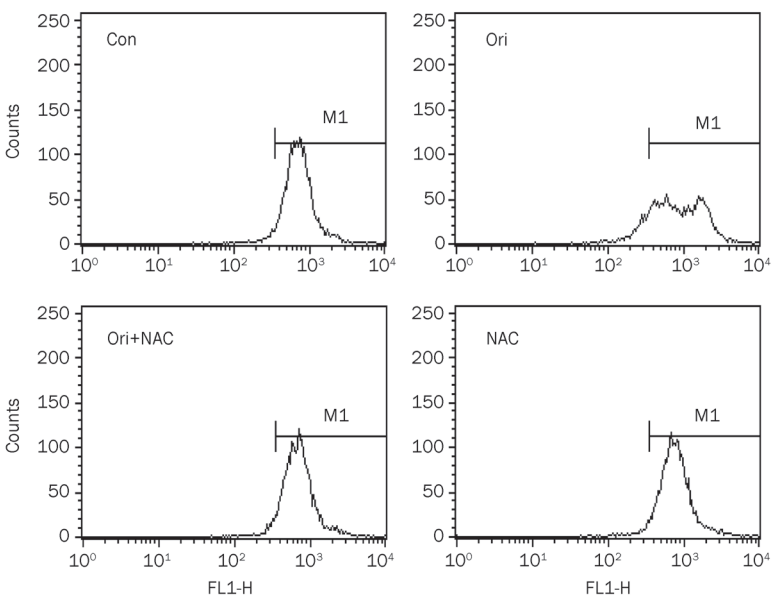


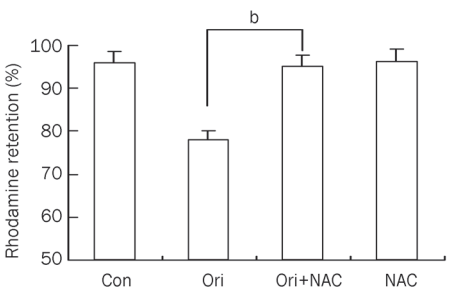


**Figure 4.** Significant reduction in mitochondrial transmembrane potential (ΔΨm) was induced by oridonin and could be rescued by NAC in HeLa cells. The cells were treated with 80 μmol/L oridonin for 24 h in the presence or absence of 5 mmol/L NAC and then were loaded with the membrane-sensitive probe rhodamine 123. The rhodamine retention was measured by flow cytometry. The corresponding linear diagram of the FACScan histograms is expressed at the base. $n$=3. Mean±SD. $^bP<0.05$ *vs* oridonin group.

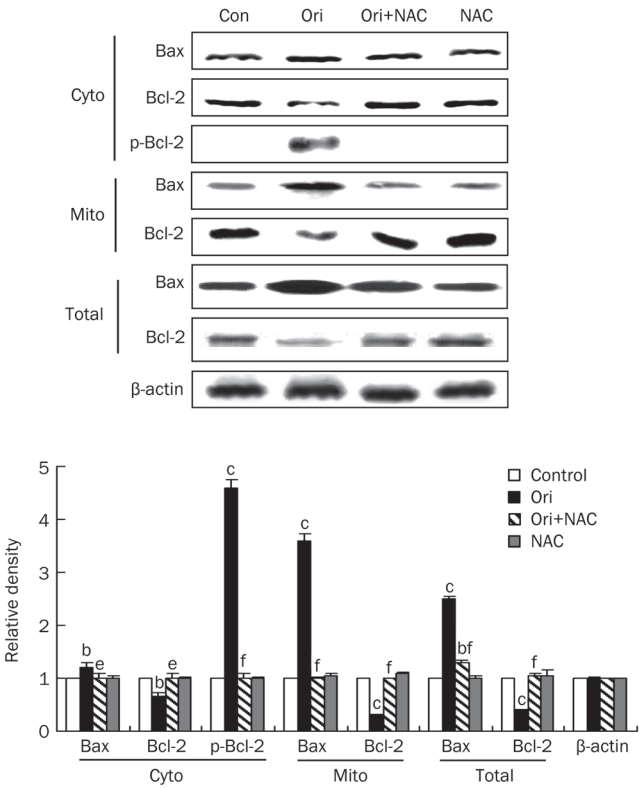


**Figure 5.** Effects of NAC on oridonin-induced Bax translocation and Bcl-2 degradation. The cells were treated with 80 μmol/L oridonin for 24 h in the presence or absence of 5 mmol/L NAC. The expression levels of Bax, p-Bcl-2, Bcl-2 both in the cytosol and the mitochondria, and the total protein expressions of Bax and Bcl-2 in the cells were detected by Western blot analysis. The corresponding histograms quantified by densitometry were expressed at bottom. $n$=3. Mean±SD. $^{b}P$<0.05, $^{c}P$<0.01 *vs* control group; $^{e}P$<0.05, $^{f}P$<0.01 *vs* oridonin group. These experiments were performed at least three times, and β-actin was used as a loading control.

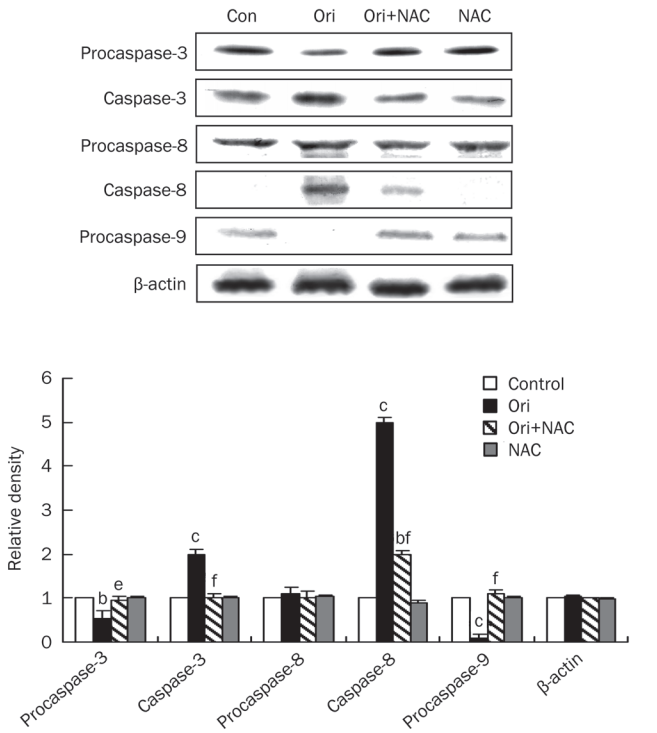


**Figure 6.** Effects of NAC on oridonin-induced activations of caspase-3, caspase-8, and caspase-9. The cells were treated with 80 μmol/L oridonin for 24 h in the presence or absence of 5 mmol/L NAC, and the expression levels of procaspase-3, caspase-3, procaspase-8, caspase-8, procaspase-9 were detected by Western blot analysis. The corresponding histograms were quantified by densitometry and were expressed at the bottom. $n$=3. Mean±SD. $^{b}P$<0.05, $^{c}P$<0.01 *vs* control group; $^{e}P$<0.05, $^{f}P$<0.01 *vs* oridonin group. Each experiment was performed at least three times, and β-actin was used as a loading control.

### Oridonin induced persistent ROS generation in HeLa cells

The data above revealed that ROS generation was the crucial event to mediate oridonin-induced apoptosis and autophagy. To further confirm this finding, we measured intracellular ROS levels for various time periods by using DCF-DA. Significant levels of ROS were generated within 1 h after oridonin treatment, and the level of ROS continued to increase for 24 h (Figure 8). The ratio of DCF-positive cells increased from 4.36% in untreated cells to 22.57%, 27.19%, 27.69%, 36.62%, and 36.34% in 1, 3, 6, 12, and 24 h-treated cells, respectively (Figure 8). This demonstrated that ROS generation was the first event stimulated by oridonin and acted as the main factor mediating oridonin-induced apoptosis and autophagy.

## Discussion

Apoptosis and autophagy have previously been correlated both positively and negatively depending on the "molecular switches" connecting them[7, 8]. In previous studies, we demonstrated that autophagy and apoptosis were both induced in oridonin-treated HeLa cells and that autophagy was a protective mechanism against apoptosis in this circumstance[22]. Here, we further confirmed these results through flow cytometric analysis and observation of changes in morphology. It is well established that autophagy may promote survival in many contexts, including nutrient deprivation, endoplasmic reticulum stress, and microbial infection[7]. Under these conditions, autophagy played a cytoprotective role in response to oridonin-induced cellular stress; apoptosis was up-regulated by the inhibition of autophagy. These results were consistent with the data of Kaushik and colleagues[19]. In addition, it has been postulated that oxidative stress can result in autophagy, apoptosis, or necrosis, depending on its severity[31]. Our work investigated the possible role of ROS in regulating oridonin-induced apoptosis and autophagy in HeLa cells.

ROS are essential intermediates in many intracellular signal pathways that lead to cell death[13]. ROS generation has been reported to be associated with a variety of stimuli such as tumor necrosis factor (TNF), endoplasmic reticulum stress (ER stress), starvation, and certain compounds[32]. The results in this study revealed that ROS generation was induced by oridonin in a dose-dependent manner in HeLa cells. Also we found that ROS production could be significantly scav-

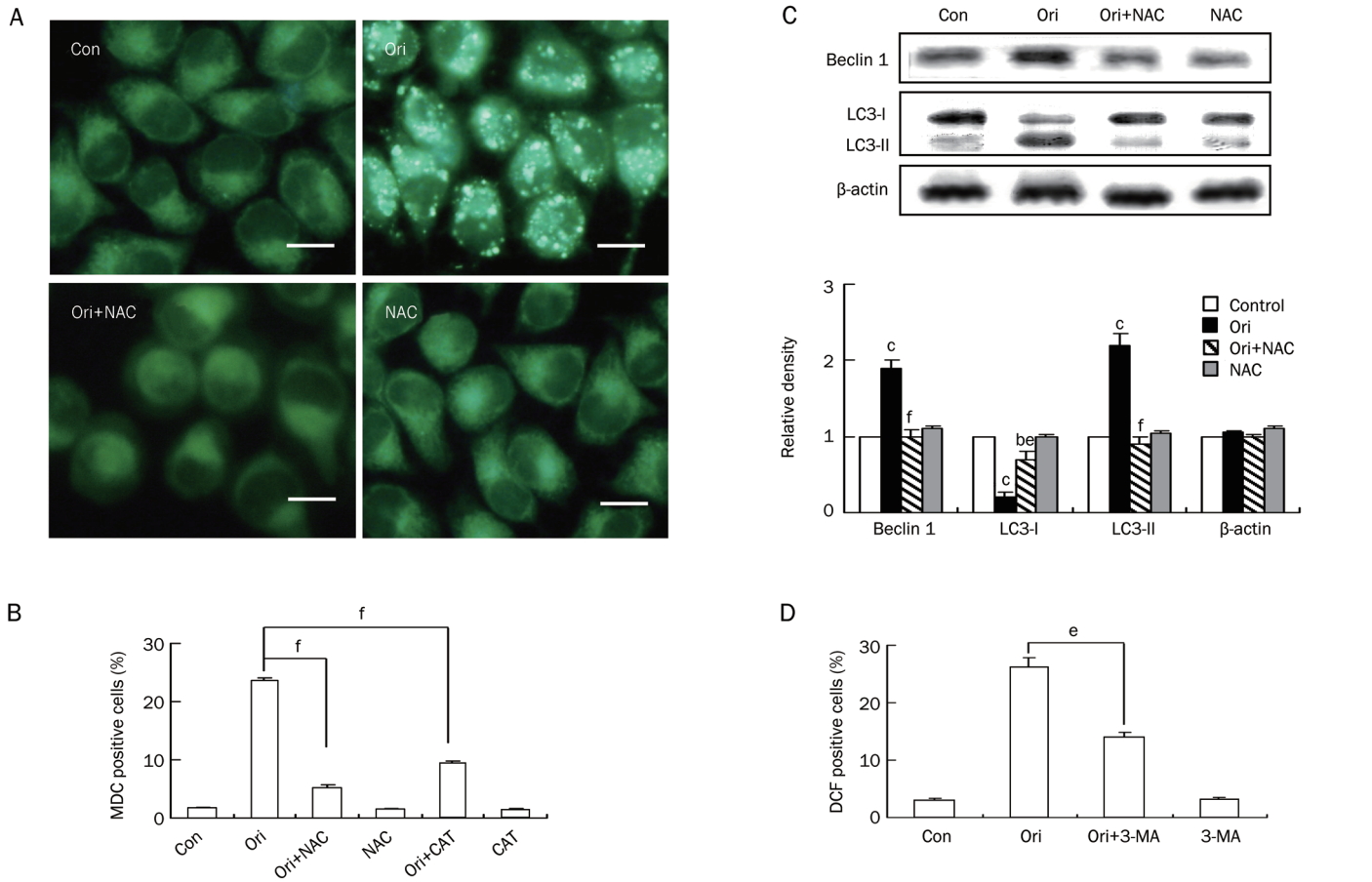


**Figure 7.** Effect of ROS on oridonin-induced autophagy in HeLa cells. (A–C) The cells were treated with 80 μmol/L oridonin for 24 h in the presence or absence of 5 mmol/L NAC or 1000 U/mL CAT. (A) The changes in cellular morphology were observed by fluorescence microscopy with MDC staining (×400 magnification, Bar=10 μm). (B) The autophagic ratio was measured by flow cytometric analysis. $n$=3. Mean±SD. $^{f}P$<0.01 *vs* oridonin group. (C) The protein levels of Beclin 1 and MAP-LC3 were detected by Western blot analysis, and the corresponding histograms quantified by densitometry were expressed at the bottom. $n$=3. Mean±SD. $^{b}P$<0.05, $^{c}P$<0.01 *vs* control group; $^{e}P$<0.05, $^{f}P$<0.01 *vs* oridonin group. Each experiment was performed at least three times, and β-actin was used as a loading control. (D) The cells were treated with 80 μmol/L oridonin for 24 h in the presence or absence of 2 mmol/L 3-MA and the DCF-positive cells was measured by flow cytometric analysis. $n$=3. Mean±SD. $^{e}P$<0.05 *vs* oridonin group.

enged by NAC. These data suggest a possible role for ROS in oridonin-induced cellular events.

There is evidence that apoptosis can be induced by ROS. It has been shown that ROS generation, which regulated p53 activation, mediated oridonin-induced apoptosis in HepG2 cells[24]. Conjugation with polyethylene glycol (PEG) could effectively reduce the polyamidoamine-induced cell apoptosis by limiting the production of ROS[33]. Consistent with these studies, our results demonstrated that the inhibition of ROS generation by NAC led to significant decrease in oridonin-induced cytotoxicity and apoptosis. As a potent inducer of apoptosis, the pathways of ROS in regulating apoptosis were investigated. Mitochondria are particularly vulnerable to oxidative stress and are major sources of intracellular ROS[34]. Many reports have documented that ROS participate in the apoptotic process by disrupting the ability to induce the mitochondrial membrane potential (MMP)[17, 33]. In addition, other studies have shown that several Bcl-2 family proteins, especially the pro-apoptotic protein Bax and the anti-apoptotic protein Bcl-2, are recognized as major players in mitochondrial-mediated apoptosis by regulating MMP[23, 35]. The ratio of Bax/Bcl-2 is critical for the induction of apoptosis[35]. In this study, we demonstrated that the suppression of ROS reversed oridonin-induced loss of $\Delta\Psi m$, Bax translocation and Bcl-2 degradation; this indicates that an increased Bax/Bcl-2 ratio may be important for inducing the MMP in the ROS-mediated and oridonin-induced apoptosis. Moreover, ROS were also found to regulate caspase-dependent apoptosis, as demonstrated by the ability of ROS to induce caspase-8, caspase-9, and eventually caspase-3 activation. This conclusion was supported by the observation that caspase-dependent spontaneous apoptosis was inhibited by NAC *in vitro* in cultured human primary B lymphocytes[36]. Together, these results suggest that ROS played a role in inducing apoptosis in oridonin-treated HeLa cells.

Autophagy is a well-conserved lysosomal degradation

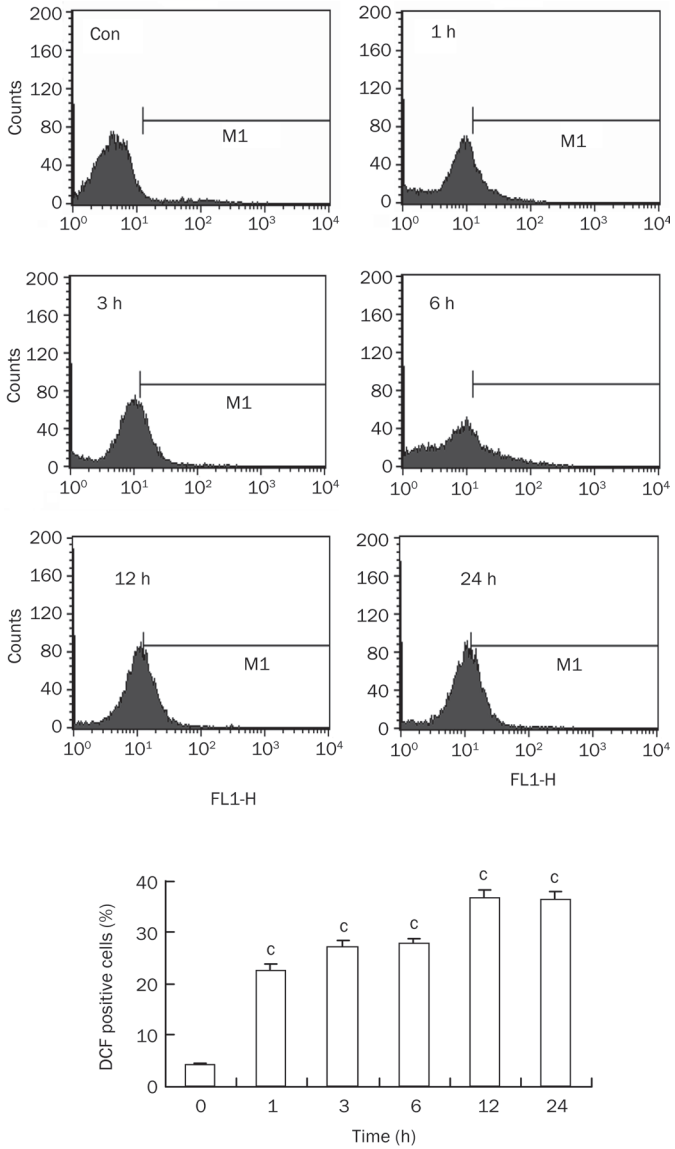


**Figure 8.** Persistent ROS generation was induced by oridonin in HeLa cells. The cells were treated with 80 μmol/L oridonin for 1, 3, 6, 12, and 24 h, and the DCF-positive cells were measured by flow cytometric analysis. The corresponding linear diagram of the FACScan histograms was expressed at the bottom. $n$=3. Mean±SD. $^{c}P$<0.01 *vs* control group.

pathway that has become an attractive area of study in recent years[4]. ROS have been reported to be involved in autophagy by regulating the activity of the redox sensitive cysteine protease HsAtg4A, which belongs to the Atg4 family[37]. Here, we found that the oridonin-induced autophagosome accumulation, the increased expression of Beclin 1 and the conversion of LC3-I to LC3-II were all inhibited by NAC, suggesting that ROS contributed to autophagy in this system. Subsequent results revealing reduced levels of ROS by the autophagy inhibitor 3-MA further confirmed this.

These findings revealed that ROS mediated the oridonin-induced apoptosis and autophagy, whereas autophagy antagonized apoptosis in this circumstance. We hypothesized that the generation of ROS was first induced by oridonin and that this was the fundamental signal molecule in oridonin-induced cellular events. In agreement with our hypothesis, our results indicate that ROS production was triggered rapidly and robustly 1 h after administration of oridonin and increased persistently.

Therefore, we hypothesized a possible mechanism for the oridonin-induced production of ROS in the cells. It is well established that mitochondria are particularly vulnerable to oxidative stress and are major sources of intracellular ROS[34]. In our study, the expression of $\Delta\Psi_m$ and some critical mitochondrial proteins were altered; thus, we presumed that oridonin induced the generation of ROS in mitochondria. We proposed that oridonin may induce a state of cellular oxidative stress by altering the redox state of glutathione or the activity of superoxide dismutase. These changes could lead to a mitochondrial permeability change either directly or indirectly, which in turn could cause the generation of ROS. Further studies will be required to confirm this.

In summary, we have demonstrated that ROS signal for the initiation of mitochondrial- and caspase-dependent apoptosis as well as autophagy in oridonin-treated HeLa cells. Our results provide new insight into the role of ROS in signaling apoptosis and autophagy. Future investigations characterizing additional signaling pathways mediated by ROS in both apoptosis and autophagy are still needed.

## Acknowledgements

This work was supported by China Postdoctoral Science Foundation Funded Project (No 20100470995) and Intramural Research Fund of He-nan University (No 2009YBZR029).

## Author contribution

Ya-hong ZHANG performed the experiments, analyzed data and wrote the manuscript. Takashi IKEJIMA and Ying-liang WU designed the study and revised the manuscript. Shin-ichi TASHIRO and Satoshi ONODERA provided the reagents.

## References

1 Lockshin RA, Zakeri Z. Apoptosis, autophagy, and more. Int J Biochem Cell Biol 2004; 36: 2405–19.
2 Gerl R, Vaux DL. Apoptosis in the development and treatment of cancer. Carcinogenesis 2005; 26: 263–70.
3 Hengartner MO. The biochemistry of apoptosis. Nature 2000; 407: 770–6.
4 Levine B. Autophagy and cancer. Nature 2007; 446: 745–7.
5 Kanzawa T, Kondo Y, Ito H, Kondo S, Germano I. Induction of autophagic cell death in malignant glioma cells by arsenic trioxide. Cancer Res 2003; 63: 2103–8.
6 Kuma A, Hatano M, Matsui M, Yamamoto A, Nakaya H, Yoshimori T. The role of autophagy during the early neonatal starvation period. Nature 2004; 432: 1032–6.
7 Mizushima N, Levine B, Cuervo AM, Klionsky DJ. Autophagy fights disease through cellular self-digestion. Nature 2008; 451: 1069–75.
8 Cui Q, Tashiro SI, Onodera S, Minami M, Ikejima T. Autophagy preceded apoptosis in oridonin-treated human breast cancer MCF-7 cells. Biol Pharm Bull 2007; 30: 859–64.

9 Pattingre S, Tassa A, Qu XP, Garuti R, Liang XH, Mizushima N. Bcl-2 antiapoptotic proteins inhibit Beclin 1-dependent autophagy. Cell 2005; 122: 927–39.
10 Wang ZH, Xu L, Duan ZL, Zeng LQ, Yan NH, Peng ZL. Beclin 1-mediated macroautophagy involves regulation of caspase-9 expression in cervical cancer HeLa cells. Gynecol Oncol 2007; 107: 107–13.
11 Crack PJ, Taylor JM. Reactive oxygen species and the modulation of stroke. Free Radic Biol Med 2005; 38: 1433–44.
12 Klamt F, Dal-Pizzol F, Conte da Frota MLJR, Walz R, Andrades ME, da Silva EG, *et al*. Imbalance of antioxidant defense in mice lacking cellular prion protein. Free Radic Biol Med 2001; 30: 1137–44.
13 Ermak G, Davies KJ. Calcium and oxidative stress: from cell signaling to cell death. Mol Immunol 2002; 38: 713–21.
14 Simbula G, Columbano A, Ledda-Columbano GM, Sanna L, Deidda M, Diana A, *et al*. Increased ROS generation and p53 activation in alpha-lipoic acid-induced apoptosis of hepatoma cells. Apoptosis 2007; 12: 113–23.
15 Reinecke F, Levanets O, Olivier Y, Louw R, Semete B, Grobler A, *et al*. Metallothionein isoform 2A expression is inducible and protects against ROS-mediated cell death in rotenone-treated HeLa cells. Biochem J 2006; 395: 405–15.
16 Kang YH, Lee E, Choi MK, Ku JL, Kim SH, Park YG, *et al*. Role of reactive oxygen species in the induction of apoptosis by alpha-tocopheryl succinate. Int J Cancer 2004; 112: 385–92.
17 Yang J, Wu JN, Tashiro S, Onodera S, Ikejima T. Critical roles of reactive oxygen species in mitochondrial permeability transition in mediating evodiamine-induced human melanoma A375-S2 cell apoptosis. Free Radic Res 2007; 41: 1099–108.
18 Kiffin R, Bandyopadhyay U, Cuervo AM. Oxidative stress and autophagy. Antioxid Redox Signal 2006; 8: 152–62.
19 Kaushik S, Cuervo AM. Autophagy as a cell-repair mechanism: activation of chaperone-mediated autophagy during oxidative stress. Mol Aspects Med 2006; 27: 444–54.
20 Osawa K, Yasuda H, Maruyama T, Morita H, Takeya K. Antibacteria trichorabdal diterpenes from *Rabdosia trichocarpa*. Phytochemistry 1994; 36: 1287–91.
21 Han QB, Li ML, Li SH, Mou YK, Lin ZW, Sun HD. Ent-kaurane diterpenoids from *Isodon rubescens var lushanensis*. Chem Pharm Bull 2003; 51: 790–3.
22 Zhang YH, Wu YL, Tashiro S, Onodera S, Ikejima T. Involvment of PKC signal pathway in oridonin-induced autophagy in HeLa cells: a protective mechanism against apoptosis. Biochem Biophys Res Commun 2009; 378: 273–8.
23 Wu JN, Huang J, Yang J, Tashiro S, Onodera S, Ikejima T. Caspase inhibition augmented oridonin-induced cell death in murine fibrosarcoma L929 by enhancing reactive oxygen species generation. J Pharmacol Sci 2008; 108: 32–9.
24 Huang J, Wu JN, Tashiro S, Onodera S, Ikejima T. Reactive oxygen species mediate oridonin-induced HepG2 apoptosis through p53, MAPK, and mitochondrial signaling pathways. J Pharmacol Sci 2008; 107: 370–9.
25 Jarrett SG, Albon J, Boulton M. The contribution of DNA repair and antioxidants in determining cell type-specific resistance to oxidative stress. Free Radic Res 2006; 40: 1155–65.
26 Li LH, Wu LJ, Zhou B, Wu Z, Tashiro S, Onodera S, *et al*. Silymarin prevents UV irradiation-induced A375-S2 cell apoptosis. Biol Pharm Bull 2004; 27: 1031–6.
27 Biederbick A, Kern HF, Elsasser HP. Monodansylcadaverine (MDC) is a specific *in vivo* marker for autophagic vacuoles. Eur J Cell Biol 1995; 66: 3–14.
28 Yang ML, Huang TS, Lee Y, Lu FJ. Free radical scavenging properties of sulfinpyrazone. Free Radic Res 2002; 36: 685–93.
29 Venkataraman S, Wagner BA, Jiang X, Wang HP, Schafer FQ, Ritchie JM, *et al*. Overexpression of manganese superoxide dismutase promotes the survival of prostate cancer cells exposed to hyperthermia. Free Radic Res 2004; 38: 1119–32.
30 Zhang YH, Wu YL, Cheng Y, Zhao ZK, Tashiro S, Onodera S, *et al*. Fas-mediated autophagy requires JNK activation in HeLa cells. Biochem Biophys Res Commun 2008; 377: 1205–10.
31 Lemasters JJ, Nieminen AL, Qian T, Trost LC, Elmore SP, Nishimura Y, *et al*. The mitochondrial permeability transition in cell death: a common mechanism in necrosis, apoptosis and autophagy. Biochim Biophys Acta 1998; 1366: 177–96.
32 Liu ZH, Lenardo MJ. Reactive oxygen species regulate autophagy through redox-sensitive proteases. Dev Cell 2007; 12: 484–5.
33 Wang W, Xiong W, Wan J, Sun X, Xu H, Yang X. The decrease of PAMAM dendrimer-induced cytotoxicity by PEGylation via attenuation of oxidative stress. Nanotechnology 2009; 20: 105103.
34 Gao J, Zhu ZR, Ding HQ, Qian Z, Zhu L, Ke Y. Vulnerability of neurons with mitochondrial dysfunction to oxidative stress is associated with down-regulation of thioredoxin. Neurochem Int 2007; 50: 379–85.
35 Tsujimoto Y. Role of Bcl-2 family proteins in apoptosis: apoptosomes and mitochondrial. Genes Cell 1998; 3: 697–707.
36 Rosati E, Sabatini R, Ayroldi E, Tabilio A, Bartoli A, Bruscoli S, *et al*. Apoptosis of human primary B lymphocytes is inhibited by *N*-acetyl-*L*-cysteine. J Leukoc Biol 2004; 76: 152–61.
37 Scherz-Shouval R, Shvets E, Fass E, Shorer H, Gil L, Elazar Z. Reactive oxygen species are essential for autophagy and specifically regulate the activity of Atg4. EMBO J 2007; 26: 1749–60.

Acta Pharmacologica Sinica (2011) 32: 1276–1284
 1671-4083/11 $32.00
www.nature.com/aps

Original Article

# Metabolism of novel anti-HIV agent 3-cyanomethyl-4-methyl-DCK by human liver microsomes and recombinant CYP enzymes

Xiao-mei ZHUANG, Jing-ting DENG, Hua LI[1, *], Wei-li KONG, Jin-xiu RUAN, Lan XIE

*The Key Laboratory of Drug Metabolism and Pharmacokinetics, Beijing Institute of Pharmacology and Toxicology, Beijing 100850, China*

**Aim:** To investigate the metabolism of 3-cyanomethyl-4-methyl-DCK (CMDCK), a novel anti-HIV agent, by human liver microsomes (HLMs) and recombinant cytochrome P450 enzymes (CYPs).
**Methods:** CMDCK was incubated with HLMs or a panel of recombinant cytochrome P450 enzymes including CYP1A2, 2B6, 2C8, 2C9, 2C19, 2D6, 3A4, and 3A5. LC-ion trap mass spectrometry was used to separate and identify CMDCK metabolites. In the experiments with recombinant cytochrome P450 enzymes, specific chemical inhibitors combined with CYP antibodies were used to identify the CYP isoforms involved in CMDCK metabolism.
**Results:** CMDCK was rapidly and extensively metabolized by HLMs. Its intrinsic hepatic clearance estimated from the *in vitro* data was 19.4 $mL \cdot min^{-1} \cdot kg^{-1}$, which was comparable to the mean human hepatic blood flow rate (20.7 $mL \cdot min^{-1} \cdot kg^{-1}$). The major metabolic pathway of CMDCK was oxidation, and a total of 14 metabolites were detected. CYP3A4 and 3A5 were found to be the principal CYP enzymes responsible for CMDCK metabolism.
**Conclusion:** CMDCK was metabolized rapidly and extensively in human hepatic microsomes to form a number of oxidative metabolites. CYP3A4 and 3A5 were the predominant enzymes responsible for the oxidation of CMDCK.

**Keywords:** anti-HIV agent; 3-cyanomethyl-4-methyl-DCK; drug metabolism; enzyme kinetics; liver microsomes; cytochrome P450; CYP3A4; CYP3A5

*Acta Pharmacologica Sinica* (2011) 32: 1276–1284; doi: 10.1038/aps.2011.91

## Introduction

Acquired Immunodeficiency syndrome (AIDS) remains an enormous health threat for humans despite the fact that available chemotherapeutic agents have increased in number and effectiveness in recent years. Currently, 7400 people become infected with human immunodeficiency virus (HIV) every day all over the world. As of 2008, the US Food and Drug Administration (FDA) and European Medicines Agency (EMA) has approved 25 anti-HIV drugs for clinical use, including 5 fixed-dose combinations to deal with the decreased sensitivity of drugs caused by the rapid emergence of drug-resistant mutants[1]. Thus, more effective drugs with novel mechanisms of action or resistance profiles different from those of currently available anti-HIV therapeutics are urgently necessary[2].

3′,4′-Dicamphanoyl-(+)-*cis*-khellactone (DCK) and its analogs are a novel class of non-nucleoside reverse transcriptase inhibitors (NNRTIs) with a novel mechanism. They inhibit DNA-dependent DNA polymerase activity, in contrast to currently marketed NNRTI drugs, which interfere with the RNA polymerase activity of HIV-1 RT[3, 4]. In our prior studies, 3-cyanomethyl-4-methyl-DCK (CMDCK), a DCK analog, was identified as a promising preclinical agent. It exhibited high potency against the replication of both laboratory-adapted HIV strains and primary HIV-1 isolates in a $CD4^+$ T cell line and PBMCs, respectively, as well as moderate efficacy against multidrug-resistant HIV strains ($EC_{50}/EC_{90}$). Preliminary pharmacokinetic studies indicated that CMDCK has a marginal oral bioavailability (approximately 15%) in rats[5]. Only a very small amount of parent compound was recovered from the urine and bile after oral administration in rats. This result indicated that metabolism was the major elimination pathway of CMDCK in the body. In *in vitro* stability tests, a higher metabolic rate was noted in HLMs than in RLMs (rat liver microsomes) and DLMs (dog liver microsomes), suggesting

* To whom correspondence should be addressed.
E-mail amms_hli@126.com
Received 2011-01-20 Accepted 2011-06-08

that CMDCK may undergo extensive first-pass metabolism in humans.

In the present study, LC-ESI/MS/MS was used to characterize the major oxidative metabolites formed in pooled human liver microsomes (HLMs). The role of CYP enzymes in the biotransformation and metabolic pathways of the candidate drug was investigated using both recombinant human CYP enzymes and HLMs combined with specific CYP antibodies and selective chemical inhibitors.

## Materials and methods

### Chemicals and materials

CMDCK and an internal standard (chemical structure presented in Figure 1) were synthesized in house with a purity of 98.5% determined by HPLC. Ketoconazole (KET), troleandomycin (TAO), ritonavir (RIT), naphthoflavone, sulfaphenazole, tranylcypromine, quinidine and NADPH were purchased from Sigma-Aldrich (St Louis, MO, USA). Pooled HLMs, human recombinant cytochrome P450 enzymes (CYP1A2, CYP2B6, CYP2C8, CYP2C9, CYP2C19, CYP2D6, CYP3A4, and CYP3A5) with reductase and anti-human CYP2D6 and CYP3A4 antibodies were purchased from BD Gentest Corporation (Woburn, MA, USA). Unless specified, all other reagents and solvents were the highest purity available and were purchased from Sigma-Aldrich Chemical Co (St Louis, USA). All buffers and reagents were prepared with high-purity water (Milli-Q; Millipore, Bedford, MA, USA).

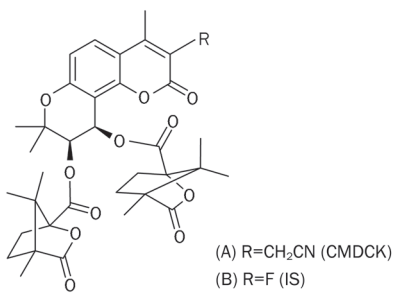


**Figure 1.** Chemical structures of (A) 3-cyanomethyl-DCK (CMDCK) and (B) IS.

### Identification of CMDCK metabolites in HLMs

The incubation mixtures contained CMDCK (10 μmol/L), pooled HLMs (1 mg/mL), and NADPH (1 mmol/L) in 100 mmol/L sodium phosphate buffer (pH 7.4). The reactions were started by the addition of an NADPH solution after a 5-min preincubation. Incubations were carried out at 37 °C for 60 min and stopped by adding an equal volume of ice-cold methanol/acetonitrile (1/4, *v/v*). The suspension was centrifuged (20000×*g*, 10 min), and an aliquot (20 μL) of the supernatant was analyzed directly by HPLC/PDA for metabolite screening and by LC/MS/MS for structural elucidation.

### CYP phenotyping of CMDCK with recombinant CYP enzymes

CMDCK (4 μmol/L, unless otherwise indicated, dissolved in incubation buffer) was incubated separately in sodium phosphate buffer (100 mmol/L, pH 7.4) containing recombinant CYP1A2, CYP2B6, CYP2C8, CYP2C9, CYP2C19, CYP2D6, CYP3A4, and CYP3A5 coexpressed with cytochrome b5 in a final volume of 200 μL. Supersomes were used at P450 protein concentrations of 25 nmol/L. After preincubation for 5 min at 37 °C, the reaction was initiated by the addition of NADPH (1.0 mmol/L) and was terminated at 30 min by adding 200 μL of cold acetonitrile. Subsequently, 400 μL of IS solution (3.8 μmol/L, dissolved in acetonitrile) was added to the samples, followed by centrifugation (10 min, 20000×*g*, 4 °C). An aliquot of 100 μL of supernatant was taken for ESI-LC-MS analysis as described below. Control microsomes prepared from insect cells infected with wild-type baculovirus were used as negative controls for native enzyme activities. The incubations were performed in triplicate.

### Chemical inhibition and immunoinhibition studies in HLMs

For chemical inhibition studies, CMDCK (4 μmol/L) was incubated with pooled HLMs in the absence (control) and presence of selective CYP chemical inhibitors for 30 min. The inhibitors used were naphthoflavone (50 μmol/L) for CYP1A2, sulfaphenazole (10 μmol/L) for CYP2C9, tranylcypromine (50 μmol/L) for CYP2C19, quinidine (10 μmol/L) for CYP2D6, and KTZ (1, 2, or 5 μmol/L), RIT (1, 2, or 5 μmol/L), and TAO (100, 250, or 500 μmol/L) for CYP3A4. TAO, a time-dependent-mechanism–based inhibitor of CYP3A4, was preincubated at 37 °C for 15 min with HLMs and NADPH before the substrate was added to start the reaction. Control incubations were carried out in appropriate solvents (incubation buffer or 0.1% DMSO) that contained no inhibitors.

In immunoinhibition studies, the concentrations of the CYP2D6 and CYP3A4 antibodies used in the experiments were in accordance with the manufacturers' instructions. The incubation conditions were from the same as those used for the kinetic analyses, except that the HLMs and antibodies were preincubated for 15 min on ice before addition of the remaining incubation constituents. Control incubations were similarly preincubated but did not contain antibodies. Experiments were performed in triplicate.

### Kinetics studies using HLMs and recombinant CYP3A4 enzymes

Preliminary experiments (data not shown) were performed to determine the optimal incubation conditions in HLMs to ensure linearity with respect to the microsomal protein concentration and the incubation time. A typical incubation contained 0.5 mg/mL of HLMs, 4 μmol/L of CMDCK, 1 mmol/L of NADPH, 5 mmol/L of $MgCl_2$, and 100 mmol/L of sodium phosphate buffer (pH 7.4) in a final volume of 200 μL. Incubation reactions were started and stopped as described above. The supernatant was directly analyzed by ESI-LC-MS as described below. Negative control incubations were performed by omitting NADPH.

Kinetic parameters (apparent $K_m$ and $V_{max}$) in the pooled HLMs (0.5 mg/mL) and CYP3A4 (25 nmol/L) samples were determined with a series of CMDCK concentrations ranging

from 0.25 to 25 μmol/L. All incubations were performed in duplicate.

### Instrumental analysis

A Thermo Finnigan Surveyor HPLC and a tandem Thermo Finnigan LCQ Ion Trap Mass Spectrometer (ITMS) equipped with an auto-sampler, a PDA detector and a Thermo Kromasil C18 analytical column (3 mm×50 mm id, 5 μm) were used for metabolite identification. A linear gradient elution was performed with the mobile phase consisting of 0.1% aqueous formic acid solution (A) and methanol (B). The gradient began with 20% B, increased linearly to 50% B in the first 4 min, then 70% B in the next 13 min, and back to the initial composition in 2 min, followed by 2 min to re-equilibrate the column. The ITMS with an electrospray ionization (ESI) source, was operated in a positive ionization mode. The operating conditions were as follows: spay voltage of 4.5 kV, capillary temperature of 225 °C, capillary voltage of 20 V, sheath gas of 40 arbitrary units, and collision energy of 50 eV. Ion trap full scan analyses were conducted from *m/z* 500 to 800.

The quantitative analysis of CMDCK was carried out using an Agilent Single Quadrupole Mass Spectrometer (Agilent, Palo Alto, CA, USA) attached to an Agilent 1100 HPLC. ChemStation (Version A 09; Agilent, Palo Alto, CA, USA) was used to control the operation of these instruments and acquire the data. CMDCK and its major metabolites were separated on a 2.1 mm×100 mm BetaBasic C18 column (Thermo Electron, USA) with a 55/45 acetonitrile/water mixture containing 0.1% formic acid. The total running time was 17 min at a flow rate of 0.2 mL/min. The MS assay was conducted using the MSDVL electro-spray interface, operating in positive selective ion monitoring (SIM) mode. The detected ions were selected at *m/z* 693 $[(M+NH_4)^+]$ for the quantitative analysis of CMDCK. The ions at 709 $[(M+O+NH_4)^+]$, 725 $[(M+2O+NH_4)^+]$, and 723 $[(M+2O-2H+NH_4)^+]$ were selected to screen mono-oxidized, di-oxidized and carboxylic metabolites, respectively.

Calibration curves and quality control samples were prepared in heat-inactivated human liver microsomal suspensions at the same protein concentration (0.5 mg/mL) used for incubations. The peak area ratios of CMDCK to the internal standard were linear over the range of 0.1–100 μmol/L. The intraday (within batch) accuracy and precision of the LC-MS assay were determined by repeatedly analyzing the spiked microsomal samples ($n$=3) at three concentration levels (low, medium and high levels) within the calibration range (*ie*, 0.25, 5, or 50 μmol/L). Inter-day data were obtained by analyzing the same set of spiked samples in duplicate over 3 consecutive days.

### Data analysis

The elimination half-life ($t_{1/2}$) of CMDCK was calculated as $t_{1/2}$=0.693/$k$, where $k$ is the slope of the line obtained by linear regression of the natural logarithmic percentage (ln %) of the remaining parent drug CMDCK versus the incubation time (min). Conversion of *in vitro* $CL_{int}$ was done using the following formula[6]:

$$CL_{int} = \frac{0.693}{in\cdot vitro\cdot T_{1/2}} \times \frac{mL\cdot incubation}{mg\cdot microsomes} \times \frac{mg\cdot microsomes}{g\cdot organ} \times \frac{g\cdot organ}{kg\cdot B.W.}$$

where the microsomal yield (mg/g organ)[7] and liver weight (g/kg body weight) were taken from the literature[8, 9].

Apparent $K_m$ and $V_{max}$ constants were determined using a Lineweaver-Burk plot. The values of CYP3A4 were normalized using nominal amounts of CYP3A4 in HLMs[10].

The *in vitro* value was extrapolated to the *in vivo* intrinsic clearance ($CL_h$, $mL\cdot min^{-1}\cdot kg^{-1}$ body weight) according to the equation[11]:

$$CL_{int} = \frac{Q \times CL_{int}}{Q + CL_{int}}$$

where $Q$ represents organ blood flow. The hepatic blood flow rate for humans used in the calculation of $CL$ was 20 $mL\cdot min^{-1}\cdot kg^{-1}$ [12].

## Results

### Metabolite profiling and identification

The biotransformation of CMDCK in HLMs was NADPH dependent, and CMDCK depletion was rapid. A typical HPLC-UV chromatogram of CMDCK metabolites in HLMs is presented in Figure 2. In addition to the parent drug, six major peaks corresponding to the metabolites M1 (+O), M4 (+O), M7 (+O-2H), M12 (+2O-2H), M13 (+3O-2H), and M14 (+3O-2H) were observed. Eight minor metabolites, namely M2-M3 (+O), M5, M6 ($-C_{10}H_{12}O_3$), and M8-M11 (+2O), were also detected in HLMs using the selected ion scan mode of the LC-ITMS (Figure 3). All these metabolites were absent from the control samples without NADPH.

The structural elucidation of CMDCK metabolites was based on ITMS mass spectra. Multiple MS involving repeated

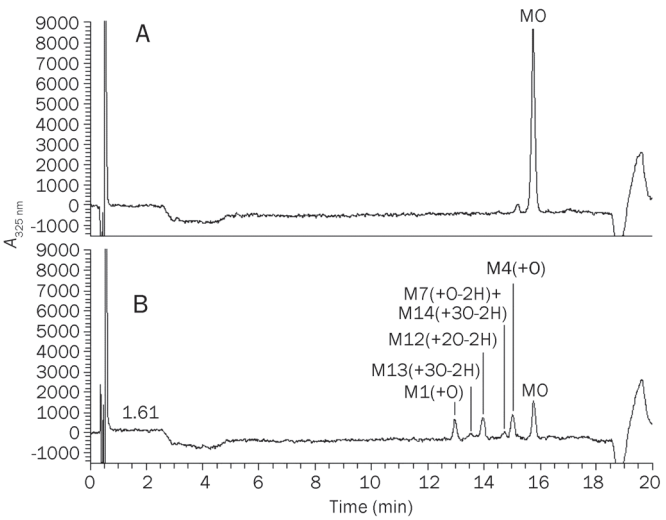


Figure 2. Representative HPLC-UV chromatograms of incubation mixtures of CMDCK with HLMs. (A) Negative control sample without NADPH. (B) Experimental sample with NADPH. CMDCK (4 μmol/L) was incubated with HLMs (0.5 mg/mL) for 30 min at 37 °C in the presence of NADPH (1.0 mmol/L). Metabolites were identified by LC/MS/MS.

trapping and fragmentation of ions was employed to obtain the fragmentation pattern of CMDCK and its metabolites. The ester/ether structure of CMDCK makes it somewhat lipophilic, and it is also lacks basic N-atoms amenable to electronspay ionization (ESI). This compound was first expected to have an unfavorable MS response. During the development of the LC-MS method, however, it was found that this compound has an extraordinarily high MS response in the positive ion mode, with $M+NH_4^+$, $M+Na^+$, and $M+K^+$ adduct ions. The abnormally high ionization potential of these ions is rationalized in Figure 4 (top). The *cis*-conformation of the two camphanic acid ester moieties of CMDCK provides an negative electron cavity that can stabilize a relatively large positive ion such as $NH_4^+$, $Na^+$, or $K^+$, whereas a proton ($H^+$) might be too small to fit. The MS detector was further tuned for the dominance of the $M+NH_4^+$ ion, as metal ion adducts such as $M+Na^+$ and $M+K^+$ are often not ideal for $MS^n$-based fragmentation and structural elucidation.

The high MS response of the $M+NH_4^+$ ion provided a solid foundation for detecting and profiling metabolites, including minor ones. The $MS^2$ spectra of the parent compound with the fragment interpretation are presented in Figure 4 (bottom). The collision energy (CE) in the $MS^2$ analysis for *m/z*=693 was optimized to 50–60 eV so that the major daughter ion in the $MS^2$ spectrum, *ie*, *m/z*=478, could undergo further collision-induced dissociation to form abundant smaller fragments that could also be produced in subsequent $MS^3$ analysis (data not shown). With this approach, $MS^2$ spectra of CMDCK and its metabolites provided rich fragmentation information for structural elucidation, while $MS^3$ spectra did not provide further useful information for the structural elucidation of the metabolites.

Three characteristic product ions from the ammonium-adducted molecular ion of CMDCK were observed at *m/z* 478, 298 and 280. The ion *m/z* 478 corresponded to the loss of either the 3′- or the 4′-camphanoyl moiety, and *m/z* 298 was generated from *m/z* 478 by further loss of the remaining camphanoxyl group. The fragment ion *m/z* 280 resulted from the loss of both 3′-and 4′-camphanoyl moieties from the ammonium-adducted molecular ion. Accordingly, a neutral loss of (*m/z* 215) could be observed for either of the two camphanoyl moieties.

The ammonium-adducted molecular ions ($[M+NH_4]^+$) of CMDCK metabolites with changes in observed mass (ΔM) relative to the parent and the spectral data of their product ions together with the fragmentation interpretation are listed in Table 1. The major metabolic pathway of CMDCK in HLMs was oxidation to form mono-oxidized (M1-M4, M7), di-oxidized (M8-M11) and tri-oxidized (M13 and M14) metabolites. The oxidation occurred on one or both the camphanoxyl groups or on the khellactone moiety. Two metabolites (M6 and M7) with one camphanoxyl group missing at either the 3′ or 4′ position as the result of ester hydrolysis were also observed. The proposed metabolic pathway and the putative metabolites of CMDCK in HLMs are presented in Figure 5. Further structural elucidation of the CMDCK metabolites would be required to identify the exact oxidized positions of the metabolites. Such experiments will have to be carried out in the late drug development stage, after standard reference substances of the metabolites are available or after purified metabolites are obtained from *in vitro* or *in vivo* samples and analyzed using other instrumental analytical techniques, such as nuclear magnetic resonance.

### Validation of the quantitative LC-MS method

The calibration curves were obtained over the CMDCK concentration range of 0.1–100 μmol/L. The mean regression equation of five replicates on different days was $Y$=-0.136787+0.00824407$X$, and the correlation coefficient ($r^2$) was greater than 0.9947. The LLOQ of 0.1 μmol/L was deter-

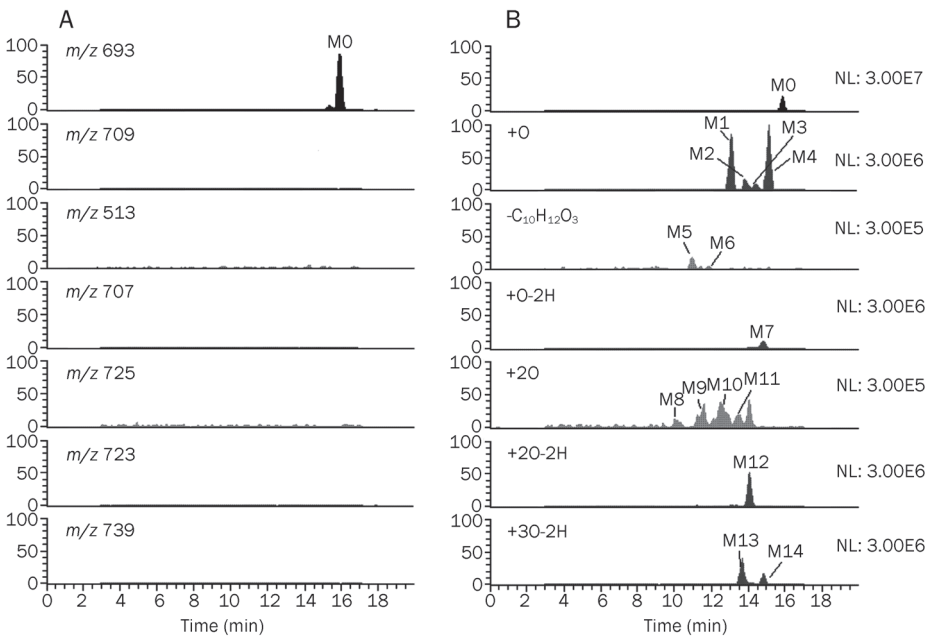


**Figure 3.** The selected ion chromatograms of CMDCK incubated with HLMs. Control sample without NADPH. (B) Experimental sample with NADPH.

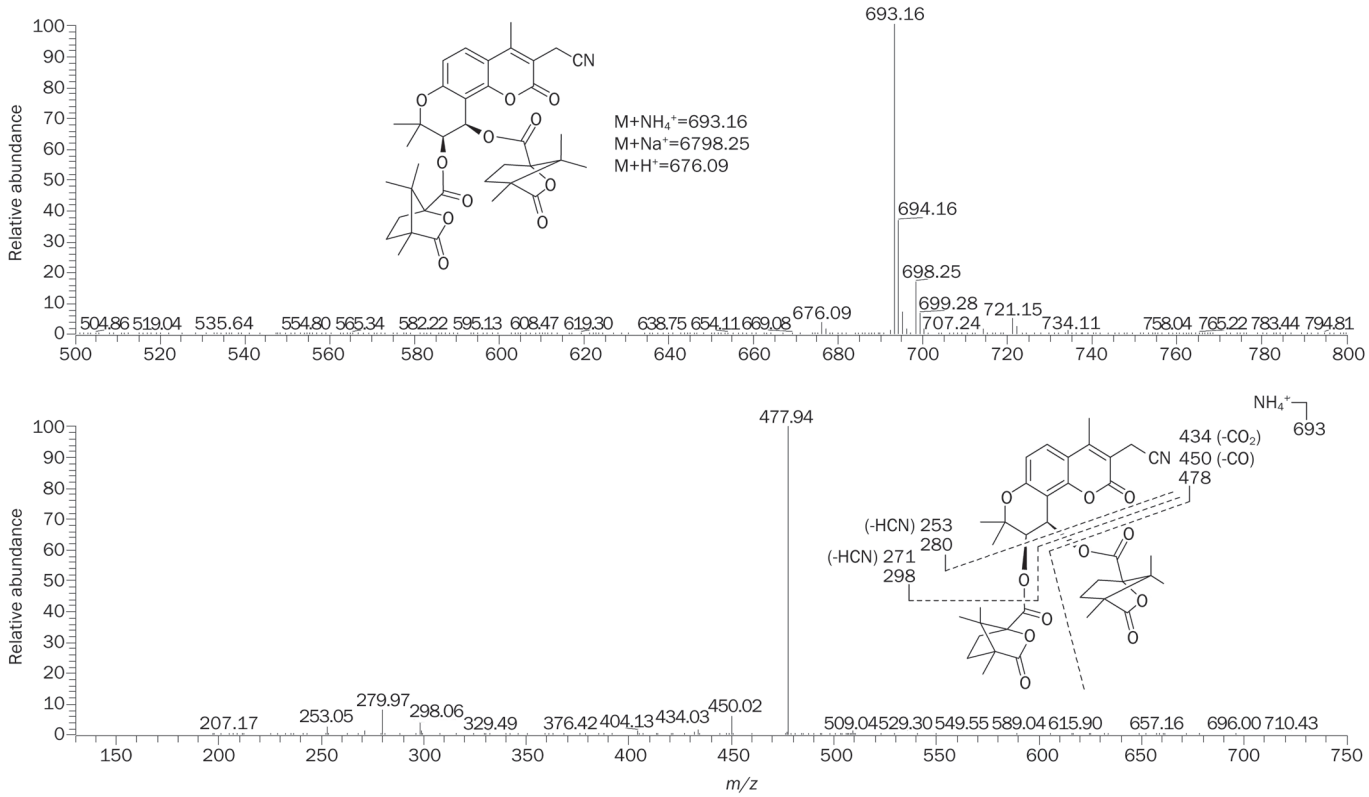


**Figure 4.** The MS and $MS^2$ spectra of CMDCK with fragment interpretation.

**Table 1.** MS fragments and the interpretation of CMDCK metabolites in human liver microsomes.

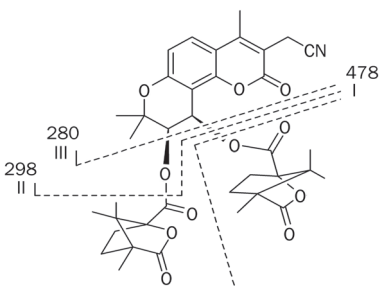


| Parent or metabolites | MW | $M+NH_4^+$ | Reaction | ΔM | Fragmentations I | II | III |
|---|---|---|---|---|---|---|---|
| M0 | 675 | 693 | | | 478 | 298 | 280 |
| M1, M2, M4 | 691 | 709 | +O | 16 | 494 | 298 | 280 |
| M3 | 691 | 709 | +O | 16 | 494 | 314 | 296 |
| M5 | 495 | 513 | $-C_{10}H_{12}O_3$ | 180 | | 298 | |
| M6 | 495 | 513 | $-C_{10}H_{12}O_3$ | 180 | 478 | 298 | |
| M7 | 689 | 707 | +O-2H | 14 | 492 | 298 | 280 |
| M8 | 707 | 725 | +2O | 32 | 494 | 298 | 280 |
| M9 | 707 | 725 | +2O | 32 | 510 | 314 | 296 |
| M10 | 707 | 725 | +2O | 32 | 510 | 298 | 280 |
| M11 | 707 | 725 | +2O | 32 | 494 | 298 | 280 |
| M12 | 705 | 723 | +2O-2H | 30 | 508 | 298 | 280 |
| M13, M14 | 721 | 739 | +3O-2H | 46 | 524 | 298 | 280 |

Fragment ion spectra of ammonium-adducted molecular ions were obtained with a Finnigan LCQ Ion Trap Mass Spectrometer (see Materials and methods).

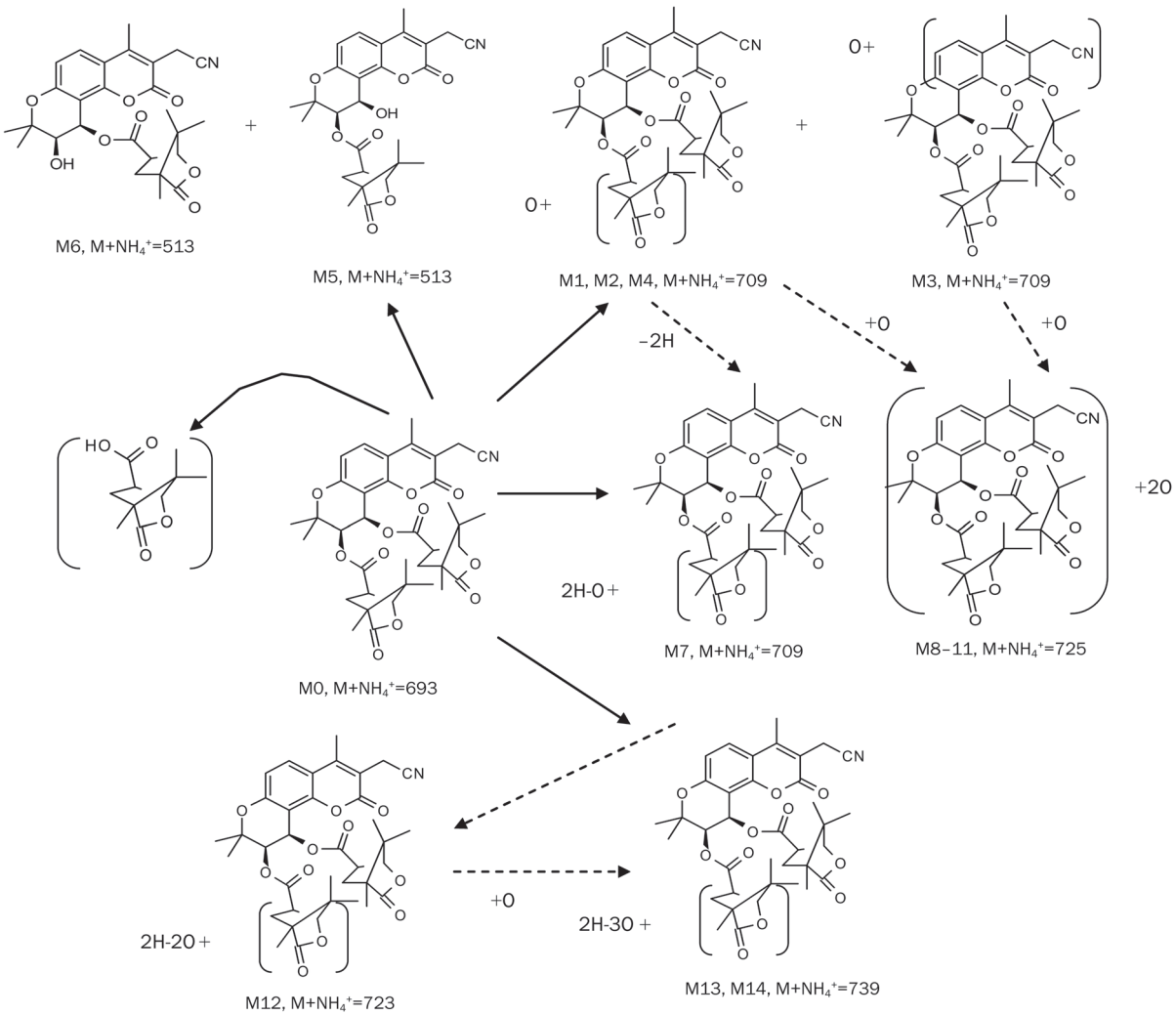


**Figure 5.** Proposed metabolic pathway of CMDCK in HLMs.

mined based on a signal/noise ratio of 6:1 and on satisfactory precision (RSD<±20%) and accuracy (RE<±20%). The intra- and inter-day precisions and accuracies for CMDCK were assessed based on the analysis of QC samples at three concentration levels (*ie*, 0.25, 5, or 50 μmol/L). The intra-day precisions, expressed as RSD, were all below 11.0%, and the inter-day precisions were <9.0%. The intra-day accuracy ranged from 91.0% to 111.6%, and the inter-day accuracy ranged from 88.6% to 112.4%. All of these values were within the acceptable range (≤15%).

### Identification of the CYP isoforms responsible for CMDCK metabolism

Among a panel of eight recombinant human CYP enzymes used for this study, CYP3A4 and 3A5 exhibited a significant catalytic activity related to CMDCK metabolism (Figure 6). All

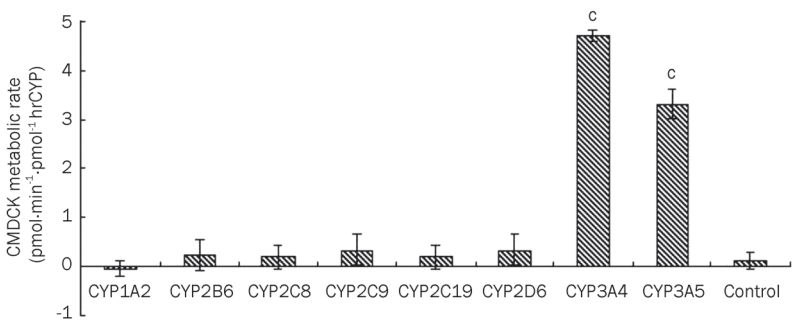


**Figure 6.** Metabolic rate of CMDCK when incubated with recombinant human CYP isoforms. Incubations were performed using 4 μmol/L of CMDCK, 25 nmol/L of P450 microsomal protein and 1 mmol/L of NADPH for 30 min at 37 °C. Each bar represents the mean of duplicate determinations. A paired *t*-test was used to determine the significant difference in the CMDCK metabolic rate between individual CYP isoforms and the control group. $^{c}P<0.01$ *vs* control.

of the major metabolites observed in HLMs were also detected in the CYP3A4 incubates, whereas no notable metabolic disappearance of the parent was observed in the samples with CYP1A2, 2B6, 2C8, 2C9, 2C19, and 2D6 compared to the control. When the reaction mixtures of these 6 CYP isoenzymes were analyzed using SIM scan mode with the selected ions for major metabolites, no substantial formation of metabolites was observed. CYP3A4 and 3A5 were determined to be the primary CYP isoforms responsible for CMDCK metabolism.

### Enzyme kinetics of CMDCK metabolism

The metabolic rates and enzyme kinetic parameters were determined based on the metabolic elimination of the parent compound because currently no standard reference substances for the metabolites are available.

The apparent enzyme kinetic parameters of CMDCK incubated with pooled HLMs and recombinant CYP3A4 are summarized in Table 2. Both the $K_m$ and $V_{max}$ for CMDCK in recombinant CYP3A4 were similar to those in HLMs.

### Inhibition of CMDCK metabolism by CYP chemical inhibitors and specific antibodies

The inhibitory effects of the selective chemical inhibitors and immunoinhibitory monoclonal antibodies on CYP3A4 were evaluated at three concentration levels (Table 3) because the substrate specificity and inhibitors for CYP3A4 and CYP3A5 overlapped. The known potent CYP3A4 inhibitors KET and RIT inhibited the formation of the major oxidative metabolites in a concentration-dependent manner. The inhibitory rates at the levels of 1, 2, and 5 μmol/L were 68.3%, 81.9%, and 90.1%, respectively, for KET and 66.7%, 77.5%, and 91.1%, respectively, for RIT. TAO, a mechanism-based CYP3A4 inhibitor, also dose-dependently attenuated CMDCK elimination in liver microsomes with inhibitory rates of 30.8%, 55.9%, and 80.2% at 100, 250, and 500 μmol/L, respectively. However, the effects of the selective inhibitors on CYP1A2, 2C9, 2C19, and 2D6 were found to be either negligible or negative, with inhibitory rates of -0.95%, -0.93%, -1.07%, and 0.45%, respectively.

When CMDCK was incubated with the pooled HLMs in the presence of immunoinhibitory CYP antibodies, only CYP3A4 antibody showed a significant inhibitory effect on CMDCK metabolism, with an inhibitory rate up to 83.9%. The effect of the CYP3A4 antibody was also concentration dependent. In contrast, the CYP2D6 antibody did not show any inhibitory effect on the metabolism of CMDCK. This result provides further evidence demonstrating the predominant role of CYP3A4/3A5 in CMDCK metabolism.

**Table 3.** Inhibitory effects of selective CYP3A4 inhibitors and specific CYP3A4 antibody on CMDCK metabolism in human liver microsomes (mean±SD, *n*=3).

| Inhibitors or monoclonal antibody to CYP3A4 | Concentrations (μmol/L or mg/mL protein) | Inhibitory rate (%) |
|---|---|---|
| Ketoconazole | 1 | 68.3±9.61 |
| | 2 | 81.9±1.60 |
| | 5 | 90.1±5.20 |
| Ritonavir | 1 | 66.7±1.76 |
| | 2 | 77.5±2.36 |
| | 5 | 91.1±5.47 |
| Troleandomycin | 100 | 30.8±4.98 |
| | 250 | 55.9±3.15 |
| | 500 | 82.0±1.70 |
| MAB-CYP3A4 | 1 | 74.9±4.37 |
| | 5 | 83.9±4.03 |

## Discussion

The metabolic stability test of fourteen DCK derivatives indicated that these compounds were all rapidly and extensively metabolized in HLMs under oxidative conditions[13]. CMDCK, a novel DCK analog, was found to have a similar metabolic stability in HLMs. Following the standard metabolic study protocol[14], the enzyme concentrations (0.2–4 mg/mL), reaction times (0–90 min), and substrate concentrations (0.25–50 μmol/L) were optimized. The metabolic kinetic study of CMDCK was subsequently conducted at an enzyme content of 0.5 mg/mL, a substrate concentration of 4 μmol/L and an incubation time of 30 min. As the key parameter for the *in vitro-in vivo* correlation, the intrinsic clearance ($CL_{int}$) for CMDCK was directly obtained from the *in vitro* $T_{1/2}$[15, 16], based on the widely accepted well-stirred model. The hepatic clearance ($CL_h$) was then estimated using *in vitro* $CL_{int}$ data (Table 2). It was noted that the $CL_h$ (19.4 mL·min$^{-1}$·kg$^{-1}$) of CMDCK was comparative to the mean human hepatic blood flow rate (20.7 mL·min$^{-1}$·kg$^{-1}$), which indicated that the liver metabolism of CMDCK would be the predominant elimination pathway *in vivo*.

The CYP reaction phenotyping of CMDCK was conducted using both cDNA-expressing human CYP enzymes and pooled HLMs combined with chemical inhibitors and mono-

**Table 2.** Kinetic parameters of CMDCK metabolism in reactions with pooled liver (HLMs) and recombinant CYP3A4 enzymes and prediction of the hepatic clearance of CMDCK.

| | $t_{1/2}$ min | $CL_{int}$ mL·min$^{-1}$·kg$^{-1}$ | $CL_h$ mL·min$^{-1}$·kg$^{-1}$ | $Q_h$ mL·min$^{-1}$·kg$^{-1}$ | $K_m$ μmol·L$^{-1}$ | $V_{max}$ pmol·min$^{-1}$·mg$^{-1}$ |
|---|---|---|---|---|---|---|
| HLM | 5.62±0.57 | 311.6±30.8 | 19.4±0.12 | 20.7 | 14.3 | 1.78 |
| CYP3A4 | 6.84±1.55 | – | – | – | 12.1 | 1.58 |

clonal antibodies. Among the eight commonly used CYP isoenzymes (CYP1A2, 2B6, 2C8, 2C9, 2C19, 2D6, 3A4, and 3A5), only CYP3A4 and 3A5 showed significant CMDCK metabolism activity. It is well known that the CYP3A subfamily, consisting mainly of CYP3A4 and 3A5 in adults, is responsible for the metabolism of more than half of therapeutic agents that undergo oxidation[17]. CYP3A4 and 3A5 share most of the same substrates[18], and *in vitro* investigations have indicated that CYP3A5 can be less susceptible to inhibition than CYP3A4. In the present study, CYP3A4 and CYP3A5 were identified to be the principal enzymes involved in CMDCK metabolism in the human liver. Oxidation was the major metabolic pathway of CMDCK. A number of metabolites including 12 oxidative products and 2 hydrolysis metabolites, were identified. The oxidation occurred on either of the two camphanoyl groups or on the khel lactone moiety. The rapid and extensive CMDCK metabolism mediated by CYP3A4 and CYP3A5 might lead to low bioavailability in the human body[19, 20].

In general, a higher conversion rate of a drug candidate *in vitro* is unfavorable because the conversion rate is predictive of higher hepatic clearance *in vivo*, resulting in a significant first pass effect for oral administration[21]. In fact, a number of clinically available anti-HIV agents exhibit significant first-pass hepatic metabolism. This problem was solved by the drug combination regime called HAART (highly active antiretroviral therapy), whose goals were same as those of the treatment of tuberculosis[22]. In this study, significant inhibitory effects on CMDCK metabolism were observed for the potent CYP3A4/3A5 inhibitors ketoconazole, ritonavir and troleandomycin. This result suggested that coadministration of CMDCK with a potent CYP3A inhibitor, such as ritonavir, would enhance its hepatic metabolic stability and subsequently improve its bioavailability in the body. Ritonavir is a protease inhibitor clinically used as an anti-HIV drug. It also widely used as a CYP3A4 inhibitor to boost the effect of other anti-HIV agents for the treatment of AIDS[23]. Some research has indicated that the elevation and prolongation of the plasma levels of some protease inhibitors (such as tipranavir, saquinavir or indinavir) by ritonavir coadministration may produce a composite suppression of HIV viral replication in excess of the sum of that was observed with either agent individually[24, 25]. The effect of ritonavir on CMDCK pharmacokinetics will be further assessed *in vitro* and *in vivo*.

In summary, CMDCK was metabolized rapidly in human hepatic microsomes to form a number of oxidative metabolites. CYP3A4 and CYP3A5 were the predominant enzymes involved in the oxidation of CMDCK.

## Acknowledgements

This study was supported by Chinese National Science & Technology Major Special Project on Major New Drug Innovation (2009ZX09102-008) and by a grant from the Beijing Municipal Science and Technology Commission (D0206001040191). We thank Dr Yao-qiu ZHU of MetabQuest Co for his generous assistance with metabolite identification.

## Author contribution

Xiao-mei ZHUANG and Hua LI were responsible for the study design, data analysis, and writing of the paper. Xiao-mei ZHUANG, Jing-ting DENG, and Wei-li KONG conducted the experiments. Lan XIE was responsible for the CMDCK project, and she also provided the CMDCK standard. Jin-xiu RUAN was a senior advisor and provided valuable advice.

## References

1 De Clercq E. Anti-HIV drugs: 25 compounds approved within 25 years after the discovery of HIV. Int J Antimicrob Agents 2009; 33: 307–20.
2 Kostova I, Raleva S, Genova P, Argirova R. Structure-activity relationships of synthetic coumarins as HIV-1 Inhibitors. Bioinorg Chem Appl 2006; 68274.
3 Huang L, Yuan X, Yu D, Lee KH, Chen CH. Mechanism of action and resistant profile of anti-HIV coumarin derivatives. Virology 2005; 332: 623–8.
4 Xie L, Zhao CH, Zhou T, Chen HF, Fan BT, Che XH, *et al*. Molecular modeling, design, synthesis, and biological evaluation of novel 3′,4′-dicamphanoyl-(+)-*cis*-khellactone (DCK) analogs as potent anti-HIV agents. Bioorg Med Chem 2005; 13: 6435–49.
5 Xie L, Guo HF, Lu H, Zhuang XM, Zhang AM, Wu G, *et al*. Development and preclinical studies of broad-spectrum anti-HIV agent (3′*R*,4′*R*)-3-cyanomethyl-4-methyl-3′,4′-di-*O*-(S)-camphanoyl-(+)-*cis*-khellactone (3-cyanomethyl-4-methyl-DCK). J Med Chem 2008; 51: 7689–96.
6 Obach RS. Prediction of human clearance of twenty-nine drugs from hepatic microsomal intrinsic clearance data: An examination of *in vitro* half-life approach and nonspecific binding to microsomes. Drug Metab Dispos 1999; 27: 1350–9.
7 Houston JB. Utility of *in vitro* drug metabolism data in prediction of *in vivo* metabolic clearance. Biochem Phannacol 1994; 47: 1469–79.
8 Davies B, Morris T. Physiological parameters in laboratory animals and humans. Pharm Res 1993; 10: 1093–5.
9 Gerlowski LE, Jain RK. Physiologically based pharmacokinetic modeling: Principles and applications. J Pham Sci 1983; 72: 1103–27.
10 Rodrigues AD. Integrated cytochrome P450 reaction phenotyping: attempting to bridge the gap between cDNA-expressed cytochromes P450 and native human liver microsomes. Biochem Pharmacol 1999; 57: 465–80.
11 Yamazaki M, Suzuki H, Sugiyama Y. Recent advances in carrier-mediated hepatic uptake and biliary excretion of xenobiotics. Pharm Res 1996; 13: 497–513.
12 Boxenbaum H. Interspecies variation in liver weight, hepatic blood flow, and antipyrine intrinsic clearance: extrapolation of data to benzodiazepines and phenytoin. J Pharmacokinet Biopharm 1980; 8: 165–76.
13 Suzuki M, Li Y, Smith PC, Swenberg JA, Martin DM, Morris-Natschke SL, *et al*. Anti-AIDS agents 65: investigation of the *in vitro* oxidative metabolism of 3′,4′-Di-*O*-(−)-camphanoyl-(+)-*cis*-khellactone derivatives as potent anti-HIV agents. Drug Metab Dispos 2005; 33: 1588–92.
14 Masimirembwa CM, Bredberg U, Andersson TB. Metabolic stability for drug discovery and development: pharmacokinetic and biochemical challenges. Clin Pharmacokinet 2003; 42: 515–28.
15 Obach RS, Baxter JG, Liston TE, Silber BM, Jones BC, MacIntyre F, *et al*. The prediction of human pharmacokinetic parameters from preclinical and *in vitro* metabolism data. J Pharmacol Exp Ther 1997; 283: 46–58.
16 Reddy A, Heimbach T, Freiwald S, Smith D, Winters R, Michael S, *et al*. Validation of a semi-automated human hepatocyte assay for the

determination and prediction of intrinsic clearance in discovery. J Pharm Biomed Anal 2005; 37: 319–26.
17 Wilkinson GR. Drug metabolism and variability among patients in drug response. N Engl J Med 2005; 352: 2211–21.
18 Huang W, Lin YS, McConn DJ 2nd, Calamia JC, Totah RA, Isoherranen N, *et al*. Evidence of significant contribution from CYP3A5 to hepatic drug metabolism. Drug Metab Dispos 2004; 32: 1434–45.
19 Li W, Liu Y, He YQ, Zhang JW, Gao Y, Ge GB, *et al*. Characterization of triptolide hydroxylation by cytochrome P450 in human and rat liver microsomes. Xenobiotica 2008; 38: 1551–65.
20 Kim AR, Lim SJ, Lee BJ. Metabolic inhibition and kinetics of raloxifene by pharmaceutical excipients in human liver microsomes. Int J Pharm 2009; 368: 37–44.
21 Shin HS, Bae SK, Lee MG. Pharmacokinetics of sildenafil after intravenous and oral administration in rats: hepatic and intestinal first-pass effects. Int J Pharm 2006; 320: 64–70.
22 Cahn P, Villacian J, Lazzarin A, Katlama C, Grinsztejn B, Arasteh K, *et al*. Ritonavir-boosted tipranavir demonstrates superior efficacy to ritonavir — boosted protease inhibitors in treatment-experienced HIV-infected patients: 24-week results of the RESIST-2 trial. Clin Infect Dis 2006; 43: 1347–56.
23 MacGregor TR, Sabo JP, Norris SH, Johnson P, Galitz L, McCallister S. Pharmacokinetic characterization of different dose combinations of coadministered tipranavir and ritonavir in healthy volunteers. HIV Clin Trials 2004; 5: 371–82.
24 Li F, Wang L, Guo GL, Ma X. Metabolism-mediated drug interactions associated with ritonavir-boosted tipranavir in mice. Drug Metab Dispos 2010; 38: 871–8.
25 Scott JD. Simplifying the treatment of HIV infection with ritonavir-boosted protease inhibitors in antiretroviral-experienced patients. Am J Health Syst Pharm 2005; 62: 809–15.

Acta Pharmacologica Sinica (2011) 32: 1285–1293
 1671-4083/11 $32.00
www.nature.com/aps

Original Article

# Modulation of pharmacokinetics of theophylline by antofloxacin, a novel 8-amino-fluoroquinolone, in humans

Li LIU[1, #], Xian PAN[1, #], Hai-yan LIU[2], Xiao-dong LIU[1, *], Hui-wen YANG[1], Lin XIE[1], Jun-lin CHENG[3], Hong-wei FAN[3], Da-wei XIAO[3]

*[1]Key Laboratory of Drug Metabolism and Pharmacokinetics, China Pharmaceutical University, Nanjing 210009, China; [2]Department of Drug Metabolism and Pharmacokinetics, Central Research Institute of Shanghai Pharmaceutical (Group) Co Ltd, Shanghai 201203, China; [3]Department of Clinical Pharmacology, Nanjing First Hospital, Nanjing 210006, China*

**Aim:** To evaluate the pharmacokinetic interactions between theophylline and antofloxacin *in vivo* and *in vitro*.
**Methods:** A randomized, 5-day treatment and 3-way crossover design was documented in 12 healthy subjects. The subjects were orally administered with antofloxacin (400 mg on d 1 and 200 mg on d 2 to 5), theophylline (100 mg twice a day and morning dose 200 mg on d 1 and 5), or theophylline plus antofloxacin. The plasma and urinary pharmacokinetics of antofloxacin and theophylline were characterized after the first and last dose. The effect of antofloxacin on theophylline metabolism was also investigated in pooled human liver microsomes.
**Results:** The 5-day treatment with antofloxacin significantly increased the area of the plasma concentration-time curve and peak plasma concentration of theophylline, accompanied by a decrease in the excretion of theophylline metabolites. On the contrary, theophylline did not affect the pharmacokinetics of antofloxacin. *In vitro* studies using pooled human hepatic microsomes demonstrated that antofloxacin was a weak reversible and mechanism-based inhibitor of CYP1A2. The clinical interaction between theophylline and antofloxacin was further validated by the *in vitro* results.
**Conclusion:** The results showed that antofloxacin increases the plasma theophylline concentration, partly by acting as a mechanism-based inhibitor of CYP1A2.

**Keywords:** antofloxacin; theophylline; drug interactions; pharmacokinetics; CYP1A2

*Acta Pharmacologica Sinica* (2011) 32: 1285–1293; doi: 10.1038/aps.2011.78; published online 5 Sep 2011

## Introduction

Antofloxacin (ATFX), developed by Anhui Global Pharmaceutical Limited Co, China, is a newly developed 8-amino derivative of levofloxacin with potent antibacterial activities *in vitro* and *in vivo*. It exhibits antibacterial activity that is markedly superior to that of conventional quinolones (ciprofloxacin, ofloxacin, and sparfloxacin) against quinolone-resistant, methicillin-resistant *Staphylococcus aureus* and *Staphylococcus epidermidis*[1]. Clinical pharmacokinetic studies have shown that ATFX is well tolerated and has high oral bioavailability, as well as favorable elimination half-life properties[2, 3]. It was recently licensed for the treatment of respiratory tract infections and is therefore likely to be administered together with theophylline (TP) in patients requiring bronchodilators.

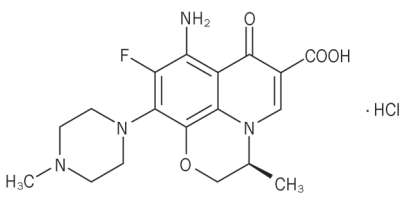

Chemical structure of ATFX.

In humans, TP is mainly metabolized by cytochrome P450s (CYP450s) in the liver to its major metabolites 1,3-dimethyluric acid (1,3-DMU), 3-methylxanthine (3-MX), and 1-methylxanthine (1-MX). 1-MX is further metabolized to 1-methyluric acid (1-MU). The metabolites 1,3-DMU, 3-MX, and 1-MU are mainly excreted in the urine[4, 5]. Accumulating reports have shown that CYP1A2 is the major enzyme responsible for TP

# These two authors contribute equally to this article.
* To whom correspondence should be addressed.
E-mail xdliu@cpu.edu.cn
Received 2010-12-25 Accepted 2011-05-18

metabolism[6–9], and TP is also a validated CYP1A2 probe that can be used to evaluate the enzymatic kinetics of CYP1A2[10]. TP has a narrow therapeutic plasma concentration range, and it is of the utmost importance to maintain constant concentrations of TP in plasma. Because asthma is often complicated by respiratory infections, the concomitant use of fluoroquinolone antimicrobials and TP may often be necessary. Concomitant use of fluoroquinolones may increase TP concentrations in the plasma, inducing clinically relevant safety issues. In 1984, Wijnands *et al* first reported severe clinical adverse effects with the concomitant use of TP and enoxacin, and they found that co-administration of enoxacin markedly increased plasma TP concentrations[11]. Consequently, a series of fluoroquinolones, including ciprofloxacin, tosufloxacin, clinafloxacin, grepafloxacin, and pefloxacin, have been reported to interfere with TP metabolism by inhibiting CYP1A2 activity[12–15]. Therefore, it is important to evaluate the interaction between ATFX and TP to understand the pharmacokinetics and safety of these drugs.

A prior study showed that ATFX has little effect on CYP1A2 activity in human liver microsomes[16]. However, our previous study demonstrated that ATFX was a mechanism-based inhibitor of CYP1A2 in rat liver microsomes through analysis of the formation of acetaminophen from phenacetin[17]. The aim of this study was to investigate whether a pharmacokinetic interaction between ATFX and TP exists *in vivo* at clinical dosages and regimens. The interaction between TP and ATFX was further investigated in an *in vitro* metabolic system with human liver microsomes through analysis of the formation of 1-MU, 1,3-DMU, and 3-MX. The relationship between the *in vivo* findings and the *in vitro* results was also evaluated.

## Materials and methods

### Chemicals

ATFX tablets and an ATFX standard were supplied by Anhui Global Pharmaceutical Co Ltd (Bengbu, China). Sustained-release TP tablets were obtained from Guangzhou Maite Xinhua Pharmaceutical Co Ltd (Guangzhou, China). TP, 1-MX, 1,3-DMU, 1-MU, and 3-MX standards, β-nicotinamide adenine dinucleotide phosphate (NADP), glucose-6-phosphate (G-6-P), and G-6-P dehydrogenase (G-6-PDH, Type V) were purchased from Sigma-Aldrich Co (St Louis, MO, USA). Pooled human liver microsomes were purchased from the Research Institute for Liver Disease Co Ltd (Shanghai, China). Information on the sources of the human liver microsome, including medication history, cause of death and the presence of viral infections was provided by the vendor and deemed suitable for these studies.

### Subjects and ethics

The study protocol was approved by the Ethics Committee of the Nanjing First Hospital. The clinical trial was conducted in accordance with the ethical principals in the Declaration of Helsinki and with the requirements in Good Clinical Practice (GCP), including the protocol design and organization, monitoring, auditing, recording, analysis, and reporting. Twelve healthy, non-smoking volunteers (six females and six males) ranging in age from 22 to 29 years within 20% of ideal body weight participated in the study. All were advised of the objectives and possible risks of the study and agreed to participate by signing an informed consent form. All subjects underwent a full medical examination 1 week prior to the study, including a medical history, a physical examination, routine biochemical and hematological tests and a resting 12-lead electrocardiogram. Hematological and biochemical tests were repeated after the study. Pregnancy tests were performed in female subjects before each study period. No drugs (including oral contraceptives) were allowed 1 week prior to and throughout the study.

### Study design

This was a randomized three-period crossover trial using a Latin-square design. Each treatment period was 5 d. The investigational medication, all given orally, was as follows: treatment A, ATFX alone; treatment B, TP alone; and treatment C, TP plus ATFX. For the ATFX treatment, subjects received 200 mg of ATFX once daily on d 2 to 5 of the 5-day study period and 400 mg of ATFX on d 1. For the TP treatment, subjects orally received 200 mg of TP twice daily on d 2 to 4 of the 5-day period and received 200 mg of TP as a single morning doses on d 1 and 5. The study periods were separated by a 1-week washout interval. No alcohol- or methylxanthine-containing beverages or food were permitted for 48 h prior to the start of each study period and for the duration of the study period.

The plasma and urinary pharmacokinetics of ATFX and TP were characterized after the first and last doses. The morning dose was administered after an overnight fast (at approximately 8:00) and the evening dose was given 12 h later (at approximately 20:00). Venous blood samples for the determination of ATFX and TP were drawn at the following time points: pre-dose and 0.5, 1, 1.5, 2, 3, 4, 6, 8, 12, 24, 48, 72, 96, 96.5, 97, 97.5, 98, 99, 100, 102, 104, 108, 120, 132, and 144 h after the first dose. At each time point, 3 mL of venous blood was collected in heparinized tube and centrifuged. The plasma samples were transferred to polypropylene tubes and stored at -20 °C until further analysis.

Urine was collected in the following fractions: pre-dose assay blank and then at 0 to 2, 2 to 4, 4 to 6, 6 to 8, 8 to 10, 10 to 12, 12 to 24, 96 to 98, 98 to 100, 100 to 102, 102 to 104, 104 to 108, 108 to 120, 120 to 132, and 132 to 144 h time intervals after dose. The volume of each fraction was recorded, and a part of the aliquot was stored at -20 °C until assays were performed.

### Registration of adverse events

Subjects were asked to document their adverse events in a diary. The diary entries were tabulated and compared among treatments.

### Effect of ATFX on CYP1A2 activity in human liver microsomes

The effect of ATFX (0, 0.24, 0.48, 1.96, 1.92, and 2.40 mmol/L) on the metabolism of TP (1, 2, 4, 5, and 8 mmol/L) in pooled human liver microsomes was investigated. Enzyme activities

were evaluated by analysis of the formation of 1-MX, 3-MX and 1,3-DMU. The incubation mixture consisted of 1 mg/mL human liver microsomes, an NADPH-regenerating system (0.5 mmol/L NADP, 10 mmol/L G-6-P, 1 U/mL G-6-PDH and 10 mmol/L $MgCl_2$) and designated concentrations of ATFX and TP in 100 mmol/L potassium phosphate buffer at pH 7.4. The final volume was 200 μL. After incubation at 37 °C for 30 min, the reaction was terminated by adding 100 μL of 10% perchloric acid.

The time- and concentration-dependent inhibition of TP by ATFX was also observed. An NADPH-generating system and different concentrations of ATFX (0, 0.24, 0.48, 0.96, and 1.92 mmol/L) were added to human liver microsomes (1 mg/mL) in a total volume of 180 μL and pre-incubated at 37 °C for 0, 20, 30, 40, and 60 min. The enzyme reaction was initiated by adding 20 μL of TP at the designated time. The final concentration of TP was set at 5 mmol/L. After incubation at 37 °C for 30 min, the reaction was terminated by adding 100 μL of 10% perchloric acid.

### Drug analysis

TP and its metabolites were measured using an HPLC-based method, as previously described[18]. The methods were validated according to the currently accepted US Food and Drug Administration (FDA) bioanalytical method validation guidelines on specificity, linearity, sensitivity, accuracy, and precision.

To analyze TP in plasma, briefly, 10 μL of solution containing 5 μg/mL propylthiouracil (internal standard) was added to the plasma (100 μL), and the mixture was deproteinized by adding 100 μL of 10% perchloric acid. After vigorous mixing and centrifugation, 20 μL of the supernatant was injected into an HPLC system with a mobile phase of water (0.1% acetic acid) and methanol (76:24 *v*/*v*). The calibration graphs were linear from 0.15 to 15 μg/mL.

To analyze TP and its metabolites in urine, a 5 mL of a mixture of dichloromethane and isopropanol (8:2) was added to 1.0 mL of urine. The mixture was vortexed for 2 min and centrifuged for 10 min at 4000×*g*. The organic layer (3.5 mL) was obtained and evaporated to dryness under a stream of $N_2$ at 45 °C. The residues were reconstituted in 200 μL of mobile phase containing 25 μg/mL of epigoitrin (internal standard). An aliquot of 20 μL was injected into an HPLC system with a mobile phase of water (0.1% acetic acid) and acetonitrile (95:5 *v*/*v*). The calibration graphs were linear from 0.31 to 40 μg/mL for TP, from 0.15 to 10 μg/mL for 1-MU, from 0.08 to 10 μg/mL for 1,3-DMU and from 0.16 to 20 μg/mL for 3-MX.

1-MX, 3-MX, and 1,3-DMU were assessed in the reaction mixtures by centrifugation at 15 000×*g* for 10 min, and 20 μL of supernatant was injected into an HPLC system. The mobile phase consisted of water (0.1% formic acid) and acetonitrile (95:5, *v*/*v*). The calibration graphs were linear from 15.6 to 125 ng/mL for 1-MX, from 7.8 to 125 ng/mL for 3-MX and from 31.25 to 500 ng/mL for 1,3-DMU.

ATFX concentrations in plasma and urine were measured by HPLC with UV detection, as previously described[19]. The calibration graphs were linear from 0.1 to 12.5 μg/mL for plasma and from 0.40 to 25.0 μg/mL for urine.

### Data analysis

The plasma and urinary pharmacokinetics of ATFX and TP on d 1 (single dose) and d 5 (steady-state) were analyzed by non-compartmental methods using the Bioavailability Program Package (BAPP, version 3.1, China Pharmaceutical University, Nanjing, China). The maximum plasma concentration ($C_{max}$) and time to $C_{max}$ ($T_{max}$) were taken directly from the plasma-time profiles. The terminal elimination constant ($\lambda_Z$) was estimated by the least squares linear regression analysis of the concentration-time data obtained over the terminal in-linear phase after the last dose. Terminal half-lives ($t_{1/2}$) were calculated as $0.693/\lambda_Z$. The area under the plasma concentration-time curve ($AUC^{0-t}$) was calculated using the linear trapezoidal rule. Total clearance (*Cl*/*F*) was calculated as *Cl*/*F*=Dose/$AUC_{ss}^{0-t}$. The accumulated amounts (*A*e) in designed intervals were also calculated. Renal clearance ($Cl_r$) was calculated as $A_{et}/AUC_{tn}$, where $A_{et}$ and $AUC_{tn}$ were the accumulated amounts excreted into urine and the AUC values during the interval, respectively. The non-renal clearance ($Cl_{nr}$) was designed to be *Cl*/*F*-$Cl_r$. Analysis of the differences between the pharmacokinetic parameters of drug alone and the combination of drugs was handled as an equivalence problem[20]. Comparison of pharmacokinetic parameters was carried out with analysis of variance (ANOVA)-based 90% confidence intervals (CI) after log-transformation. Those were calculated for the test (drug combination) and reference (drug alone) for all parameters, except $T_{max}$ and $t_{1/2}$, for which the differences were used. A lack of interaction was assumed if the values of CI for the ratios $\mu_{test}/\mu_{reference}$ were completely within the 0.80–1.25 equivalence range.

Reversible inhibition enzymatic constants ($K_m$, $V_{max}$, and $K_I$) were estimated from the observed metabolite formation rate ($v$), the TP concentration [*S*] and inhibitor concentration [*I*] by nonlinear regression analysis using the extended Michaelis-Menten equation:

$$v=\frac{V_{max}\cdot[S]}{K_m(1+\frac{[I]}{K_I})+[S]} \quad (1)$$

The parameters of the corresponding enzyme inactivation ($k_{obs,i}$, $k_{inact,i}$ and $K_{app,i}$) by ATFX were estimated as follows. The logarithm of the enzymatic activity (formation rate of metabolite) was plotted against the pre-incubation time, and the observed inactivation rate constant ($k_{obs,i}$) was calculated from the slope of the initial linear phase. The reciprocal of the $k_{obs,i}$ obtained was plotted against the reciprocal of the ATFX concentration to determine $k_{inact,i}$ and $K_{app,i}$, according to equation 2[21].

$$k_{obs,i}=\frac{k_{inact,i}\cdot[I]}{K_{app,i}+[I]} \quad (2)$$

where $k_{inact,i}$ is maximum inactivation rate constant for the *i*th metabolite, [*I*] is the initial concentration of inhibitor and $K_{app,i}$

is the inhibitor concentration when $k_{obs,i}=k_{inact,i}/2$.

### Simulation

The *in vitro* data describing the mechanism-based inhibition of CYP1A2 by ATFX were further used to rationalize the observed clinical drug interactions. The following assumptions were made: TP is well absorbed; the substrate exhibits linear pharmacokinetics; the drug is eliminated via both metabolism in the liver and excretion in the kidney; and the inhibitor has no effect on the absorption or kidney clearance of the substrate. The hepatic clearance of the substrate is adequately described by the well-stirred model, and degradation of the enzyme is a first order process. Furthermore, the inhibitor has no effect on the rate of synthesis of the enzyme.

An attempt was made to evaluate the effects on the oral pharmacokinetics of TP involved in multi-elimination pathways, according to equation 3[22].

$$\frac{AUC_i}{AUC_c}=\frac{1}{\dfrac{f_m}{1+\Sigma\dfrac{k_{inact,i}\cdot I_u}{k_{deg}\cdot(K_{app,i}+I_u)}}+(1-f_m)} \quad (3)$$

where $AUC_i$ and $AUC_c$ are the AUC values of TP in the presence and absence of inhibitors, respectively. $f_m$ represents the fraction of total hepatic elimination via CYPs. $K_{app,i}$ and $k_{inact,i}$ are the parameters describing inactivation of the enzyme that forms the *i*th metabolite. $k_{deg}$ represents the rate constant of degradation of the enzyme. Estimates of the concentration of the inhibitor at the enzyme ($I_u$) were based on the free plasma concentrations. To determine the effect of ATFX on CYP1A2, the *in vitro* $K_{app,i}$ and $k_{inact,i}$ data obtained in the study were used in the simulations. Values of $k_{deg}$ were set to be 0.000769 $min^{-1}$ or 0.00128 $min^{-1}$, as cited by Wang *et al*[22]. The steady-state concentrations of ATFX in plasma ($C_{max}$ and $C_{av}$) obtained in the study were used for simulation after being corrected for $f_u$=0.825. The simulated AUC change was compared with that observed in the clinic.

## Results

### Clinical observations

All 12 enrolled volunteers completed the study in accordance with the protocol. Adverse events were reported by 7 subjects. The numbers of subjects reporting adverse events were 4 for ATFX, 3 for TP and 7 for TP plus ATFX. The adverse events included neurological symptoms (mainly drowsiness, headache and sleeplessness) and gastrointestinal complaints (diarrhea, nausea, lack of appetite and stomach disorders). Neurological symptoms were reported by 3, 3, and 6 subjects; gastrointestinal events were reported by 0, 4, and 6 subjects in periods with TP alone, ATFX alone and TP plus ATFX, respectively. The results showed that the incidence of adverse events was higher in the period with TP plus ATFX. Neither serious nor severe adverse experiences were observed, and most of the adverse experiences were mild and transient. All symptoms had resolved by the time of the follow-up examination. No clinically relevant changes were observed in the laboratory safety tests either during the study or at the follow-up examination.

### Pharmacokinetics of TP

The mean plasma concentration-time courses of TP during the administration of multiple doses (complete profiles after morning doses on d 1 and 5, morning trough concentrations on d 2 to 5) for TP treatment alone and for TP treatment with ATFX are shown in Figure 1. The individual accumulated amounts (0 to 24 h) of TP and its three metabolites excreted into urine were calculated. The corresponding pharmacokinetic parameters for the first dose and last dose are summarized in Table 1. Comparison of treatments was carried out with analysis of variance-based 90% confidence intervals (CI) as an equivalence problem. After the first dose (on d 1), estimated plasma pharmacokinetic parameters for the two treatments were equivalent in terms of $AUC^{0-24}$ (106.6%, CI: 94.4% to 120.4%) and $C_{max}$ (106.4%, CI: 88.7% to 124.6%). The accumulated amounts of TP and its three metabolites in the urine in the two treatments were similar. However, after multiple doses (on d 5), the mean $C^{SS}_{max}$ of 9.32 μg/mL, mean $C^{SS}_{min}$ of 6.02 μg/mL and $AUC^{0-12}_{SS}$ of 92.4 μg·h/mL in the period of TP alone significantly increased to a $C^{SS}_{max}$ of 12.02 μg/mL (132.1%, CI: 114.0% to 153.1%), $C^{SS}_{min}$ of 8.04 μg/mL (139.2%, CI: 122.4% to 156.0%) and $AUC^{0-12}_{SS}$ of 117.7 μg·h/mL (129.4%, CI: 113.7% to 147.3%) in the period of co-administration with ATFX, respectively, accompanied by a decrease in clearance (2.36±0.81 L/h in periods of TP alone *vs* 1.78±0.39 L/h in the period of combination). For comparison of the pharmacokinetic parameters of TP between the two treatments at steady state, the parametric point estimates of the $\mu_{test}/\mu_{reference}$ ratios and corresponding CI for AUC, *Cl*, and $C_{max}$ were partially or


**Figure 1.** Comparison of TP concentration in plasma after an oral dose of TP alone (open circle) and co-administration of ATFX (filled circle). For TP, on d 1 and 5, 200 mg of TP was given to subjects as a single morning dose, and on d 2 to 4, 400 mg of TP was given to subjects twice daily (morning dose and evening dose). For ATFX, on d 1, 400 mg was given to subjects as a single morning dose, and on d 2 to 5, 200 mg of ATFX was given to subjects once daily (morning dose). The results are expressed as the mean±SD ($n$=12).

**Table 1.** Pharmacokinetic parameters of TP alone and the co-administration of ATFX.

| | Parameters | TP alone | TP plus ATFX | Point estimate (90% CI) |
|---|---|---|---|---|
| 1st day | $AUC^{0-24}$ (μg·h/mL) | 50.00±14.49 | 51.77±10.27 | 106.6% (94.4%–120.4%) |
| | $C_{max}$ (μg /mL) | 3.00±0.91 | 3.23±1.30 | 106.4% (88.7%–124.6%) |
| | $T_{max}$ (h) | 4.8±2.8 | 6.2±1.8 | / |
| | *Cl* (L/h) | 4.45±1.74 | 4.01±0.81 | 95.7% (86.3%–105.2%) |
| | $Ae^{(0-24)}$ | | | / |
| | 1-MX (mg) | 3.82±3.22 | 5.19±2.67 | / |
| | 3-MX (mg) | 6.13±2.12 | 5.36±1.39 | / |
| | 1,3-DMU (mg) | 5.93±3.15 | 6.60±5.21 | / |
| | TP (mg) | 21.46±5.83 | 20.21±4.33 | / |
| 5th day | $AUC^{0-12}$ (μg·h/mL) | 92.64±27.08 | 117.72±27.77[b] | 129.4% (113.7%–147.3%) |
| | $AUC^{0-24}$ (μg·h/mL) | 152.95±43.06 | 200.04±525[b] | 132.7% (118.7%–148.5%) |
| | $C_{max}$ (μg/mL) | 9.32±2.70 | 12.02±2.41[b] | 132.1% (114.0%–153.1%) |
| | $T_{max}$ (h) | 3.0±1.2 | 3.3±0.9 | / |
| | $t_{1/2}$ (h) | 17.93±5.08 | 18.66±5.04 | / |
| | *Cl* (L/h) | 2.36±0.81 | 1.78±0.39[b] | 77.2% (67.8%–87.9%) |
| | $Cl_r$ (L/h) | 0.34±0.07 | 0.32±0.08 | 93.6% (78.9%–111.3%) |
| | $Cl_{nr}$ (L/h) | 2.03±0.78 | 1.46±0.37[c] | 74.4% (65.7%–84.3%) |
| | $Ae^{(0-24)}$ | | | / |
| | 1-MX (mg) | 25.49±21.17 | 9.76±5.07[b] | / |
| | 3-MX (mg) | 28.75±13.38 | 19.44±5.06[b] | / |
| | 1,3-DMU (mg) | 39.24±29.70 | 20.77±15.60[b] | / |
| | TP (mg) | 53.13±17.23 | 66.75±15.69[b] | / |

For TP, on d 1 and 5, 200 mg of TP was given to subjects as a single morning dose. On d 2 to 4, 400 mg of TP was given to subjects twice daily (morning dose and evening dose). For ATFX, on d 1, 400 mg was given to subjects as a single morning dose, and on d 2 to 5, 200 mg of ATFX was given to subjects once daily (morning dose). The results are expressed as the mean±SD ($n$=12). [b]$P$<0.05, [c]$P$<0.01 *vs* TP alone.

completely outside the predefined interval of no interaction (0.80 to 1.25).

Urinary excretion of TP and its metabolites were measured both on d 1 and 5 of TP administration alone and co-administration with ATFX. It was found that a 1-day period of co-administration with 400 mg of ATFX did not alter the excretion levels of TP, 3-MX, 1-MU, or 1,3-DMU. However, a 5-day period of the co-administration with 200 mg of ATFX resulted in decreases of all urinary TP metabolites and increases in urinary TP (Table 1). The renal clearance ($Cl_r$) and non-renal clearance ($Cl_{nr}$) of TP were also calculated. It was observed that the non-renal clearances of TP in the period of combination significantly decreased, but no alteration of TP renal clearance was noted. The decrease of $Cl_{nr}$ was associated with decreased amounts of the three TP metabolites in urine.

### Pharmacokinetics of ATFX

The mean plasma concentration-time courses of ATFX during the administration of multiple doses (complete profiles after morning dose on d 1 and 5, morning trough concentrations on d 2 to 5) of ATFX treatment alone and ATFX treatment with TP are shown in Figure 2. The accumulated amounts (0 to 24 h) of ATFX excreted into the urine were also calculated.

The respective pharmacokinetic parameters for the first and last doses of the treatment are summarized in Table 2. After the first dose, the plasma pharmacokinetics of ATFX for the two treatments were equivalent in terms of $AUC^{0-24}$ (98.9%, CI: 86.5% to 113.1%) and $C_{max}$ (98.6%, CI: 83.2% to 116.8%). The mean $T_{max}$ was also similar for the two treatments. The amount of ATFX excreted into the urine showed a trend of increasing in the period of combination, even though no significance was found. After multiple doses, similar plasma pharmacokinetic parameters were observed in the two treatments. Parametric point estimates of the $\mu_{test}/\mu_{reference}$ ratios and the corresponding CI for $C_{max}$, AUC, and *Cl* following the first and last doses were within the equivalence interval from 0.80 to 1.25. The results indicated that TP does not affect the pharmacokinetics of ATFX in humans.

### *In vitro* inhibition of TP metabolism by ATFX in human liver microsomes

The effects of ATFX on the formation of 1-MX, 3-MX, and 1,3-DMU from TP were investigated with human liver microsomes in the presence of an NADPH-generating system. The reversible inhibition parameters were estimated (Table 3). To measure accurate kinetic parameters, the concentration of the given substrate (TP in this study) should approach $K_m$[23]. We established TP concentrations for *in vitro* study according to several previous studies[24, 25]. Additionally, ATFX concentrations for the *in vitro* study were selected according to our previous study[17].

It was noted that ATFX may inhibit TP metabolism in

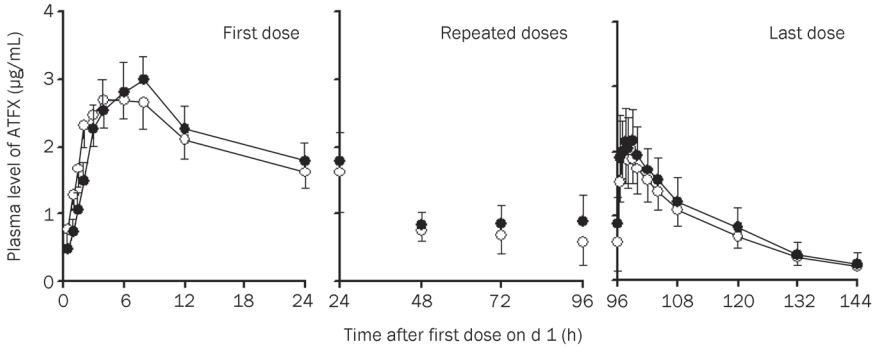


**Figure 2.** Comparison of ATFX concentrations in plasma after an oral dose of ATFX alone (open circle) and co-administration of TP (filled circle). For TP, on d 1 and 5, 200 mg of TP was given to subjects as a single morning dose, and on d 2 to 4, 400 mg of TP was given to subjects twice daily (morning dose and evening dose). For ATFX, on d 1, 400 mg was given to subjects as a single morning dose, and on d 2 to 5, 200 mg of ATFX was given to subjects once daily (morning dose). The results are expressed as the mean±SD (*n*=12).

**Table 2.** Pharmacokinetic parameters of ATFX alone and the co-administration of TP.

| | Parameters | ATFX | ATFX plus TP | Point estimate (90% CI) |
|---|---|---|---|---|
| 1st day | $AUC^{0-24}$ (μg·h/mL) | 39.93±8.86 | 38.46±8.36 | 98.9% (86.5%–113.1%) |
| | $C_{max}$ (μg/mL) | 2.94±0.78 | 2.90±0.85 | 98.6% (83.2%–116.8%) |
| | $T_{max}$ (h) | 1.3±1.0 | 2.1±1.1 | / |
| | *Cl* (L/h) | 10.76±2.41 | 10.83±2.17 | 104.1% (91.8%–116.5%) |
| | $Ae^{(0-24)}$ (mg) | 226.40±56.26 | 266.42±46.82 | / |
| 5th day | $AUC^{0-24}{}_{SS}$ (μg·h/mL) | 24.32±6.03 | 27.57±6.98 | 113.5% (104.9%–122.8%) |
| | $C^{SS}{}_{max}$ (μg /mL) | 2.10±0.39 | 2.36±0.48 | 112.5% (104.6%–121.0%) |
| | $C_{av}$ (μg /mL) | 1.03±0.25 | 1.15±0.29 | 113.5% (104.9%–122.8%) |
| | $T_{max}$ (h) | 1.5±0.7 | 1.8±1.2 | / |
| | $t_{1/2}$ (h) | 13.56±3.75 | 15.01±4.11 | / |
| | *Cl* (L/h) | 8.62±1.83 | 7.57±1.44 | 88.1% (81.4%–95.4%) |
| | $Ae^{(0-24)}$ (mg) | 193.36±59.48 | 209.35±26.61 | / |
| | $Cl_r$ (L/h) | 8.55±2.42 | 7.60±1.91 | 90.6% (80.3%–110.6%) |

For ATFX, on d 1, 400 mg was given to subjects as a single morning dose, and on d 2 to 5, 200 mg of ATFX given to subjects once daily (morning dose). For TP, on d 1 and 5, 200 mg of TP was given to subjects as a single morning dose. On d 2 to 4, 400 mg of TP was given to subjects twice daily (morning dose and evening dose). The results are expressed as the mean±SD (*n*=12).

**Table 3.** Inhibitory effect of ATFX on TP metabolites in human liver microsomes *in vitro*. Data represent mean±SD of three experiments.

| | $K_I$ (μmol/L) | $K_{app,i}$ (μmol/L) | $k_{inact,i}$ ($min^{-1}$) | $k_{inact,i}/K_{app,i}$ ($\times10^{-5}$) ($min^{-1}{\cdot}M^{-1}$) |
|---|---|---|---|---|
| 3-MX | 1209.2±66.3 | 265.88±18.81 | 0.0097±0.0016 | 3.68±0.84 |
| 1-MX | 1033.2±78.9 | 353.29±16.20 | 0.0073±0.0012 | 2.06±0.37 |
| 1,3-DMU | 1519.4±56.6 | 430.21±14.19 | 0.0047±0.0080 | 1.08±0.15 |

human liver microsomes. The inhibition of TP metabolism by ATFX is pathway-dependent. The inhibition is more selective for 3-MX than for 1-MX and 1,3-DMU. For example, co-incubation of 1 mg/mL ATFX with 2 mmol/L TP induced decreases in 3-MX, 1-MX, and 1,3-DMU formation from the controls by 63%, 54%, and 38%, respectively. The estimated reversible inhibition index ($K_I$) values for the formation of the three metabolites were over 1000 μmol/L (corresponding 412 μg/mL) (Table 3); however, these concentrations do not occur in the human body. These results indicated that ATFX was a weak, reversible inhibitor of CYP1A2, and this mechanism-based inhibition was further investigated. When pre-incubated with NADPH-fortified human microsomes in the absence of the substrate, ATFX was shown to have inhibitory effects on the metabolism of TP to 1-MX, 3-MX, and 1,3-DMU. The effect was NADPH-, time-, and concentration-dependent (Figure 3). It is well known that time-dependent inhibition of enzymes is one of the characteristics of mechanism-based inhibition. Therefore, our data suggested that ATFX behaves as a mechanism-based inhibitor of CYP1A2. Upon further study, the maximal inactivation rate constant ($k_{inact,i}$), apparent rate constant $K_{app,i}$ and ratios of $k_{inact,i}/K_{app,i}$ were estimated (Table 3). The mechanism-based inhibition was also pathway-dependent, and the $k_{inact,i}/K_{app,i}$ ratios were estimated to be

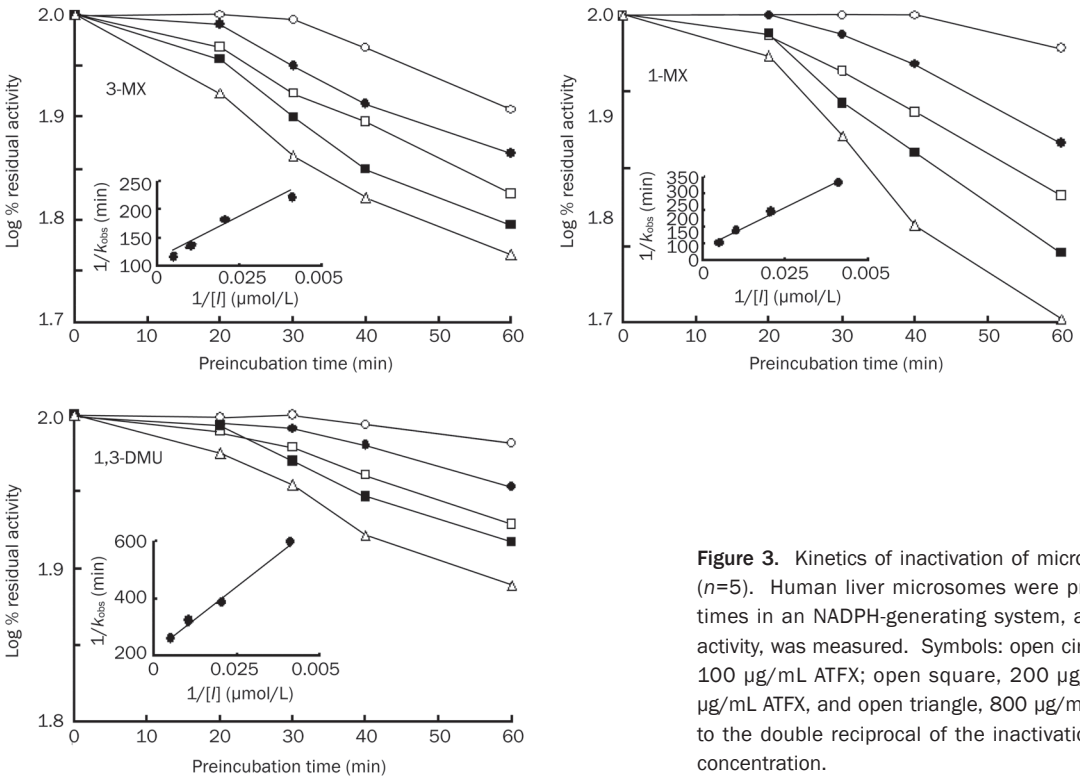


**Figure 3.** Kinetics of inactivation of microsomal TP metabolism by ATFX ($n$=5). Human liver microsomes were pre-incubated for the indicated times in an NADPH-generating system, and ATFX, followed by CYP1A2 activity, was measured. Symbols: open circle, 0 μg/mL ATFX; filled circle, 100 μg/mL ATFX; open square, 200 μg/mL ATFX; filled square, 400 μg/mL ATFX, and open triangle, 800 μg/mL ATFX. The insets correspond to the double reciprocal of the inactivation rates as a function of ATFX concentration.

0.0000368 $min^{-1}·\mu M^{-1}$ for 3-MX, 0.0000206 $min^{-1}·\mu M^{-1}$ for 1-MX and 0.0000108 $min^{-1}·\mu M^{-1}$ for 1,3-MDU, which indicated that the mechanism-based inhibition was favorable for 3-MX.

### Retrospective *in vitro-in vivo* correlations

After it was determined that ATFX behaves as a mechanism-based inhibitor of CYP1A2 in human liver microsomes, an attempt was made to relate the *in vitro* data ($K_{app,i}$ and $k_{inact,i}$) to the pharmacokinetics of ATFX. In turn, the effect of ATFX on the pharmacokinetics (AUC) of TP (a CYP1A2 substrate) was simulated, assuming that the degradation of CYP1A2 was a first order process and that $k_{deg}$ was set to be 0.000769 $min^{-1}$ or 0.00128 $min^{-1}$, as cited by Wang *et al*[22]. $f_m$ (fraction of total hepatic elimination via CYPs) values were estimated to be 0.86 using the ratio of $Cl_{nr}$ to total clearance of TP in the absence of ATFX in the study. After correction for binding to human plasma proteins, $f_u$=0.825 (unpublished data), the $C_{max}$ (5.73 μmol/L≈2.36 μg/mL) at steady state and $C_{av}$ (2.79 μmol/L≈1.15 μg/mL) of ATFX obtained in the study were used for simulating AUC changes. Upon implementation, good simulation was found using $C_{max}$ (5.73 μmol/L) and $k_{deg}$ (0.000769 $min^{-1}$). The estimated change of AUC was 1.32-fold, which was close to the 1.29-fold change observed in the study. However, $C_{av}$ (2.79 μmol/L) or $k_{deg}$ (0.00128 $min^{-1}$) gave an underestimation of AUC changes, as the estimated changes were 1.16- and 1.20-fold, respectively.

## Discussion

This study is different from a traditional three-period cross-over trial. A randomized, 5-day treatment and 3-way cross-over design was documented in 12 healthy subjects. The oral medications prescribed were ATFX, TP, or TP plus ATFX. For the ATFX treatment, subjects received 200 mg of ATFX once daily on d 2 to 5 of the 5-day study period and 400 mg of ATFX on d 1. For the TP treatment, subjects orally received 200 mg of TP twice daily on d 2 to 4 of the 5-day period and 200 mg of TP as a single morning dose on d 1 and 5. The purpose of the study was to investigate the pharmacokinetic interaction between TP and ATFX in healthy Chinese volunteers. After the three-period trial, we compared either ATFX alone with ATFX plus TP, or TP alone with ATFX plus TP. However, we could not compare ATFX alone with TP alone. The significant difference between the three periods was not our emphasis for the purpose of the study.

The present study clearly demonstrated that ATFX increased the $C_{max}$ and AUC of TP at steady state by 32% and 29%, respectively. According to the rule of Niki's classification[26], ATFX belongs to the class II quinolones because the increase in $C_{max}$ and AUC of TP is between 15% and 39%. A significant decrease of formation of TP metabolites was also found, as evidenced by decreased urinary excretion. It is well known that TP is mainly metabolized via CYP1A2. These results indicated that ATFX may elicit an increase in the concentration of TP in plasma by inhibiting hepatic microsomal CYP1A2. However, the effect of ATFX on the TP concentration was time-dependent. This was in contrast to the findings at steady state (d 5) that the co-administration of ATFX on d 1 did not alter the plasma concentrations of TP or the urinary excretion of TP metabolites (Figure 1 and Table 1), although the ATFX concentrations in plasma on d 1 were higher than those on d 5

(Figure 2 and Table 2). Similar phenomena were found for the effects of tosufloxacin on TP plasma concentrations and the effects of enoxacin on caffeine concentrations[20, 27]. The *in vitro* results using human liver microsomes showed that ATFX is a weak reversible inhibitor of CYP1A2, but ATFX appears to be a clinically relevant inhibitor. The clinical observations cannot be reconciled with the *in vitro* results, as the *in vivo* findings were simply not explained using a reversible inhibition of CYP1A2. Instead, ATFX may be a mechanism-based inhibitor of CYP1A2 activity. Further experiments were designed to verify the hypothesis using human liver microsomes to analyze 1-MX, 3-MX, and 1,3-DMU formation, and the results were positive. Inhibition of the formation of the three metabolites of TP by ATFX was time-, concentration- and NADPH-dependent, which is characteristic of mechanism-based inhibition. Similar findings were observed using rat liver microsomes to assess the formation of acetaminophen from phenacetin[17].

The inhibitory effect of ATFX on metabolite formation in human liver microsomes was amenable to kinetic analysis, yielding estimates of $k_{inact,i}$, $K_{app,i}$, and $k_{inact,i}/K_{app,i}$ ratios (Table 3). The $k_{inact,i}/K_{app,i}$ ratios of ATFX were considerably lower than those reported for furafylline (0.229 $min^{-1} \cdot \mu M^{-1}$)[28] and zileuton (0.0003 $min^{-1} \cdot \mu M^{-1}$)[29]. We sought to relate the *in vitro* inhibition parameters of ATFX to rationalize the observed interaction between ATFX and TP in the study. Efforts have been made to evaluate the mechanism-based inhibition of CYPs using physiologically based models[17, 21, 30, 31]. Overall, it is accepted that the net effect of inhibitors is dependent on the $k_{inact,i}/K_{app,i}$ ratio, $k_{deg}$ and concentration of inhibitor at the enzyme active site. For the sake of simplicity, retrospective analysis of the ATFX data were based on a kinetic model (Equation 3) using the values of $k_{deg}$ cited by Wang *et al*[22] (0.00128 $min^{-1}$ or 0.000769 $min^{-1}$). The parameters of inactivation of the enzyme with $C_{max}$ at steady state or $C_{av}$ (corrected for $f_u$) are listed in Table 3. It was noted that the simulated AUC changes were in agreement with the observed values using $C_{max}$ at steady state and a $k_{deg}$ of 0.000769 $min^{-1}$, which indicated that it is possible to reconcile the clinical drug interactions between TP and ATFX with the *in vitro* results according to a mechanism-based inhibition. The mechanism-based inhibition may explain why ATFX causes an increase in TP levels in plasma and why the inhibitory effect of ATFX is time-dependent.

A recent report has demonstrated that treatment with ciprofloxacin is associated with a significant increase in the risk of TP toxicity in elderly patients[32]. Our study confirmed the idea that the co-administration of ATFX increases the plasma levels of TP in young populations. These results indicate that ATFX probably decreases TP clearance and increases the risk of TP toxicity in elderly patients. Further studies are required to investigate the pharmacokinetic interactions between ATFX and TP in elderly populations.

Based on the results of our study, it was concluded that ATFX appears to be a clinical mechanism-based inhibitor of CYP1A2. Co-administration of ATFX may increase TP concentrations in plasma, which would raise the risk of TP toxicity in patients. We suggest that when patients receiving TP require treatment with antibiotics, avoidance of ATFX may be clinically appropriate. Alternatively, close monitoring for TP concentrations and toxicity is warranted in cases where the use of ATFX is required.

## Acknowledgements

This work was supported by the "Eleventh five-year Plan"–Technical Platform for Drug Development from the Ministry of Science and Technology of the People's Republic of China (No 2009ZX09304-001).

## Author contribution

Li LIU and Xian PAN performed the research; Hai-yan LIU and Hui-wen YANG measured the plasma concentrations of theophylline and antofloxacin; Li LIU wrote the manuscript; Xiao-dong LIU and Lin XIE reviewed and revised the manuscript; and Jun-lin CHENG, Hong-wei FAN, and Da-wei XIAO participated in the clinical study and reviewed the manuscript.

## References

1 Ye H, Wu JM, Yang YS, Chen KX, Ji RY. Antibacterial activities of the derivatives-YH54 and YH57 of levofloxacin *in vitro*. Chin Pharmacol Bull 2002; 18: 112–3.
2 Xiao Y, Lu Y, Kang Z, Hou F, Wang S, Li T, *et al*. Tolerability and pharmacokinetics of antofloxacin hydrochloride after multiple oral dose administration in healthy Chinese male volunteers. Int J Clin Pharmacol Ther 2008; 46: 172–9.
3 Xiao Y, Lu Y, Kang Z, Zhang M, Liu Y, Zhang M, *et al*. Pharmacokinetics of antofloxacin hydrochloride, a new fluoroquinolone antibiotic, after single oral dose administration in Chinese healthy male volunteers. Biopharm Drug Dispos 2008; 29: 167–72.
4 Gundert-Remy U, Hildebrandt R, Hengen N, Weber E. Non-linear elimination processes of theophylline. Eur J Clin Pharmacol 1983; 24: 71–8.
5 Tang-Liu DD, Williams RL, Riegelman S. Nonlinear theophylline elimination. Clin Pharmacol Ther 1982; 31: 358–69.
6 Campbell ME, Grant DM, Inaba T, Kalow W. Biotransformation of caffeine, paraxanthine, theophylline and theobromine by polycyclic aromatic hydrocarbon-inducible cytochrome P450 in human liver microsomes. Drug Metab Dispos 1987; 15: 237–49.
7 Ha HR, Chen J, Freiburghaus AU, Follath F. Metabolism of theophylline by cDNA expressed human cytochromes P-450. Br J Clin Pharmacol 1995; 39: 321–6.
8 Sarkar MA, Hunt C, Guzelian PS, Karnes HT. Characterization of human liver cytochrome P-450 involved in theophylline metabolism. Drug Metab Dispos 1992; 20: 31–7.
9 Tjia JF, Colbert J, Back DJ. Theophylline metabolism in human liver microsomes: inhibition studies. J Pharmacol Exp Ther 1996; 276: 912–7.
10 Bachmann K, White D, Jauregui L, Schwartz JI, Agrawal NG, Mazenko R, *et al*. An evaluation of the dose-dependent inhibition of CYP1A2 by rofecoxib using theophylline as a CYP1A2 probe. J Clin Pharmacol 2003; 43: 1082–90.
11 Wijnands WJA, Van Herwaarden CLA, Vreeet TB. Enoxacin raises plasma theophylline concentrations. Lancet 1984; 2: 108–9.
12 Edwards DJ, Bowles SK, Svensson CK, Rybak MJ. Inhibition of drug metabolism by quinolone antibiotics. Clin Pharmacokinet 1988; 15:

194–204.

13 Fuhr U, Anders EM, Mahr G, Sörgel F, Staib AH. Inhibitory potency of quinolone antibacterial agents against cytochrome P450IA2 activity *in vivo* and *in vitro*. Antimicrob Agents Chemother 1992; 36: 942–8.

14 Loi CM, Parker BM, Cusack BJ, Vestal R. Individual and combined effects of cimetidine and ciprofloxacin on theophylline metabolism in male nonsmokers. Br J Clin Pharmacol 1993; 36: 195–200.

15 Matuschka PR, Vissing RS. Clinafloxacin-theophylline drug interaction. Ann Pharmacother 1995; 29: 378–80.

16 Zhang L, Wei MJ, Zhao CY, Qi HM. Determination of the inhibitory potential of 6 fluoroquinolones on CYP1A2 and CYP2C9 in liver microsomes. Acta Pharmacol Sin 2008; 29: 1507–14.

17 Zhu Q, Liao J, Xie L, Wang GJ, Liu XD. Mechanism-based inhibition of CYP1A2 by antofloxacin, an 8-NH2 derivative of levofloxacin in rats. Xenobiotica 2009; 39: 293–301.

18 Nie SL, Liu HY, Xie L. Reversed-phase high performance liquid chromatographic method for simultaneous determination of theophylline and its two metabolites in human urine. Chin J Clin Pharmacol Ther 2009; 14: 1386–91.

19 Pang XY, Xie L, Xu X, Liu HY, Liu L, Liu XD. Pharmacokinetics of ATFX in rats coadministered with non-steroidal anti-inflammatory drugs. Chin J New Drugs 2007; 16: 600–3.

20 Kinzig-Schippers M, Fuhr U, Zaigler M, Dammeyer J, Rüsing G, Labedzki A, *et al*. Interaction of pefloxacin and enoxacin with the human cytochrome P450 enzyme CYP1A2. Clin Pharmacol Ther 1999; 65: 262–74.

21 Mayhew BS, Jones DR, Hall SD. An *in vitro* model for predicting *in vivo* inhibition of cytochrome P450 3A4 by metabolic intermediate complex formation. Drug Metab Dispos 2000; 28: 1031–7.

22 Wang YH, Jones DR, Hall SD. Prediction of cytochrome P450 3A inhibition by verapamil enantiomers and their metabolites. Drug Metab Dispos 2004; 32: 259–66.

23 Fowler S, Zhang H. *In vitro* evaluation of reversible and irreversible cytochrome P450 inhibition: current status on methodologies and their utility for predicting drug-drug interactions. AAPS J 2008; 10: 410–24.

24 Sarkar M, Polk RE, Guzelian PS, Hunt C, Karnes HT. *In vitro* effect of fluoroquinolones on theophylline metabolism in human liver microsomes. Antimicrob Agents Chemother 1990; 34: 594–9.

25 Kim EJ, Suh OK, Lee MG. Pharmacokinetics of intravenous theophylline in mutant Nagase analbuminemic rats. Life Sci 2003; 72: 1231–45.

26 Niki Y, Watanabe S, Yshida K, Miyashita N, Nakajima M, Matsushima T. Effect of pazufloxacin mesilate on the serum concentration of theophylline. J Infect Chemother 2002; 8: 33–6.

27 Niki Y. Pharmacokinetics and safety assessment of tosufloxacin tosilate. J Infect Chemother 2002; 8: 1–18.

28 Fairman DA, Collins C, Chapple S. Progress curves analysis of CYP1A2 inhibition: a more information approach to assessment of mechanism-based inactivation? Drug Metab Dispos 2007; 35: 2159–65.

29 Lu P, Schrag ML, Slaughter DE, Raab CE, Shou M, Rodrigues AD. Mechanism-based inhibition of human liver microsomal cytochromes P450 1A2 by zileuton, a 5-lipoxygenase inhibitor. Drug Metab Dispos 2003; 31: 1352–60.

30 Ito K, Iwatsubo T, Kanamitsu S, Ueda K, Suzuki H, Sugiyama Y. Prediction of pharmacokinetic alterations caused by drug-drug interactions: metabolic interaction in the liver. Pharmacol Rev 1998; 50: 387–411.

31 Ito K, Iwatsubo T, Kanamitsu S, Itoh T. Prediction of the *in vivo* interaction between midazolam and macrolides based on *in vitro* studies using human liver microsomes. Drug Metab Dispos 2003; 31: 945–54.

32 Antoniou T, Gomes T, Mamdani MM, Juurlink DN. Ciprofloxacin-induced theophylline toxicity: a population-based study. Eur J Clin Pharmacol 2011; 67: 521–6.

Acta Pharmacologica Sinica (2011) 32: 1294–1302
 1671-4083/11 $32.00
www.nature.com/aps

Original Article

# Novel gastroretentive sustained-release tablet of tacrolimus based on self-microemulsifying mixture: *in vitro* evaluation and *in vivo* bioavailability test

Yan-ping WANG, Yong GAN, Xin-xin ZHANG*

*Shanghai Institute of Materia Medica, Shanghai Institutes for Biological Sciences, Chinese Academy of Science, Shanghai 201203, China*

**Aim:** To develop a novel gastroretentive drug delivery system based on a self-microemulsifying (SME) lipid mixture for improving the oral absorption of the immunosuppressant tacrolimus.
**Methods:** Liquid SME mixture, composed of Cremophor RH40 and monocaprylin glycerate, was blended with polyethylene oxide, chitosan, polyvinylpyrrolidone and mannitol, and then transformed into tablets via granulation, with ethanol as the wetting agent. The tablets were characterized in respect of swelling, bioadhesive and SME properties. *In vitro* dissolution was conducted using an HCl buffer at pH 1.2. Oral bioavailability of the tablets was examined in fasted beagle dogs.
**Results:** The tablet could expand to 13.5 mm in diameter and 15 mm in thickness during the initial 20 min of contact with the HCl buffer at pH 1.2. The bioadhesive strength was as high as 0.98±0.06 N/cm$^2$. The SME gastroretentive sustained-release tablets preserved the SME capability of the liquid SME formations under transmission electron microscope. The drug-release curve was fit to the zero-order release model, which was helpful in reducing fluctuations in blood concentration. Compared with the commercially available capsules of tacrolimus, the relative bioavailability of the SME gastroretentive sustained-release tablets was 553.4%±353.8%.
**Conclusion:** SME gastroretentive sustained-release tablets can enhance the oral bioavailability of tacrolimus with poor solubility and a narrow absorption window.

**Keywords:** immunosuppressants; tacrolimus; bioavailability; self-microemulsifying lipid mixture; gastroretentive sustained-release tablet

*Acta Pharmacologica Sinica* (2011) 32: 1294–1302; doi: 10.1038/aps.2011.90; published online 19 Sep 2011

## Introduction

Tacrolimus, a 23-member macrolide lactone, was isolated from *Streptomyces tsukubaensis* early in 1984[1, 2]. Its use is now well established for primary immunosuppression in liver and kidney transplantation. Meanwhile, experience with its use in other types of solid-organ transplantation, including heart, lung, pancreas and intestinal, as well as its use for the prevention of graft-versus-host disease in allogeneic bone marrow transplantation (BMT), is rapidly accumulating[3]. However, being a BCS class II drug, the clinical efficacy of tacrolimus is very limited because of its poor water solubility (5–8 μg/mL), which is responsible for its low oral bioavailability[2, 4]. The dissolution rate of tacrolimus is one of the rate-limiting steps for its *in vivo* absorption. A self-microemulsifying drug delivery system (SMEDDS) has been used to improve the oral bioavailability of poorly soluble drugs by presenting and maintaining the drug in a dissolved state during its entire transit through the gastrointestinal tract[5]. Therefore, SMEDDS was designed in this study to improve the dissolution and oral bioavailability of tacrolimus. At present, there are four drug products, Sandimmune®, Sandimmun Neoral® (cyclosporine A), Norvir® (ritonavir), and Fortovase® (saquinavir) on the pharmaceutical market, the active compounds of which have been formulated into the specific SMEDDS. Significant improvement in the oral bioavailability of these drug compounds has been demonstrated for each case, which further justifies this study[6].

SMEDDS is usually formulated in a liquid form, which has some disadvantages, especially in the manufacturing process, leading to high production costs. Furthermore, incompatibility problems with the capsule shell are common[7]. Recently, with the development of new materials and a novel preparation process, there is growing interest in the study of solid self-

* To whom correspondence should be addressed.
E-mail simm2122@vip.sina.com
Received 2011-01-18 Accepted 2011-05-25

microemulsifying drug delivery systems (S-SMEDDS)[5, 7–14]. Compared with the traditional SMEDDS, S-SMEDDS can increase stability, extend storage time, reduce gastrointestinal irritation, and improve patient compliance. Furthermore, it was reported that the bioavailability of the self-microemulsifying mixture in a solid dosage form was equivalent to that of a liquid form[15].

Similar to cyclosporin A, tacrolimus has a very narrow therapeutic window, and it exhibits large intra- and inter-individual variability of bioavailability, ranging from 4% to 89% (mean of around 25%)[16, 17]. A high blood concentration will not only cause renal toxicity in the patient but also trigger the immune over-infection; however, a low concentration often leads to graft rejection. Post-treatment monitoring of blood levels is an integral part of patient care to maintain drug levels within the therapeutic range to optimize therapy and reduce undesirable toxic effects. This results in a significant inconvenience in the clinical application of tacrolimus. Therefore, designing a sustained-release formulation for tacrolimus that can control the drug blood concentration at a suitable level is quite essential. A tacrolimus sustained-release capsule developed by Astellas was approved both in Europe (Advagraf®) and Japan (Graceptor®). In addition, Life Cycle Pharma A/S has developed a tacrolimus sustained-release tablet, and a clinical phase III trial is in progress[18]. Some *in vitro* and *in vivo* studies have shown that these formulations can reduce blood concentration fluctuations, and the differences in intra- and inter-individual levels have also been improved. However, these sustained-release capsules do not improve the bioavailability of tacrolimus, which is equivalent to the immediate-release capsules. The objective of developing SME sustained-release tablets in our study was not only to reduce the blood concentration fluctuations but also to improve the bioavailability.

Tacrolimus shows significant site dependence in intestinal permeability, and it is absorbed predominantly in the upper part of the small intestine[19, 20]. It was reported that differences in P-gp and P450 function in each intestinal site could be a main cause of the site selectivity and large variability in tacrolimus absorption[16]. The gastroretentive drug delivery system (GRDDS) is a preferable approach to improve the oral bioavailability and variability of a drug with a narrow absorption window in the upper part of the gastrointestinal tract (*ie*, stomach and small intestine). Prolonged gastric residence is expected to lead to an increased contact interval with the main absorption site of tacrolimus, the mucosa of the upper small intestine. Owing to its improved bioavailability combined with reduced frequency of administration and thus improved patient compliance, gastric retentive devices may also be used as extended-release drug delivery systems[21, 22]. Several gastroretentive extended-release products are available on the market at present. Glumetza® (metformin hydrochloride) and Proquin® XR (ciprofloxacin hydrochloride) extended-release tables were designed based on the mechanism of expansion and bioadhesion. They could release the drug in the upper gastrointestinal tract and showed higher plasma concentrations than the immediate-release formulation[23]. In this study, we developed tacrolimus solid SME sustained-release GRDDS combining the advantages of solid SME and sustained-release gastric retention agents to improve the bioavailability and reduce the blood concentration variability of tacrolimus.

## Materials and methods

### Materials

Tacrolimus (FK506) was purchased from Zhejiang Laiyi Biotechnologies Co, Ltd. Monocaprylin glycerate (GMC) was a gift from Henan Zhengtong Chemical Co, Ltd (Zhengzhou, China). Polyoxyl 40 Hydrogenated Castor Oil (Cremophor RH40) was obtained from the BASF Corporation. Polyethylene oxide (PEO WSR N60K) was gifted from the DOW Chemical Company (Midland, MI, USA). Polyvinylpyrrolidone (PVP) K90 was gifted from the International Specialty Products (ISP) Corporation. Mannitol and chitosan (deacylation rate ≥90.0%, viscosity=150 mPa·s) were purchased from Shandong Jiejing Group Corporation (Rizhao, China) and Sinopharm Chemical Reagent Co, Ltd (Shanghai, China), respectively. The tacrolimus capsules: brand name Prograf; standard 1 mg/tablet; batch number 1D5261A. All other chemicals were of reagent or HPLC grade. Deionized water was obtained from a Millipore® Milli-Q System (Molsheim, France) in the laboratory.

### Animals

New Zealand rabbits (body weight 2.5±0.5 kg) were obtained from the Medical Animal Test Center of the Shanghai Institute of Materia Medica (Shanghai, China). Six adult beagle dogs (three male and three female, average weight 8.6±1.5 kg) were provided by the School of the Agriculture of Shanghai Jiao Tong University experiment and teaching practice field. License No: SCXK (Shanghai) 27-0004. All experiments were performed according to the Shanghai Institute of Materia Medica guidelines for experimental animal care.

### Preparation of the solid-state self-microemulsifying dosage form

The solid self-microemulsifying drug delivery system (S-SMEDDS) of tacrolimus was prepared as follows: Cremophor RH40 and GMC at a ratio of 4:6 were accurately weighed into a glass vial, melted in a water bath at 40 °C and mixed by a vortex to form a homogenous mixture. Tacrolimus was then dispersed into this mixture of oil and surfactant by vortex mixing and shaking at 37 °C until a transparent solution of SMEDDS was obtained. Microemulsion adsorbed granular material was obtained from a mixture of SMEDDS solution, PEO N60K, PVP K90, mannitol and chitosan by constant stirring with ethanol as a wetting agent. The dried granules were lubricated with magnesium stearate and compressed into tablets on a single station tablet press (TDP-I, Shanghai Huamao Industrial & Commercial Co, Shanghai, China).

The amounts of PEO, chitosan, mannitol and PVP added to the formulation to make one tablet containing 102 mg of SMEDDS are listed in Table 1.

### Expanding study

The swelling of the tablets can be measured by their abil-

**Table 1.** Composition of the investigated tablets.

| Ingredients | Composition (mg/tablet) |
|---|---|
| Tacrolimus | 2 |
| GMC | 60 |
| Cremophor RH40 | 40 |
| Polyethylene oxide | 300 |
| Chitosan | 300 |
| Mannitol | 250 |
| Polyvinylpyrrolidone | 50 |

ity to absorb water and the degree to which they swell. The swelling property of the formulation was determined by various techniques. Swelling index, water absorption rate and exposed size parameter are essential parameters to predict the gastroretentive performance of the expandable systems[24]. In this study, the exposed size parameter was chosen to measure the tablets' swelling. The water uptake study of the tablets was performed according to the Chinese Pharmacopoeia (CP) XC basket method. The medium used was 500 mL of an HCl buffer at pH 1.2 rotated at 50 rotations per minute (r/min). The medium was maintained at 37±0.5 °C throughout the study. At a selected time interval, the tablets were withdrawn to measure their diameter and thickness.

### Bioadhesive strength study

The adhesive strength of the tablets to rabbit stomach mucosa was evaluated using a self-made system with pallet scales. As shown in Figure 1, a hanging platform consisting of a cord and a glass slide attached with stomach mucosa was fixed to the pallet scales by a thick iron wire with a hook. A flat surfaced steel block was used as a lower static platform. The mucosa was mounted onto the lower platform using a medical rubber adhesive. The tablets were attached to the bottom of the hanging platform. The hanging platform with the tablets was brought down and placed over the surface of the mucosa with an applied force of 100 G for 15 min, and the force required to detach the tablets from the mucosal surface was determined by the weight of the added water. The test was performed at room temperature (23–25 °C), and the mean of the three measurements was used as the mucoadhesive strength of the tablets.

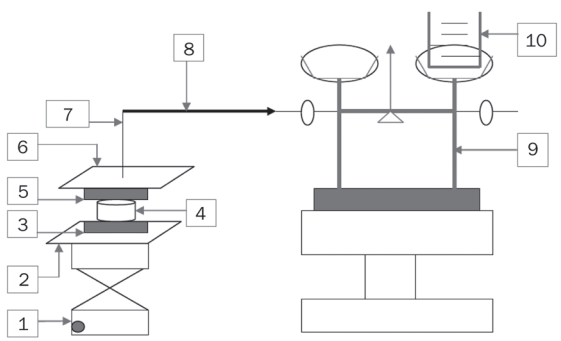


1. Height adjustment
2. Glass slide
3. Stomach tissue
4. Test table
5. Stomach tissue
6. Glass slide
7. Cord
8. Thick iron wire with hook
9. Balance
10. Beaker

**Figure 1.** Schematic diagram of the bioadhesion testing device.

### Self-microemulsifying study

To assess the self-microemulsifying properties, the tablet was introduced into 250 mL of 37 °C HCl buffer at pH 1.2 under a gentle agitation of 50 r/min in a rotating basket dissolution apparatus. When the tablet was completely eroded, a sample was withdrawn and investigated using the transmission electron microscope (JEM-1230, JEOL, Japan). The sample was stained with phosphotungstic acid for visualization and placed on copper grids for viewing at 25±2 °C. The droplet size distribution of the resultant emulsion was also determined by photon correlation spectroscopy (PCS) using a PSS Nicomp 380 ZLS (PSS Nicomp, Santa Barbara, CA, USA). Particle size distribution was expressed in a nicomp distribution. The sample was filtered through a 0.45-μm micropore filter.

### Drug-release study

Drug redispersibility and the release profiles of tacrolimus from the self-microemulsifying tablets and reference commercial immediate capsules were determined using the CP XC rotating basket method (RCZ-8B dissolution tester, RZQ-8A automatic sampler, RDB-8A peristaltic pump, Tian Da Tian Fa, Tianjin, China) at 37 °C. The rotating speed was 50 r/min, and the dissolution medium was 900 mL of HCl buffer at pH 1.2 containing 0.005% (*w/v*) of hydroxypropylmethyl cellulose (HPC-M). Dissolution studies were conducted over 12 h to evaluate the sustained-release properties of the preparations.

Samples (8 mL) were withdrawn at predetermined time intervals and were assayed for tacrolimus by HPLC at 210 nm. The HPLC system was composed of an autosampler (G1313A ALS), a pump (G1311 Quatpump), a column oven (G1316A Column), a UV detector (G1314A VWD) and data processing software (HP Chemstation Rev.A.10.01). Briefly, tacrolimus was analyzed using Agilent Zorbax XDB C8 (150×4.6 mm, 5 μm) a reverse phase chromatography column. The mobile phase consisted of acetonitrile-0.25% phosphoric acid (65:35, *v/v*) and was pumped at a flow rate of 1.0 mL/min.

*In vitro* release data of the sustained-release tablets were analyzed using the zero-order release model ($Q=kt$), Higuchi model ($Q=kts^{1/2}$) and the first-order release model [$\ln(100-Q)=\ln 100-kt$], where $Q$ is the percentage of drug released at $t$ time and $k$ is the release rate constant.

### *In vivo* pharmacokinetics study in beagle dogs

Six healthy beagle dogs that had fasted but had free access to water for 12 h prior to the experiment were used in this study. They were allocated at random to two treatment groups and were orally administered gastroretentive tablets and two reference commercial capsules of tacrolimus once a day in a cross-

over design with a 1-week washout period between dosing. The dose of tacrolimus administered was 2 mg.

At a predetermined time interval, a blood sample (3.0 mL) was withdrawn at 0, 1, 2, 4, 6, 8, 10, 12, 24, and 36 h for the gastroretentive tablet group and 0.5, 1, 1.5, 2, 3, 4, 6, 8, 10, 12, and 24 h for the reference capsule group. Blood samples collected from the thigh vein were syringed into centrifuge tubes containing heparin and then kept frozen at -20 °C until analysis. The tacrolimus concentrations in the whole blood samples were determined by high performance liquid chromatography mass spectrometry (HPLC-MS) with a low quantitation limit of 0.2 ng/mL.

A selective, rapid and sensitive HPLC-MS method was developed for the quantification of tacrolimus in dog whole blood. A two-step liquid-liquid extraction was included in the sample pretreatment. Then, 1 mL of a 70% acetonitrile solution was added to 1 mL of the whole blood. After vortex mixing for 30 s, 4 mL of dichloromethane solution containing 1% isoamyl alcohol was added and vortexed for 15 min. After centrifugation at 4000 r/min for 10 min, the lower organic phase was collected, and the residue was extracted with 4 mL of dichloromethane solution containing 1% isoamyl alcohol. The lower organic phase was combined and dried under nitrogen gas at 70 °C. The residue was reconstituted with 200 μL of the mobile phase. Separation was carried out on an Alltech-Alltima$^{TM}$-C18 column (150 mm×2.1 mm, 3 μm) with methanol as the mobile phase at a flow rate of 0.2 mL/min.

Detection was performed by a Thermo Finnigan LTQ HPLC-MS (Thermo Finnigan, USA). The mass spectrometer was operated with an electrospray ionization (ESI) interface in positive ionization mode and with multiple-reaction monitoring mode. The selected reaction monitoring (SRM) of tacrolimus was *m/z* 826.48. The concentration of tacrolimus was determined by a standard linear calibration curve in the concentration range of 0.2–20 ng/mL.

The maximum whole blood concentration ($C_{max}$), time to $C_{max}$ ($t_{max}$), and the area under the whole blood concentration versus time curve (AUC) were calculated from observed data points with the Drug and Statistics (DAS 2.1.1) pharmacokinetic software. Statistical analysis ($C_{max}$, $t_{max}$, AUC) was also conducted with the DAS 2.1.1 software. The relative bioavailability (F) of the gastroretentive tablet to the commercial capsule (reference) was calculated using the following equation:

$$F=\frac{AUC_{test}}{AUC_{reference}}\times 100\%$$

### Statistical analysis

Results are expressed as the mean±standard deviation. Statistical comparisons were performed using a bilateral *t*-test ($C_{max}$, AUC) and a non-parametric test ($t_{max}$) with the DAS 2.1.1 software. A $P$ value <0.05 was considered statistically significant.

## Results

### Development of the tablet

Self-microemulsifying systems form fine oil-water emulsions with only gentle agitation upon their introduction into aqueous media. Therefore, the selection of the oil, surfactant, and mixing ratio play an important role in the formulation of the microemulsion. In the present study, Cremophor RH40 and GMC were tested for phase behavior. The influence of the oil and surfactant ratio on the particle size distribution was evaluated. As seen in Figure 2, Cremophor RH40 gave a wide microemulsion region. Increasing the oil ratio resulted in a larger particle size. Cremophor RH40 and monocaprylin glycerate at a ratio of 4:6 have the optimal particle size distribution, so it was selected for the formulation study.

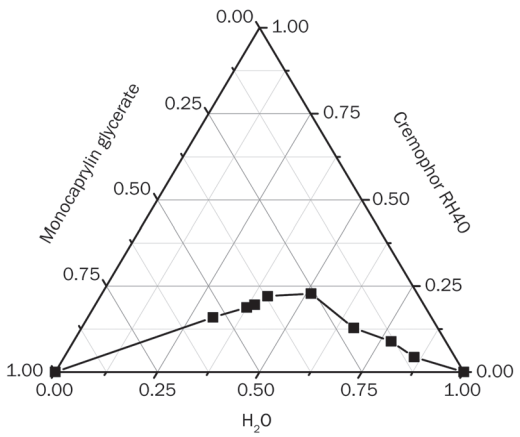


| Formulation | Cremophor RH40: Monocaprylin glycerate | Mean particle size (nm) | Polydispersity index |
|---|---|---|---|
| S1 | 8:2 | 15.1±1.5 | 0.21±0.02 |
| S2 | 6:4 | 24.3±2.1 | 0.38±0.047 |
| S3 | 4:6 | 25.9±2.3 | 0.04±0.007 |
| S4 | 3:7 | 44.4±2.8 | 0.28±0.032 |
| S5 | 2:8 | 104.6±3.6 | 0.44±0.051 |

**Figure 2.** Phase diagram and particle size distribution of SMEDDS containing Cremophor RH40 and monocaprylin glycerate.

On the basis of previous studies on the swelling properties of matrix tablets, we concluded that the polyethylene oxide (PEO) polymer is an excellent vehicle for swelling tablets[25–27]. Earlier studies have demonstrated that PEO also has good adhesion. Therefore, PEO was chosen as the skeleton material of the tablet, which provided swelling and adhesion capability for the tablet. PVP is a nonirritant material that is extensively used as a tablet binder[27]. It is well known that the expanded form must maintain its integrity and have adequate strength to withstand the force in the stomach[28]. Moreover, the high molecular weight grades of PVP offer higher binding capacity. Therefore, PVP K90 was introduced as a tablet binder and was simultaneously used to increase the ability of the resistance to the gastric motility of the swelling tablet.

The goals of gastric retention and controlling release are not

always compatible. PEO is a matrix material that possesses the characteristics of both swelling and controlling release; however, PEO takes a very long time to completely erode when it is used at the amount needed for sufficient swelling to achieve gastric retention. Some other matrix materials can also swell but offer the benefit of faster and more even erosion in the gastric environment, which means that the dosage form made with these materials can pass through the gastrointestinal tract more predictably after a few hours of drug release. One such material is chitosan, which swells, but not to the same degree as PEO. Chitosan can generate synergies with PEO in the expansion of matrix tablets, and the releases that are controlled by the erosion of the polymeric matrix are also easier. Moreover, chitosan also has very strong adhesion, which has a prominent role in enhancing the adhesion force of the tablet. Hence, we developed a PEO and chitosan combination gastric retention tablet, which not only maintained good swelling of the tablets but also insured that the tablets completely eroded at the scheduled time, taking double advantage of the chitosan. In this study, mannitol was used to further regulate the drug-release rate.

### Expanding study

It is reported that the dosage form size has a great influence on its residual effects in the stomach. Due to the retropulsion reflex, gastroretentivity may simply be achieved by large dimensions that are physically unable to pass through the pyloric sphincter[29]. The pyloric sphincter has a diameter of 12.8±7 mm in humans[29]. To achieve a size adequate for preventing passage through the pylorus yet small enough to be swallowed requires very significant expansion in at least two dimensions[28]. The tablet we developed expanded to 13.5 mm in diameter and 15 mm in thickness after 20 min, and then to 16 mm in diameter and 20 mm in thickness after 3 h of contact with an HCl buffer at pH 1.2. The two dimensions of the size of the tablet at different times are shown in Figure 3. The results revealed that the tablet swelled rapidly when immersed in the HCl buffer at pH 1.2, and the tablet maintained this large size for at least 8 h. These results indicated that the tablet had a very good capacity to improve the effectiveness of gastric retention.

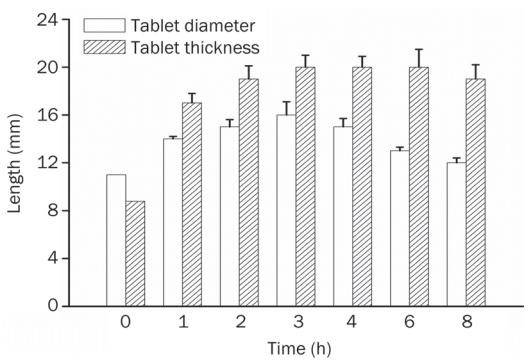


**Figure 3.** Gel layer diameter and thickness of the self-microemulsifying gastroretentive sustained-release tablets during contact with the HCl buffer at pH 1.2. *n*=6. Mean±SD.

### Bioadhesive strength study

Gastroretention can be achieved by the swelling property of the tablet, and bioadhesion may be an important property for further strengthening of the gastroretentive feature of tablets. PEO polymers are reported to have potential bioadhesive properties. To reinforce the mucoadhesion feature, chitosan, which is widely used as a bioadhesive polymer, was added to the formulation. Its mucoadhesive properties are mediated by ionic interactions of the positively charged amino groups and negatively charged substructures of the gastrointestinal mucus, mainly sialic acid[30]. The dissolution time and bioadhesion force with and without chitosan are shown in Table 2. As depicted in Table 2, the result of the bioadhesion study indicated that chitosan had a more significant effect than PEO on bioadhesion. This may be due to different adhesion mechanisms in PEO and chitosan, which resulted in different contributions to the adhesion of the tablet. Moreover, tablets with chitosan took less time to completely erode. The bioadhesive strength of PEO N60K tablet with chitosan was 0.98±0.06 $N/cm^2$, which ensured that the tablet could adhere to the gastric mucosa.

**Table 2.** Bioadhesion and time for 95% drug release of PEO tablets. *n*=6. Mean±SD.

| Code# | Composition | Bioadhesion ($N/cm^2$) | Time for 95% drug release (h) |
|---|---|---|---|
| 1 | PEO 600 mg | 0.81±0.09 | 21.8±1.2 |
| 2 | PEO 300 mg+Chitosan 300 mg | 0.98±0.06 | 12.1±0.8 |

PEO, polyethylene oxide. Formation #1 and #2 also include 2 mg tacrolimus, 60 mg monocaprylin glycerate, 40 mg Cremophor RH40, 250 mg mannitol, 50 mg polyvinylpyrrolidone.

### Self-microemulsifying study

The incorporation of the self-microemulsifying mixture into a solid dosage form is desirable, but challenging, because self-microemulsifying properties are harder to achieve with solid materials[7]. Therefore, it is necessary to determine whether or not the tablet that is composed of a self-microemulsifying mixture and solid materials can self-microemulsify when it contacts water or SGF. The droplet size nicomp distribution of the liquid SMEDDS and solid SMEDDS are shown in Figure 4. The average dispersing droplet size of the liquid SMEDDS and solid SMEDDS were 28.9 nm and 26.2 nm, respectively. These results indicated that the solid self-microemulsifying formulation (SMEF) preserved the self-microemulsification performance of the liquid SMEF. TEM (Figure 5) showed that the reconstituted microemulsions were released from the solid SMEF when exposed to SGF. The size range was narrow, and the droplet size was very small (approximately

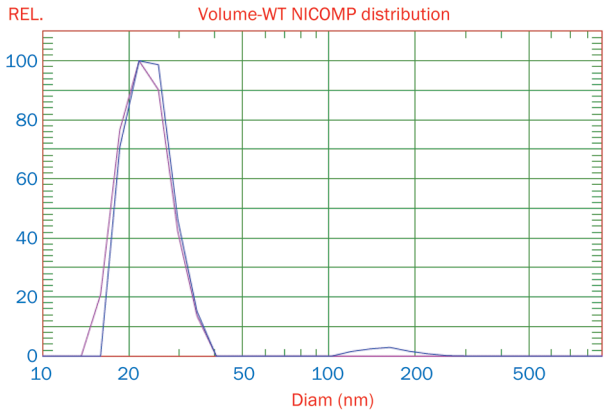


**Figure 4.** Microemulsion droplet size distribution: solid SMEDDS (blue line); liquid SMEDDS (red line).

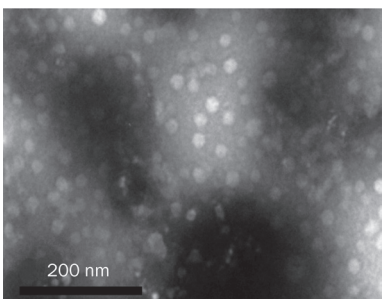


**Figure 5.** Transmission electron micrograph of the reconstituted microemulsion released from the gastroretentive sustained-release tablet.

20–30 nm). These results were consistent with the results of the PCS analysis. TEM showed the quality of the microemulsion that was formed. Emulsion droplet size is a decisive factor in self-microemulsifying formulation performance because it determines the rate and the extent of drug release. Smaller droplet size improves the drug release and provides a larger interfacial area across which the drug can diffuse into the gastrointestinal fluids, and thus, it increases drug absorption[31, 32]. TEM and nicomp distribution results confirmed that the tablet could self-microemulsify in the gastrointestinal tract, and the droplet size of the emulsion drops was small, which could achieve the purpose of increasing drug solubility and improving drug absorption.

### Drug-release study

For drug candidates with lower aqueous solubility, the drug-release rate is dependent mainly on the erosion of the polymeric matrix[33, 34]. As demonstrated in Figure 6, about 100% of the tacrolimus is released within 2 h from the commercial capsules. In contrast, for the tacrolimus self-microemulsifying gastroretentive sustained-release tablets, the concentration of drug released was very low within two hours, and almost no drug was released in the first hour. This was because the matrix swelling was much faster compared with the erosion

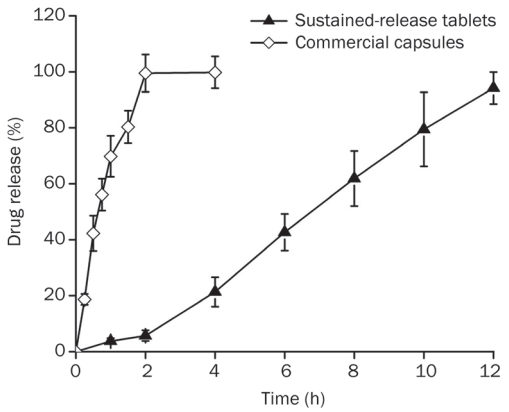


**Figure 6.** Dissolution profiles of tacrolimus from the sustained-release self-microemulsifying gastroretentive tablets and the commercial immediate-release capsules. (2 mg tacrolimus; $n$=6, arithmetic mean±SD).

process during the initial contact with the dissolution medium; therefore, matrix erosion did not occur during this time.

The fitting equations of the drug-release curve are shown in Table 3. According to the correlation coefficient of the fitting curve, the release curve was fit to the zero-order release model, which was helpful in reducing fluctuations in blood concentrations. The release mechanism of tacrolimus from the PEO, chitosan and mannitol coupling gastric retention matrix tablets was mainly based on erosion.

**Table 3.** The release pattern of tacrolimus self-microemulsifying sustained release tablets.

| Release pattern | Fitting equation | $R^2$ | Adj $R^2$ |
|---|---|---|---|
| Zero order | $Q$=8.70426$t$–9.30741 | 0.9938 | 0.9925 |
| First order | Ln (100–$Q$)=-0.23325$t$+5.13975 | 0.8768 | 0.8522 |
| Higuchi | $Q$=38.55712$t^{1/2}$–45.72334 | 0.9586 | 0.9503 |

### *In vivo* pharmacokinetics study in beagle dogs

Mean whole blood levels of tacrolimus at each time point are summarized in Figure 7. From Table 4, it can be seen that the $AUC_{(0-\infty)}$ was approximately five times greater when tacrolimus was administered as gastroretentive tablets as compared to the commercial capsules. The mean value of $C_{max}$ for the gastroretentive tablets (8.86 ng/mL) was 2.3 times greater than the $C_{max}$ obtained with the same dose of tacrolimus administered as the commercial capsules (3.78 ng/mL). Gastroretentive tablets resulted in an average $t_{max}$ of 6.67 h, which was obviously longer than the $t_{max}$ of the commercial capsules (1 h). The gastroretentive tablets resulted in a significant absorption of tacrolimus compared to the commercial capsules ($P$<0.05).

**Table 4.** Pharmacokinetic parameters of tacrolimus from self-microemulsifying gastricretentive sustained release tablets and commerical capsules.

| No | Order of administration | $AUC_{(0-t)}$ (ng·h·mL$^{-1}$) | | $AUC_{(0-\infty)}$ (ng·h·mL$^{-1}$) | | $t_{max}$ (h) | | $C_{max}$ (ng·mL$^{-1}$) | | F% |
|---|---|---|---|---|---|---|---|---|---|---|
| | | SEGT[a] | CC[b] | SEGT | CC | SEGT | CC | SEGT | CC | |
| 1 | SMEGSRT/CC | 88.20 | 28.54 | 126.22 | 40.56 | 4 | 1 | 6.61 | 4.82 | 309.0 |
| 2 | SMEGSRT/CC | 206.91 | 18.67 | 252.52 | 25.68 | 8 | 1 | 11.54 | 2.50 | 1107.8 |
| 3 | SMEGSRT/CC | 74.48 | 43.99 | 85.39 | 68.74 | 6 | 1 | 6.02 | 5.01 | 169.3 |
| 4 | CC/SMEGSRT | 209.91 | 32.11 | 320.47 | 48.21 | 10 | 1 | 11.23 | 3.98 | 653.7 |
| 5 | CC/SMEGSRT | 82.73 | 26.21 | 103.03 | 35.65 | 4 | 1 | 7.80 | 3.47 | 315.6 |
| 6 | CC/SMEGSRT | 194.35 | 25.41 | 265.86 | 33.14 | 8 | 1 | 9.96 | 2.88 | 764.9 |
| | Mean | 142.76 | 29.16 | 192.25 | 42.00 | 6.67 | 1 | 8.86 | 3.78 | 553.4 |
| | SD | 67.12 | 8.51 | 99.23 | 15.10 | 2.42 | 0 | 2.38 | 1.02 | 353.8 |

[a] SMEGSRT self-microemulsifying gastricretentive sustained release tablets.
[b] CC commercial capsules.

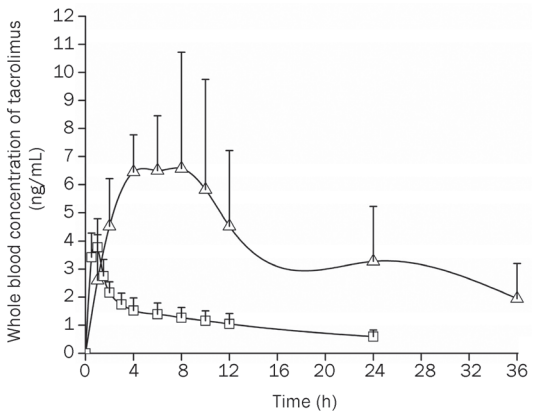


**Figure 7.** Whole blood concentration versus time curve (arithmetic mean±SD, *n*=6) of tacrolimus (2 mg per dog) in beagle dogs after oral administration of the self-microemulsifying gastroretentive sustained-release tablets (Δ) or commercial capsules (□).

## Discussion

There is a clear pharmaceutical need for advanced delivery systems that continuously supply drugs with narrow absorption window to their absorption site for an extended time period. This approach would provide effective and sustained drug concentrations in the blood for prolonged periods of time. It would also eliminate the need for frequent drug administration and the use of inconvenient modes of administration. This is particularly true for tacrolimus to prolong the release of drug in the duodenum by a gastroretentive dosage form (GRDF).

The current investigation presents a novel and promising sustained-release GRDF based on the combination of large dimensions, bioadhesive strength, sustained release of the loaded drug and self-microemulsification. In this study, the sustained-release GRDF of tacrolimus was prepared using a combination of PEO and chitosan as a solid carrier. The SME gastroretentive sustained-release tablets preserved the self-microemulsification performance of the liquid SMEDDS. The optimized formulation followed zero-order release kinetics. Swelling studies indicated significant water uptake and swelling, which may be significant in gastroretention. The bioadhesive properties were also studied, and the developed formulation showed significant bioadhesion. Thus, by combining these approaches of gastroretention together, the *in vivo* gastroretention could be predicted more reliably. Based on these promising *in vitro* results, *in vivo* studies in beagle dogs were carried out to determine various pharmacokinetic parameters. The relative oral bioavailability of the model drug, tacrolimus, was 5.5-fold compared to the commercial capsules. Gastroretentive tablets resulted in an average $t_{max}$ of 6.67 h, which was obviously longer than the $t_{max}$ obtained from the commercial capsules (1 h).

The higher bioavailability of hydrophobic drugs incorporated in a SMEDDS has been reported elsewhere[35–37]. The contribution of the GRDF approach extended the length of the absorption phase in comparison with the non-gastroretentive dosage form. This allows the desired therapeutic concentration to be achieved for prolonged periods of time. Thus, a combination of SMEDDS and GRDF can usually further improve the bioavailability of drugs. However, in terms of some rapid metabolism of drugs in the gastrointestinal tract, GRDF, which inputs the drug into the intestinal epithelial cells with the sustained mode, may enhance the efficacy of first pass metabolism in the intestinal wall. This phenomenon may reduce the bioavailability of drugs in some cases. Therefore, whether the sustained-release gastroretentive tablets can enhance the bioavailability of self-microemulsifying agents needs further study according to the specific absorption and metabolism characteristics of drugs.

Several factors have been suggested as possible determinants of the low oral bioavailability of tacrolimus. These include a low solubility in the intestine, extensive metabolism by CYP3A4 in the gut, and P-gp-mediated drug efflux. Regional differences in the functional expression of P-gp were investigated in the human intestine, indicating that there is higher activity of P-gp in the ileum and the colon than in the jejunum[16]. Therefore, the sustained-release gastroreten-

tive tablets we prepared in this study can avoid extensive CYP3A4 metabolism and P-gp-mediated efflux by releasing tacrolimus in the upper part of the small intestine, promote the drug absorption, and further enhance the bioavailability of SME. Both SME, which increased drug solubility, and gastroretention technology, which prolonged the time that the drug remains in the upper part of the gastrointestinal tract, are responsible for the enhanced bioavailability of tacrolimus.

In conclusion, the current study demonstrates that a self-microemulsifying, swellable and bioadhesive gastroretentive delivery system, which has great potential to reduce the blood concentration fluctuations and increase the overall bioavailability of the model drug tacrolimus, has been successfully developed. The presence of highly swellable and strongly bioadhesive polymers within the developed systems provided rapid swelling and significant bioadhesive force. Soluble mannitol made the matrix more liable to erosion, which resulted in drug release in a predetermined manner by varying the mannitol concentration. The drug release was characterized by a substantial zero-order profile, which was helpful in reducing blood concentration fluctuations. Complete dissolution or erosion of the formulation matrix in a timely manner is important for gastroretentive dosage forms because very slow erosion or dissolution may lead to expulsion and other gastrointestinal safety issues. The tablet we developed could completely erode within approximately 12 h, so it would avoid the safety problems that were previously mentioned. We can come to the conclusion that PEO in combination with chitosan is a promising carrier for gastroretentive drug delivery systems and solid self-microemulsifying drug delivery systems. SME gastroretentive sustained-release tablets are potential vehicles for drugs with poor solubility and a narrow absorption window. Moreover, it possesses broad prospects for industrial application.

## Acknowledgements

We are grateful to DOW Chemical for the generous gift of PEO WSR N60K and to the ISP Corporation for kindly providing PVP K90.

## Author contribution

This research was designed by Yong GAN and Xin-xin ZHANG. The experiments were performed by Yan-ping WANG. The manuscript was written by Yan-ping WANG and Xin-xin ZHANG.

## References

1 Yamashita K, Nakate T, Okimoto K, Ohike A, Tokunaga Y, Ibuki R, *et al*. Establishment of new preparation method for solid dispersion formulation of tacrolimus. Int J Pharm 2003; 267: 79–91.

2 Kino T, Hatanaka H, Hashimoto M, Nishiyama M, Goto T, Okuhara M, *et al*. FK 506, a novel immunosuppressant isolated from a *Streptomyces* I. Fermentation, isolation and physico-chemical and biological characteristics. J Antibiot 1987; 42: 1249–55.

3 Plosker GL, Foster RH. Tacrolimus–a further update of its pharmacology and therapeutic use in the management of organ transplantation. Drugs 2000; 59: 323–89.

4 Borhade V, Nair H, Hegde D. Design and evaluation of self-microemulsifying drug delivery system (SMEDDS) of tacrolimus. AAPS PharmSciTech 2008; 9: 13–21.

5 Abdalla A, Klein S, Mader K. A new self-emulsifying drug delivery system (SEDDS) for poorly soluble drugs: characterization, dissolution, *in vitro* digestion and incorporation into solid pellets. Eur J Pharm Sci 2008; 35: 457–64.

6 Gursoy RN, Benita S. Self-emulsifying drug delivery systems (SEDDS) for improved oral delivery of lipophilic drugs. Biomed Pharmacother 2004; 58: 173–82.

7 Abdalla A, Mader K. Preparation and characterization of a self-emulsifying pellet formulation. Eur J Pharm Biopharm 2007; 66: 220–6.

8 Nazzal S, Khan MA. Controlled release of a self-emulsifying formulation from a tablet dosage form: stability assessment and optimization of some processing parameters. Int J Pharm 2006; 315: 110–21.

9 Patil P, Joshi P, Paradkar A. Effect of formulation variables on preparation and evaluation of gelled self-emulsifying drug delivery system (SEDDS) of ketoprofen. AAPS PharmSciTech 2004; 5: e42.

10 Joseph S, inventors; AluhaRx Inc., assignee. Solid self-emulsifying dosage form for improved delivery of poorly soluble hydrophobic compounds and the process for preparation there of. US Patent 10252158. 2002 Sep 23.

11 Tang B, Cheng G, Gu JC, Xu CH. Development of solid self-emulsifying drug delivery systems: preparation techniques and dosage forms. Drug Discovery Today 2008; 13: 606–12.

12 Serratoni M, Newton M, Booth S, Clarke A. Controlled drug release from pellets containing water-insoluble drugs dissolved in a self-emulsifying system. Eur J Pharm Biopharm 2007; 65: 94–8.

13 Balakrishnan P, Lee BJ, Oh DH, Kim JO, Hong MJ, Jee JP, *et al*. Enhanced oral bioavailability of dexibuprofen by a novel solid self-emulsifying drug delivery system (SEDDS). Eur J Pharm Biopharm 2009; 72: 539–45.

14 Nazzal S, Nutan M, Palamakula A, Shah R, Zaghloul AA, Khan MA. Optimization of a self-nanoemulsified tablet dosage form of ubiquinone using response surface methodology: effect of formulation ingredients. Int J Pharm 2002; 240: 103–14.

15 Tuleu C, Newton M, Rose J, Euler D, Saklatvala R, Clarke A, *et al*. Comparative bioavailability study in dogs of a self-emulsifying formulation of progesterone presented in a pellet and liquid form compared with an aqueous suspension of progesterone. J Pharm Sci 2004; 93: 1495–502.

16 Tamura S, Tokunaga Y, Ibuki R, Amidon GL, Sezaki H, Yamashita S. The site-specific transport and metabolism of tacrolimus in rat small intestine. J Pharmacol Exp Ther 2003; 306: 310–6.

17 Venkataramanan R, Swaminathan A, Prasad T, Jain A, Zuckerman S, Warty V, *et al*. Clinical pharmacokinetics of tacrolimus. Clin Pharmacokinet 1995; 29: 404–30.

18 Holm P, Norling T, Lademann AM, inventors; LIFECYCLE PHARMA A/S, assignee. Once daily oral dosage form comprising tacrolimus. Patent WO2008/145143. 2008 May 30.

19 Kagayama A, Tanimoto S, Fujisaki J, Kaibara A, Ohara K, Iwasaki K, *et al*. Oral absorption of FK506 in rats. Pharm Res 1993; 10: 1446–50.

20 Shigeki T, Atsuo O, Rinta I, Gordon L, Shinji Y. Tacrolimus is a class II low-solubility high-permeability drug: the effect of P-glycoprotein efflux on regional permeability of tacrolimus in rats. J Pharm Sci 2002; 91: 719–29.

21 Streubel A, Siepmann J, Bodmeier R. Gastroretentive drug delivery systems. Expert Opin Drug Deliv 2006; 3: 217–33.

22 Strubing S, Abboud T, Contri RV, Metz H, Mader K. New insights on poly(vinyl acetate)-based coated floating tablets: Characterisation

of hydration and $CO_2$ generation by benchtop MRI and its relation to drug release and floating strength. Eur J Pharm Biopharm 2008; 69: 708–17.

23 Ramji AKA, Chandra SRG, Prabhakar RV. Formulation and evaluation of swellable and floating gastroretentive ciprofloxacin hydrochloride tablets. AAPS PharmSciTech 2009; 10: 220–6.

24 Parikh DC, Amin AF. *In vitro* and *in vivo* techniques to assess the performance of gastro-retentive drug delivery systems: a review. Expert Opin Drug Deliv 2008; 5: 951–65.

25 Gusler G, Berner B, Chau M, Berner B, inventors; Depomed, Inc, assignee. Optimal polymer mixtures for gastric. Patent AU2002337974. 2002 Oct 22.

26 Wu N, Wang LS, Tan DCW, Moochhala SM, Yang YY. Mathematical modeling and *in vitro* study of controlled drug release via a highly swellable and dissoluble polymer matrix: polyethylene oxide with high molecular weights. J Control Release 2005; 102: 569–81.

27 Mahalingam R, Jasti B, Birudaraj R, Stefanidis D, Killion R, Alfredson T, *et al*. Evaluation of polyethylene oxide compacts as gastroretentive delivery systems. AAPS PharmSciTech 2009; 10: 98–103.

28 Waterman KC. A critical review of gastric retentive controlled drug delivery. Pharm Dev Technol 2007; 12: 1–10.

29 Klausner EA, Lavy E, Friedman M, Hoffman A. Expandable gastroretentive dosage forms. J Control Release 2003; 90: 143–62.

30 Werle M, Bernkop SA. Thiolated chitosans: useful excipients for oral drug delivery. J Pharm Pharmacol 2008; 60: 273–81.

31 Chambin O, Jannin V, Champion D, Chevalier C, Rochat-Gonthier MH, Pourcelot Y. Influence of cryogenic grinding on properties of a self-emulsifying formulation. Int J Pharm 2004; 278: 79–89.

32 Constantinides PP. Lipid microemulsions for improving drug dissolution and oral absorption: physical and biopharmaceutical aspects. Pharm Res 1995; 12: 1561–72.

33 Li HT, Hardy RJ, Gu XC. Effect of drug solubility on polymer hydration and drug dissolution from polyethylene oxide (PEO) matrix tablets. AAPS PharmSciTech 2008; 9: 437–43.

34 Kim CJ. Effects of drug solubility, drug loading, and polymer molecular weight on drug release from Polyox® tablets. Drug Dev Ind Pharm 1998; 24: 645–51.

35 Shah NH, Carvajal MT, Patel CI, Infeld MH, Malick AW. Self-emulsifying drug delivery systems (SEDDS) with polyglycolized glycerides for improving *in vitro* dissolution and oral absorption of lipophilic drugs. Int J Pharm 1994; 106: 15–23.

36 Hauss DJ, Fogal SE, Ficorilli JV, Price CA, Roy T, Jayaraj AA, *et al*. Lipid-based delivery systems for improving the bioavailability and lymphatic transport of a poorly water-soluble LTB4 inhibitor. J Pharm Sci 1998; 87: 164–9.

37 Fischl MA, Richman DD, Flexner C, Para MF, Jaubrich R, Karim A, *et al*. Phase I/II study of the toxicity, pharmacokinetics, and activity of the HIV protease inhibitor SC-52151. J Acquir Immune Defic Syndr Hum Retrovirol 1997; 15: 28–34.

Acta Pharmacologica Sinica (2011) 32: 1303–1308
 1671-4083/11 $32.00
www.nature.com/aps

Original Article

# Frequency of *CYP2C9* alleles in Koreans and their effects on losartan pharmacokinetics

Jung-woo BAE[1, 3, #], Chang-ik CHOI[1, #], Mi-jeong KIM[1], Da-hee OH[1], Seul-ki KEUM[1], Jung-in PARK[1], Bo-hye KIM[1], Hye-kyoung BANG[1], Sung-gon OH[1], Byung-sung KANG[1], Hye-in LEE[1], Yun-jeong LEE[1], Hyun-joo PARK[2], Hae-deun KIM[2], Ji-hey HA[2], Hee-jung SHIN[2], Young-hoon KIM[2], Han-sung NA[2], Myeon-woo CHUNG[2], Soon-young HAN[2], Seung-hee KIM[2], Choon-gon JANG[1], Seok-yong LEE[1, *]

[1]*School of Pharmacy, Sungkyunkwan University, Suwon, 440–746, Korea;* [2]*National Institute of Food and Drug Safety Evaluation, KFDA, Cheongwon-gun, 363–951, Korea;* [3]*College of Pharmacy, Keimyung University, Daegu, 704–701, Korea*

**Aim:** CYP2C9 enzyme metabolizes numerous clinically important drugs. The aim of this study is to investigate the frequencies of *CYP2C9* genotypes and the effects of selected alleles on losartan pharmacokinetics in a large sample of the Korean population.
**Methods:** The *CYP2C9* gene was genotyped in 1796 healthy Korean subjects. *CYP2C9* alleles (*CYP2C9*1, *2, *3,* and **13* alleles) were measured using polymerase chain reaction-restriction fragment length polymorphism (PCR-RFLP) assay and direct sequencing assay. The enzymatic activity of each *CYP2C9* genotype was evaluated using losartan as the substrate.
**Results:** The frequencies of *CYP2C9*1, *3,* and **13* allele were 0.952 (95% confidence interval 0.945–0.959), 0.044 (95% CI 0.037–0.051), and 0.005 (95% CI 0.003–0.007), respectively. The frequencies of the *CYP2C9*1/*1, *1/*3, *1/*13*, and **3/*3* genotypes were 0.904 (95% CI 0.890–0.918), 0.085 (95% CI 0.072–0.098), 0.009 (95% CI 0.005–0.013), and 0.001 (95% CI 0.000–0.002), respectively. In the pharmacokinetics studies, the $AUC_{0-\infty}$ of losartan in *CYP2C9*3/*3* subject was 1.42-fold larger than that in *CYP2C9*1/*1* subjects, and the $AUC_{0-\infty}$ of E-3174, a more active metabolite of losartan, in *CYP2C9*3/*3* subject was only 12% of that in *CYP2C9*1/*1* subjects.
**Conclusion:** The results confirmed the frequencies of *CYP2C9* genotypes in a large cohort of Koreans, and detected the *CYP2C9*3/*3* genotype. *CYP2C9*3/*3* subjects metabolized much less losartan into E-3174 than *CYP2C9*1/*1* subjects.

**Keywords:** CYP2C9; allele; genotype; Korean; pharmacokinetics; losartan

*Acta Pharmacologica Sinica* (2011) 32: 1303–1308; doi: 10.1038/aps.2011.100; published online 15 Aug 2011

## Introduction

The cytochrome P450 (CYP) 2C9 enzyme oxidizes many clinically important compounds, including drugs with narrow therapeutic indexes such as warfarin, tolbutamide, and phenytoin, as well as other common drugs such as glibenclamide, glimepiride, glipizide, losartan, irbesartan, torsemide, and many anti-inflammatory drugs[1, 2]. Genetic polymorphisms in enzymes that metabolize drugs are major determinants of variability in individual response. Thirty-five alleles of the *CYP2C9* gene have been reported (http://www.cypalleles.ki.se/cyp2c9.htm) and three of these, *CYP2C9*1, *2,* and **3*, are frequently identified in most populations. The *CYP2C9*2* allele is the most common deleterious allele among people of European descent, with a frequency of 0.080 to 0.191. The *CYP2C9*3* allele is less common (0.033–0.162)[3]. In contrast, the *CYP2C9*2* allele is rare among East Asians[3, 4], and *CYP2C9*3* is more common than that in Europeans (0.007 to 0.060)[5]. In addition, *CYP2C9*3* homozygotes are seldom detected in East Asian populations[5]. *CYP2C9*3* has the lowest metabolic activity *in vitro*, while *CYP2C9*2* has an intermediate enzyme activity, and *CYP2C9*1* has the highest activity[6]. Individuals with mutant *CYP2C9* variants may not metabolize drugs adequately, leading to drug toxicity. Therefore, drug doses must be adjusted according to genotype. The frequencies of *CYP2C9* alleles vary between populations, information that is useful for clinical pharmacotherapy. The frequencies of *CYP2C9* alleles and genotypes in the Korean population have been calculated[5, 7–9], however, there are significant discrepancies in the reported *CYP2C9*3* frequencies. Thus, we measured the *CYP2C9* allele and genotype frequencies in a large Korean cohort, where we

# These authors contributed equally to this work.
* To whom correspondence should be addressed.
E-mail sylee@skku.ac.kr
Received 2011-03-17 Accepted 2011-06-15

detected the *CYP2C9*3/*3* genotype and analyzed the effects of the *CYP2C9*3/*3* genotype on losartan pharmacokinetics.

## Materials and methods

### Subjects

We enrolled 1796 unrelated healthy Korean volunteers in this genotyping study. Written informed consent was obtained from all volunteers.

### Genotyping tests

Genomic DNA was isolated from peripheral blood leukocytes using the Wizard® Genomic DNA Kit (Promega, Madison, WI, USA) according to the manufacturer's instructions. Analyses of the *CYP2C9*2, *3,* and **13* alleles were performed using polymerase chain reaction restriction fragment length polymorphism (PCR-RFLP), as described previously[5]. The *CYP2C9*1* allele was assigned in the absence of other detectable alleles. The genotypes identified by PCR-RFLP were confirmed by sequence analysis. Exons and exon/intron junctions of the *CYP2C9* gene were amplified as described with slight modifications[5, 10]. The PCR products were purified using a PCR purification kit (AxyPrep® PCR Clean-up Kit, Axygen Bioscience Inc, Union City, CA, USA) and sequenced on an ABI3730 automatic sequencer (Applied Biosystems Inc, Foster City, CA, USA) using a BigDye Terminator Cycle Sequencing Ready Reaction Kit (Applied Biosystems Inc, Delaware, USA).

### Protocol for pharmacokinetic studies

Thirteen healthy male Korean subjects with *CYP2C9*1/*1* ($n$=12) or *CYP2C9*3/*3* ($n$=1) genotypes were selected for a pharmacokinetic study of losartan. Although two subjects with *CYP2C9*3/*3* were detected, one did not provide written informed consent. Thus, only one subject with *CYP2C9*3/*3* was enrolled in the pharmacokinetic study.

The subjects were between 20 and 26 years old and had body mass indexes between 21 and 25 kg/m$^2$. All subjects were healthy as defined by medical history, physical examination, and routine laboratory tests (blood chemistry, hematology, and urine analysis). The subjects were asked to refrain from ingesting medications, caffeine, grapefruit products, and alcoholic beverages and from smoking for at least 1 week before and during the study period. All subjects provided verbal and written informed consent after being given an explanation of the experimental procedures and purpose of the study. The institutional ethics committee of the School of Pharmacy, Sungkyunkwan University, Korea approved the study protocol. All procedures were performed in accordance with the recommendations of the Declaration of Helsinki on biomedical research involving human subjects.

On the day of the study, each subject received 50 mg of losartan potassium (Cozaar®, MSD-Korea, Seoul, Korea) orally with 240 mL of water after an overnight fast. The subjects maintained the fasting state for 4 h after receiving the drug. Before and at 0.5, 1, 1.5, 2, 3, 4, 6, 8, 10, and 24 h, venous blood samples (10 mL) were collected in heparinized tubes and centrifuged for 10 min at 3000 r/min. The plasma was separated and stored at -70 °C until needed.

### Assay of losartan and E-3174 in plasma

CYP2C9 metabolizes losartan to a more active metabolite, E-3174[11]. Thus, the losartan and E-3174 concentrations in the plasma were determined by HPLC with a fluorescence detector as previously reported with modifications[12]. Briefly, 1.0 mL of plasma, 150 ng of valsartan (IS), and 200 μL of 1 mol/L phosphoric acid were mixed in a glass tube, and extracted with 7 mL of methyl *tert*-butyl ether (MTBE) with constant vigorous stirring for 1 min. After centrifuging (2500 r/min for 10 min), the organic layer was transferred to another tube with 200 μL of 0.05 mol/L sodium hydroxide and stirred vigorously for 1 min. The samples were again centrifuged at 2500 r/min for 10 min. The aqueous layer was collected, and residual MTBE was removed by nitrogen evaporation. The sodium hydroxide layer was acidified with 50 μL of 0.2 mol/L phosphoric acid and mixed. The aqueous fraction was washed by adding 6 mL of *n*-hexane and mixing for 1 min. After centrifuging, the hexane was discarded, and residual *n*-hexane was removed by nitrogen evaporation. Methanol (150 μL) was added to 250 μL of the re-extracted water phase, and 100 μL of the resulting mixture was injected into the HPLC system. The HPLC system consisted of a Waters Model 515 HPLC pump, a Waters Model 717 Plus autosampler, a Waters 474 scanning fluorescence detector, and column oven (Waters, Milford, MA, USA). Separations were performed on a 5 μm Luna CN column (4.5 mm×250 mm; Phenomenex, Torrance, CA, USA). The mobile phase was 15 mmol/L phosphoric acid/acetonitrile (65:35, *v/v*) adjusted to pH 3.0 with 5 mol/L sodium hydroxide at 1 mL/min. The effluents were detected by fluorescence with excitation at 250 nm and emission at 380 nm. The standard curves for losartan and E-3174 were linear from 5 to 1000 ng/mL ($r^2$>0.999). The mean accuracy for losartan and E-3174 were 90%–102% and 96%–101%, respectively. The coefficients of variation (within-day and between-day precisions) of losartan and E-3174 were <9% and 10%, respectively.

### Pharmacokinetic analysis

The pharmacokinetic parameters of losartan and E-3174 were calculated by non-compartmental methods from the blood sampling times, maximum plasma concentration ($C_{max}$), and time to reach $C_{max}$ ($t_{max}$) using the BA Calc 2007 analysis program (KFDA, Seoul, Korea). The area under the curve (AUC) for plasma concentration-time was calculated using the linear trapezoidal rule. The elimination rate constant ($k_e$) was determined by linear regression analysis of the log-linear portion of the plasma concentration-time curve. The AUC from 0 to infinity ($AUC_{0-\infty}$) was calculated as $AUC_{0-\infty}=AUC+C_t/k_e$ ($C_t$ being the final plasma concentration). The half-life ($t_{1/2}$) was calculated as $t_{1/2}=\ln 2/k_e$. The apparent oral clearance (CL/F) of losartan was calculated as $CL/F=Dose/AUC_{0-\infty}$.

### Statistical analysis

Data were compiled according to the genotype and allele frequencies. The frequencies of each allele are reported with

95% confidence intervals. Hardy-Weinberg equilibrium was evaluated by comparing the genotype frequencies with the expected values using a contingency table $\chi^2$ test. Statistical significance was determined by $\chi^2$ test; a *P*-value less than 0.05 was considered significant. The pharmacokinetic data are expressed as mean±SD.

## Results

### Frequencies of *CYP2C9* alleles and genotypes

The estimated frequencies of the *CYP2C9* alleles and genotypes in the Korean population are summarized in Table 1. The genotype frequency distribution did not deviate significantly from Hardy-Weinberg equilibrium. *CYP2C9*1* was the most common allele (0.952, 95% CI: 0.945–0.959). The most common variant allele was *CYP2C9*3* (0.044, 95% CI: 0.037–0.051). The *CYP2C9*1/*3* frequency in this study was more than four times higher than previously reported[7] (*P*<0.01, Table 2). The *CYP2C9*13* frequency in our sample was 0.005 (95% CI: 0.003–0.007). There were 1624 subjects with the *CYP2C9*1/*1* genotype (0.904, 95% CI: 0.890–0.918), 153 with the *CYP2C9*1/*3* genotype (0.085, 95% CI: 0.072–0.098), 17 with the *CYP2C9*1/*13* genotype (0.009, 95% CI: 0.005–0.013), and 2 with the *CYP2C9*3/*3* genotype (0.001, 95% CI: 0.000–0.002) (Table 1). The genotype results from PCR-RFLP corresponded with the sequencing results (data not shown).

**Table 1.** *CYP2C9* allele (A) and genotype (B) frequencies in a large Korean sample. The expected genotype frequencies were calculated from the allele frequencies using the Hardy-Weinberg equation.

A

| Allele | *n* (3592) | Frequency | 95% CI |
|---|---|---|---|
| *CYP2C9*1* | 3418 | 0.952 | 0.945–0.959 |
| *CYP2C9*2* | 0 | 0.000 | 0.000–0.000 |
| *CYP2C9*3* | 157 | 0.044 | 0.037–0.051 |
| *CYP2C9*13* | 17 | 0.005 | 0.003–0.007 |

B

| Genotype | Number of subjects | Observed frequency | 95% CI | Expected frequency |
|---|---|---|---|---|
| *CYP2C9*1/*1* | 1624 | 0.904 | 0.890–0.918 | 0.905 |
| *CYP2C9*1/*3* | 153 | 0.085 | 0.072–0.098 | 0.083 |
| *CYP2C9*1/*13* | 17 | 0.009 | 0.005–0.013 | 0.009 |
| *CYP2C9*3/*3* | 2 | 0.001 | 0.000–0.002 | 0.002 |
| *CYP2C9*3/*13* | 0 | 0.000 | 0.000–0.000 | 0.000 |
| *CYP2C9*13/*13* | 0 | 0.000 | 0.000–0.000 | 0.000 |

The *CYP2C9*3* allele frequency in our Korean sample was slightly (although not significantly) higher than in Chinese samples, and was significantly higher than in Japanese samples (*P*<0.01) (Table 3). The *CYP2C9*13* allele frequency in our sample was slightly lower than in Chinese samples, and slightly higher than in Japanese samples, although these differences were not significant (Table 3).

### Pharmacokinetics of losartan

The losartan and E-3174 pharmacokinetic parameters were measured in one subject with the *CYP2C9*3/*3* genotype, a rare genotype in Koreans (0.1%, Table 1). In this subject, the $C_{max}$ and $AUC_{0-\infty}$ of losartan were slightly higher and the CL/F was lower than in *CYP2C9*1/*1* subjects, but losartan metabolism to E-3174 was almost completely blocked (Figure 1, Table 4).

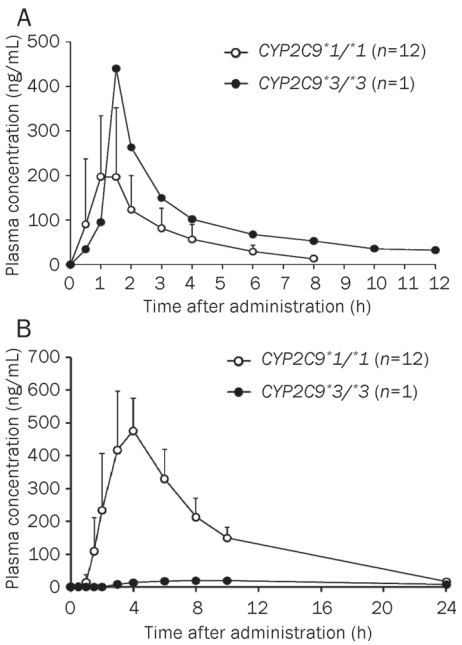


**Figure 1.** Plasma concentration-time profiles of losartan (A) and E-3174 (B) in subjects with the *CYP2C9*1/*1* (*n*=12, open circles) or *CYP2C9*3/*3* (*n*=1, closed circles) genotypes after administration of a single 50 mg oral dose of losartan.

## Discussion

CYP2C9 catalyzes phase I metabolism for approximately 15%–20% of the drugs subject to this reaction. The CYP2C9 allelic variants *CYP2C9*2*, *CYP2C9*3*, and *CYP2C9*13* code for enzymes with approximately 10%–40%, 5%–15%, and 1%–12% of the activity of *CYP2C9*1*, respectively[4, 10, 29]. The *CYP2C9*2* allele is the most common variant allele among people of European descent with a frequency of approximately 0.132[4, 9, 16, 30]. In contrast, the *CYP2C9*2* allele is rare in East Asians[3] (Table 3). To date, the *CYP2C9*2* allele has been detected in only two East Asian subjects, both Chinese with the *CYP2C9*1/*2* genotype[9, 16]. We did not detect the *CYP2C9*2* allele in our sample of 2154 Koreans (Table 3).

Functionally, the *CYP2C9*3* allele has the lowest metabolic activity *in vitro*, while *CYP2C9*2* lies between *CYP2C9*3* and *CYP2C9*1*[6]. Europeans have significant heterogeneity in

**Table 2.** Comparisons of reported *CYP2C9* allele frequencies in Koreans.

| *n* | *CYP2C9* allele frequency | | | | Reference |
|---|---|---|---|---|---|
| | **1* | **2* | **3* | **13* | |
| 3592 | 0.952 (0.945–0.959) | 0.000 (0.000–0.000) | 0.044 (0.037–0.051) | 0.005 (0.003–0.007) | Present study |
| 716 | 0.934 (0.916–0.952) | 0.000 (0.000–0.000) | 0.060 (0.043–0.077) | 0.006 (0.000–0.012) | [5] |
| 1148 | 0.989 (0.983–0.995) | 0.000 (0.000–0.000) | 0.011[c] (0.005–0.017) | ND | [7] |
| 590 | 0.947 (0.929–0.965) | 0.000 (0.000–0.000) | 0.051 (0.033–0.069) | 0.002 (0.000–0.006) | [13] |

Values in parentheses represent 95% confidence intervals; *n*=number of alleles; differences between frequency data were calculated using the chi-square test. ND=Not determined. [c]*P*<0.01 between present and previous studies [7] (95% CI on the difference 0.024–0.042).

**Table 3.** *CYP2C9* allele frequencies in East Asian populations.

| Populations | *n* | CYP2C9 allele frequency | | | | Reference |
|---|---|---|---|---|---|---|
| | | **1* | **2* | **3* | **13* | |
| Korean | 4308 | 0.949 (0.942–0.956) | 0.000 (0.000–0.000) | 0.046 (0.040–0.052) | 0.005 (0.003–0.007) | Present study[#] |
| Chinese | 2174 | 0.964 | 0.000 | 0.036 | ND | [14] |
| | 1008 | 0.967 | 0.000 | 0.033 | ND | [15] |
| | 788 | 0.963 | 0.001 | 0.036 | ND | [16] |
| | 400 | 0.975 | 0.000 | 0.025 | ND | [8] |
| | 338 | 0.967 | 0.000 | 0.033 | ND | [17] |
| | 230 | 0.983 | 0.000 | 0.017 | ND | [18] |
| | 204 | 0.951 | 0.000 | 0.049 | ND | [19] |
| | 796 | 0.958 | 0.001 | 0.041 | ND | [9] |
| | 658 | - | - | - | 0.006 | [20] |
| | 294 | - | - | - | 0.010 | [21] |
| Sum of Chinese | 5938 (952)[*] | 0.964 (0.959–0.969) | 0.003 (0.002–0.004) | 0.035 (0.030–0.040) | 0.007 (0.003–0.011) | |
| Japanese | 1000 | 0.966 | 0.000 | 0.034 | ND | [9] |
| | 1448 | 0.968 | 0.000 | 0.032 | ND | [22] |
| | 1200 | 0.979 | 0.000 | 0.021 | ND | [23] |
| | 524 | 0.968 | 0.000 | 0.031 | 0.002 | [10] |
| | 436 | 0.979 | 0.000 | 0.021 | ND | [24] |
| | 400 | 0.965 | 0.000 | 0.035 | ND | [8] |
| | 280 | 0.982 | 0.000 | 0.018 | ND | [25] |
| | 236 | 0.970 | 0.000 | 0.030 | ND | [26] |
| | 246 | 0.955 | 0.000 | 0.045 | ND | [27] |
| | 294 | 0.993 | 0.000 | 0.007 | ND | [28] |
| Sum of Japanese | 6064 (524)[&] | 0.972 (0.968–0.976) | 0.000 (0.000–0.000) | 0.028[c] (0.024–0.032) | 0.002 (0.000–0.005) | |

Values in parentheses represent 95% confidence intervals; *n*=number of alleles; differences between frequency data were calculated using the chi-square test. ND=Not determined.

#, Data were combined with a previous study[5].

*, &, Values in parentheses represent the total numbers with the *CYP2C9*13* allele.

[c]*P*<0.01 between present study and sum of Japanese (95% CI on the difference 0.010–0.026).

the *CYP2C9*2* allele frequency (ranging from 0.033 to 0.162), whereas the *CYP2C9*3* allele is less common[6]. The *CYP2C9*3* frequency in Koreans was previously reported as 0.011[7], but we previously found it to be 0.060[5]. Because these results are so different, an additional study was needed. In addition, the first study found no difference in the *CYP2C9*3* frequency between Korean and Japanese samples, but our previous report did[5]. In Korean population (2154 unrelated subjects), the *CYP2C9*3* frequency was 0.046, significantly higher ($P$<0.001) than the mean frequency in Japanese (0.028), but similar to the frequency in Chinese (0.035) (Table 3). Because the *CYP2C9* allele and genotype frequencies vary among studies, a large sample, such as ours, should reflect actual genotype frequencies. A recent study of 295 Koreans reported a *CYP2C9*3* frequency similar to the one found in this study[13], but the *CYP2C9*13* frequency was lower. The *CYP2C9*13* frequency in our study was 2.5-fold higher. Because the number of samples in this study ($n$=3592) was much higher

**Table 4.** Pharmacokinetic parameters of oral losartan in subjects with the *CYP2C9*1/*1* and *CYP2C9*3/*3* genotypes. Mean±SD.

| Variable | CYP2C9*1/*1 (*n*=12) | CYP2C9*3/*3 (*n*=1) |
|---|---|---|
| Losartan | | |
| $C_{max}$ (ng/mL) | 235.1±98.4 (172.6, 297.6) | 440.2 |
| $t_{1/2}$ (h) | 1.92±0.76 (1.44, 2.40) | 4.72 |
| CL/F (L/h) | 0.094±0.018 (0.082, 0.106) | 0.037 |
| $AUC_{0-\infty}$ (ng·h/mL) | 552.2±102.2 (487.3, 617.1) | 1334.9 |
| E-3174 | | |
| $C_{max}$ (ng/mL) | 524.3±84.1 (470.8, 577.8) | 19.1 |
| $t_{1/2}$ (h) | 4.29±0.40 (4.04, 4.54) | 10.56 |
| $AUC_{0-\infty}$ (ng·h/mL) | 3471.9±466.2 (3175.7, 3768.1) | 400.9 |

Values in parentheses represent 95% confidence intervals. $C_{max}$, maximum plasma concentration; $AUC_{0-\infty}$, area under the plasma concentration-time curve from time 0 to infinity; $t_{1/2}$, elimination half-life; CL/F, apparent oral clearance; *n*, number of subjects.

than that in other study (*n*=590)[13], this study may serve more reliable information on the frequencies of *CYP2C9* alleles in Korean population.

The *CYP2C9*13* allele was first identified in a Chinese sample, and the *CYP2C9*3/*13* genotype confers a remarkable reduction in metabolic activity[21]. In this study, 17 of 1796 subjects had the *CYP2C9*1/*13* genotype, while *CYP2C9*13/*13* and **3/*13* were not found (Table 1). The *CYP2C9*13* variant has impaired activity towards a number of substrates *in vivo*[20, 29, 31], and has only been found in East Asians (Table 3). It is apparently absent from African-American, European, Hispanic, and Ashkenazi Jewish populations[32].

In this study, two subjects were homozygous for *CYP2C9*3/*3*, but one did not provide written informed consent for inclusion in the pharmacokinetic study. We evaluated the enzymatic activity of the remaining *CYP2C9*3/*3* homozygote using losartan. In the *CYP2C9*3/*3* subject, the $C_{max}$ (187% of *CYP2C9*1/*1*) and AUC (242% of *CYP2C9*1/*1*) of losartan increased and the $C_{max}$ (3.6% of *CYP2C9*1/*1*) and AUC (11.5% of *CYP2C9*1/*1*) of E-3174 decreased compared with *CYP2C9*1/*1* subjects. In the *CYP2C9*3/*3* subject, E-3174 formation from losartan decreased markedly compared to *CYP2C9*1/*1* subjects, therefore the $AUC_{0-\infty}$ was about 1/9th that of *CYP2C9*1/*1* subjects. These results agree with a previous report from Sweden[33]. Although both losartan and E-3174 block angiotensin II receptors, E-3174 is at least 10-fold more potent than losartan[34], and the clinical effects of losartan are mainly due to E-3174. Thus, losartan may have reduced antihypertensive effects in *CYP2C9*3/*3* subjects than in *CYP2C9*1/*1* subjects. Therefore, *CYP2C9*3/*3* patients with hypertension might do well to take other hypertensive agents that are not metabolized by *CYP2C9*. In previous studies, losartan conversion to E-3174 was significantly reduced in the *CYP2C9*1/*3* (50%–95% of that in *CYP2C9*1/*1*)[20, 33, 35, 36] and **1/*13* genotypes (62% of that in *CYP2C9*1/*1*)[20]. Because the $AUC_{0-\infty}$ of E-3174 did not differ significantly between *CYP2C9*1/*1* subjects and *CYP2C9*3* or *13 heterozygotes, these genotypes did not affect the clinical effects of losartan. Because the *CYP2C9*3/*3* genotype has almost no enzyme activity, the use of warfarin, phenytoin, and oral hypoglycemic agents might be hazardous[1, 2, 6].

In summary, the *CYP2C9*3* frequency in the Korean population was estimated to be 0.044 (95% CI 0.037–0.051) and the *CYP2C9*13* frequency was estimated to be 0.005 (95% CI 0.003–0.007). Only four genotypes (*CYP2C9*1/*1*, **1/*3*, **1/*13*, and **3/*3*) were found in a large Korean sample. *CYP2C9*3/*3* subjects formed markedly less E-3174 from losartan than *CYP2C9*1/*1* subjects, suggesting a profound reduction in antihypertensive effect of losartan in this genotype.

## Acknowledgements

This study was supported by a grant (No 09172KFDA646) from Korea Food & Drug Administration in 2009–2010.

## Author contribution

Jung-woo BAE performed genotyping and PK study and wrote the paper. Chang-ik CHOI performed genotyping and PK study and wrote the paper. Mi-jeong KIM performed volunteer recruiting and genotyping. Da-hee OH performed genotyping and PK study. Seul-ki KEUM performed genotyping and PK study. Jung-in PARK performed volunteer recruiting and genotyping. Bo-hye KIM performed genotyping and PK study. Hye-kyoung BANG performed volunteer recruiting and genotyping. Sung-gon OH performed genotyping and PK study. Byung-sung KANG performed volunteer recruiting and genotyping. Hye-in LEE determined losartan concentration in plasma. Yun-jeong LEE performed volunteer recruiting and genotyping. Hyun-joo PARK performed volunteer recruiting and genotyping. Hae-deun KIM performed volunteer recruiting and genotyping. Ji-hey HA performed volunteer recruiting and genotyping. Hee-jung SHIN performed volunteer recruiting and genotyping. Young-hoon KIM performed volunteer recruiting and genotyping. Han-sung NA performed volunteer recruiting and genotyping. Myeon-woo CHUNG performed volunteer recruiting and genotyping. Soon-young HAN determined losartan concentration in plasma. Seung-hee KIM determined losartan concentration in plasma. Choon-gon JANG analyzed data. Seok-yong LEE designed research and wrote the paper.

## References

1 Miners JO, Birkett DJ. Cytochrome P4502C9: an enzyme of major importance in human drug metabolism. Br J Clin Pharmacol 1998; 45: 525–38.
2 Schwarz UI. Clinical relevance of genetic polymorphisms in the human CYP2C9 gene. Eur J Clin Invest 2003; 33: 23–30.
3 García-Martín E, Martínez C, Ladero JM, Agúndez JA. Interethnic and intraethnic variability of CYP2C8 and CYP2C9 polymorphisms in healthy individuals. Mol Diagn Ther 2006; 10: 29–40.
4 Scordo MG, Caputi AP, D'Arrigo C, Fava G, Spina E. Allele and genotype frequencies of CYP2C9, CYP2C19 and CYP2D6 in an Italian population. Pharmacol Res 2004; 50: 195–200.

5 Bae JW, Kim HK, Kim JH, Yang SI, Kim MJ, Jang CG, *et al*. Allele and genotype frequencies of CYP2C9 in a Korean population. Br J Clin Pharmacol 2005; 60: 418–22.
6 Lee CR, Goldstein JA, Pieper JA. Cytochrome P450 2C9 polymorphisms: a comprehensive review of the *in-vivo* and human data. Pharmacogenetics 2002; 12: 251–63.
7 Yoon YR, Shon JH, Kim MK, Lim YC, Lee HR, Park JY, *et al*. Frequency of cytochrome P450 2C9 mutant alleles in a Korean population. Br J Clin Pharmacol 2001; 51: 277–80.
8 Myrand SP, Sekiguchi K, Man MZ, Lin X, Tzeng RY, Teng CH, *et al*. Pharmacokinetics/genotype associations for major cytochrome P450 enzymes in native and first- and third-generation Japanese populations: comparison with Korean, Chinese, and Caucasian populations. Clin Pharmacol Ther 2008; 84: 347–61.
9 Man M, Farmen M, Dumaual C, Teng CH, Moser B, Irie S, *et al*. Genetic variation in metabolizing enzyme and transporter genes: comprehensive assessment in 3 major East Asian subpopulations with comparison to Caucasians and Africans. J Clin Pharmacol 2010; 50: 929–40.
10 Maekawa K, Fukushima-Uesaka H, Tohkin M, Hasegawa R, Kajio H, Kuzuya N, *et al*. Four novel defective alleles and comprehensive haplotype analysis of CYP2C9 in Japanese. Pharmacogenet Genomics 2006; 16: 497–514.
11 Stearns RA, Chakravarty PK, Chen R, Chiu SH. Biotransformation of losartan to its active carboxylic acid metabolite in human liver microsomes. Role of cytochrome P4502C and 3A subfamily members. Drug Metab Dispos 1995; 23: 207–15.
12 Ritter MA, Furtek CI, Lo MW. An improved method for the simultaneous determination of losartan and its major metabolite, EXP3174, in human plasma and urine by high-performance liquid chromatography with fluorescence detection. J Pharm Biomed Anal 1997; 15: 1021–9.
13 Lee HW, Lim MS, Lee J, Jegal MY, Kim DW, Lee WK, *et al*. Frequency of CYP2C9 variant alleles, including CYP2C9*13 in a Korean population and effect on glimepiride pharmacokinetics. J Clin Pharm Ther 2011. doi: 10.1111/j.1365-2710.2010.01238.x.
14 Hong X, Zhang S, Mao G, Jiang S, Zhang Y, Yu Y, *et al*. CYP2C9*3 allelic variant is associated with metabolism of irbesartan in Chinese population. Eur J Clin Pharmacol 2005; 61: 627–34.
15 Yu BN, Luo CH, Wang D, Wang A, Li Z, Zhang W, *et al*. CYP2C9 allele variants in Chinese hypertension patients and healthy controls. Clin Chim Acta 2004; 348: 57–61.
16 Yang JQ, Morin S, Verstuyft C, Fan LA, Zhang Y, Xu CD, *et al*. Frequency of cytochrome P450 2C9 allelic variants in the Chinese and French populations. Fund Clin Pharmacol 2003; 17: 373–6.
17 Chen K, Wang R, Wen SY, Li J, Wang SQ. Relationship of P450 2C9 genetic polymorphisms in Chinese and the pharmacokinetics of tolbutamide. J Clin Pharm Ther 2005; 30: 241–9.
18 Wang SL, Huang J, Lai MD, Tsai JJ. Detection of CYP2C9 polymorphism based on the polymerase chain reaction in Chinese. Pharmacogenetics 1995; 5: 37–42.
19 Gaedigk A, Casley WL, Tyndale RF, Sellers EM, Jurima-Romet M, Leeder JS. Cytochrome P-4502C9 (CYP2C9) allele frequencies in Canadian Native Indian and Inuit populations. Can J Physiol Pharmacol 2001; 79: 841–7.
20 Li Z, Wang G, Wang LS, Zhang W, Tan ZR, Fan L, *et al*. Effects of the CYP2C9*13 allele on the pharmacokinetics of losartan in healthy male subjects. Xenobiotica 2009; 39: 788–93.
21 Si D, Guo Y, Zhang Y, Yang L, Zhou H, Zhong D. Identification of a novel variant CYP2C9 allele in Chinese. Pharmacogenetics 2004; 14: 465–9.
22 Yin T, Maekawa K, Kamide K, Saito Y, Hanada H, Miyashita K, *et al*. Genetic variations of CYP2C9 in 724 Japanese individuals and their impact on the antihypertensive effects of losartan. Hypertens Res 2008; 31: 1549–57.
23 Yoshizawa M, Hayashi H, Tashiro Y, Sakawa S, Moriwaki H, Akimoto T, *et al*. Effect of VKORC1-1639 G>A polymorphism, body weight, age, and serum albumin alterations on warfarin response in Japanese patients. Thromb Res 2009; 124: 161–6.
24 Nasu K, Kubota T, Ishizaki T. Genetic analysis of CYP2C9 polymorphism in a Japanese population. Pharmacogenetics 1997; 7: 405–9.
25 Kimura M, Ieiri I, Mamiya K, Urae A, Higuchi S. Genetic polymorphism of cytochrome P-450s, CYP2C19, and CYP2C9 in a Japanese population. Ther Drug Monitor 1998; 20: 243–7.
26 Obayashi K, Nakamura K, Kawana J, Ogata H, Hanada K, Kurabayashi M, *et al*. VKORC1 gene variations are the major contributors of variation in warfarin dose in Japanese patients. Clin Pharmacol Ther 2006; 80: 169–78.
27 Xie HG, Prasad H, Landau R, Kim RB, Cai WM, Ieiri I, *et al*. Frequency of the defective CYP2C9 variant alleles in different ethinc groups [abstract]. Clin Pharmacol Ther 2002; 71: P102.
28 Nakai K, Habano W, Nakai K, Fukushima N, Suwabe A, Moriya S, *et al*. Ethnic differences in *CYP2C9*2* (Arg144Cys) and *CYP2C9*3* (Ile359Leu) genotypes in Japanese and Israeli populations. Life Sci 2005; 78: 107–11.
29 Guo Y, Zhang Y, Wang Y, Chen X, Si D, Zhong D, *et al*. Role of CYP2C9 and its variants (CYP2C9*3 and CYP2C9*13) in the metabolism of lornoxicam in humans. Drug Metab Dispos 2005; 33: 749–53.
30 Yasar U, Eliasson E, Dahl ML, Johansson I, Ingelman-Sundberg M, Sjöqvist F. Validation of methods for CYP2C9 genotyping: frequencies of mutant alleles in a Swedish population. Biochem Biophys Res Commun 1999; 254: 628–31.
31 Bae JW, Choi CI, Jang CG, Lee SY. Effects of CYP2C9*1/*13 on the pharmacokinetics and pharmacodynamics of meloxicam. Br J Clin Pharmacol 2011; 71: 550–5.
32 Scott SA, Khasawneh R, Peter I, Kornreich R, Desnick RJ. Combined CYP2C9, VKORC1 and CYP4F2 frequencies among racial and ethnic groups. Pharmacogenomics 2010; 11: 781–91.
33 Yasar U, Forslund-Bergengren C, Tybring G, Dorado P, Llerena A, Sjöqvist F, *et al*. Pharmacokinetics of losartan and its metabolite E-3174 in relation to the CYP2C9 genotype. Clin Pharmacol Ther 2002; 71: 89–98.
34 Sachinidis A, Ko Y, Weisser P, Meyer zu Brickwedde MK, Düsing R, Christian R, *et al*. EXP3174, a metabolite of losartan [MK 954, DuP 753] is more potent than losartan in blocking the angiotensin II-induced responses in vascular smooth muscle cells. J Hypertens 1993; 11: 155–62.
35 Sekino K, Kubota T, Okada Y, Yamada Y, Yamamoto K, Horiuchi R, *et al*. Effect of the single CYP2C9*3 allele on pharmacokinetics and pharmacodynamics of losartan in healthy Japanese subjects. Eur J Clin Pharmacol 2003; 59: 589–92.
36 Lee CR, Pieper JA, Hinderliter AL, Blaisdell JA, Goldstein JA. Losartan and E3174 pharmacokinetics in cytochrome P450 2C9*1/*1, *1/*2, and *1/*3 individuals. Pharmacotherapy 2003; 23: 720–5.